

Cardiff University

School of Chemistry



**NOVEL LUMINESCENT PLATINUM (II) AND
LANTHANIDE (III) COMPLEXES TOWARDS
IMAGING, DIAGNOSTICS AND THERAPEUTICS**

Thesis submitted for the degree of Doctor of Philosophy by:

Oliver James Stacey

April 2015

CARDIFF UNIVERSITY

SCHOOL OF CHEMISTRY

ABSTRACT

Doctor of Philosophy

NOVEL LUMINESCENT PLATINUM (II) AND LANTHANIDE (III)
COMPLEXES TOWARDS IMAGING, DIAGNOSTICS AND
THERAPEUTICS

By Oliver James Stacey

This thesis discusses the development and synthesis of ligands for coordination to *d*- and *f*- block metal ions. The subsequent coordination chemistry to Pt^{II} and a range of Ln^{III} metal ions is outlined, along with the photophysical properties of the resultant compounds towards bimodal imaging agents and probes for diagnostic and therapeutic applications.

Chapter 2 presents the synthesis and characterisation of a range of Pt^{II} complexes using functionalised 2-phenylquinoline ligands. A range of products were synthesised by utilising a variety of ancillary ligands, including β -diketones, 8-hydroxyquinoline, 2,2'-bipyridine and pyridine, in order to investigate any effects on the photophysical properties. X-ray crystallography confirmed the anticipated structures of several compounds whilst ¹⁹⁵Pt NMR was employed to probe the metal environment in the different complexes.

Chapter 3 builds on the investigations in the previous chapter by altering the functionality of the 2-phenylquinoline ligand in order to tune the solubility. The second part of Chapter 3 exploits the facile coordination of pyridine, as found in Chapter 2, by introducing pendant pyridine-appended macrocycles encapsulating Ln^{III} ions. This provided bimetallic complexes with good water solubility, which allowed relaxivity measurements to be carried out. Photophysical measurements also gave evidence of direct sensitisation of the Ln^{III} ion by Pt^{II} based ³MLCT emission.

Chapter 4 extends the 2-phenylquinoline functionality to incorporate naphthyl, anthracenyl and pyrenyl chromophores with suitable solubility in common organic solvents. The complexes were investigated to determine whether it was possible to observe interactions between the excited state of the chromophore and the metal-centred excited state. Low temperature and degassed steady state luminescence and lifetime measurements were obtained in order to build energy level diagrams to explain the interplay of excited states.

Chapter 5 discusses the development of anthraquinone-based polypyridyl ligand scaffolds for the incorporation of Ln^{III} ions. The ligands possess subtle differences that result in changes in the coordination sphere of the Ln^{III} ion. This was confirmed by determining the inner-sphere hydration of the Ln^{III} ions through observing the luminescence properties of the complexes.

Acknowledgements

I would firstly like to thank my supervisors, Simon, Angelo and Damien, for their determination in obtaining funding for my PhD; without their hard work and commitment, none of this would have been possible. I would like to thank Simon for his constant belief in my ability, even after months of fruitless research, and for his brilliant ideas that seem to now reach into every corner of inorganic chemistry, for dedicating so much time to helping me obtain data and finally for all the insightful conversations we have shared over the last few years. To Angelo: thank you primarily for checking we were still alive in Simon's absence! Thanks also for all the knowledge you have imparted, the synthetic guidance you have given me and the time you have spent helping me relax. Finally, a big thank you to Damien for not appearing disappointed that, despite attempts, we never managed to get to a point where we could run any EPR or ENDOR measurements that gave conclusive data – my reliance on ^1H NMR for conclusive proof will forever remain my Achilles' heel. Along side my supervisors I'd like to say a big thank you to Jamie for the invaluable DFT calculations and to Hallett and Woody for their years (most of which have been accrued by Woody) of insight and knowledge that I did my best to exploit over the last few years.

A massive thank you to all the technical staff at Cardiff: Rob for his knowledge in everything analytical that allowed me to obtain some great ^{195}Pt NMR and MALDI data, Robin and Simon for their tireless efforts to obtain meaningful mass spec data that magically jumped queues towards the end of my PhD as deadlines grew closer. Thanks also to Gaz and Jamie for supplying me with all the essentials for the lab (and to Simon for supplying fans – also essential at times). Thanks to Rob and Louise for the laughs during demonstrating and also for the steady supply of unused equipment over the past three years – many a column has been done on the glassware you no longer used! Big thanks to Terrie and Al for all the fun chats and to Tom for all the hours of demonstrating he gave me to keep me afloat financially!

A special thank you to Bec, Flo and Coogs who inspired me to do a PhD in the first place. There've been times, since, when I've cursed your existence but it seems to have worked out okay in the end! A massive thanks also to the wonderful inorganic section, past and present, (and Dayna) who have made the last three years much more fun than they should have been: Andy, Woody, Dayna, Si, Bec, Flo, Owen, Tim, Kate, Tracy, Tom, Brendan, Mark, Mauro, Lenali, Emily, Lara, Emma, Jules and, because I wanted to leave the best 'til last, Stokes.

To my friends outside of uni life and Cardiff – thank you for putting up with me being inappropriately unsociable for the last few years and for not visiting home as often as I would have liked. I will look forward to a few cheeky drinks when I finish!

It goes without saying that I would never have got to university in the first place without the drive nurtured into me by my parents, who have worked tirelessly as far back as I can remember to provide the best upbringing possible. To my Dad who worked long hours all over the world in order to support the family financially so that we could fulfil our dreams: thank you. To my Mum, who raised my sister and I to be inquisitive and to want to learn, who has always been the rock of the family, despite none of us ever showing just how grateful we are: thank you will never be enough. To my grandparents, including those who've passed over the course of my PhD: I will cherish the memories you have given me for the rest of my life. This is for you.

Contents

Chapter 1: Introduction.....	1
1.1. Coordination chemistry.....	2
1.1.1. Transition metal coordination complexes.....	2
1.1.2. Chelate effect.....	5
1.1.3. Lanthanide coordination.....	7
1.1.4. Macrocyclic effect.....	11
1.2. Luminescence.....	14
1.2.1. Light.....	14
1.2.2. Fluorescence.....	16
1.2.3. Phosphorescence.....	18
1.2.4. Lifetimes.....	18
1.2.5. Quenching.....	19
1.2.6. Solvent effects.....	21
1.2.7. Quantum yields.....	22
1.2.8. Luminescent transition metal complexes.....	23
1.2.9. Luminescent lanthanide complexes.....	23
1.3. References.....	25
Chapter 2: Tuning the photophysical properties of platinum (II) complexes.....	29
2.1. Introduction.....	30
2.1.1. Use of platinum (II) complexes in cancer treatment.....	30
2.1.2. Photophysical properties of platinum (II) complexes.....	32
2.1.3. Ancillary ligands for cyclometallated platinum (II) complexes.....	35
2.1.4. Imaging and bioimaging applications of platinum (II) complexes.....	37
2.1.5. ¹⁹⁵ Pt NMR spectroscopy.....	38
2.1.6. Functionalised phenylquinolines.....	39
2.2. Aims.....	41
2.3. Results and Discussion.....	42
2.3.1. Ligand synthesis.....	42
2.3.2. Synthesis and characterisation of cyclometallated platinum (II) complexes.....	42
2.3.3. ¹⁹⁵ Pt NMR spectroscopy analysis.....	49
2.3.4. X-ray crystal structures.....	52
2.3.5. X-ray crystal structure of [Pt(L1)(DMSO)Cl].....	54
2.3.6. X-ray crystal structure of [Pt(L1)(acac)].....	55
2.3.7. X-ray crystal structure of [Pt(L1)(bpy)](PF ₆).....	56
2.3.8. X-ray crystal structure data.....	57
2.3.9. Electronic absorption spectroscopy and DFT calculations.....	58
2.4. Conclusion.....	66
2.5. Experimental.....	67
2.5.1. General physical measurements.....	67
2.5.2. Density functional theory.....	67
2.5.3. X-ray crystallography.....	68
2.5.4. Ligand synthesis.....	68
2.5.5. Complex synthesis.....	69
2.6. References.....	77

Chapter 3: Adapting platinum (II) complexes towards diagnostic and therapeutic applications	84
3.1. Introduction.....	85
3.1.1. Amyloid- β peptide and Alzheimer's disease – The amyloid hypothesis ..	85
3.1.2. Peptide binding	86
3.1.3. Magnetic resonance imaging	88
3.1.4. Relaxivity	89
3.1.5. Contrast agents	90
3.1.6. Photophysical properties of lanthanides	92
3.1.7. Bimodal contrast agents	94
3.2. Aims.....	96
3.3. Results and Discussion.....	97
3.3.1. Development and synthesis of 2-phenylquinoline ligand functionalisation	97
3.3.2. Synthesis and characterisation of platinum (II) complexes	98
3.3.3. X-ray crystal structures	100
3.3.4. X-ray crystal structure of [Pt(L5)(acac)]	101
3.3.5. X-ray crystal structure of [Pt(L9)(DMSO)Cl]	102
3.3.6. Crystal structure data	103
3.3.7. Photophysical properties of complexes	104
3.3.8. Development of a bimodal contrast agent incorporating platinum (II) ...	105
3.4. Conclusion	110
3.5. Experimental	111
3.5.1. General physical measurements	111
3.5.2. Precursor synthesis.....	111
3.5.3. Ligand synthesis.....	112
3.5.4. Synthesis of platinum (II) complexes	114
3.6. References	121
Chapter 4: Examining the photophysical properties of chromophore appended platinum (II) complexes.....	124
4.1. Introduction.....	125
4.1.1. Photophysical properties of pyrene monomers.....	125
4.1.2. Photophysical properties of pyrene excimers	126
4.1.3. Pyrene in biological imaging	126
4.1.4. Development of long lifetime complexes using pyrene	127
4.1.5. Pyrene in platinum (II) complexes.....	130
4.2. Aims.....	132
4.3. Results and Discussion.....	133
4.3.1. Ligand development and synthesis	133
4.3.2. Synthesis and characterisation of cyclometallated platinum (II) complexes	136
4.3.3. X-ray crystal structures	138
4.3.4. X-ray crystal structure of [Pt(L15)(acac)]	139
4.3.5. X-ray crystal structure of [Pt(L16)(acac)]	140
4.3.6. X-ray crystal data	141
4.3.7. Electronic absorption spectroscopy	142
4.3.8. Luminescence spectroscopy.....	143
4.4. Conclusion	149
4.5. Experimental	150

4.5.1. General physical measurements.....	150
4.5.2. Molecular structure calculations	150
4.5.3. Precursor synthesis.....	150
4.5.4. Ligand synthesis.....	152
4.5.5. Synthesis of platinum (II) complexes	155
4.6. References	160

Chapter 5: Development of anthraquinone-derived scaffolds for lanthanide (III) ion coordination.....

5.1. Introduction.....	164
5.1.1. Anthraquinone.....	164
5.2. Aims.....	168
5.3. Results and Discussion.....	169
5.3.1. Precursor and ligand synthesis.....	169
5.3.2. Complex synthesis	170
5.3.3. Electronic absorption spectroscopy	170
5.3.4. Luminescence spectroscopy.....	171
5.3.5. Relaxivity	174
5.4. Conclusion	177
5.5. Experimental	178
5.5.1. General physical measurements.....	178
5.5.2. Precursor synthesis.....	178
5.5.3. Ligand synthesis.....	179
5.5.4. Synthesis of Complexes	180
5.6. References	184

List of Figures

Figure 1.1 MO diagram for the σ -bonds of an O_h complex. ⁶	3
Figure 1.2 Selection of well-known square planar d^8 transition metal complexes.	4
Figure 1.3 d orbital splitting for low spin square planar (<i>left</i>) and high spin tetrahedral (<i>right</i>) d^8 complexes.	4
Figure 1.4 Preorganisation of a 5-membered chelate ring in phen compared with the rearrangement required by bpy in order to form a 5-membered chelate.	6
Figure 1.5 Examples of chelating square planar Pt^{II} complexes in the literature.	7
Figure 1.6 Radial part of the hydrogenic wave functions for the $4f$, $5d$ and $6s$ orbitals of cerium. ¹⁹	8
Figure 1.7 Tricapped trigonal prismatic structure of a nonaqua lanthanide ion. ²⁵	10
Figure 1.8 Structures of some chelating and macrocyclic Ln^{III} complexes.	11
Figure 1.9 Comparative macrocyclic and open-chain Cu^{II} complexes with very different stabilities.	11
Figure 1.10 Cyclam (<i>left</i>) and a corresponding open chain derivative (<i>right</i>) that have been used to demonstrate the enthalpic and entropic contributions towards the macrocyclic effect using Ni^{II} .	12
Figure 1.11 Diagrammatic representation of the reason for slow formation of macrocyclic compounds. ²⁴	13
Figure 1.12 Electromagnetic spectrum with relevant frequencies for the different categories of light. ³⁹	15
Figure 1.13 Jablonski diagram illustrating the radiative (solid arrows) and non-radiative (dashed arrows) processes that can occur within a molecule.	16
Figure 1.14 Diagram representing the vertical transitions outlined in the Franck-Condon principle. ⁴²	17
Figure 1.15 Intermolecular interactions leading to the deactivation of excited state molecules.	19
Figure 1.16 Normalised emission spectra of Ln^{III} ion complexes demonstrating the breadth of the lanthanide series' emission and the narrow emission profile of the individual lanthanide ions. ¹⁸	24
Figure 2.1 Structures of some Pt^{II} complexes used as chemotherapy drugs.	31
Figure 2.2 Cisplatin pathways into, within and out of cells as well as means of inactivation. ⁹	31
Figure 2.3 Charge transfer processes within a generic transition metal complex. ¹⁴	33
Figure 2.4 Simplified molecular orbital (MO) diagram of interacting square-planar Pt^{II} complexes showing influence of d_z^2 interaction on the energy levels of the MOs.	34
Figure 2.5 A selection of ancillary ligands found on cyclometallated Pt^{II} complexes.	35
Figure 2.6 Range of cyclometallated Pt^{II} complexes where the cationic species localise in nuclei (<i>top</i>) and neutral compounds exhibit cytoplasmic localisation (<i>bottom</i>).	37
Figure 2.7 Complexes synthesised by Botchway <i>et al.</i> for cellular imaging using TPE and TREM.	38
Figure 2.8 Structures of a range of phenylquinoline compounds with biological activity. Of note are cinchophen (<i>bottom left</i>) and Talnetant (<i>top right</i>), which have undergone clinical trials.	39
Figure 2.9 Examples of some Ir^{III} and Pt^{II} complexes incorporating phenylquinoline ligands.	40

Figure 2.10 Structures of the ligands utilised in Chapter 2.....	42
Figure 2.11 Synthesis of [Pt(L)(μ-Cl)] ₂ and [Pt(L)(DMSO)Cl] R = OEt (L1), HN <i>t</i> -butyl (L2), HN <i>p</i> -fluorobenzene (L3), OH (L4).....	43
Figure 2.12 ¹ H NMR spectrum for [Pt(L1)(DMSO)Cl]. Highlighted: SO(CH ₃) ₂ with ³ J _{HPt} coupling.	44
Figure 2.13 Synthesis of [Pt(L)(py)Cl], [Pt(L)(8-Q)] and [Pt(L)(β-diketonate)]: R = OEt (L1), HN <i>t</i> -butyl (L2), HN <i>p</i> -fluorobenzene (L3), OH (L4); R' = CH ₃ (acac), C(CH ₃) ₃ (hmacac), CF ₃ (hfacac).....	45
Figure 2.14 ¹ H NMR spectrum for [Pt(L1)(acac)]. Highlighted: CH ₃ C=OCHC=OCH ₃ (<i>middle</i>), CH ₃ C=OCHC=OCH ₃ (<i>right</i>).....	46
Figure 2.15 ¹ H NMR spectrum of [Pt(L1)(8-Q)]. Highlighted: NC ² H of 8-quinolinato with ³ J _{HPt} coupling.	47
Figure 2.16 ¹ H NMR spectrum for [Pt(L1)(py)Cl]. Highlighted: NC ² H of pyridine (<i>left</i>), PtCCH of L1 (<i>right</i>) showing ³ J _{HPt} coupling.	48
Figure 2.17 Schematic of the first attempts to synthesise a cationic Pt ^{II} complex.	48
Figure 2.18 Schematic of the successful synthetic route to [Pt(L)(bpy)] ⁺	49
Figure 2.19 Ball and stick X-ray crystal structure of [Pt(L1)(DMSO)Cl] (<i>top</i>) and the unit cell packing (<i>bottom</i>).	54
Figure 2.20 Ball and stick X-ray crystal structure of [Pt(L1)(acac)] (<i>top</i>), the Pt-Pt interaction (<i>middle</i>) and the unit cell packing (<i>bottom</i>).....	55
Figure 2.22 Absorption profiles (normalised) for complexes in chloroform.....	59
Figure 2.23 Absorption profiles (normalised) against excitation bands predicted using DFT.....	62
Figure 2.24 Normalised emission profiles of a selection of complexes from Chapter 2.	64
Figure 2.25 Normalised lifetime decay profiles.	65
Figure 3.1 Structure of amyloid-β peptide in water determined by NMR spectroscopy (<i>left</i>) ² and amyloid cascade process (<i>right</i>). ³	85
Figure 3.2 Structures (<i>left to right</i>) of bathocuproine, bathocuproine sulfonic acid and the three L-PtCl ₂ complexes investigated by Barnham <i>et al.</i> ¹²	87
Figure 3.3 Interaction of [Pt(Cl) ₂ (phen)] with Aβ ₁₋₁₆ . ¹³	87
Figure 3.4 Binding of a cyclometallated Pt ^{II} complex with Aβ ₁₋₁₆ . ¹⁴	88
Figure 3.5 Graphical depiction of the factors influencing <i>r</i> ₁ relaxation rates. ²⁶	90
Figure 3.6 Commonly used Gd ^{III} contrast agents.	91
Figure 3.7 Structures of compounds with enhanced <i>r</i> ₁ values.	91
Figure 3.8 Schematic representation of the energy pathways within organically and inorganically sensitised lanthanide(III) complexes. S _n = excited singlet state, ILCT = intra-ligand charge transfer, T ₁ = excited triplet state, LMCT = ligand-to-metal charge transfer, S = singlet energy transfer, ISC = intersystem crossing, IL = intra-ligand energy transfer, LM = ligand-metal energy transfer, 4 <i>f</i> [*] = excited 4 <i>f</i> electronic state. Back transfer processes are omitted for clarity. ³³	93
Figure 3.9 Structures of dimetallic complexes incorporating transition metals and a Ln ^{III} ions.....	94
Figure 3.10 Three functionalised MRI contrast agents exhibiting bimodal properties.	95
Figure 3.11 Structures of ligands LH5 to LH9	97
Figure 3.12 Ball and stick X-ray crystal structure of [Pt(L5)(acac)] (<i>top</i>), the Pt-Pt interaction (<i>middle</i>) and the unit cell packing (<i>bottom</i>).....	101
Figure 3.13 Ball and stick X-ray crystal structure of [Pt(L9)(DMSO)Cl] (<i>top</i>) and the unit cell packing (<i>bottom</i>).	102

Figure 3.14 Synthetic route for a pyridine functionalised DO3A as used by Koullourou <i>et al.</i> ⁴³	105
Figure 3.15 Synthetic route to L10 based on work by Crich and Andre <i>et al.</i> ^{50, 51}	106
Figure 3.16 Structure (<i>top left</i>) and MALDI-TOF MS spectrum (<i>top right</i>) of [Pt(L9){(L10)Gd}] and the UV-vis spectra of (L10), [Gd(L10)], [Yb(L10)], [Pt(L9)(DMSO)Cl], [Pt(L9){Gd(L10)}Cl] and [Pt(L9){Gd(L10)}Cl] (<i>bottom</i>).	107
Figure 3.17 Excitation and emission profiles for [Pt(L9){Yb(L10)}Cl] where excitation is in black, ³ MLCT emission is in green and ² F _{5/2} ² F _{7/2} Yb ^{III} emission is in red.	107
Figure 3.18 Fitted ¹ H NMRD plots of [Gd(L10)] and [Pt(L9){Gd(L10)}Cl].	109
Figure 4.1 Absorption spectrum of pyrene in cyclohexane with transitional assignments (<i>left</i>) ¹ and structure of pyrene (<i>right</i>).	125
Figure 4.2 Pyrene excimer emission ($\lambda_{em} = 492\text{ nm}$). ⁶	126
Figure 4.3 Pyrene-labelled mRNA bases leading to the formation of pyrene excimers. ¹⁷	127
Figure 4.4 Ru ^{II} complexes incorporating pyrene functionalisation.	128
Figure 4.5 Energy pathways associated with pyrene acting as an antenna. ²³	129
Figure 4.6 Ir ^{III} and Re ^I complexes incorporating pyrene functionalised ligands.	129
Figure 4.7 Examples of pyrene incorporated into Pt ^{II} complexes for photophysical investigations.	130
Figure 4.8 Structure of LH11 (<i>left</i>) and the development of a suitably soluble ligand with an appended anthracene chromophore from LH12 to eventually give LH15 (<i>right</i>).	133
Figure 4.9 Structures of the precursors, P6 – P9 .	133
Figure 4.11 5 – 6 ppm region of the ¹ H NMR spectrum of LH16 demonstrating the inequivalence of the protons on the methyl linker between the amide and the pyrene chromophore (<i>left</i>). Geometrically optimised structures for the two isomers of LH16 (<i>right</i>).	135
Figure 4.12 ¹ H NMR spectrum of [Pt(L16)(acac)] highlighting evidence of the two isomers.	136
Figure 4.13 Ball and stick X-ray crystal structure of [Pt(L15)(acac)] (<i>top</i>), the Pt-Pt interaction (<i>middle</i>) and the packing arrangement (<i>bottom</i>).	139
Figure 4.14 Ball and stick X-ray crystal structure of [Pt(L16)(acac)] (<i>top</i>) and the packing arrangement (<i>bottom</i>).	140
Figure 4.15 Absorption profiles for the ligands and complexes in chloroform.	142
Figure 4.17 Comparison of the aerated and degassed emission in chloroform (<i>left</i>) and room temperature and low temperature emission in 1:1 chloroform and ethanol (<i>right</i>) of [Pt(L15)(acac)]. Room temperature and low temperature emission of LH15 is also included with dashed lines (<i>right</i>).	145
Figure 4.18 Comparison of the aerated and degassed emission in chloroform (<i>left</i>) and room temperature and low temperature emission in 1:1 chloroform and ethanol (<i>right</i>) of [Pt(L16)(acac)]. Room temperature and low temperature emission of LH16 is also included with dashed lines (<i>right</i>). Insert: Expanded section of LH16 at low temperature to show evidence of ³ IL emission.	146
Figure 4.19 Energy level diagram of the relevant excited states of [Pt(L14)(acac)].	148
Figure 4.20 Energy level diagram of the relevant excited states of [Pt(L15)(acac)].	148
Figure 4.21 Energy level diagram of the relevant excited states of [Pt(L16)(acac)].	148
Figure 5.1 Structure and numbering of anthraquinone.	164

Figure 5.2 Structures of some naturally occurring (<i>top</i>) and commercially available (<i>bottom</i>) AQs. ¹⁰	165
Figure 5.3 Structures of a Ru-AQ (alizarin) complex under different conditions (<i>left</i>) and the redox products of Ru-dppzAQ (<i>right</i>).....	166
Figure 5.4 Pt ₂ -AQ complex, which exhibits Pt-Pt interactions resulting in low energy emission.	166
Figure 5.5 Structures of AQ-Ln complexes where AQ acts as a sensitiser for near-IR Ln ^{III} metal ion emission.	167
Figure 5.6 Hg ^{II} sensitive AQ-Ln probe with a multidentate Hg ^{II} binding site (highlighted in green).....	167
Figure 5.7 Synthetic pathway to the synthesis of L17 , L18 and L19 via P10 , P11 and P12 , respectively, from 1,8-dichloroanthraquinone (<i>left</i>).....	169
Figure 5.8 Excitation and emission (room temperature and low temperature) of [Gd(L18)](OTf) ₃	171
Figure 5.9 Excitation and emission profiles for [Yb(L19)](OTf) ₃ , where excitation is in black, ligand emission is in green and ² F _{5/2} → ² F _{7/2} Yb ^{III} emission is in red.	172
Figure 5.10 Decay profiles, with fit residuals, for Yb ^{III} (<i>left</i>), Nd ^{III} (<i>middle</i>) and Er ^{III} (<i>right</i>) complexes in CD ₃ OD, λ _{ex} at 355 nm.	173
Figure 5.11 Proposed coordination modes of [Ln(L17-L19)](OTf) ₃ based on <i>q</i> values.	174
Figure 5.12 ¹ H NMRD profiles for GdCl ₃ in various H ₂ O/DMSO ratios at 37 °C with various field strengths (<i>left</i>) and change in relaxivity at 30 and 0.01 MHz and the change in viscosity of a water/DMSO solution at solvent ratios (<i>right</i>). ²¹	174
Figure 5.13 ¹ H NMRD profiles of GdCl ₃ in H ₂ O and H ₂ O/DMSO (1:1) and [Gd(L17-L19)](OTf) ₃ in H ₂ O/DMSO (1:1) at 37 °C.....	176

List of Tables

Table 1.1 Comparison of the change in the Gibbs free energies upon ligand exchange with various monodentate and related bidentate ligands from $[\text{Ni}(\text{OH}_2)_6]^{2+}$. ³	6
Table 1.2 Changes in the enthalpic and entropic effects between a cyclic and open-chain Ni^{II} complex.	13
Table 1.3 Stability constants of Gd^{III} complexes with a range of monodentate, polydentate and macrocyclic ligand architectures.	14
Table 1.4 The effect of solvent polarity on the $(n \rightarrow \pi^*)$ transition in acetone. ⁴⁹	22
Table 2.1 ^{195}Pt NMR spectroscopy chemical shifts for all complexes in Chapter 2 (<i>left</i>) along with related shifts for analogous ppy complexes (<i>right</i>).	51
Table 2.2 Crystal structure data for $[\text{Pt}(\text{L1})(\text{DMSO})\text{Cl}]$, $[\text{Pt}(\text{L1})(\text{acac})]$ and $[\text{Pt}(\text{L1})(\text{bpy})](\text{PF}_6)$.	57
Table 2.3 Absorption maxima (λ_{max}) for complexes in Chapter 2.	58
Table 2.4 Calculated representations for the HOMO-1s (and HOMO-2s) (<i>left</i>), HOMOs (and HOMO-1s) (<i>middle</i>) and LUMOs (<i>right</i>) of a series of Pt^{II} complexes along with the band gaps.	60
Table 2.5 Percentage <i>d</i> -orbital character predicted for the HOMO-2, HOMO-1, HOMO and LUMO, where the orbitals involved in observable transitions in the UV-vis spectra are highlighted in bold.	61
Table 2.6 Photophysical properties of the complexes synthesised in Chapter 2.	63
Table 3.1 Crystal structure data for $[\text{Pt}(\text{L5})(\text{acac})]$ and $[\text{Pt}(\text{L9})(\text{DMSO})\text{Cl}]$.	103
Table 3.2 Photophysical properties, in chloroform solutions, of the complexes synthesised in Chapter 3.	104
Table 3.3 Photophysical data for the Pt^{II} / Ln^{III} complexes.	108
Table 4.1 Crystal structure data for $[\text{Pt}(\text{L15})(\text{acac})]$ and $[\text{Pt}(\text{L16})(\text{acac})]$.	141
Table 4.2 Absorption maxima (λ_{max}) for ligands and complexes.	142
Table 4.3 Excitation, emission and lifetime data for the ^1IL and ^3IL components of the ligands and complexes. Excited at 350 nm unless otherwise stated.	143
Table 4.4 Excitation, emission and lifetime data for the $^3\text{MLCT}$ component of the complexes. Excited at 350 nm unless otherwise stated.	143
Table 5.2 r_1 values for GdCl_3 in water and GdCl_3 and the anthraquinone complexes in a 1:1 mixture of $\text{H}_2\text{O}/\text{DMSO}$.	175

Abbreviations

Chemicals

$^1\text{O}_2$	singlet oxygen
$^3\text{O}_2$	triplet oxygen
8-HQ	8-hydroxyquinoline
8-Q	8-quinolino
A β	amyloid beta peptide
acac	2,4-pentanedione / diketone
AlCl ₃	aluminium chloride
anthr	anthracene
APP	amyloid precursor protein
AQ	anthraquinone
Asp	aspartate
bpy	2,2'-bipyridine
Bu	butyl
Bu ₄ N	tetrabutylammonium
cyclam	1,4,8,11-tetraazacyclotetradecane
cyclen	1,4,7,10-tetraazacyclododecane
d ₆ -DMSO	deuterated dimethylsulfoxide
dbacac	1,3-diphenyl-1,3-propanedione / diketone
DMF	dimethylformamide
DMSO	dimethylsulfoxide
DNA	deoxyribonucleic acid
DO3A	1,4,7,10-tetraazacyclododecane-1,4,7-trisacetic acid
DOTA	1,4,7,10-tetraazacyclododecane-1,4,7,10-tetraacetic acid
dppz	dipyrido-[3,2- <i>a</i> :2',3'- <i>c</i>]-phenazine
DTPA	diethylene triamine pentaacetic acid
DTTA	diethylene triamine tetraacetic acid
EDTA	ethylenediaminetetraacetic acid
en	ethylenediamine
Et	ethyl
EtNiPr ₂	diisopropylethyl amine
G	guanine
GdCl ₃	gadolinium chloride
H ₂ SO ₄	sulphuric acid
HBr	hydrogen bromide
HCl	hydrochloric acid
hfacac	1,1,1,5,5,5-hexafluoro-2,4-pentanedione / diketone
His	histidine
hmacac	2,2,6,6-tetramethyl-3,5-heptanedione / diketone
Lys	lysine
Me	methyl
MeOH	methanol
MgSO ₄	magnesium sulphate
mRNA	messenger ribonucleic acid
Na ₂ CO ₃	sodium carbonate
NaBH ₄	sodium borohydride
NaHCO ₃	sodium hydrogen carbonate

NaOH	sodium hydroxide
nap	naphthalene
OTf / triflate	trifluoromethanesulfonate
<i>p</i> -	<i>para</i> -
PEG	polyethylene glycol
PF ₆	hexafluorophosphate
phen	1,10-phenanthroline
PPh ₃	triphenylphosphine
ppyH / ppy	2-phenylpyridine
pqH/ pq	2-phenylquinoline
PtCl ₄	tetrachloroplatinate
py	pyridine
pyr	pyrene
<i>t</i> -butyl	tertiary butyl
<i>tert</i> -	tertiary
TFA	trifluoroacetic acid
tfacac	1,1,1-trifluoro-2,4-pentanedione /diketonate
tpy	2,2':6',2''-terpyridine
trien	triethylenetetramine
tz	thiazole

Other abbreviations

{ ¹ H}	proton decoupled
¹ MLCT	singlet excited state
³ MLCT	triplet excited state
A / abs	absorbance
Å	angstrom
a.u.	arbitrary units
ATR	attenuated total reflection
br.	broad
c	concentration
<i>c</i>	velocity
<i>ca.</i>	<i>circa</i>
calcd.	calculated
<i>cf.</i>	<i>confer</i>
CFT	Crystal-field theory
cm	centimetre
cP	centipoise
CT	charge transfer
d	doublet
D	diffusion coefficient
dd	double doublet
DFT	density functional theory
dm	decimetre
DSSC	dye sensitised solar cell
E	energy
em	emission
eq	equivalent(s)
ES	electrospray
eV	electron volt

ex	excitation
g	gram
G	Gibbs free energy
H	enthalpy
h	hour
h	Planck's constant
HOMO	highest occupied molecular orbital
HR	high resolution
Hz	hertz
<i>i.e.</i>	<i>id est</i>
IC	internal conversion
IR	infra-red
ISC	intersystem crossing
IUPAC	International Union of Pure and Applied Chemistry
J	joule
k_d	rate of diffusion
k_{ET}	rate of energy transfer
kg	kilogram
kHz	kilohertz
k_{IC}	rate of internal conversion
k_{ISC}	rate of intersystem crossing
k_{nr}	rate of non-radiative decay
k_q	rate of quenching
k_r	rate of radiative decay
l	path length
LC	ligand centred
LD	laser desorption
LD50	lethal dose 50%
LED	light emitting diode
LGO	ligand group orbital
LL	ligand-to-ligand
LLCT	ligand-to-ligand charge transfer
LMCT	ligand-to-metal charge transfer
LMMCT	ligand-to-metal-to-metal charge transfer
LUMO	lowest unoccupied molecular orbital
M	molar
m	multiplet
m/z	mass/charge ratio
MALDI	matrix assisted laser desorption ionisation
max	maximum
MC	metal centred
MHz	megahertz
ML	metal-to-ligand
MLCT	metal-to-ligand charge transfer
mM	millimolar
MO	molecular orbital
mol	mole
MR	magnetic resonance
MRI	magnetic resonance imaging
ms	millisecond

MS	mass spectrometry
N_A	Avogadro's number
NIR	near infra-red
ng	nanogram
nm	nanometre
NMR	nuclear magnetic resonance
NMRD	nuclear magnetic relaxation dispersion
O_h	octahedral
OLED	organic light emitting diode
P	pairing energy
PDT	photodynamic therapy
PLED	polymer light emitting diode
ppm	parts per millions
q	quartet
q	lanthanide hydration number
r	radius
ROS	reactive oxygen species
s	singlet
S	singlet state
soln	solution
t	triplet
T	triplet state / teslar
TD	time dependent
TLC	thin layer chromatography
TM	transition metal
TOF	time of flight
TPE	two photon excitation
TREM	time resolved emission imaging microscopy
UFF	universal force field
UV	ultraviolet
UV-vis	ultraviolet-visible
VT	variable temperature
XRD	X-ray diffraction
Γ	luminescence / emissive rate
δ	chemical shift
Δ_0	crystal-field splitting parameter
ε	extinction coefficient
λ	wavelength
μs	microsecond
ν	frequency
τ	lifetime
Φ	quantum yield

Chapter 1: Introduction

1.1. Coordination chemistry

Coordination chemistry has been investigated since the nineteenth century when workers such as Werner, who disband the link between metal oxidation state and coordination number and coined the term coordination compounds, started to develop coordination chemistry into its current state.¹ Coordination chemistry is the study of coordination compounds or complexes, which are distinguished, according to IUPAC recommendations, as having a coordination entity: “*an ion or neutral molecule that is composed of a central atom, usually that of a metal, to which is attached a surrounding array of other atoms or groups of atoms, each of which is called a ligand.*”²

Another feature of almost all metal complexes is the incomplete filling of the valence shell of electrons: more specifically, the partially filled *d* orbitals in transition metal complexes and the incomplete filling of the *f* orbitals in lanthanide and actinide complexes. This leads to the rich array of coordination compounds that frequent the literature with interesting spectroscopic properties. It is this relationship between coordination compounds and their photophysical properties that has led to the investigation into the development of the photophysical characteristic of transition metal ion and lanthanide ion complexes within this thesis.

1.1.1. Transition metal coordination complexes

As mentioned in the previous paragraphs, transition metal complexes are often brightly coloured due to the incomplete filling of the *d* orbitals; it is the partially filled nature of these orbitals that influences physical attributes such as the coordination geometry, the types of ligands likely to associate with the metal ion, the stability of the complexes, including the susceptibility to oxidation and reduction, and the photophysical properties of the compounds.

If molecular orbital (MO) theory is assumed, the bonds between ligand and metal ion can be treated as having mostly covalent character, whereby a ligand approaches a metal ion resulting in the overlap of *s*, *p* and *d* orbitals of the ligand group orbitals and the central ion, where the symmetry is suitable. According to crystal-field theory (CFT) this interaction results in the loss in degeneracy of the *d* orbitals due to the orientation of these orbitals in relation to the electron density of the bonding orbitals.³

In six-coordinate, octahedral (O_h) complexes, for example, such as those incorporating Re^{I} , Ru^{II} and Ir^{III} , the five d orbitals split into two non-degenerate energies where three non-bonding orbitals, with t_{2g} symmetry lie at lower energies and correspond to d_{xy} , d_{xz} , and d_{yz} whilst the two e_g symmetric anti-bonding orbitals, $d_{x^2-y^2}$ and d_{z^2} , orbitals lie at higher energy (Figure 1.1). The energy difference between the t_{2g} and e_g sets is known as the crystal-field splitting parameter (Δ_o) and is due to the degree of overlap between the metallic orbitals and the ligand orbitals; in CFT this is known as the field strength.⁴ The crystal-field strength is determined by the ligand types involved in the coordination; CN^- , CO and PPh_3 result in a large Δ_o , whilst I^- and Br^- are weak field ligands.⁵ It is the partial filling of these orbitals that allows for electronic transitions ($t_{2g} \rightarrow e_g$) to occur when the energy of irradiation is equal to Δ_o . The release of energy from the excited electron in the e_g orbital to reoccupy a t_{2g} orbital (covered in depth later) is what often gives transition metal complexes their characteristically colourful appearance.

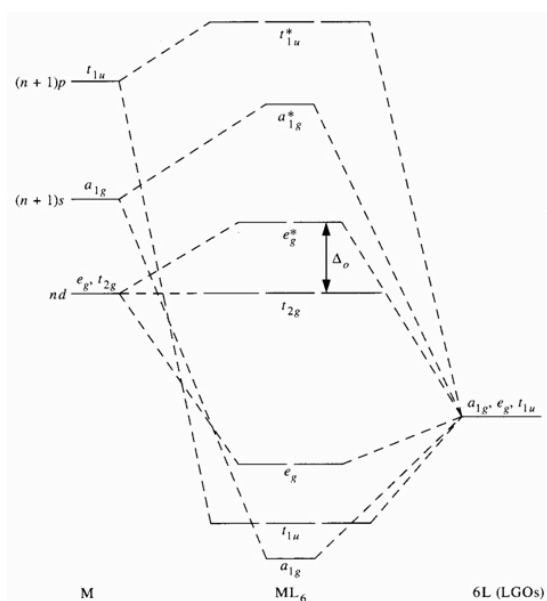


Figure 1.1 MO diagram for the σ -bonds of an O_h complex.⁶

The filling of the orbitals follows the Aufbau principle, which dictates that orbitals with the lowest energy are filled first. This means that the twelve electrons from the ligands occupy the lowest energy bonding orbitals, which leaves the t_{2g} and e_g sets to be filled by the d electrons from the metal ion. Complexes with unfilled d orbitals can form high spin and low spin complexes depending upon the magnitude of Δ_o and the energy required to overcome the electrostatic repulsion associated with pairing electrons, the pairing energy (P). The d electron configuration in high field complexes follow Hund's rule, whereby available orbitals are singularly occupied before

additional electrons pair up with those in the singularly occupied orbitals; this is only favourable when $\Delta_o < P$. When the crystal-field splitting energy is much greater, which is often the case for ligands such as phenylpyridine (ppyH), it is more energetically favourable to pair electrons rather than ‘placing’ them in orbitals of higher energy.⁷

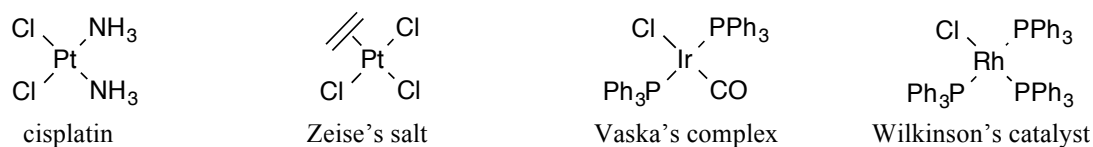


Figure 1.2 Selection of well-known square planar d^8 transition metal complexes.

In the case of d^8 metals, which are more applicable to the type of complexes that will be discussed in this thesis, the Ni triad is the most well known. Famous examples of Pt^{II} complexes include cisplatin (discussed in greater detail in Chapter 2) and Zeise's salt (Figure 1.2).⁴ There are also other famous examples in the +1 oxidation state of d^8 metal complexes such as Vaska's complex and Wilkinson's catalyst (Figure 1.2) for Ir^{I} and Rh^{I} , respectively.⁴ These all form four-coordinate square planar complexes as they have relatively high field ligands so form low spin complexes. Where low field ligands are coordinated, tetrahedral complexes are usually favourable, especially for Ni^{II} complexes. Unlike most other inert complexes, which have an electron count of 18 (thus filling the bonding and non-bonding orbitals in an O_h geometry), d^8 square planar complexes most often deviate from the 18-electron rule and have an electron count of just 16, which is the most stable configuration as it leaves the anti-bonding $d_{x^2-y^2}$ orbitals unoccupied (Figure 1.3).

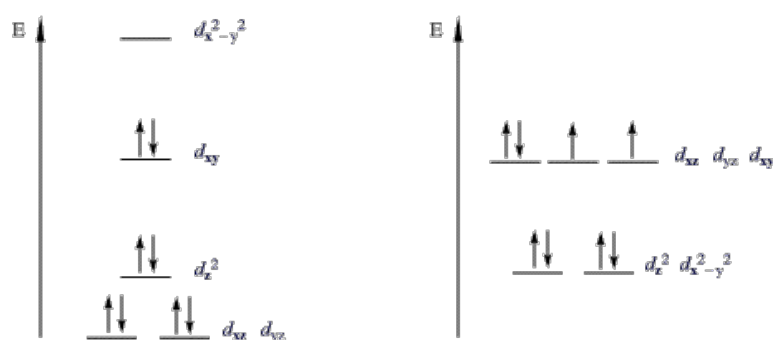


Figure 1.3 d orbital splitting for low spin square planar (*left*) and high spin tetrahedral (*right*) d^8 complexes.

1.1.2. Chelate effect

The type of ligand, as it has been shown, can affect the physical properties of a metal complex. Ligands range from simple monoatomic structures, such as halides to large macromolecules with many coordination sites. The number of sites on a molecule that are capable of coordinating is known as the denticity. Compounds with one coordination site, such as pyridine, are referred to as being monodentate whilst compounds with more than one are classed as polydentate. These polydentate ligands lend themselves to a phenomenon known as the *chelate effect*, outlined in 1964 by Curtis.⁸ Simply put, the chelate effect results in an O_h complex, for example, being more stable with three bidentate ligands than with six monodentate ligands with the same characteristics (such as pyridine and 2,2'-bipyridine).⁴ The reason for this increased stability is due to the thermodynamically favourability for polydentate ligands over monodentate ligands.

$$\Delta G = \Delta H - T\Delta S \quad (1)$$

The thermodynamic stability can be related to the Gibbs free energy of a system, denoted in equation (1) by G . The stability is often increased (lower ΔG) in polydentate complexes through a favourable change in the entropy, ΔS , and enthalpy, ΔH .

From an entropic perspective, which is commonly referred to as the disorder of a system, forming a complex whereby MX_6 becomes ML_3 (where X is a monodentate ligand and L is a bidentate ligand) results in the formation of seven molecules from four, leading to an increase in the disorder of the system, which is favourable as the universe tends towards disorder.

If we consider the reaction of $[\text{Ni}(\text{NH}_3)_6]^{2+}$ with ethylene diamine (en) to give $[\text{Ni}(\text{en})_3]^{2+}$, the change in the Gibbs free energy (ΔG) is -53 kJ mol^{-1} . This reaction is driven mostly by the increase in entropy, with $T\Delta S$ having a value of 36.2 kJ mol^{-1} (at 298 K), whilst ΔH has a smaller value of $-16.8 \text{ kJ mol}^{-1}$. This greatly increased entropy means that replacing just two NH_3 molecules for one ethylene diimine results in a roughly 300-fold increase in stability.³ Stability increases more with the introduction of each additional chelating ligand, as can be seen in Table 1.1.

Monodentate	$\Delta G / \text{kJ mol}^{-1}$	Bidentate	$\Delta G / \text{kJ mol}^{-1}$
<i>with pyridine (py) or 2,2'-bipyridine (bpy)</i>			
2 py	-20	1 bpy	-39
4 py	-32	2 bpy	-78
6 py	-56	3 bpy	-110
<i>with ammonia (NH₃) or ethylene diamine (en)</i>			
2 NH ₃	-28	1 en	-43
4 NH ₃	-44	2 en	-79
6 NH ₃	-49	3 en	-104

Table 1.1 Comparison of the change in the Gibbs free energies upon ligand exchange with various monodentate and related bidentate ligands from $[\text{Ni}(\text{OH}_2)_6]^{2+}$.

The enthalpic contribution comes from the fact that, in order to fully dissociate a polydentate ligand, each of the coordinative bonds must be broken. For example, in order to dissociate 2,2'-bipyridine from Ru^{II} two Ru-N bonds must be broken, which requires more energy than breaking a single Ru-N bond, as would be the case for pyridine. Further to this, once a polydentate ligand has successfully coordinated through one binding site, the local concentration of unbound coordinating sites are increased, allowing for a greater chance of reaction of the subsequent coordination sites as less translational energy is required. Not only are the coordination sites in closer proximity, they are often much more restricted in their rotation meaning that they are more frequently in the correct orientation to coordinate. This is especially the case with molecules such as 1,10-phenanthroline (phen), where the rigidity allows for the instant creation of a 5-membered chelate ring. Bpy, on the other hand, often has to rearrange itself in order to coordinate successfully (Figure 1.4).

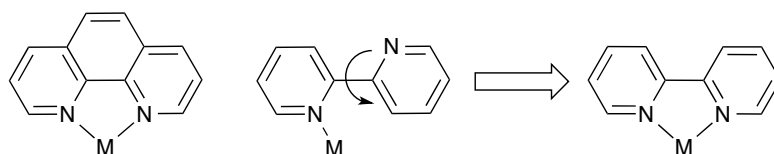


Figure 1.4 Preorganisation of a 5-membered chelate ring in phen compared with the rearrangement required by bpy in order to form a 5-membered chelate.

From a dissociative perspective, if one coordinative bond is broken there is a very high chance that, due to the restriction in the ligand's movement by the other coordinative bond(s), the rate of bond reformation is greatly increased. In other words, in order for a polydentate ligand to be successfully removed from a metal centre, all coordinative bonds need to be broken almost instantaneously. With the case of square planar complexes, a dissociative mechanism is unlikely as this would result in a three-coordinate complex; it is much more likely that association of a ligand into

a vacant axial position will result in displacement of a coordinated ligand in the xy plane. In order for associative ligand displacement to release a bidentate ligand, the association must provide enough of a driving force to break both of the coordinative bonds within the chelate ring. This is much more unlikely than when the ligands being removed are monodentate.

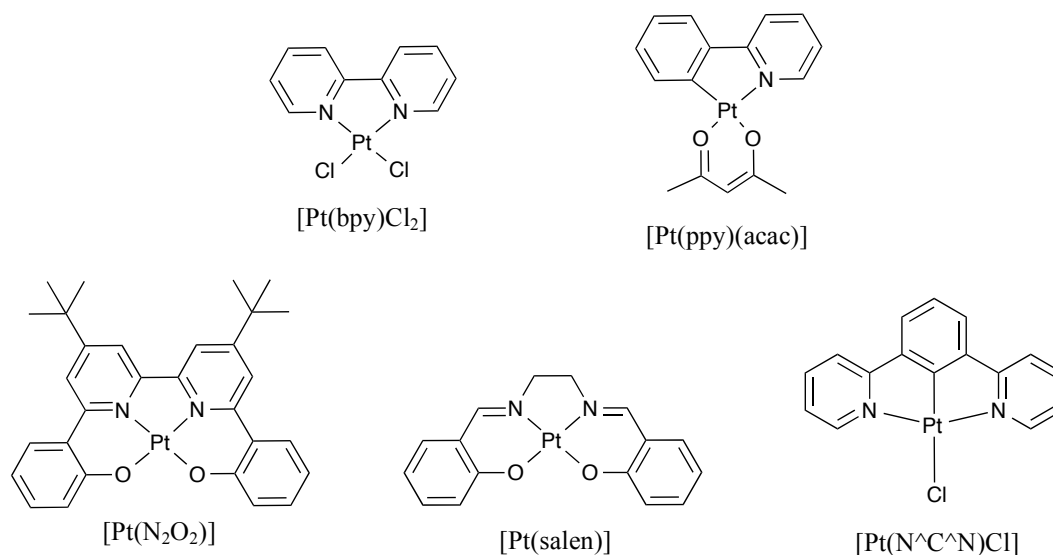


Figure 1.5 Examples of chelating square planar Pt^{II} complexes in the literature.

In square planar Pt^{II} complexes there are a range of examples of chelating motifs that have been employed to tune the photophysical properties (discussed below and in Chapter 2) and to increase the stability of the complexes. These chelates range from bidentate donors such as bpy,⁹ ppy and 2,4-acetylacetonate (acac)^{10, 11} to tridentate complexes, including functionalised 1,3-dipyridylbenzene ($\text{N}^{\wedge}\text{C}^{\wedge}\text{N}$) derived ligands.¹² There are also examples of tetradentate complexes in which the entire square planar ligand is one molecule, which encapsulates the metal ion to further increase the stability. The ligand systems drawn both have N_2O_4 coordination modes, where one is the classic ligand of this type, salen,^{13, 14} and the other is a bpy-derived compound with additional phenol moieties appended to yield a salen-like coordination site.¹⁵

1.1.3. Lanthanide coordination

In order to go into detail about the coordination of lanthanides, it is useful to provide some background into the physical properties of lanthanides as, unlike the d -block metals, their properties are very similar and their trends are very uniform across the row. This pronounced similarity meant that the identity of many of the rare earth

metals, which aren't in fact rare at all, were not discovered until as recently as 1907 (for lutetium).¹⁶

Lanthanides are located in the *f*-block of the periodic table due to the fact that their valence electrons fill the *4f*-orbitals. Initially, the *5d* subshell is lower in energy than the *4f* however, as the effective nuclear charge increases, the *4f* orbitals contract and it becomes more energetically favourable to fill these closer lying orbitals (Figure 1.6).¹⁷ The only exception to this is Gd, which has the electron configuration $[\text{Xe}]6s^2 5d^1 4f^7$ due to the fact that the half-filled *4f* shell's stability results in the next electron being placed in the *5d* shell.¹⁶ After this anomaly, the trend continues with terbium's configuration being $[\text{Xe}]6s^2 4f^9$. The reason for their similar properties and following trends is mainly down to the fact that most lanthanide chemistry is dominated by the +3 oxidation state. This is due, in part, to the fact that the fourth ionisation energy is greater than the sum of the first three ionisation energies.¹⁸ This renders the +4 oxidation state almost completely inaccessible, as bond formation alone cannot provide the energy to remove a fourth electron. The electrons lost in the ionisation to the +3 oxidation state are from the *6s* and *5d* shells, giving the Ln^{3+} ions an electron configuration of $[\text{Xe}]4f^n$ (where $n = 1 - 14$). The only exceptions to this are Eu and Yb where the +2 oxidation state is preferred as this results in a half-filled and fully-filled *4f* shell, respectively, which are more favourable than the $4f^6$ and $4f^{13}$ configurations.¹⁶

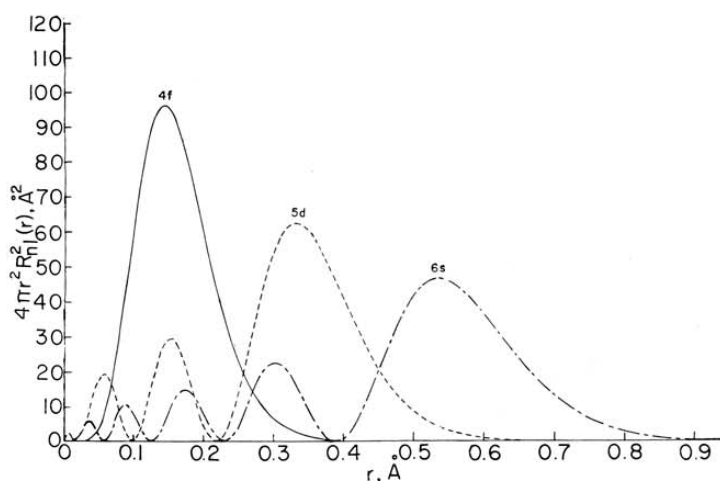


Figure 1.6 Radial part of the hydrogenic wave functions for the *4f*, *5d* and *6s* orbitals of cerium.¹⁹

The contraction of the *4f* orbitals, as mentioned above, is due to the poor ability of *f* electrons to screen other valence electrons from the nuclear charge. The poor screening is predominantly because of the high angular nodality of the *f*-orbitals,¹⁸

however relativistic effects also play a part due to the heavier mass of the lanthanide atoms. The result of both of these is a phenomenon known as *lanthanide contraction*.¹⁶

As mentioned, relativity plays a small part in lanthanide contraction and, although relativity is usually associated with very large objects, it also has a significant impact at the atomic level.²⁰ There are two main consequences of relativity: modification of the atomic orbital energies and the effects of spin-orbit coupling.^{16, 21} Whilst the modification of atomic orbital energies is not as important in the context of this thesis, spin-orbit coupling is something that plays a profound impact on the photophysical properties of luminescent compounds incorporating heavy atoms as spin-orbit coupling, in a simplified manner, increases with nuclear charge. The states produced by spin-orbit coupling are described based on their spin and orbital angular momenta.¹⁶ When the spin-orbit coupling is weak in comparison with the interelectronic repulsion, as is the case for all examples in this thesis, *LS* or Russell-Saunders coupling is the most useful approach.²²

This coupling considers that the individual orbital angular momenta of all the electrons combine into a total atomic orbital angular momentum with quantum number L . This is also the case for the electronic spin component so that all of the electronic spin angular momenta are combined to give a total spin angular momenta for the atom with quantum number S . The total atomic angular momentum is given by the coupling of L and S , which is described by quantum number J . The energy levels of atoms or ions are characterised by a term symbol with the general form $(2S+1)L_J$.¹⁶ This notation is used to describe the ($f \rightarrow f$) transitions in luminescent lanthanide complexes in both Chapters 3 and 5.

The contraction of the lanthanides has a direct impact on the means in which lanthanide ions coordinate to ligands as it results in the inability of the $4f$ orbitals to overlap with ligand orbitals. Consequently, they do not participate in bonding to any significant degree and their isolation from the ligands means the crystal-field effects, which gives rise to the spectroscopic properties of transition metal complexes, are very small.²³ This leads to the lanthanides' electronic spectra and magnetic properties (discussed in more detail later in this chapter) being almost completely unaffected by the environment. It also means that these hard Lewis acids bond mostly through ionic

or electrostatic means, in contrast to the *d*-block elements, which typically form covalent bonds.^{18, 24} The hard Lewis acid nature of the Ln^{III} ions means they favour coordination to hard bases such as oxygen and nitrogen donors. The charge densities are also relatively high and this property is exacerbated across the period due to the lanthanide contraction phenomenon, resulting in stronger ionic bonds across the row due to the increase in charge density.^{16, 18}

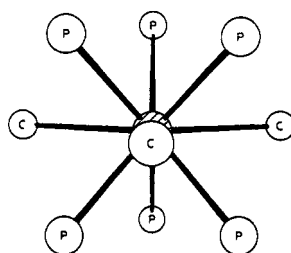
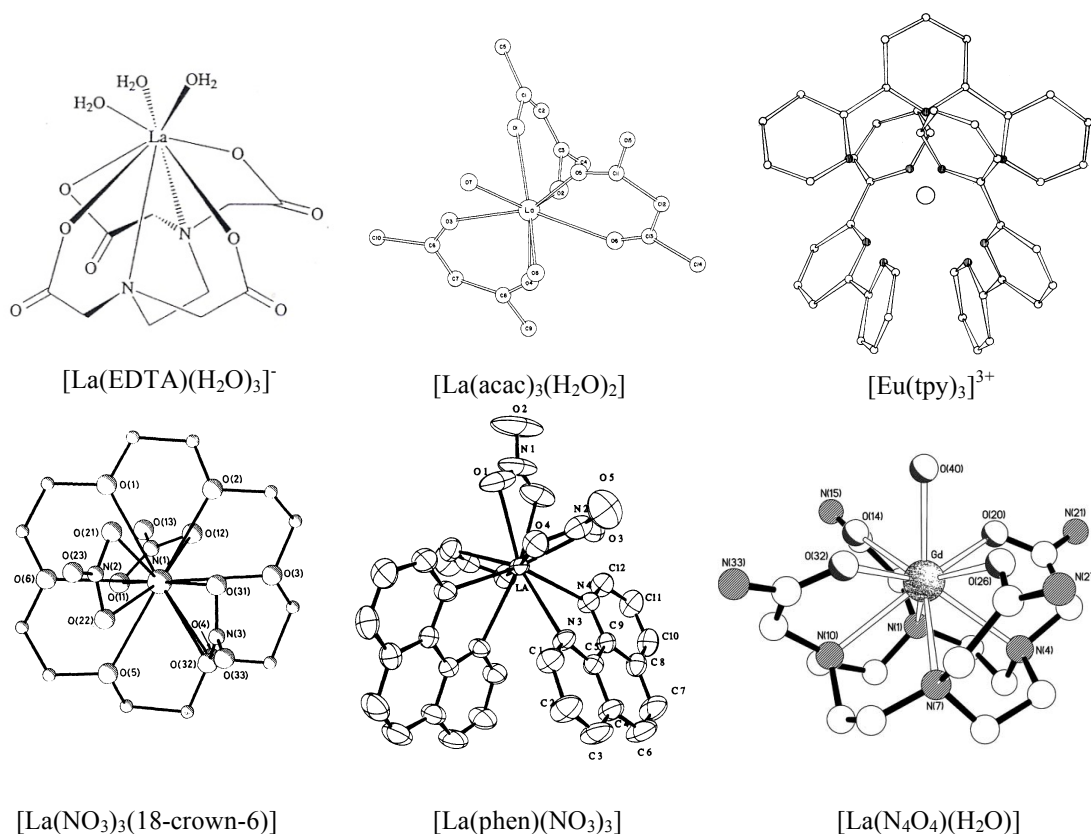


Figure 1.7 Tricapped trigonal prismatic structure of a nonaaqualanthanide ion.²⁵

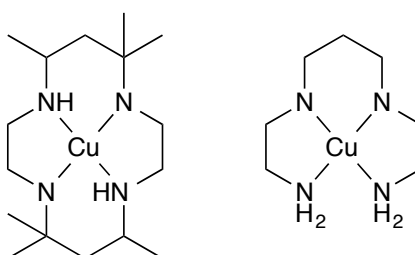
Lanthanides typically form eight or nine coordinate species, especially in aqueous solution where water molecules often coordinate to any vacant sites around the ion. The complexes also exhibit rapid ligand exchange, except in the case of multidentate ligands, with water coordination residency times of around 10^{-9} s, essentially meaning that the rate of exchange is determined by the diffusion of water molecules about the inner coordination sphere.¹⁸ This means that monodentate ligands are extremely unstable and highly kinetically inert lanthanide complexes can only be obtained through the incorporation of the ion into a macrocycle-based or rigid polydentate ligand, due to the factors outlined above for the chelate effect and below for the macrocyclic effect.

There are a wide range of examples of polydentate ligands that have been incorporated into lanthanide complexes, including bidentate ligands such as phen and acac,^{26, 27} tridentate ligands like 2,2';6',2''-terpyridine (tpy),²⁸ polydentate open chain ligands such as ethylenediaminetetraacetic acid (EDTA)²⁹ and macrocyclic ligands including crown ethers,³⁰ and DOTA-like compounds (where DOTA = 1,4,7,10-tetraazacyclododecane-1,4,7,10-tetacetic acid) with N_4O_4 donors.³¹

Figure 1.8 Structures of some chelating and macrocyclic Ln^{III} complexes.

1.1.4. Macrocyclic effect

For the scope of this thesis, a macrocycle can be thought of as being a large cyclic molecule containing donor atoms capable of forming coordinate bonds to metal centres. In order to exclude compounds such as ethylene oxide and 1,3-dithiane, a macrocycle is typically thought to contain at least three donor atoms in a ring consisting of at least nine atoms. This means that a macrocycle is capable of binding a metal within the central cavity of the ring although this is not always strictly necessary as the term macrocycle is often used to describe a range of coordination compounds where the metal ion sits slightly above (or below) the plane of the cyclic component, as is the case with $[\text{Ln}(\text{DOTA})]$ -like complexes discussed above.³²

Figure 1.9 Comparative macrocyclic and open-chain Cu^{II} complexes with very different stabilities.

It has been made known that polydentate ligands form more stable complexes than those with the same number of equivalent monodentate ligands. The *macrocyclic effect*,³³ as described by Cabbiness *et al.* in 1969, (or *multiple juxtapositional fixedness*)³⁴ is an extension of the chelate effect whereby cyclic ligands give more stable complexes than the corresponding open-chain ligands do. Two Cu^{II} complexes (Figure 1.9) with very similar ligand structures, where one is an open chain and the other a macrocycle, differ in stability hugely: the macrocyclic compound is *ca.* 10^4 times more stable. It was also noted that the macrocyclic compound coordinated much slower ($10^3 - 10^4$ times) than the open chain ligand.³² Both of these trends are not exclusive to this example and both the increase in stability and decrease in coordination rates are commonplace throughout macrocyclic coordination chemistry.⁷

This increase in stability, as with the chelate effect, is proposed to come from the entropic and enthalpic effects favouring macrocyclic compounds. The change in enthalpy has been related to the difference in the solvation of open-chain and macrocyclic compounds, although Kodama *et al.* found that the increased stability in $[\text{Cu}(\text{cyclen})]$, compared to $[\text{Cu}(\text{trien})]$ (trien = triethylenetetramine), was solely due to the entropic term.³⁵ They proposed that this was due to the fact that, in the trien complex, disorder is lost upon complexation as the trien loses its ability to rotate freely whilst cyclen is already restricted due to the steric constraints of cyclic compounds. The distorted coordination geometry associated with cyclic ligands also reduces the inner-sphere solvation,³⁶ which favourably results in less molecules becoming ordered upon complexation and reduces the enthalpic cost of desolvating the ligand. The addition of a cation to the macrocycle also reduces the unfavourable interaction of the donor lone pairs, which is not seen in open chain systems where the ligands can freely change orientation to prevent unfavourable donor interactions.

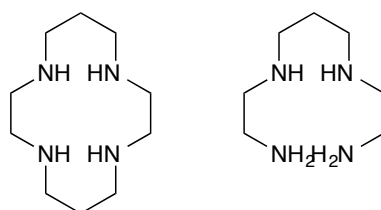


Figure 1.10 Cyclam (*left*) and a corresponding open chain derivative (*right*) that have been used to demonstrate the enthalpic and entropic contributions towards the macrocyclic effect using Ni^{II} .

Despite Kodama *et al.*'s results, there are data for low spin Ni^{II} complexes of cyclam and corresponding open chain complex (Figure 1.10) that suggests there is an

enthalpic contribution in some complexes even if, as with the chelate effect, the entropic contribution dominates the increase in stability (Table 1.2).³²

Ligand	$\Delta H / \text{kJ mol}^{-1}$	$T\Delta S / \text{kJ mol}^{-1}$
cyclam	-78.2	49.3
open-chain tetramine	-66.1	21.7

Table 1.2 Changes in the enthalpic and entropic effects between a cyclic and open-chain Ni^{II} complex.

From the perspective of lanthanides, the macrocyclic effect is extremely important as the complexes can often form up to 9 coordinate species and are therefore often encapsulated in polydentate macrocyclic ligand architectures. Of particular interest is the Gd^{III} ion, as this is where most of the research has focussed due to the incorporation of Gd^{III} in many contrast agents for magnetic resonance imaging (covered in more depth in Chapter 3).



In the above example,²⁴ if an aquated Gd^{III} ion is reacted with a macrocyclic ligand, entropically speaking, the reaction is extremely favourable as the reaction generates at least eight molecules from the reaction of two. As described earlier, the Ln^{III} ions have a very high charge density and the incorporation of this strong Lewis acid into a ligand with nucleophiles such as amines and basic hydroxide moieties (as is found in DOTA-type ligands) results in a highly favourable electrostatic interaction, further enhancing the stability of the complexes (especially when the release of 3H^+ ions is also accounted for in the enhanced entropic effect).

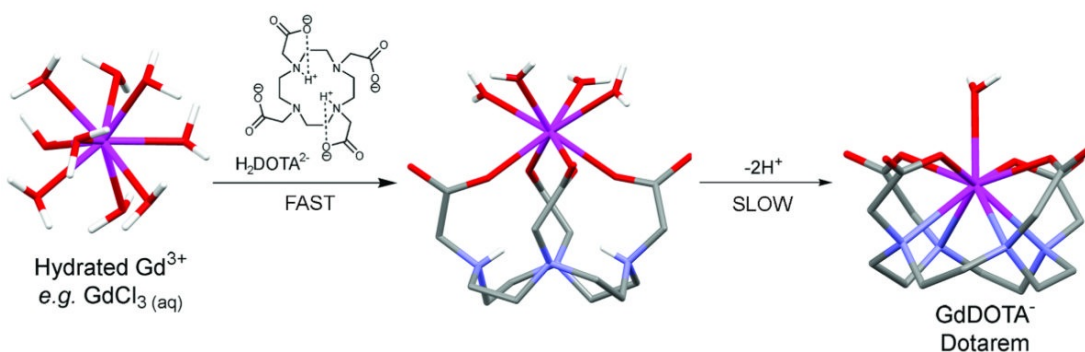


Figure 1.11 Diagrammatic representation of the reason for slow formation of macrocyclic compounds.²⁴

From a dissociative point of view, the removal of a metal ion, such as Gd^{III} , from a macrocycle takes much longer than it does to remove the same metal ion from a corresponding linear polydentate ligand. This is due to the principle of microscopic

reversibility,³⁷ which states that for any reversible reaction, the mechanism in one direction is the exact opposite of the mechanism in the other direction. This means that, as it takes much longer for the macrocyclic compounds to form due to the strain required to encapsulate the metal ion within the cavity, as shown diagrammatically in Figure 1.11, it also takes much longer for them to dissociate as the same strain must be imposed in order to release the ion.

The results of the chelate and macrocyclic effects can be summarised in the stability constants seen below (Table 1.3) for a range of Gd^{III} complexes.^{16, 38} Although there is not a direct likeness between the ligands, it highlights the increase in stability from a monodentate ligand to a polydentate open chain ligand to macrocyclic ligand, utilised as a contrast agent in magnetic resonance imaging (see Chapter 3).

Ligand	Thermodynamic stability constants / log <i>K</i>
F ⁻	3.31
EDTA ⁴⁻	17.35
DTPA ⁵⁻	22.46
DOTA ⁴⁻	24.7

Table 1.3 Stability constants of Gd^{III} complexes with a range of monodentate, polydentate and macrocyclic ligand architectures.

1.2. Luminescence

This thesis aims to design, synthesise and develop a series of luminescent transition metal and lanthanide ion complexes in order to assess their photophysical properties, amongst other attributes. In order to fully appreciate their photophysics, it is important to understand the fundamental aspects that are associated with luminescence and the factors that can influence the emissive properties of these complexes.

1.2.1. Light

For the purposes of this thesis, photophysics and photochemistry can be thought of as the study of how light influences the structure and chemistry at the molecular level. Given this, it is imperative to outline the fundamental properties of light and how it interacts with molecules.

Light can be thought of as electromagnetic radiation, defined by three intimately related quantities, wavelength, λ , frequency, ν , and velocity, c , which can be used to

from equation (2), below. Both wavelength and frequency are variable over a wide range of values (Figure 1.12), whilst c , commonly known as the speed of light, is a fixed quantity with a value of $2.998 \times 10^8 \text{ m s}^{-1}$ in a vacuum.

$$\lambda\nu = c \quad (2)$$

Light can also be thought of as a stream of discrete packets of energy, called photons. These photons have a specific energy, E , which is related to the frequency of the radiation, ν . This gives us a second equation, (3), which relates these two properties through Planck's constant, h , which has a value of $6.63 \times 10^{-34} \text{ J s}$.

$$E = h\nu \quad (3)$$

In the field of photochemistry and photophysics, the term use of 'light' is limited to the range of electromagnetic radiation energetically suitable to invoke electronic excitation (discussed below); this is typically energy between 1.5×10^{15} to 3×10^{14} Hz (200 to 1000 nm), although there are some exceptions. This means that light suitable of exciting an electron falls within the ultraviolet (UV), visible or infra-red (IR) regions.

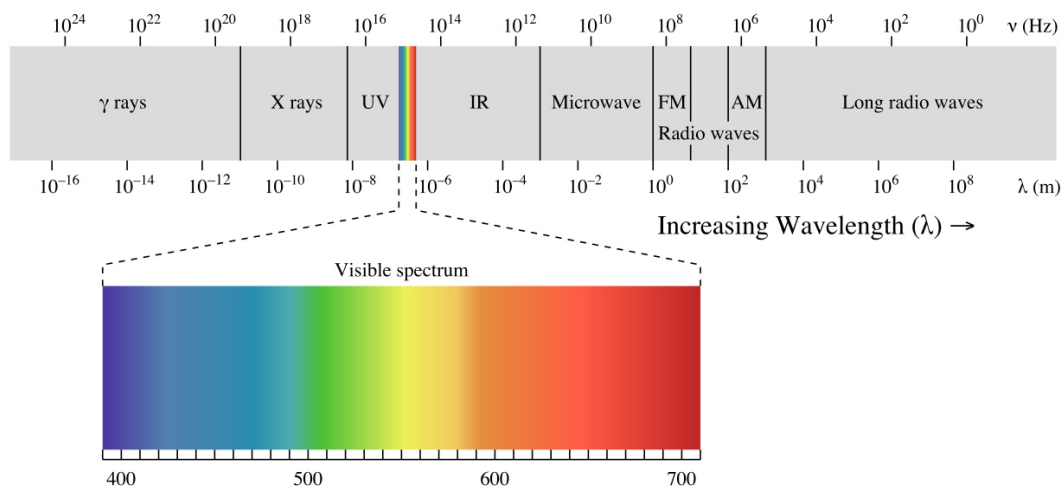
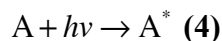


Figure 1.12 Electromagnetic spectrum with relevant frequencies for the different categories of light.³⁹

When light interacts with a molecule, it most frequently involves one molecule and one photon. This can be represented through equation (4) where the molecule in the ground state, A , is excited by a photon of light, $h\nu$, promoting the molecule to its electronically excited state, A^* . This means that A^* possesses $h\nu$ more energy than A , where $h\nu$ is between 9.95×10^{-19} and $1.99 \times 10^{-19} \text{ J}$, using equations (2) and (3) given the range of energy suitable for electronic excitation.



Only photons of light absorbed by molecules can promote molecules from A to A^* , which is never the entire photon flux. It is fundamentally important, as it will become apparent, to know how much light of a certain wavelength is absorbed by a given number of molecules in a transparent medium. Equation (5), the Beer-Lambert law, provides a relationship between the incident light, I_0 , the transmitted light, I , the molar absorption coefficient, ϵ , which is the ability of a molecule to absorb light of a given wavelength (in $\text{mol}^{-1} \text{ dm}^3 \text{ cm}^{-1}$), the path length, l , and the concentration of the photophysically active molecules, c , in solution. These values can be rearranged to give the absorbance, in equation (6), which describes how much light has been absorbed at each given wavelength, and is typically the form of the values given by spectrophotometers.

$$I = I_0 \times 10^{-\epsilon cl} \quad (5)$$

$$A = \log(I_0/I) = \epsilon cl \quad (6)$$

1.2.2. Fluorescence

Luminescence is the emission of light from a molecule upon its relaxation to the ground state, S_0 , from its electronically excited state, S_1 or T_1 .⁴⁰ The Jablonski diagram (Figure 1.13) is used to demonstrate the processes that can occur upon excitation into the higher energy levels.⁴¹

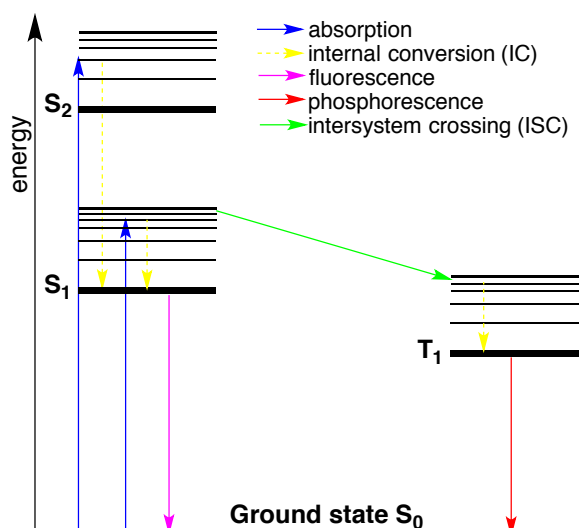


Figure 1.13 Jablonski diagram illustrating the radiative (solid arrows) and non-radiative (dashed arrows) processes that can occur within a molecule.

Energy, in the form of a photon, can only be absorbed by a molecule, or ion, when a photon's energy is of equal energy to difference in energy between A and A^* , where

A is a molecule in the ground state, S_0 , and A^* is in an excited state, $S_{1,2,\dots}$, which is summarized in the Bohr equation (7).

$$h\nu = E_{A^*} - E_A \quad (7)$$

As well as this necessity, there is a requirement for a specific interaction between the electromagnetic field and the molecule. In most cases the magnetic field can be disregarded, as the transitions generated by the oscillating magnetic field are weaker (by *ca.* 10^5 times) than the electric-dipole transitions. This means it is only necessary to focus on the interaction between the electric vector of the electromagnetic wave and the electric dipole of the molecule as, in the presence of light, the light's sinusoidal electric vector results in oscillating forces on the charged particles of the excited state molecule.

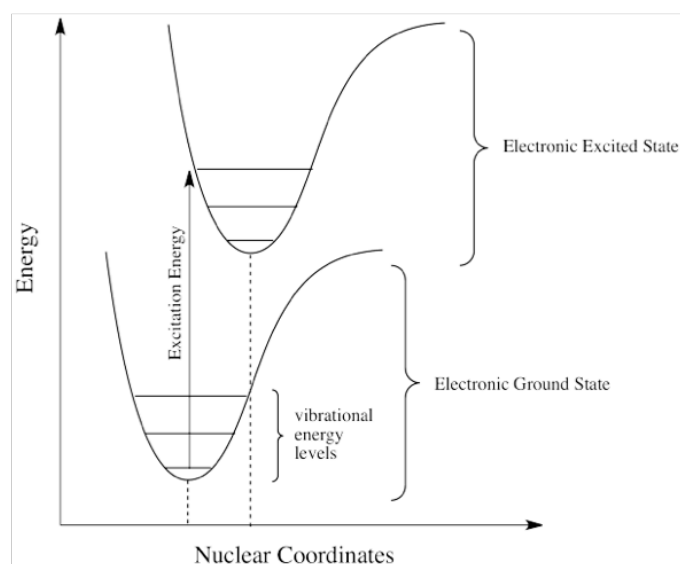


Figure 1.14 Diagram representing the vertical transitions outlined in the Franck-Condon principle.⁴²

Upon excitation to the excited state, the electronic spins retain their spin-paired (opposite spin) configuration, resulting in a spin-conserved process ($\Delta S = 0$). The Franck-Condon principle dictates that these transitions be represented as vertical lines (Figure 1.14) due to the fact that, during the timeframe of the electronic transition (10^{-15} s), the nuclear framework remains the same, as the vibrational transitions occur much slower (10^{-8} s).⁴³ This results in vibronic relaxation after the excitation has occurred, *via* internal conversion (IC) to the lowest vibrational energy level of the corresponding excited state (often S_1). This relaxation results in the emission being of lower energy than the excitation, and the difference between these two energies is referred to as the Stokes' shift.⁴⁴

Repopulation of S_0 results in the emission of a photon of equal energy to the energy gap between the two energy levels. This emission is defined as fluorescence given that it is a spin-allowed process resulting in short lifetimes (typically < 50 ns).⁴¹

1.2.3. Phosphorescence

It is also possible to populate the triplet excited state (T_1) *via* intersystem crossing (ISC), a non-radiative process that results in the electron in the ground and excited state having the same spin orientation. Decay to the ground state requires a spin-forbidden process, according to Laporte's parity selection rules, which facilitates a much longer lifetime. Emission by this process is classified as phosphorescence and both the ISC and emission are facilitated by spin-orbit coupling whereby the spin's magnetic interaction and the orbital angular momenta of individual electrons couple with one another.¹⁸ As discussed above, this is often more prevalent in the presence of a heavy atom such as a transition metal, lanthanide or halogen due to the heavy atom effect.⁴⁵

1.2.4. Lifetimes

As mentioned, different systems (fluorescence and phosphorescence) have very different emissive characteristics, dominated by the length of the emissive lifetime. The lifetime (τ) is the average time molecules spend in the excited state before relaxing to the ground state. There are several ways that a molecule can relax from the excited state to the ground state. Using the paradigm set out above in equation (4),⁴⁴ these deactivation processes can be expressed in the scheme below (Figure 1.15).⁴¹ k_p denotes a unimolecular chemical process to give a chemically different product, A' , k_r is the radiative process whereby A^* relaxes to the ground state to give A and light at a lower energy, $h\nu'$, due to IC (Figure 1.13), whilst k_{nr} describes a non-radiative physical process whereby energy is released from A^* as heat in order for relaxation to S_0 to occur.

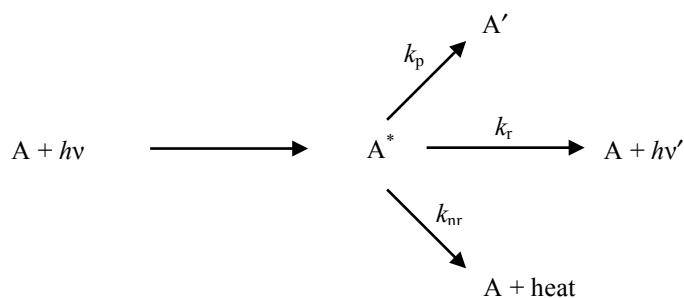


Figure 1.15 Intermolecular interactions leading to the deactivation of excited state molecules.

The lifetime of the excited state can therefore be expressed in terms of the rates of the three relaxation processes highlighted above (Figure 1.15) to give equation (8).²⁰

$$\tau(A^*) = \frac{1}{k_p + k_r + k_{nr}} \quad (8)$$

Given that one of the main interests of this thesis are the luminescent properties of metal complexes, the lifetime that matters within the scope of the research is the luminescence lifetime, a first-order kinetic process referred to hereon in as τ . This can be expressed in terms of the rates of luminescence, Γ , ISC, k_{ISC} , and IC, k_{IC} using equation (9).

$$\tau = \frac{1}{\Gamma + k_{ISC} + k_{IC}} \quad (9)$$

Along with the aforementioned difference in lifetimes between fluorescence and phosphorescence, there are other factors that can have a profound effect on the emissive lifetime. One of these is a change in temperature; it is commonly observed that a decrease in temperature results in an extended emissive lifetime, primarily through a reduced rate of non-radiative decay, k_{nr} , which incorporates k_{IC} and k_{ISC} .^{46, 47}

1.2.5. Quenching

Another very important factor that affects the emissive lifetime, as well as non-radiative processes, is quenching. This is a process in which a molecule in an excited state releases energy to a quencher in order to return to the ground state.⁴¹ Quenching can occur intramolecularly, especially in supramolecular systems, where the excited states can be very short lived due to the efficient cascade of energy transfer from one component to another.⁴⁴

Where intramolecular deactivation is not too fast, quenching can also take place in an intermolecular manner through second-order rate kinetics. This can occur through either energy-transfer or electron-transfer processes, the latter of which involves oxidation or reduction of the excited state, A^* . In systems where intermolecular energy-transfer occurs the excited quencher, B^* , undergoes its own deactivation mechanism which, as with the deactivation of A^* , can involve radiative decay, known as sensitised luminescence.⁴⁴ This means that, in the presence of a quencher, B, Figure 1.15 has an additional arrow where the rate of quenching, k_q , also leads to deactivation of A^* .

The rate of change of $[A^*]$ in the presence and absence of a quencher can be expressed in equations (10) and (11), respectively, where $\tau^0(A^*)$ is the lifetime of A^* in the absence of a quencher and $\tau(A^*)$ is in the presence of a quencher, B. This gives equation (12) for the overall lifetime of A^* in the presence of B.

$$-\frac{d[A^*]_{\text{intra}}}{dt} = (k_r + k_p + k_{nr})[A^*] = \frac{1}{\tau^0(A^*)}[A^*] \quad (10)$$

$$-\frac{d[A^*]_{\text{inter}}}{dt} = k_q[A^*][B] \quad (11)$$

$$\tau(A^*) = \frac{1}{k_r + k_p + k_{nr} + k_q[B]} \quad (12)$$

These can be combined to give a ratio of the lifetimes in the absence and presence of B to give a Stern-Volmer plot using equation (13).²⁰ The Smoluchowski Equation, (14), expresses the diffusion rate constant, k_d , which, in conjunction with equation (13) makes it possible to calculate how much effect the concentration of quencher will have on the lifetime of A^* , where R_A and R_B are the collision radii of A^* and B and D_A and D_B are the diffusion coefficients of A^* and B.⁴⁴

$$\frac{\tau^0(A^*)}{\tau(A^*)} = 1 + \tau^0 k_q [B] \quad (13)$$

$$k_d = 4\pi N_A (R_A + R_B)(D_A + D_B) \quad (14)$$

Using a very simple example, in a system where the excited state decays *via* fluorescence ($\tau^0 = 10^{-6}$ s), in order to quench 50% of A^* , $[B] \sim 10^{-2}$ M, whereas in a

system where decay is *via* phosphorescence ($\tau^0 = 10^{-3}$ s), the same degree of quenching requires $[B] \sim 10^{-6}$ M.⁴⁴ This is why, for phosphorescent systems, the lifetimes observed, τ , are often considerably less than the unquenched lifetimes, τ^0 . In order to get values closer to τ^0 , systems are often degassed to remove dissolved oxygen, which is the most common quenching species and can quench through various means, including energy-transfer, electron-transfer and catalysed deactivation. When energy-transfer occurs, the oxygen molecule can undergo ISC from the triplet ground state ($^3\text{O}_2$) to the highly reactive oxygen singlet state ($^1\text{O}_2$).

Quenching can also happen through a static mechanism where non-emissive structures are formed between the fluorophores and quenching molecules; this means that this form of quenching is not dependent upon diffusion or collision of quenchers.⁴¹

1.2.6. Solvent effects

When the absorption spectra of samples in solution are measured, it is often found that varying the solvent results in changes in the observed spectra. This is due to the fact that irradiation by light leads to the redistribution of electron density within a molecule.⁴⁴ This alters the interactions between the solute and any molecules that are solvating the excited molecule. The perturbation of the absorption or emission band is referred to as *solvatochromism* and the extent of its effect varies depending upon the solvent nature, the chromophoric molecule and the type of transition that occurs. The effect is more pronounced when a molecule's excitation induces a change in the dipole moment, which is common in samples that show charge transfer (CT) character.⁴⁸ The timeframe in which the electronic transition occurs means that there is not time for the solvent molecules to rearrange themselves around the excited state in order to most efficiently stabilise the altered dipole moment until after the transition to the excited state has occurred. This increases the energy of the transition and these effects are exaggerated with increasingly polar solvents, especially when solvents such as methanol and water are involved as the hydrogen bonding interactions are much stronger than the dipolar contacts.⁴⁴ This leads to the ($n \rightarrow \pi^*$) transition in acetone (Table 1.4) ranging from 279 nm in hexane to 265 nm in water, as the n orbital of the oxygen is only half filled and, as such, cannot participate in hydrogen bonding. Due to the Franck-Condon principle, the solvent dipoles remain

orientated in such a way as to hydrogen bond with the oxygen atom so are distributed unfavourably when the molecule is in its excited state, destabilising this state and resulting in larger excitation energies.

Solvent	Water	Methanol	Ethanol	Chloroform	Hexane
$\lambda_{\max} / \text{nm}$	265	270	272	277	279

Table 1.4 The effect of solvent polarity on the ($n \rightarrow \pi^*$) transition in acetone.⁴⁹

The effect of dissolved oxygen on the nature of the luminescent lifetime has already been discussed, but it is important to note that the concentration of dissolved oxygen in solution is solvent dependent and, as a result, the solvent can impact on the lifetime through its capacity to dissolve oxygen. DMSO, for example, has an oxygen concentration of 2.1 mM at 25 °C, whilst the capacity for pyridine to dissolve oxygen is much greater with concentrations approaching 5 mM.⁵⁰

1.2.7. Quantum yields

Another important parameter in fluorescence is quantum yield, Φ , which is the number of emitted photons in relation to the number of photons absorbed, as portrayed by equation (15). It describes the efficiency of the radiative emission process and takes into account the emissive rate, Γ , and also the rate of non-radiative decay, k_{nr} , as shown in equation (16).²⁰ A high quantum yield (close to unity), requires that Γ be much greater than k_{nr} , although it is not possible to reach unity because of factors such as quenching.⁴¹

$$\Phi = \frac{\text{number of emitted photons}}{\text{number of absorbed photons}} \quad (15)$$

$$\Phi = \frac{\Gamma}{\Gamma + k_{\text{nr}}} \quad (16)$$

The quantum yields can be calculated experimentally by comparison with a standard, denoted by subscript R, such as $[\text{Ru}(\text{bpy})_3](\text{PF}_6)_2$, by using equation (17), where S is the area below the emission spectrum, A is the absorbance at the excitation wavelength and n is the refractive index of the solvent.⁴⁴

$$\Phi = \Phi_{\text{R}} \frac{S}{S_{\text{R}}} \frac{A_{\text{R}}}{A} \frac{n^2}{n_{\text{R}}^2} \quad (17)$$

1.2.8. Luminescent transition metal complexes

Luminescent transition metal (TM) complexes have, in the past, focussed on diimine coordinated compounds utilising d^6 metals like Re^{I} , Ru^{II} and Ir^{III} . The classical example is $[\text{Ru}(\text{bpy})_3]^{2+}$, from which many hundreds of derivatives have been synthesised and assessed for their photophysical properties.⁵¹⁻⁵³ These luminescent complexes typically emit from a triplet metal-to-ligand charge transfer ($^3\text{MLCT}$) state which, due to the parity forbidden nature of the transition, have much longer lifetimes (10 ns – 10 μs) than those of the corresponding ligand fluorescence. In the case of $[\text{Ru}(\text{bpy})_3]^{2+}$, the absorption of a photon results in oxidation of the metal, whilst the diimine is simultaneously reduced. Despite the majority of work in the literature being based on d^6 metals, complexes of d^8 metals, such as Pt^{II} , Rh^{II} and Au^{III} are also known and often offer a range of photophysical features unique to their electronic configuration. The photophysical properties of Pt^{II} complexes are discussed in much more detail in Chapter 2. Whilst luminescent Ru^{II} complexes have focussed on diimine-based ligands, many luminescent Pt^{II} complexes incorporate cyclometallated ligands due to the increased stability of this type of chelate. This is primarily due to the strong ligand field influence of the aromatic carbon atom and the increased stabilisation of π donation from the metal to the ligand.⁵⁴

d^8 transition metal complexes are often low spin, square planar complexes, which lend themselves to intermolecular metallic interactions, which can provide a wealth of photophysical diversity.⁵⁵ Although they do not always boast the high stability found with the d^6 metal complexes, this has often been utilised to facilitate intentional ligand exchange and dissociation for applications in DNA and peptide binding, such as cisplatin. More recently this concept has been expanded to drug delivery systems by exploiting the reducing nature of tumour cells to reduce octahedral Pt^{IV} complexes in order to form the square planar Pt^{II} complexes and liberate the axially coordinated ligand species into solution.⁵⁶

1.2.9. Luminescent lanthanide complexes

Lanthanides are most often found in their +3 oxidation state forming hard metal ions with $4f$ valence electrons.¹⁶ These orbitals are shielded by outlying $5s^2 5p^6$ subshells, which results in the emission from ($4f \rightarrow 4f$) transitions being very well defined and unresponsive to environmental changes.⁵⁷ A poor shielding of the valence electrons

from the increased nuclear charge associated with an increase in atomic number also results in a reduced ionic radius which, as mentioned, is known as lanthanide contraction and results in a large change in the ionic size across a period.⁴

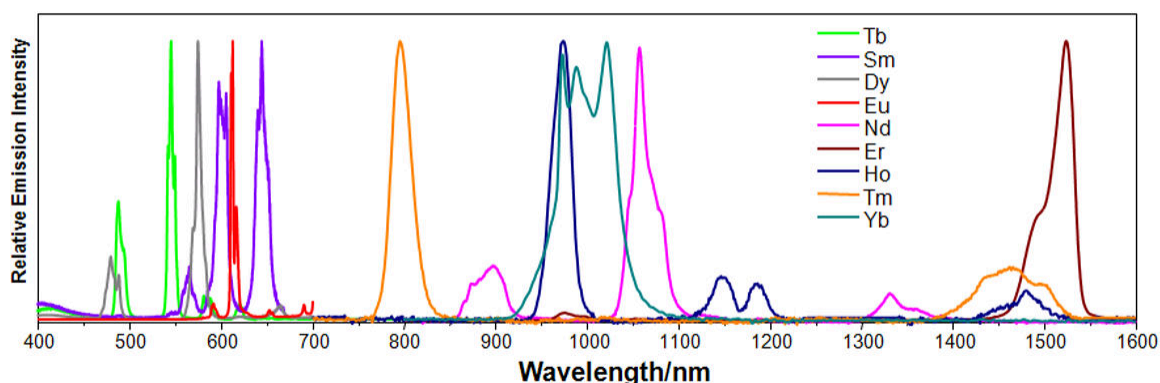


Figure 1.16 Normalised emission spectra of Ln^{III} ion complexes demonstrating the breadth of the lanthanide series' emission and the narrow emission profile of the individual lanthanide ions.¹⁸

The fact that the f orbitals are buried within the more diffuse $5s^25p^6$ subshells prevents meaningful interaction between the f orbitals with the ligand orbitals. This means that luminescence is dependent upon ($4f \rightarrow 4f$) transitions, which are parity forbidden. These transitions are characteristically sharp and unique for each lanthanide ion making them readily distinguishable (Figure 1.16). The range at which emission occurs is much broader than most fluorescent and TM phosphorescent species with high energy emission coming from Tb^{III} and Dy^{III} ions at *ca.* 500 – 550 nm and low energy emission from Er^{III} at *ca.* 1530 nm; the near-IR emitting examples (Yb^{III} , Nd^{III} and Er^{III}) are ideal candidates for biological systems where tissue possesses an optical window in the near-IR region. The fact they are Laporte forbidden also means their lifetimes are very long lived (μs – ms). The Stokes' shifts are also very large due to their need for sensitisation (detailed in Chapter 3) in order to access the luminescent potential of the ions, again making them ideal for biological imaging applications.

As mentioned, accessing the luminescent emission through an MLCT-type state is not possible due to the weakly interacting f and ligand orbitals. It is also difficult to directly excite electrons in the f orbitals due to fact that they are parity forbidden and, as a result, suffer from extremely low molar absorptions.⁵⁸ In order to combat this, an antenna can be utilised to sensitise the emission (discussed in greater detail in Chapter 3). Although electric dipole transitions usually dominate in TM complexes, magnetic dipole transitions are more often observed in Ln^{III} complexes due to spin-orbit coupling.¹⁶

1.3. References

1. K. Bowman-James, *Acc. Chem. Res.*, 2005, **38**, 671-678.
2. N. G. Connelly, T. Damhus, R. M. Hartshorn and A. T. Hutton, eds., *Nomenclature of Inorganic Chemistry. IUPAC Recommendations 2005*, Royal Society of Chemistry, Cambridge, 2005.
3. G. A. Lawrence, *Introduction to Coordination Chemistry*, John Wiley and Sons Ltd, Chichester, 2010.
4. D. F. Shriver, P. W. Atkins, T. L. Overton, J. P. Rourke, M. T. Weller and F. A. Armstrong, *Inorganic Chemistry*, Oxford University Press, Oxford, 4th edn., 2006.
5. J. E. Huheey, E. A. Keiter and R. L. Keiter, *Inorganic Chemistry: Principles of Structure and Reactivity*, Harper Collins, New York, 4th edn., 1993.
6. http://www.ch.ntu.edu.tw/~jtchen/course/inorganic/coord_chem.html, Accessed 13th October, 2014.
7. J. G. Gispert, *Coordination Chemistry*, Wiley-VCH Verlag GmbH and Co., Weinheim, 2008.
8. N. F. Curtis, *J. Chem. Soc.*, 1964, 2644-2650.
9. R. Valiente, J. M. Garcia-Lastra, P. Garcia-Fernandez, S. Garcia-Revilla and O. S. Wenger, *Eur. J. Inorg. Chem.*, 2007, 5735-5742.
10. S. J. Farley, D. L. Rochester, A. L. Thompson, J. A. K. Howard and J. A. G. Williams, *Inorg. Chem.*, 2005, **44**, 9690-9703.
11. A. Bossi, A. F. Rausch, M. J. Leitzl, R. Czerwieniec, M. T. Whited, P. I. Djurovich, H. Yersin and M. E. Thompson, *Inorg. Chem.*, 2013, **52**, 12403-12415.
12. W. A. Tarran, G. R. Freeman, L. Murphy, A. M. Benham, R. Katakya and J. A. G. Williams, *Inorg. Chem.*, 2014, **53**, 5738-5749.
13. C. M. Che, S. C. Chan, H. F. Xiang, M. C. W. Chan, Y. Liu and Y. Wang, *Chem. Commun.*, 2004, 1484-1485.
14. C. M. Che, C. C. Kwok, S. W. Lai, A. F. Rausch, W. J. Finkenzeller, N. Y. Zhu and H. Yersin, *Chem. Eur. J.*, 2010, **16**, 233-247.
15. Y. Y. Lin, S. C. Chan, M. C. W. Chan, Y. J. Hou, N. Y. Zhu, C. M. Che, Y. Liu and Y. Wang, *Chem. Eur. J.*, 2003, **9**, 1263-1272.
16. S. Cotton, *Lanthanide and Actinide Chemistry*, John Wiley and Sons, Chichester, 2006.
17. S. Cotton, *Lanthanides and Actinides*, Macmillan Education, London, 1991.

18. N. Kaltsoyannis and P. Scott, *The f elements*, Oxford University Press, Oxford, 1999.
19. H. G. Friedman, G. R. Choppin and D. G. Feuerbacher, *J. Chem. Educ.*, 1964, **41**, 354.
20. P. Atkins and J. de Paula, *Physical Chemistry*, Oxford University Press, Oxford, 8th edn., 2006.
21. D. J. Griffiths, *Introduction to Quantum Mechanics*, Pearson Prentice Hall, Upper Saddle River, 2nd edn., 2005.
22. H. N. Russell and F. A. Saunders, *Astrophys. J.*, 1925, **61**, 38-69.
23. H. J. Emeléus and K. W. Bagnall (eds), *Lanthanides and Actinides*, Butterworth and Co Ltd, London, 1972.
24. A. D. Sherry, P. Caravan and R. E. Lenkinski, *J. Magn. Reson. Imaging*, 2009, **30**, 1240-1248.
25. B. P. Hay, *Inorg. Chem.*, 1991, **30**, 2876-2884.
26. M. Frechette, I. R. Butler, R. Hynes and C. Detellier, *Inorg. Chem.*, 1992, **31**, 1650-1656.
27. T. Phillips, D. E. Sands and W. F. Wagner, *Inorg. Chem.*, 1968, **7**, 2295-2299.
28. G. H. Frost, F. A. Hart, C. Heath and Hursthou.Mb, *J. Chem. Soc. D.*, 1969, 1421-1422.
29. J. Yang, Q. Zeng, L. Peng, M. Lei, H. Song, B. Tie and J. Gu, *J. Environ. Sci.*, 2013, **25**, 413-418.
30. J. D. J. Backerdirks, J. E. Cooke, A. M. R. Galas, J. S. Ghotra, C. J. Gray, F. A. Hart and M. B. Hursthouse, *J. Chem. Soc., Dalton Trans.*, 1980, 2191-2198.
31. J. Martinelli, B. Balali-Mood, R. Panizzo, M. F. Lythgoe, A. J. P. White, P. Ferretti, J. H. G. Steinke and R. Vilar, *Dalton Trans.*, 2010, **39**, 10056-10067.
32. E. C. Constable, *Coordination Chemistry of Macrocyclic Compounds*, Oxford University Press Inc., New York, 1999.
33. D. K. Cabbines and D. W. Margerum, *J. Am. Chem. Soc.*, 1969, **91**, 6540-6541.
34. D. H. Busch, K. Farmery, V. Goedken, V. Katovic, A. C. Melnyk, C. R. Sperati and N. Tokel, *Adv. Chem. Ser.*, 1971, 44-78.
35. M. Kodama and E. Kimura, *J. Chem. Soc., Chem. Commun.*, 1975, 326-327.
36. B. Bosnich, C. K. Poon and M. L. Tobe, *Inorg. Chem.*, 1965, **4**, 1102-1108.
37. G. N. Lewis, *Proc. Natl. Acad. Sci. U. S. A.*, 1925, **11**, 179-183.

38. A. Merbach, L. Helm and É. Tóth (eds), *The Chemistry of Contrast Agents in Medical Magnetic Resonance Imaging*, John Wiley and Sons Ltd., Chichester, 2nd edn., 2013.
39. http://upload.wikimedia.org/wikipedia/commons/f/f1/EM_spectrum.svg, Accessed 25th October, 2014.
40. B. Valeur, *Molecular Fluorescence: Principles and Applications*, Wiley-VCH Verlag, Germany, 2002.
41. J. R. Lakowicz, *Principles of Fluorescence Spectroscopy*, Springer, New York, 3rd edn., 2006.
42. C. Schaller, Photochemistry: absorbance rules, <http://employees.csbsju.edu/cschaller/Reactivity/photochem/PCrules.htm>, Accessed 12th October, 2014.
43. E. A. V. Ebsworth, D. W. H. Rankin and S. Cradock, *Structural Methods in Inorganic Chemistry*, Blackwell Scientific Publications, Oxford, 2nd edn., 1991.
44. V. Balzani, P. Ceroni and A. Juris, *Photochemistry and Photophysics*, Wiley-VCH Verlag GmbH and Co., Weinheim, 2014.
45. S. P. McGlynn, T. Azumi and M. Kinoshita, *Molecular spectroscopy of the triplet state*, Prentice-Hall, Englewood Cliffs, 1969.
46. L. S. Forster, *Coord. Chem. Rev.*, 2002, **227**, 59-92.
47. A. Juris, V. Balzani, F. Barigelletti, S. Campagna, P. Belser and A. Vonzelewsky, *Coord. Chem. Rev.*, 1988, **84**, 85-277.
48. D. L. Pavia, G. M. Lampman, G. S. Kriz and J. R. Vyvyan, *Introduction to Spectroscopy*, Brooks/Cole, Belmont, 4th edn., 2009.
49. H. H. Jaffé and M. Orchin, *Theory and Applications of Ultraviolet Spectroscopy*, John Wiley & Sons, Inc, New York, 1962.
50. J. M. Achord and C. L. Hussey, *Anal. Chem.*, 1980, **52**, 601-602.
51. S. Bonnet and J. P. Collin, *Chem. Soc. Rev.*, 2008, **37**, 1207-1217.
52. M. J. Han, Z. M. Duan, Q. Hao, S. Z. Zheng and K. Z. Wang, *J. Phys. Chem. C*, 2007, **111**, 16577-16585.
53. Z. D. Luo, L. L. Yu, F. Yang, Z. N. Zhao, B. Yu, H. Q. Lai, K. H. Wong, S. M. Ngai, W. J. Zheng and T. F. Chen, *Metallomics*, 2014, **6**, 1480-1490.
54. P. I. Kvam, M. V. Puzyk, K. P. Balashev and J. Songstad, *Acta Chem. Scand.*, 1995, **49**, 335-343.
55. A. Diez, J. Fornies, C. Larraz, E. Lalinde, J. A. Lopez, A. Martin, M. T. Moreno and V. Sicilia, *Inorg. Chem.*, 2010, **49**, 3239-3251.

56. Y. R. Zheng, K. Suntharalingam, T. C. Johnstone, H. Yoo, W. Lin, J. G. Brooks and S. J. Lippard, *J. Am. Chem. Soc.*, 2014, **136**, 8790-8798.
57. J.-C. G. Bünzli and S. V. Eliseeva, in *Lanthanide Luminescence: Photophysical, Analytical and Biological Aspects*, eds. P. Hänninen and H. Härmä, Springer-Verlag, Berlin, 2010.
58. C. M. G. dos Santos, A. J. Harte, S. J. Quinn and T. Gunnlaugsson, *Coord. Chem. Rev.*, 2008, **252**, 2512-2527.

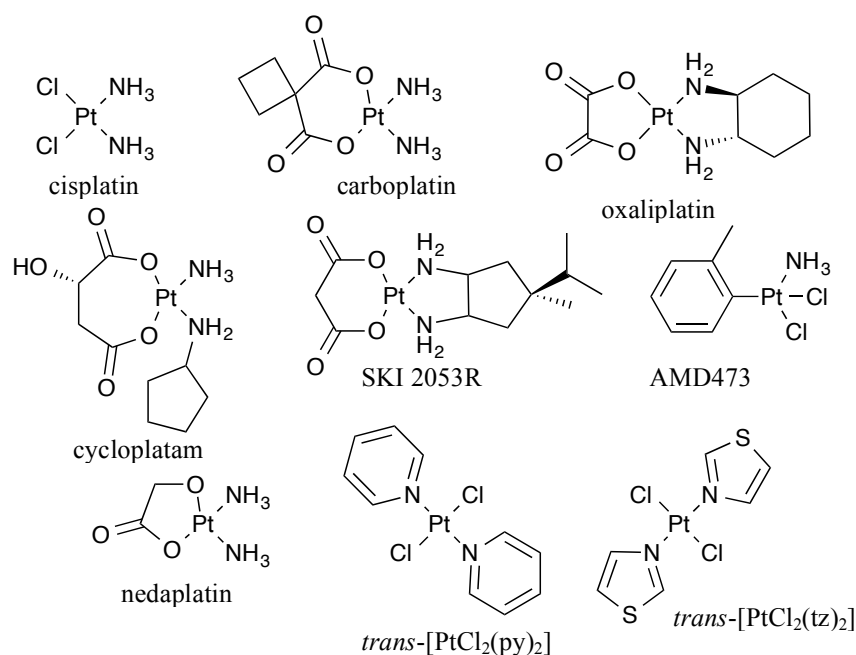
**Chapter 2: Tuning the photophysical properties of platinum
(II) complexes**

2.1. Introduction

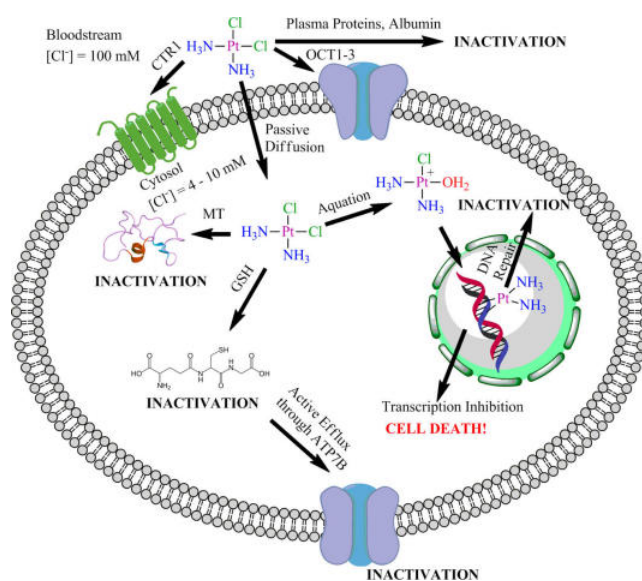
Chapter 2 aims to investigate the photophysical properties of a class of Pt^{II} complexes incorporating functionalised cyclometallating 2-phenylpyridine ligands and how adaptation of the functionality in the 4-position modulates the photophysical attributes. As well as altering the cyclometallating ligand's functionalisation, this chapter will also aim to provide a greater understanding of how different ancillary ligands can affect the photophysical properties. Alongside these measurements, the chapter will detail how these adaptations alter the δ_{Pt} in the ¹⁹⁵Pt NMR spectra and shed light on the electronic properties of the Pt^{II} ion in different coordinative environments.

2.1.1. Use of platinum (II) complexes in cancer treatment

One of the primary reasons for investigating Pt^{II} complexes is because of the profound impact platinum, in its +2 oxidation state, has had on the medical world. Pt^{II} has been used therapeutically for decades since the approval of cisplatin in the United States of America in 1978 for the treatment of various cancers.^{1,2} Since then other compounds such as carboplatin and oxaliplatin have also shown great promise in chemotherapy, with carboplatin being similar in utility to cisplatin but having less side effects.³ Upon injection of the drug into a cancer patient, relative concentrations of chloride and water within cells results in aquation, whereby ligand exchange of a chloride with a water molecule occurs.⁴ The relatively weak coordination of water allows for further ligand exchange with much stronger coordinating donors such as nitrogen. Guanine (G) is a base pair within DNA that is particularly susceptible to interactions with cisplatin due to the nitrogen at the 7-position being favoured by cisplatin as a coordination site. This results in the formation of intrastrand cross-linkage by cisplatin to form a [Pt(NH₃)(G₂)]²⁺ complex.² The coordination to DNA results in a local bend in the structure that unwinds the double helix by *ca.* 25%, arresting the transcription process and resulting in apoptosis.^{2,5}

Figure 2.1 Structures of some Pt^{II} complexes used as chemotherapy drugs.

Cisplatin, however, is not without limitations and risks. The low relative selectivity for tumour cells over healthy cells means it is highly toxic and causes various side effects to patients undergoing chemotherapy, which include kidney damage and seizures.⁶ Some patients also show resistance to treatment with cisplatin through reduced drug transport or improved DNA repair or tolerance for platinum-DNA adducts, which has resulted in the development of cisplatin-like analogues to combat the weak links found in the first generation drug.^{7, 8}

Figure 2.2 Cisplatin pathways into, within and out of cells as well as means of inactivation.⁹

To combat these flaws, many attempts have been made to synthesise structurally similar complexes. Most have been based on simple analogues of cisplatin,

carboplatin and oxaliplatin however, despite more than 3000 compounds being tested by Ziegler *et al.* in 2000, only four of these were deemed suitable for further study based on their promising activity against tumour cells.¹⁰ This has led to a shift from the traditional approach whereby complexes were made based on the structural properties of cisplatin (*cis* geometry, charge neutrality and minimal steric bulk).¹¹ Since the first generation compounds were discovered, complexes involving *trans* orientations, such as *trans*-[PtCl₂(tz)₂] (tz = thiazole), have shown higher activity than cisplatin against certain tumours, whilst the more bulky AMD473 has shown activity within cells that have become resistant to cisplatin.¹²

2.1.2. Photophysical properties of platinum (II) complexes

So that we can have a greater understanding of the factors that will contribute to the photophysical properties of the cyclometallated Pt^{II} complexes, it is important to firstly understand how the physical and electronic structure of Pt^{II} complexes lend themselves to luminescent compounds. It is also important to put the photophysical characteristics of cyclometallated Pt^{II} complexes into context in line with different coordinative motifs that have been found to give emissive Pt^{II} complexes.

The photophysical properties of Pt^{II}, as with other *d*-block metals, are defined by the ligand character, the interaction of the ligand with the metal's valence electrons and the oxidation state of the metal. It is possible to modulate both the excitation and emission profile of Pt^{II} complexes by changing the type of coordination sphere around the metal ion or by altering the functionality of the ligand itself. Pt^{II} complexes most commonly adopt square planar geometries, as described in Chapter 1, which results in the formation of non-degenerate molecular orbitals. This gives rise to the emission of photons in the visible spectrum after electronic excitation. As well as *d-d*, metal-centred (MC), transitions, there are other means by which Pt^{II} complexes can emit visible light (Figure 2.3). An electron can be excited from a strongly bonded ligand-centred orbital to an antibonding metal-centred orbital, known as ligand-to-metal charge transfer (LMCT). Transitions can also occur from a metal-centred orbital to an antibonding ligand-centred orbital, known as metal-to-ligand charge transfer (MLCT), and through ligand-centred (LC) transitions.

MC transitions occur more frequently in first row transition metal complexes whilst LC transitions can be preferred when there are large aromatic systems with extended

π and π^* orbitals. MLCT occurs most frequently when the metal can be readily oxidised and the ligand reduced, and LMCT exists in systems where the ligand can be oxidised and the metal reduced.¹³

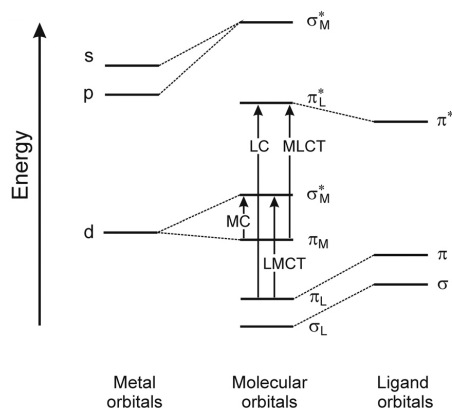


Figure 2.3 Charge transfer processes within a generic transition metal complex.¹⁴

As it has been noted above, certain emissive states require specific characteristics of the ligand, such as easy reducibility for MLCT states. Valiente *et al.* found that the red luminescence from $[\text{Pt}(\text{bpy})\text{Cl}_2]$ derives from a $^3\text{MLCT}$ state due to $d\sigma^*(\text{bpy}) \rightarrow \pi^*(\text{Pt})$ transition, in which the bpy ligand is reduced whilst Pt^{II} is simultaneously oxidized to Pt^{III} .¹⁵ This is in contrast to tetracyanidoplatinates where the emissive state is MC through a $p\sigma^*(\text{Pt}) \rightarrow d\sigma^*(\text{Pt})$ transition.^{16, 17} Cyclometallated phenylpyridine compounds, on the other hand, have been shown to be almost entirely ^3LC in character, which is strongly perturbed by admixing with the $^1\text{MLCT}$ through spin-orbit coupling.¹⁸⁻²³ Reports by Mou *et al.* contradict these findings, to some extent, claiming that the excited states of their $[\text{Pt}(\text{ppy})(\text{O}^{\wedge}\text{O})]$ complexes can be mostly attributed to charge-transfer states, due to the temperature sensitivity, including $^3\text{MLCT}$ and $^3\text{LLCT}$ states.²⁴ They claim that there is only a small contribution from a ^3LC on the cyclometallated ring.²⁵

The emissive wavelength of cyclometallating complexes is also very sensitive to local perturbation of the ligand either through, for example, the addition of fluorine atoms in the 4- and 6-position of the phenyl ring or by extension of the conjugation on the cyclometallated ligand to give hypsochromic and bathochromic shifts, respectively.^{26, 27}

The square planar nature of Pt^{II} complexes leaves their vacant axial sites prone to interaction with solvent molecules as well as intermolecular Pt-Pt contacts. The formation of Pt-Pt bridged dimers can lead to favourable physical properties whereby

the vacant axial sites are no longer susceptible to interactions with reactive species such as singlet oxygen ($^1\text{O}_2$) and others in the local environment.¹⁴ The highly toxic oxygen species can be generated through non-radiative deactivation of the T_1 state by the excitation of ground state dioxygen ($^3\text{O}_2$).²⁸ This makes them much more stable than the monomers, which are capable of forming a transient +4 oxidation state upon direct coordination of the reactive oxygen species (ROS).²⁹ It is important to note that the formation of dimers occurs most frequently in the solid state.

When excimers form through metal-metal interactions it causes the destabilisation of the occupied d_{z^2} orbitals so, where the transition was characterised by $d\pi \rightarrow \pi^*$ in the monomer, the new lower energy transition involves $d\sigma^* \rightarrow \pi^*$.³⁰ These new excited states involve ligand-to-metal-metal charge transfer (LMMCT) and metal-metal-to-ligand charge transfer (MMLCT) and, due to the increased energy through destabilisation of the highest occupied molecular orbital (HOMO), often show lower energy absorption and emission profiles.¹⁴ This bathochromic shift in the absorption is ideal due to the deeper penetration and less harmful nature of longer wavelength light. The occupation of the axial sites also prevents quenching by solvent molecules or dissolved oxygen, often leading to the advantageous extension of emissive lifetimes and higher quantum yields.

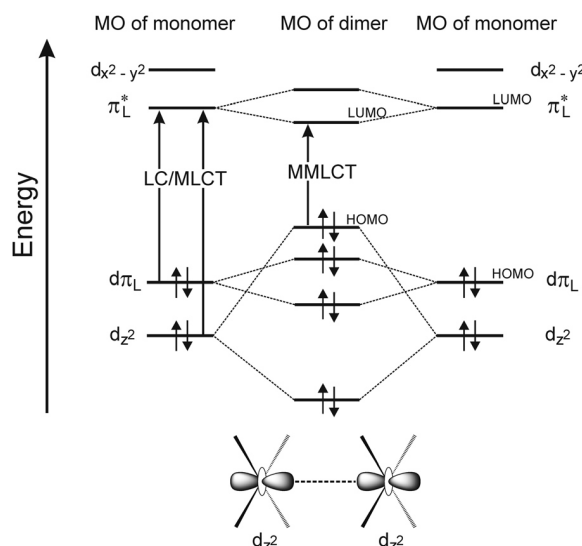


Figure 2.4 Simplified molecular orbital (MO) diagram of interacting square-planar Pt^{II} complexes showing influence of d_{z^2} interaction on the energy levels of the MOs.

Although these advantageous properties are appealing, the intermolecular interactions can also have a detrimental impact, both physically and photophysically. The lifetimes can suffer as a result of induced quenching through triplet-triplet

annihilation.³¹ They can also aggregate, reducing the solubility, resulting in their precipitation.¹⁴

Most of the literature regarding luminescent d^8 complexes focuses on Pt^{II} complexes, although there are a plethora of luminescent Pd^{II} compounds reported. Despite having similar properties to those of their platinum counterparts, the higher ionisation potential for the $4d$ orbital of palladium compared to that of the $5d$ orbital for platinum results in blue-shifted absorption and emission profiles from around 430 nm for platinum to 390 nm for the coordinatively identical palladium complex.^{30, 32}

2.1.3. Ancillary ligands for cyclometallated platinum (II) complexes

Ancillary ligands can be incorporated to help tune a number of properties. They are frequently employed to alter the photophysical properties of a complex but can also be used to aid solubility and affect the physical attributes, such as charge.³³ Cyclometallated μ -dichloro-bridged dimers of Pt^{II} complexes, such as $[\text{Pt}(\text{ppy})(\mu\text{-Cl})]_2$, like analogous Ir^{III} precursor complexes, can be split using ancillary ligands to produce the monometallic target compound, which can possess much greater solubility. Whilst literature on Ir^{III} complexes is dominated by diimines such as 2,2'-bipyridine and 1,10-phenanthroline, Pt^{II} complexes predominantly incorporate β -diketones such as 2,4-pentanedione (acac), dipivaloylmethane (hmacac) and dibenzoylmethane (dbacac).²⁷

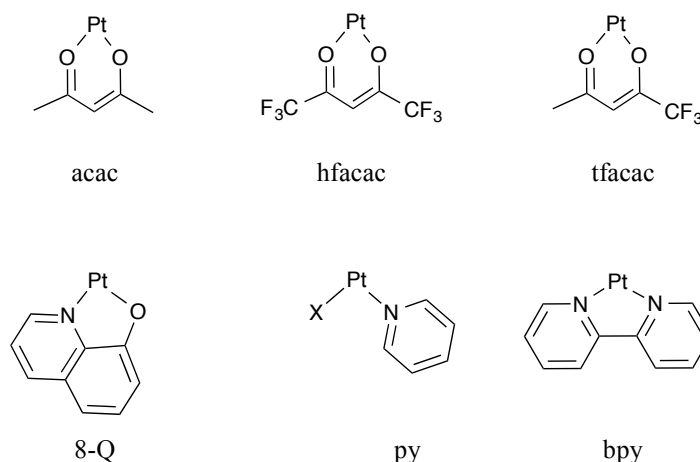


Figure 2.5 A selection of ancillary ligands found on cyclometallated Pt^{II} complexes.

Coordinated β -diketonates offer a great deal of diversity and allow tuning of the photophysical properties by introduction of aromatic functionalisation in the 1- and 5-positions. Other alterations, beyond the extension of conjugation, have also been

found to have dramatic influences on the photophysical properties of the complex. Replacement of the $-\text{CH}_3$ groups on acac with $-\text{CF}_3$ moieties has been reported to result in a loss of emission from cyclometallated complexes.³⁴ DFT measurements revealed that the lowest unoccupied molecular orbital (LUMO) for the hexafluoroacetylacetonate (hfacac) complexes showed electron density predominantly on the ancillary ligand (seen in the LUMO+2 for the acac complexes). This was proposed as being a result of the electron withdrawing CF_3 groups stabilising the π^* orbitals to such a degree that the LUMO shifts from lying on the cyclometallating ligand. This suggests that the lack of emission is most probably a result of the poor overlap of orbitals involved in excitation as the frontier orbitals are localised on different parts of the molecule.³⁵

Hydroxyquinoline (8-HQ), and its analogues, have also been used as ancillary ligands on cyclometallated Pt^{II} complexes and show promise as highly efficient singlet oxygen generators as well as having desirable photophysical properties.³⁶ These compounds have absorption profiles well into the visible region with λ_{max} close to 500 nm and emit well beyond 700 nm with lifetimes of more than 5 μs .

Esmaeilbeig *et al.* utilised the labile Pt^{II} coordinated solvent molecule, namely DMSO, to undergo ligand exchange with a monodentate, *N*-aromatic ligand, such as imidazole and pyridine (py).³⁷ They found that complexes of the type $[\text{Pt}(\text{ppy})(N)\text{Cl}]$, where *N* is the monodentate *N*-aromatic ligand, display antitumor properties and were assessed for their viability for such applications. It was found that the size of the *N*-aromatic ligand plays a key role in the biological activity of the complexes. The reactions all proceeded to completion in acetone without the need for external heat sources, which opens up the possibility of utilising this easy reactivity to appending greater functionalisation to the Pt^{II} complexes through this readily formed Pt-N bond.

Kvam *et al.* originally investigated the photophysical properties of mixed $\text{C}^{\wedge}\text{N} \text{ N}^{\wedge}\text{N}$ Pt^{II} complexes in 1995, where $\text{N}^{\wedge}\text{N}$ is 2,2'-bipyridine (bpy) or a functionalised analogue.³⁸ This investigation was later repeated by Jenkins *et al.* who found that, whilst most of Kvam's conclusions were correct, the reduction of the ligands in the two reversible reductions in dimethylformamide (DMF) are attributed to the π^* orbitals of the diimine ligand with a small contribution from the π^* character of the cyclometallated ligand. They again concluded that, unlike most *d*-block diimine

complexes, the emission observed is not $^3\text{MLCT}$ in character but, instead, ^3LC with significant metal character perturbed by a low-lying $^1\text{MLCT}$ state.³⁹

2.1.4. Imaging and bioimaging applications of platinum (II) complexes

There has been a vast array of research on luminescent transition metal complexes, resulting in an equally expansive set of applications including optoelectronics,^{40, 41} photo-catalysis,^{42, 43} components for electron transfer systems,⁴⁴ bio-sensing and bio-imaging,^{45, 46} dye-sensitized solar cells (DSSCs) and organic light emitting diodes (OLEDs).^{47, 48} Despite their attractive physical and photophysical properties, relatively few systems incorporating Pt^{II} have been documented in comparison to the heavily investigated systems utilising d^6 transition metals and lanthanides.

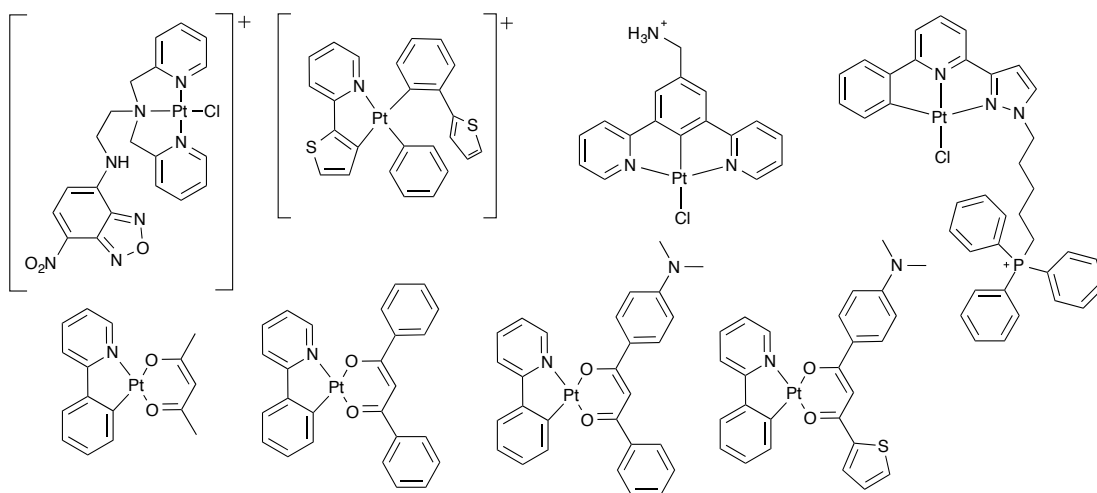


Figure 2.6 Range of cyclometallated Pt^{II} complexes where the cationic species localise in nuclei (*top*) and neutral compounds exhibit cytoplasmic localisation (*bottom*).

Their utility as cellular imaging agents is amongst one of the most prevalent areas of interest for luminescent Pt^{II} complexes. These range from neutral complexes, which have been shown to localise in the cytoplasm, to cationic structures localising in organelles such as the endoplasmic reticulum and nucleus.¹⁴ Cyclometallated, or orthometallated, bidentate complexes show high stability and impressive emissive properties and, despite the abundance of cyclometallated Pt^{II} complexes in the literature, very few are suitable for imaging due to their lack of hydrophilicity. Examples do exist, however, including compounds by Lai *et al.*, which exhibit higher cytotoxicity upon irradiation than in dark studies, suggestive of a high efficacy for $^1\text{O}_2$ generation.⁴⁹ Mou *et al.* found that cyclometallated compounds with ancillary β -diketonate ligands also show promise in cellular imaging with exclusive cytoplasmic localisation and low toxicity. They discovered that the emissive properties could be

tuned through adaptation of the β -diketonate by lowering the triplet-state energy of the ancillary ligand.²⁵

Botchway *et al.* expanded on the development of cellular imaging agents in the synthesis of a series of Pt^{II} compounds (Figure 2.7) with tridentate ligands that expressed remarkably high quantum yields (up to 70 %) and emissive lifetimes (μs timeframe) that localise intracellularly with low cytotoxicity.⁵⁰ They also found that the photostability of the compounds was sufficient to allow for two-photon excitation (TPE), a tissue-friendly method where a high flux of low energy photons provide two photons of low energy simultaneously for one excitation, resulting in an emissive wavelength that is lower than that of each photon absorbed. The long lifetimes and highly emissive states also made it possible to use the compounds for time-resolved emission imaging microscopy (TREM), which allows discrimination between changes in lifetime and the time-gated removal of short-lived autofluorescence.⁵¹

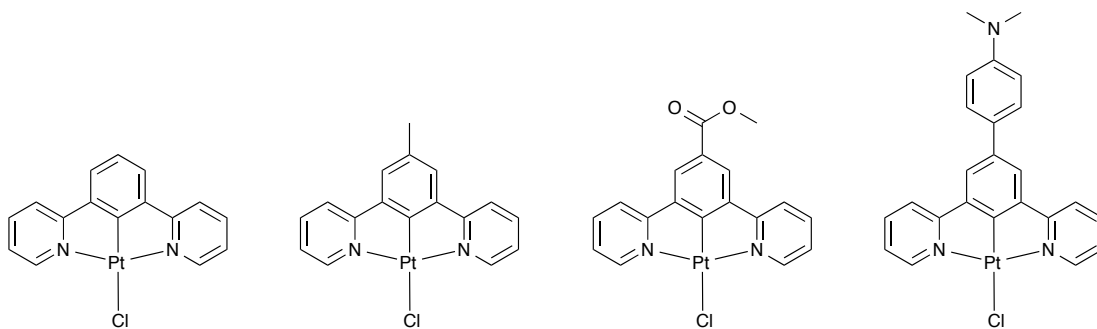


Figure 2.7 Complexes synthesised by Botchway *et al.* for cellular imaging using TPE and TREM.

2.1.5. ^{195}Pt NMR spectroscopy

^{195}Pt is the only spin active isotope of platinum. It has a good natural abundance resulting in a relative sensitivity of 0.01 (where 1 is ^1H) and a spin quantum number, I , of $\frac{1}{2}$.⁵² This makes it extremely useful as a means of probing the electronic environment of the metal centre. Importantly, studies have revealed the sensitivity of the chemical shift (δ) to changes in oxidation state, ligand substitution and stereochemistry.^{53, 54} As the chemical shift of ^{195}Pt spans ± 7000 ppm, subtle changes such as ligand substitution can often result in shifts of over 100 ppm.⁵⁵ The technique has been used in a wide range of applications, including structural determination of the binding and interaction of platinum to drugs and biological components such as peptides and DNA.^{56, 57}

Despite the marked advantages of this technique, the sensitivity of δ for ^{195}Pt makes comparable data hard to come by as many factors can affect the shift; changes in temperature (as much as 1 ppm K $^{-1}$), solvent, isotopomers and the internal reference have all been reported as contributing to difficulties in referencing ^{195}Pt NMR spectra reliably.^{58, 59}

2.1.6. Functionalised phenylquinolines

Phenylquinoline (pqH) derivatives have been used for over a hundred years in medicine: cinchophen (2-phenyl-4-quinolinecarboxylic acid) was used from 1910 as an analgesic to treat gout for over twenty years before it was found to cause severe liver damage.⁶⁰ Since then, many derivatives have been synthesised for a range of applications. The most researched are compounds based on 2-phenyl-4-quinolinecarboxamides (Figure 2.8) as they are known to be antagonists for tachykinin receptors, giving potential for therapeutics relating to neurological diseases, including schizophrenia.⁶¹⁻⁶³

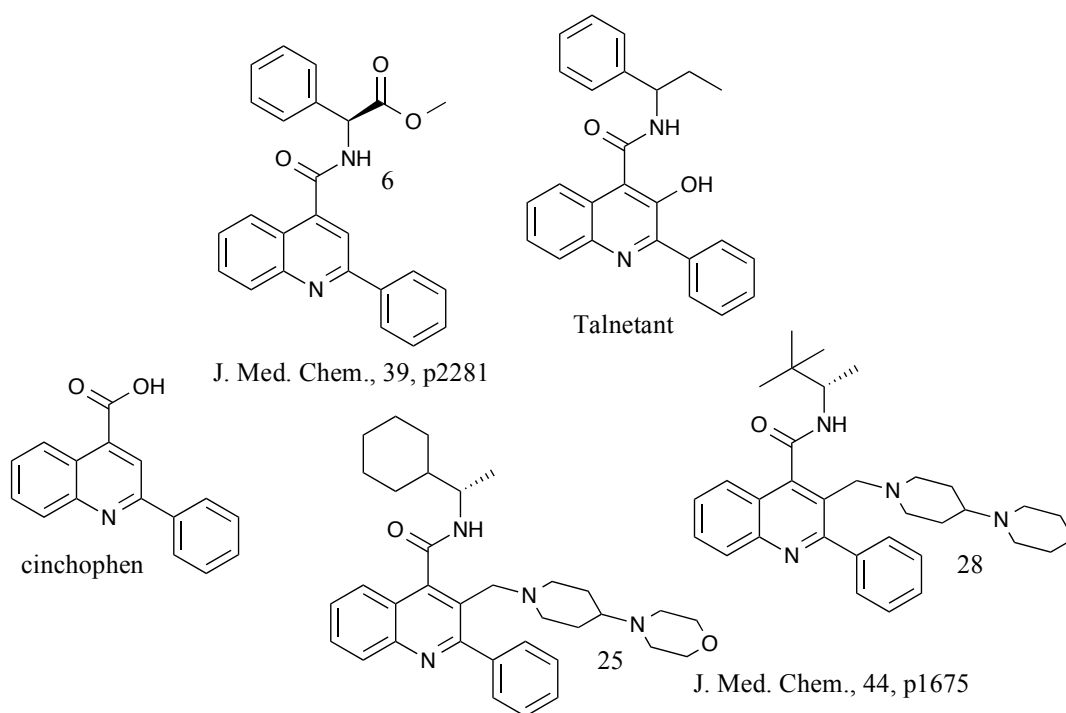


Figure 2.8 Structures of a range of phenylquinoline compounds with biological activity. Of note are cinchophen (*bottom left*) and Talnetant (*top right*), which have undergone clinical trials.

Phenylquinolines also show frequent use in coordination chemistry due to their potential bidentate, N[^]C coordination mode. They show advantageous photophysical properties compared to phenylpyridine (ppyH) owing to the extended π -conjugation from the addition of an aromatic ring, which lowers the π^* orbital energy resulting in

bathochromically shifted $^1\text{MLCT}$ absorption and $^3\text{MLCT}$ emission. For this reason, there are an array of Ir^{III} complexes (Figure 2.9) that incorporate functionalised cyclometallated phenylquinoline complexes in the literature with applications ranging from OLEDs to biotin-tagged imaging agents.⁶⁴⁻⁷⁴ There are also reports of cyclometallated Pt^{II} complexes with phenylquinoline moieties (Figure 2.9) with potential utilities in a variety of areas including polymer light emitting devices (PLEDs), OLEDs and photosensitisers for singlet oxygen.^{18, 19, 27, 75-78}

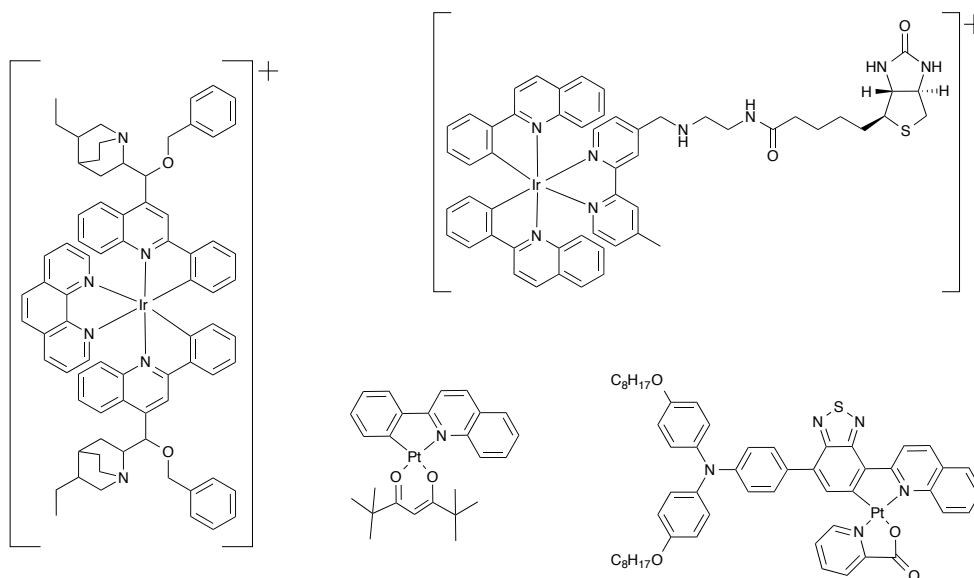


Figure 2.9 Examples of some Ir^{III} and Pt^{II} complexes incorporating phenylquinoline ligands.

2.2. Aims

Chapter 2 discusses the photophysical properties of Pt^{II} complexes with functionalised cyclometallated phenylquinoline ligands. The functionality of the ligand was altered to ascertain how this impacted the luminescent characteristics of the complexes by varying the electronic nature of the ligand. The effects of the ancillary ligands on the luminescent properties were also investigated by altering the electronic nature of β -diketonates and also by changing the coordination motif around the Pt^{II} atom through the introduction of different ligand types. The compounds were characterised, where possible, by ¹⁹⁵Pt NMR spectroscopy to give a greater understanding of the changes in the electronics occurring at the metal centre.

2.3. Results and Discussion

2.3.1. Ligand synthesis

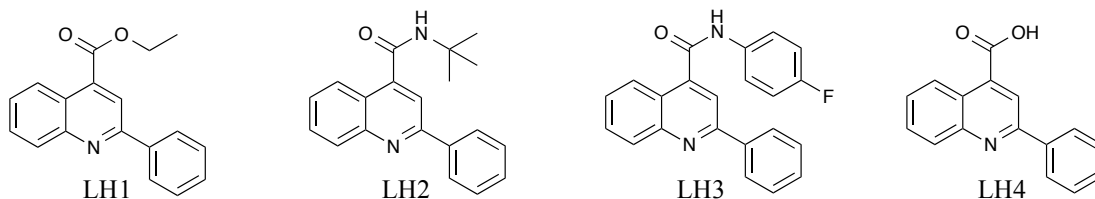


Figure 2.10 Structures of the ligands utilised in Chapter 2.

The ligands have all been previously reported in the literature and have been coordinated to Ir^{III} in a cyclometallated manner.⁷⁹ **LH1** was obtained by a simple esterification reaction using a literature methodology.⁸⁰ **LH2** and **LH3** were formed through the reaction of an acyl chloride and commercially available primary amines based on a modified literature methodology.⁷⁹ Chloroform was used instead of acetonitrile as it acted as a better solvent for the acyl chloride, resulting in almost instantaneous reactivity upon addition of the amine and EtNiPr₂ at room temperature. The isolated ligands were analysed by ¹H NMR spectroscopy for purity and compared with literature values to ensure the reactions were successful.

2.3.2. Synthesis and characterisation of cyclometallated platinum (II) complexes

2.3.2.1. [Pt(L)(μ-Cl)]₂ complexes

The cyclometallated Pt^{II} μ-dichloro-bridged dimers, [Pt(L)(μ-Cl)]₂, were obtained from reactions with potassium tetrachloroplatinate (II) and the corresponding ligand, **LH**. Exhaustive attempts at synthesising the complexes were made using a wide range of synthetic methodologies before a suitable reaction route was found. Initial trials were based on previous experience with the synthesis of analogous cyclometallated Ir^{III} chloro-bridged dimers with **LH1** utilising 2-methoxyethanol and water (3:1) and heating the reaction to 100 °C for 48 h.⁸¹ This yielded a grey, insoluble solid, which was precipitated with water and filtered. The solid was washed with dichloromethane and the filtrate was dried and characterised and was found to be free ligand in almost stoichiometric yield.

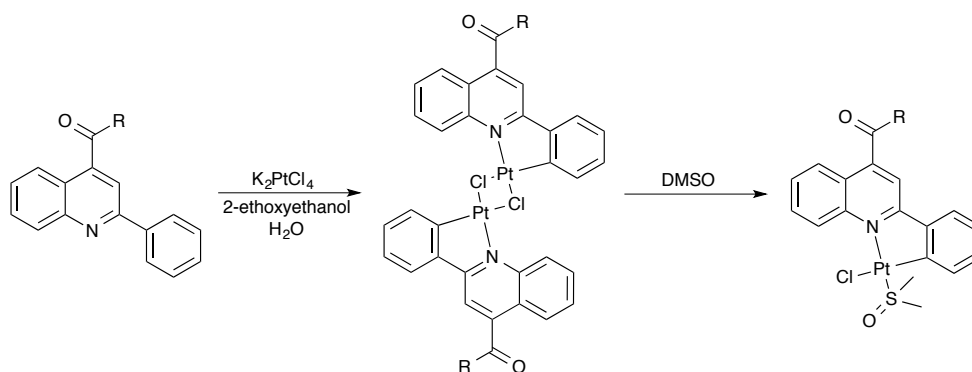


Figure 2.11 Synthesis of $[Pt(L)(\mu-Cl)]_2$ and $[Pt(L)(DMSO)Cl]$ R = OEt (**L1**), HNT-butyl (**L2**), HNp-fluorobenzene (**L3**), OH (**L4**).

Upon further investigation in the literature, it was found that, in the presence of alcohol and under elevated temperatures ($> 30\text{ }^{\circ}\text{C}$), the platinate (II) readily reduces to Pt^0 giving rise to the insoluble black solid found in the previous experimental methods.^{36, 82} The conditions outlined by Shavaleev *et al.* using $[PtCl_4](Bu_4N)_2$ in ethanol and dichloromethane overcome this issue by reacting at $30\text{ }^{\circ}\text{C}$ for 7 days. However, despite the apparent lack of any black solid, the reaction yielded free ligand as the major component.

An experimental procedure was finally selected whereby the ligand was dissolved in 2-ethoxyethanol and the platinate (II) was added dropwise as an aqueous solution with a solvent ratio of 3:1 of 2-ethoxyethanol to water.⁸³ Experience suggested that the excessive reduction of Pt^0 could be minimised by ensuring that the platinate (II) was kept mostly in solution by increasing the volume of solvent accordingly, whilst maintaining the 3:1 ratio (typically, using 50 – 100 mg of platinate (II) required 8 mL of solvent). The reaction vessel was flushed with nitrogen and wrapped in foil to prevent photoreduction.⁸⁴⁻⁸⁶ The mixtures were then heated to $80\text{ }^{\circ}\text{C}$ for 24 – 48 h before being cooled to room temperature. The products were precipitated using brine to give green/yellow/brown solids upon filtration. Purification was carried out in the later steps and the dimers were used as isolated.

The Pt^{II} μ -dichloro-bridged dimers were uncharacterised except for $[Pt(\mathbf{L1})Cl]_2$, for which the ^{195}Pt NMR spectrum was obtained for reference. ^1H NMR spectra were often mixtures of the desired dimer, free ligand and a small trace of ligand-split dimer, forming an N_2CCl coordination sphere.⁸⁷ The formation of the $[Pt(ppy)(ppyH)Cl]$ complex is noted frequently in the literature and reacts with DMSO to form the $[Pt(L)(DMSO)Cl]$ complex in the same way as the μ -dichloro bridged dimer.⁸⁸

2.3.2.2. [Pt(L)(DMSO)Cl] complexes

The dimers were split following a preparative method described by Godbert *et al.* by dissolution of the complex with a minimal volume of dimethylsulfoxide,⁸² followed by filtration through cotton wool (to remove any small residues of Pt⁰). Brine was added to precipitate the product before it was washed with plenty of water to remove excess dimethylsulfoxide. The adducts were purified in the next step, upon coordination of an ancillary ligand, except for [Pt(L1)(DMSO)Cl] which was found to be spectroscopically clean from the reaction. Although characterisation by ¹H, ¹³C and ¹⁹⁵Pt NMR spectroscopies all indicated that the product was pure, thin layer chromatography (TLC) analysis revealed that there was a dark species with a retention factor of zero and a relatively fast moving yellow spot with a 9:1 mixture of dichloromethane and ethyl acetate as the mobile phase. Subsequent purification by flash column chromatography on silica yielded the product as a dark orange solid. The complex could, however, be used without purification as the spectroscopically pure brown solid.

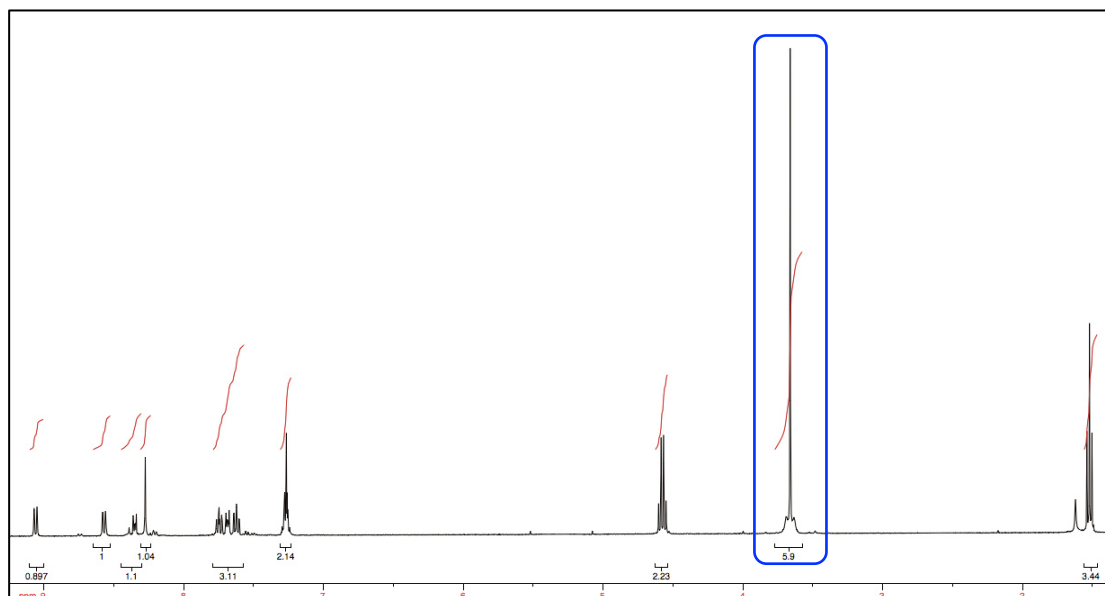


Figure 2.12 ¹H NMR spectrum for [Pt(L1)(DMSO)Cl]. Highlighted: SO(CH₃)₂ with ³J_{HPt} coupling.

¹H NMR spectroscopy provided key data confirming the synthesis of the product, with a peak at *ca.* 3.5 ppm with characteristic ¹⁹⁵Pt satellites related to ³J_{HPt} coupling for the methyl groups on the coordinated DMSO ligand. Given the high level of purity, [Pt(L1)(DMSO)Cl] was fully characterised by ¹H, ¹³C and ¹⁹⁵Pt NMR spectroscopies as well as UV-vis and IR spectroscopies. ¹H NMR spectrum of [Pt(L1)(DMSO)Cl] revealed the presence of the ³J_{HPt} coupling for the proton on the

carbon adjacent to the cyclometallated carbon at 8.4 ppm. $^2J_{\text{CPt}}$ coupling was observed in the ^{13}C NMR spectrum for the DMSO methyl groups at 46.3 ppm.

From the $[\text{Pt}(\text{L})(\text{DMSO})\text{Cl}]$ complex, a variety of other compounds could be obtained through different synthetic pathways (Figure 2.13). A number of these were selected to assess the changes in photophysical properties when different ancillary ligands were coordinated.

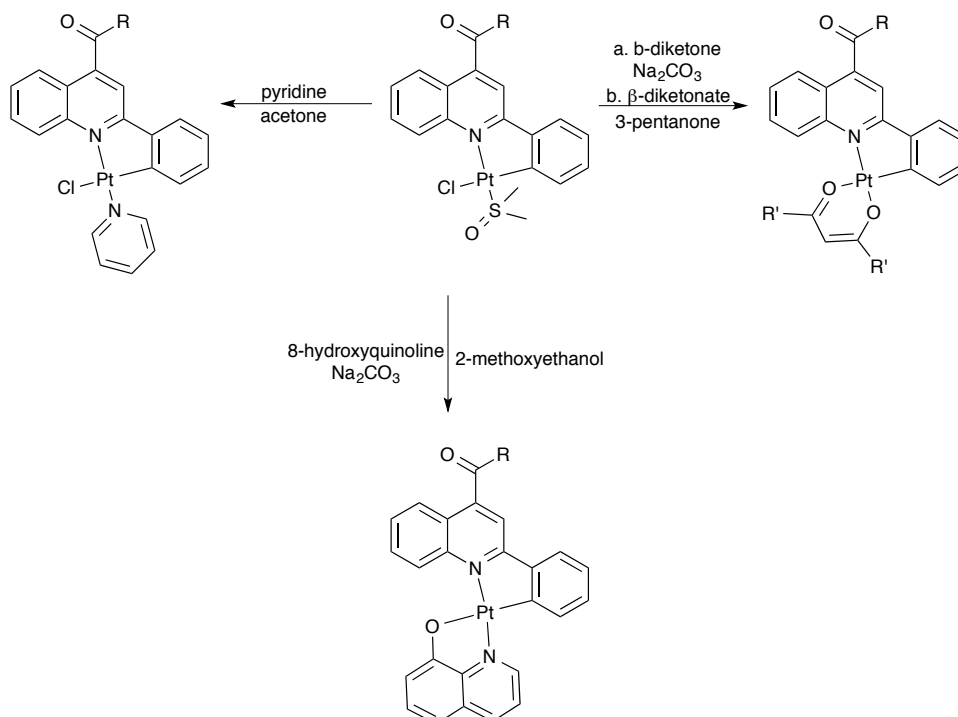


Figure 2.13 Synthesis of $[\text{Pt}(\text{L})(\text{py})\text{Cl}]$, $[\text{Pt}(\text{L})(8\text{-Q})]$ and $[\text{Pt}(\text{L})(\beta\text{-diketonate})]$: $\text{R} = \text{OEt}$ (**L1**), $\text{HN}t\text{-butyl}$ (**L2**), $\text{HN}p\text{-fluorobenzene}$ (**L3**), OH (**L4**); $\text{R}' = \text{CH}_3$ (acac), $\text{C}(\text{CH}_3)_3$ (hmacac), CF_3 (hfacac).

2.3.2.3. $[\text{Pt}(\text{L})(\beta\text{-diketonate})]$ complexes

Sodium salts of acetylacetone and hexamethylacetylacetone were synthesised based on the methodology outlined by Spencer *et al.* through deprotonation with sodium hydride in refluxing petroleum ether to yield the sodium salt as a monohydrate.³⁵ For the fluorinated β -diketone, hexafluoroacetylacetone was used without preparation of the sodium salt owing to the increased acidity of the α -proton. The $[\text{Pt}(\text{L})(\text{DMSO})\text{Cl}]$ complexes were dissolved in a small volume (*ca.* 5 mL) of 3-pentanone before the sodium salt of the β -diketonate monohydrate (hmacac and acac) or the β -diketone (hfacac) was added. Sodium carbonate was added to the reaction with the β -diketone to neutralise the change in pH from the formation of HCl. Ten equivalents of both acac and hfacac were used whilst only one equivalent of the hmacac was used owing

to issues in the separation of excess hmacac from the desired product. The complexes were purified by flash column chromatography on silica with dichloromethane and were all eluted as the first yellow/orange band.

[Pt(**L4**)(acac)] was accessed from [Pt(**L1**)(acac)] by following a methodology for the same ethyl ester deprotection of [Ir(**L1**)₂(bpy)](PF₆) by dissolving the complex in equal volumes of acetone and 1M NaOH solution.⁸¹

The complexes were all characterised by ¹H, ¹³C and ¹⁹⁵Pt NMR spectroscopies as well as UV-vis, IR spectroscopies and, in some cases, mass spectrometry although obtaining data proved troublesome, possibly due to the species being neutral. ¹H NMR spectroscopy was used to observe both the α-proton on the β-diketonate at *ca.* 5.5 ppm as well as the methyl groups as two very close singlets at *ca.* 2 ppm. ³J_{HPt} satellites can, again, just be made out at 7.8 ppm for the adjacent proton to the cyclometallated carbon.

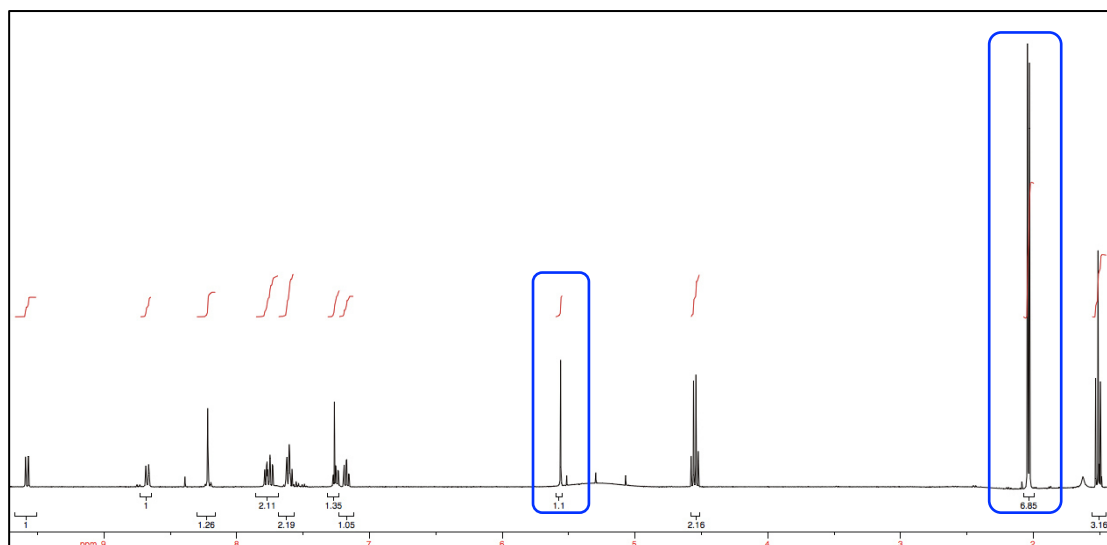


Figure 2.14 ¹H NMR spectrum for [Pt(**L1**)(acac)]. Highlighted: CH₃C=OHC=OCH₃ (*middle*), CH₃C=OHC=OCH₃ (*right*).

2.3.2.4. [Pt(**L1**)(8-Q)] complex

After attempts following a similar synthetic methodology to the preparation of the β-diketonate complexes failed using the sodium salt of 8-hydroxyquinoline (prepared in a similar manner), a methodology used by Shavaleev *et al.* was adopted.³⁶ Sodium carbonate, 8-hydroxyquinoline and [Pt(**L**)(DMSO)Cl] were dissolved in 2-methoxymethanol before being heated to 100 °C under dinitrogen. The cooled solution was dried *in vacuo* before being dissolved in dichloromethane and washed

with water to remove inorganic salts. The organic phase was then purified either through precipitation with diethyl ether followed by washing with a small volume of cold methanol or, if precipitation was unsuccessful, by column chromatography on silica in dichloromethane. They were then eluted as the first orange/dark red band, closely preceded by the cream coloured band of 8-hydroquinoline. Characterisation of the complex using ^1H NMR spectroscopy was more difficult due to the number of aromatic protons increasing the complexity in the 7-10 ppm range. Despite this, comparison to the $[\text{Pt}(\text{L1})(\text{DMSO})\text{Cl}]$ spectra revealed a wider range in the aromatic protons with downfield shifts close to 9.9 ppm and upfield shifts to 6.8 ppm. The presence of a second set of satellites at 9.2 ppm relating to $^3J_{\text{HPt}}$ coupling for the proton in the 2-position of the 8-Q was also used to confirm the presence of a coordinated 8-Q species.

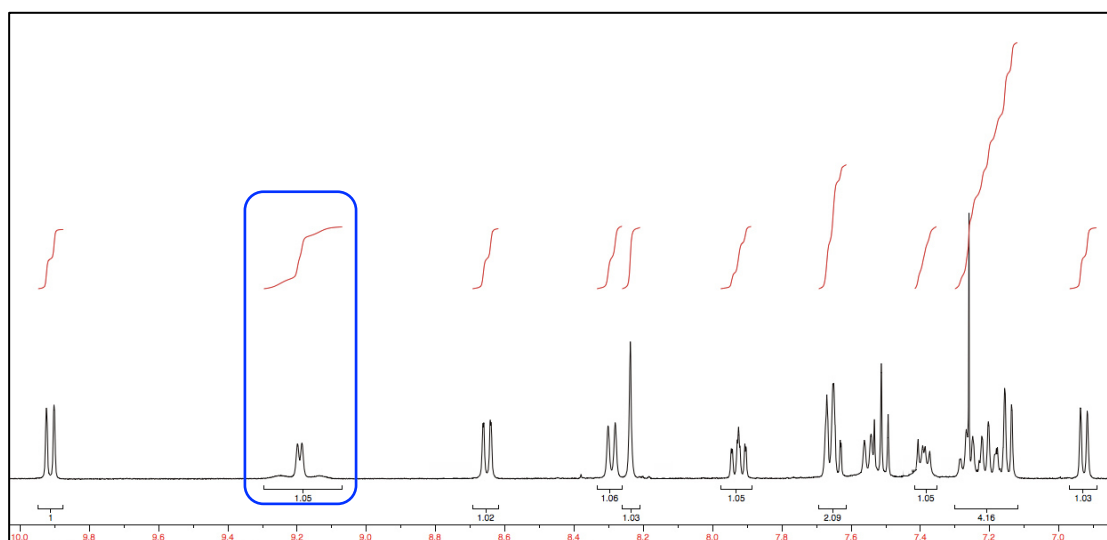


Figure 2.15 ^1H NMR spectrum of $[\text{Pt}(\text{L1})(8\text{-Q})]$. Highlighted: NC^2H of 8-quinolinato with $^3J_{\text{HPt}}$ coupling.

2.3.2.5. $[\text{Pt}(\text{L1})(\text{py})\text{Cl}]$ complex

$[\text{Pt}(\text{L1})(\text{DMSO})\text{Cl}]$ was dissolved in acetone (*ca.* 5 mL) before pyridine was added in slight excess.³⁷ The mixture was stirred for 16 h and then the solvent was reduced to a minimal volume and diethyl ether was added to precipitate the product. The solid was then washed with a small volume of diethyl ether to remove any excess pyridine before being characterised fully. The ^1H NMR spectrum revealed two equivalent protons with ^{195}Pt satellites at 9.0 ppm corresponding to the two protons in the 2- and 6-position of the pyridyl ligand, with $^3J_{\text{HPt}}$ coupling. Interestingly, the proton adjacent to the cyclometallating carbon shifts substantially upfield compared to any of the other observed species at 6.3 ppm.

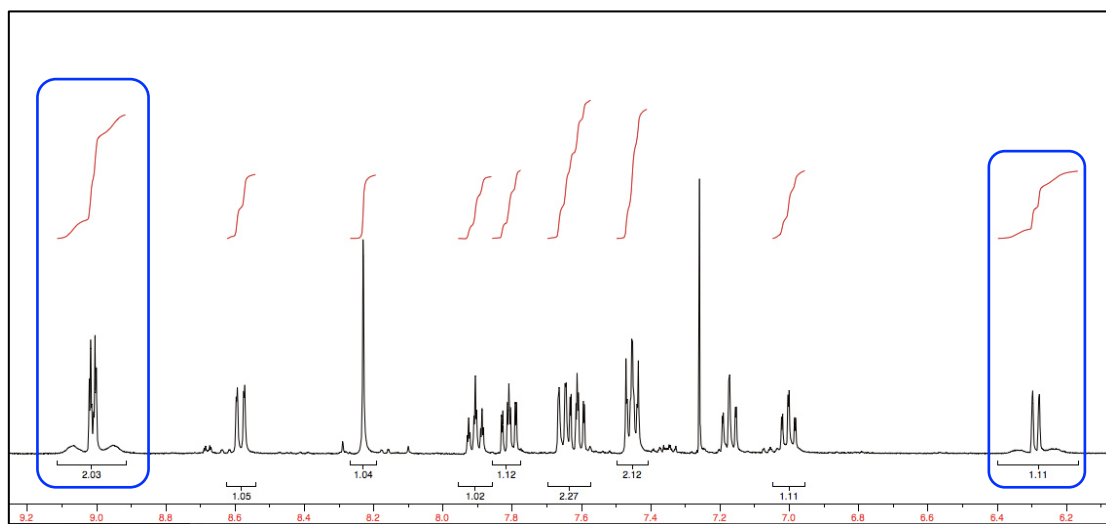


Figure 2.16 ^1H NMR spectrum for $[\text{Pt}(\text{L1})(\text{py})\text{Cl}]$. Highlighted: NC^2H of pyridine (*left*), PtCCH of **L1** (*right*) showing $^3J_{\text{HPt}}$ coupling.

2.3.2.6. Cationic platinum (II) complexes

Given the uptake of cationic Pt^{II} complexes by organelles such as the nucleus, it was of interest to try to synthesise a cationic analogue of the complexes.¹⁴ This was attempted through modulation of the ligand, to afford a locally cationic quaternary nitrogen, and through coordination of a neutral diimine to create a universally cationic complex.

The first route involved synthesis of an imidazolium moiety through reaction of a halide with methylimidazole in refluxing toluene (Figure 2.17).⁸⁹ This was done, firstly, on the free ligand to assess the viability and then on a complex incorporating an alkyl chain with a pendant halide for reactivity at the later stages. Unfortunately this route did not yield any meaningful results, which was most likely down to the harsh reaction conditions and the presence of an imidazole, which could form coordinative bonds with the complex, preventing reactivity in the desired fashion.

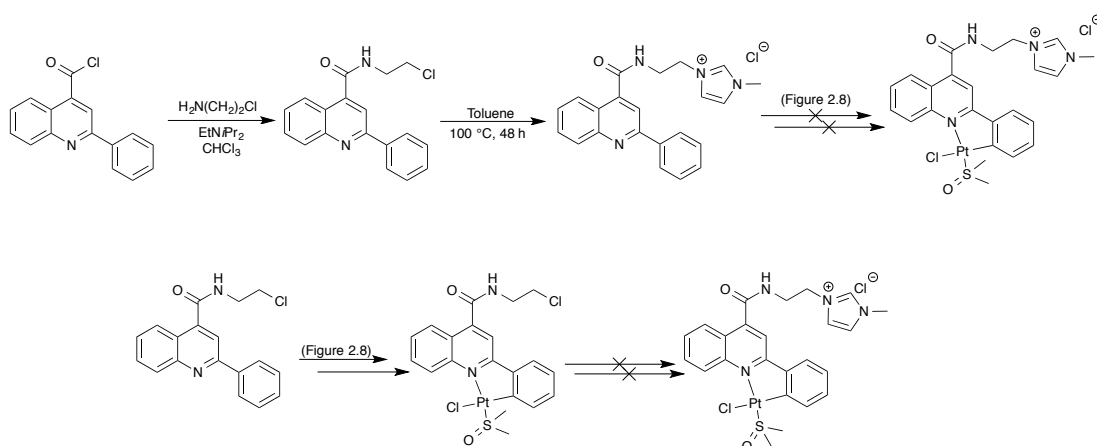


Figure 2.17 Schematic of the first attempts to synthesise a cationic Pt^{II} complex.

The second route (Figure 2.18) involved the reaction of a $[\text{Pt}(\text{L})(\text{DMSO})\text{Cl}]$ complex with 2,2'-bipyridine (bpy) in order to synthesise $[\text{Pt}(\text{L})(\text{bpy})]^+$. This reaction was carried out based upon a similar methodology by Jenkins *et al.* using DMF as the solvent and heating overnight to 65 °C.³⁹

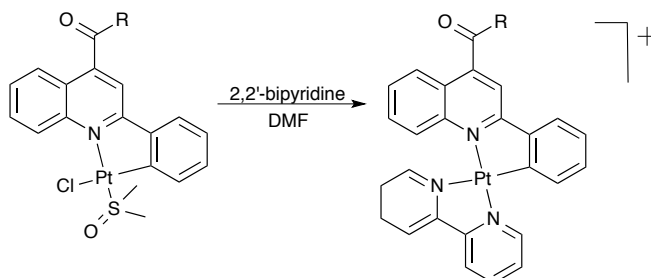


Figure 2.18 Schematic of the successful synthetic route to $[\text{Pt}(\text{L})(\text{bpy})]^+$.

Whilst the product, $[\text{Pt}(\text{L1})(\text{bpy})]^+$, was observed by mass spectrometry, initial attempts to characterise using ^1H NMR spectroscopy yielded very broad, poorly defined signals. Eventually, after extending the reacting time from the reported 18 h to 48 – 72 h, it was found that, after precipitation with diethyl ether, the complex could be partially dissolved in acetonitrile before the counterion was exchanged for hexafluorophosphate to aid solubility by addition of a saturated solution of the potassium salt. Purification by extraction and precipitation resulted in the desired complex being formed.

2.3.3. ^{195}Pt NMR spectroscopy analysis

The ^{195}Pt NMR spectrum of $[\text{Pt}(\text{L1})(\mu\text{-Cl})]_2$ revealed two distinct ^{195}Pt environments with chemical shifts of -3186 and -3219 ppm, most likely corresponding to $[\text{Pt}(\text{L1})(\text{LH1})\text{Cl}]$ and $[\text{Pt}(\text{L1})(\mu\text{-Cl})]_2$, respectively. Both Pazderski *et al.* and Ghavale *et al.* have observed the δ_{Pt} for $[\text{Pt}(\text{ppy})(\text{ppyH})\text{Cl}]$ at -3212 and -3201 ppm, whilst data for $[\text{Pt}(\text{ppy})(\mu\text{-Cl})]_2$ were reported to be unobtainable due to a lack of solubility.^{33, 90} These values compare to the δ_{Pt} of -3186 ppm observed for $[\text{Pt}(\text{L1})(\text{LH1})\text{Cl}]$, formed in the synthesis of $[\text{Pt}(\text{L1})(\mu\text{-Cl})]_2$. The data suggest that the Pt^{II} is slightly more deshielded in $[\text{Pt}(\text{L1})(\text{LH1})\text{Cl}]$ than in $[\text{Pt}(\text{ppy})(\text{ppyH})\text{Cl}]$ hence the upfield shift of approximately 15 ppm.

Whilst Pazderski and Ghavale quote near identical shifts, within error, for the $[\text{Pt}(\text{ppy})(\text{ppyH})\text{Cl}]$ complex, the literature seems to dispute the chemical shift for the ^{195}Pt NMR spectroscopy of $[\text{Pt}(\text{ppy})(\text{DMSO})\text{Cl}]$.^{33, 90} Whilst the reasons for this are

unclear, synthesis of $[\text{Pt}(\text{ppy})(\text{DMSO})\text{Cl}]$ following the standard methodology resulted in a δ_{Pt} of -3815 ppm which is consistent with the shift observed of -3807 ppm by Ghavale, suggesting that Pazderski's data are incorrect.

There appears to be very little influence upon the chemical shift of the ^{195}Pt when the functionality at the 4-position is varied: values range from -2765 to -2779 ppm for the acac complexes of **L1** – **L3** (it is not possible to include the data for $[\text{Pt}(\text{L4})(\text{acac})]$ due to the change in solvent and the fact that solvent can affect the observed shift in ^{195}Pt NMR spectroscopy).⁵²

However, altering the ancillary ligand induced a much greater change. Within the β -diketonates, a shift of almost 100 ppm was observed between acac and hfacac, which can be explained by the extremely powerful electron withdrawing influence of the fluorine atoms, resulting in reduced electron density on the Pt^{II} . Interestingly, the electron donating hmacac does not follow the same trend and, instead, also results in a more deshielded metal. This is unexpected and could be due to the more bulky *t*-butyl groups influencing the shift, either through a change in the solvation or intramolecular interactions with the Pt^{II} .

Changing the coordination mode *via* the ancillary ligand induced an even greater range of chemical shifts. $[\text{Pt}(\text{L1})(\text{DMSO})\text{Cl}]$ has a shift of -3662 ppm, the most upfield shift observed throughout the complexes, whilst the β -diketonate complexes gave rise to the most deshielded metal centres and lie around -2770 ppm. $[\text{Pt}(\text{L1})(8\text{-Q})]$ and $[\text{Pt}(\text{L1})(\text{py})\text{Cl}]$ lie in the middle with somewhat similar chemical shifts for the metal of -2922 and -3158 ppm, respectively. This could be explained by the fact that the coordination modes are relatively alike, which is also the case for $[\text{Pt}(\text{L1})(\text{LH1})\text{Cl}]$ which, too, has a similar shift of -3186 ppm. The only difference between the 8-Q and py complexes is the coordination of an O donor compared to a Cl donor, and both are strongly electronegative, hard bases.

^{195}Pt NMR spectroscopic studies of the cationic $[\text{Pt}(\text{L1})(\text{bpy})](\text{PF}_6)$ complex revealed a shift of -3097 ppm, in CD_3CN . Due to the solubility of the complex, direct comparison between this and the other compounds is not possible however, despite the change in solvent, the shift is still small relative to the possible range of values found in ^{195}Pt NMR spectroscopy.

Compound	δ_{Pt}	Related compound	δ_{Pt}
[Pt(L1)(μ -Cl)] ₂	-3219	[Pt(ppy)(μ -Cl)] ₂	^a
[Pt(L1)(LH1)Cl]	-3186	[Pt(ppy)(ppyH)Cl]	-3212, ⁹⁰ -3201, ³³ -3203 ^b
[Pt(L1)(DMSO)Cl]	-3662	[Pt(ppy)(DMSO)Cl]	-3351, ⁹⁰ -3807, ³³ -3815 ^b
[Pt(L1)(acac)]	-2765	[Pt(ppy)(acac)]	-2868 ^b
[Pt(L2)(acac)]	-2779		
[Pt(L3)(acac)]	-2769		
[Pt(L4)(acac)] ^c	-2781		
[Pt(L1)(hmacac)]	-2733		
[Pt(L1)(hfacac)]	-2693		
[Pt(L1)(8-Q)]	-2922	[Pt(ppy)(8-Q)]	^d
[Pt(L1)(py)Cl]	-3158	[Pt(ppy)(py)Cl]	-1632 ^e
[Pt(L1)(bpy)](PF ₆) ^f	-3097		

^a too insoluble to observe. ^b prepared for reference according to literature^{33,90}. ^c recorded in CD₃OD. ^d no comparable data available. ^e recorded in d₆-acetone. ^f recorded in CD₃CN.

Table 2.1 ¹⁹⁵Pt NMR spectroscopy chemical shifts for all complexes in Chapter 2 (*left*) along with related shifts for analogous ppy complexes (*right*).

The data suggest that, throughout the series, coordination of **L1** results in less electron density on the Pt^{II} than is observed in the analogous ppy complexes. This could be due, in part, to the electron withdrawing nature of esters and amides. Another possibility is apparent distortion in the square planar configuration due to the added bulk of the quinoline ring system in the ligand. The proton in the 8-position appears to be situated in very close proximity to the ancillary ligands and, as a result, distorts the planar aromatic system, and hence the square planar configuration, in order to avoid unfavourable interactions.

2.3.4. X-ray crystal structures

The crystal structure of [Pt(**L1**)(DMSO)Cl] revealed a very distorted arrangement around the central Pt atom, with only a 160.43(7)° C-Pt-Cl angle. The bond lengths of 2.010(2), 2.0788(19), 2.4070(5) and 2.2184(6) Å for the Pt-C, Pt-N, Pt-Cl and Pt-S bonds, respectively, are all within error of the values found for [Pt(ppy)(DMSO)Cl] by Godbert *et al.*⁸² This suggests that the most stable coordination geometry is sacrificed in order to maintain the coordinative bond strengths. The resultant strain induces a twist in the molecule whereby the S-Pt-Cl plane is at a 48° angle to the quinoline ring in order to reduce the Cl-H interactions. This strain means that there are no Pt-Pt interactions within the crystal packing; the head-to-tail motif still exists but, in this example, the cyclometallated ligand of one molecule sits over the cyclometallated ligand of another resulting in π - π interactions but no metallophilic contacts. This is also observed in Godbert's structure suggesting that the lack of Pt-Pt interactions is most likely due to the out of plane orientation of the methyl groups of the DMSO ligand.

The bond lengths in the inner-coordination sphere of [Pt(**L1**)(acac)] were found to be 1.960(4) and 2.045(3) Å for Pt-C and Pt-N, respectively. These compare to 1.948(8) and 1.979(6) Å for the Pt-C and Pt-N bond lengths of [Pt(ppy)(acac)].²⁶ The Pt-O bond lengths were found to be 1.999(3) and 2.101(3) Å, with the shorter bond length being in the *trans* position to the coordinated N atom. These compare to the results outlined by Bossi *et al.* of 2.007(5) and 2.065(6) Å, respectively. These values suggest that the bond lengths around the coordination sphere are very similar, within error, and that altering the phenylpyridine for a phenylquinoline-like moiety does not change the strength of the cyclometallating bonds. Unlike the planar structure observed by Bossi *et al.* for the ppy complex, the crystal structure of [Pt(**L1**)(acac)] revealed a departure from planarity, most prominently from the extra benzene ring within the quinolyl moiety. This is most likely a result of the unfavourable interaction of the proton in the 8-position of the quinoline ring with the ancillary ligand. The distances between the protons in the 8-position of the quinolyl moiety and the 3-position of the phenyl group are approximately 2.5 Å from the oxygen atoms of the ancillary ligand in Bossi's crystal structure. The distance on the phenyl side of [Pt(**L1**)(acac)] is very similar, at around 2.5 Å, whilst the proton in the 8-position of the quinoline ring is approximately 2.0 Å from the ancillary ligand, despite more than

20° of torsion. There appear to be metallophilic interactions within the solid state, with Pt-Pt distances of approximately 3.3 Å compared to around 3.7 Å in [Pt(ppy)(acac)]. The reduced bond length could be due to the increased conjugation around the cyclometallated ring system leading to greater π - π interactions. Both structures pack in a similar manner with a head-to-tail arrangement whereby the cyclometallated ligand of one molecule lies above or below the ancillary ligand of another.

The X-ray crystal structure of [Pt(**L1**)(bpy)](PF₆), as with the DMSO complex, displays a high degree of distortion in the square planar geometry with an angle between the plane of the bpy and the plane of the cyclometallated ligand of 42° due to unfavourable H-H interactions between the two ligands. The bond lengths within the inner-sphere coordination are 2.012(6) and 2.046(5) Å for the Pt-C and Pt-N of the phenylquinoline ligand and 2.145(5) and 2.022(5) Å for the Pt-N bonds of the bpy, where the shorter bond is *trans* to the coordinated quinolyl moiety. The closest comparable crystal structure, obtained by Sooksawat *et al.*, contains a 2,6-diphenylpyridine with a C^N coordination mode and a N^N coordinated 4,4'-bimethyl-2,2'-bipyridine.⁹¹ This compound was found to have bond lengths of 1.997(7), 2.063(7), 2.137(6) and 2.027(7) Å for the Pt-C, Pt-N, Pt-N (*trans* to C) and Pt-N (*trans* to N) bond distances, respectively. The cyclometallating ligand's Pt bond lengths are very similar to those of the acac and DMSO complexes detailed above. This suggests that, once again the bond strength is maintained at the expense of the planarity of the two ligands, which are highly distorted. Despite this, unlike the DMSO complex, a Pt-Pt interaction is visible although it is much longer than the acac complex and, at around 4.3 Å, is at the limits of interactivity based on the van der Waal's radius calculated by Alvarez for Pt.⁹²

2.3.5. X-ray crystal structure of [Pt(L1)(DMSO)Cl]

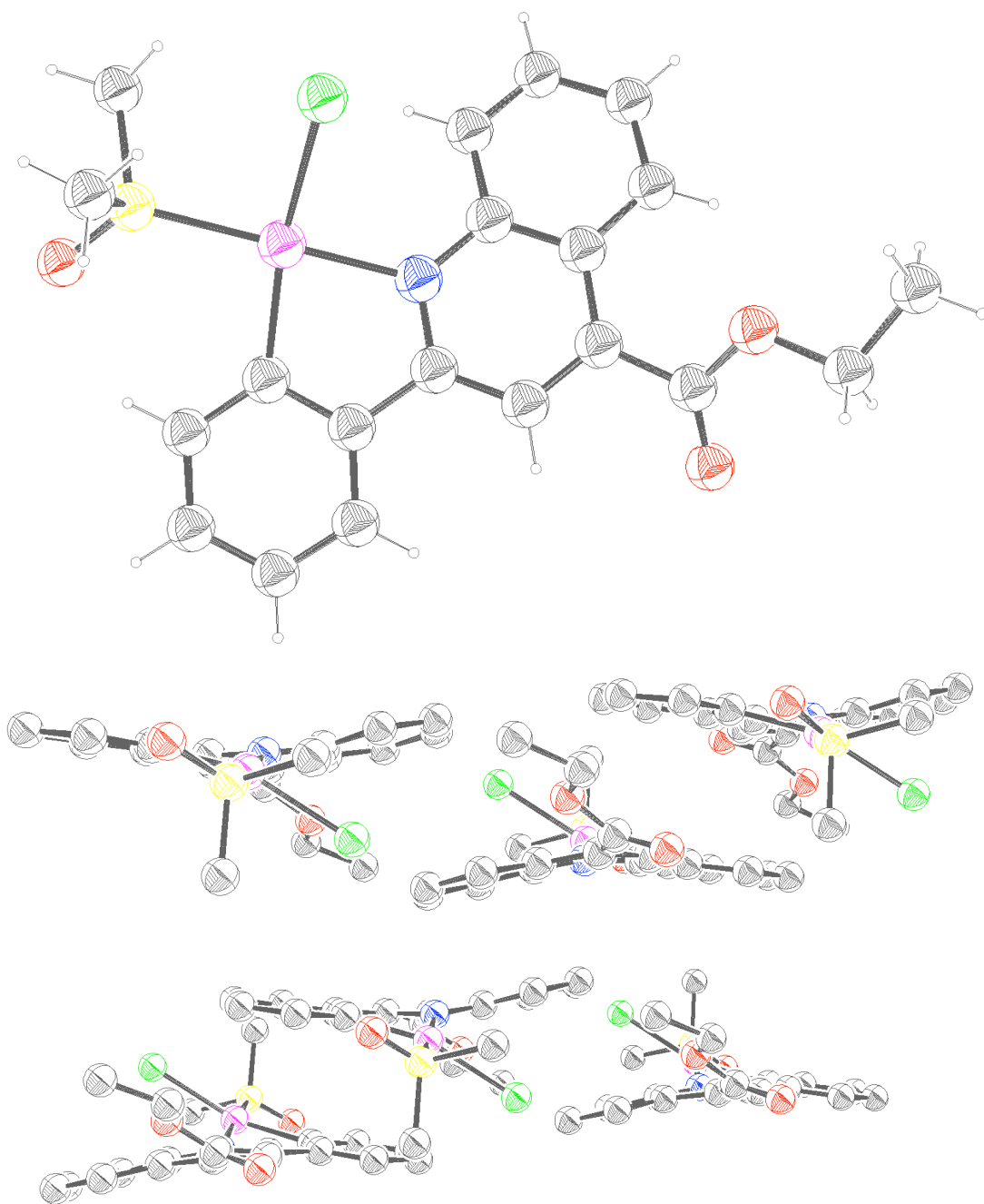


Figure 2.19 Ball and stick X-ray crystal structure of [Pt(L1)(DMSO)Cl] (*top*) and the unit cell packing (*bottom*).

2.3.6. X-ray crystal structure of [Pt(L1)(acac)]

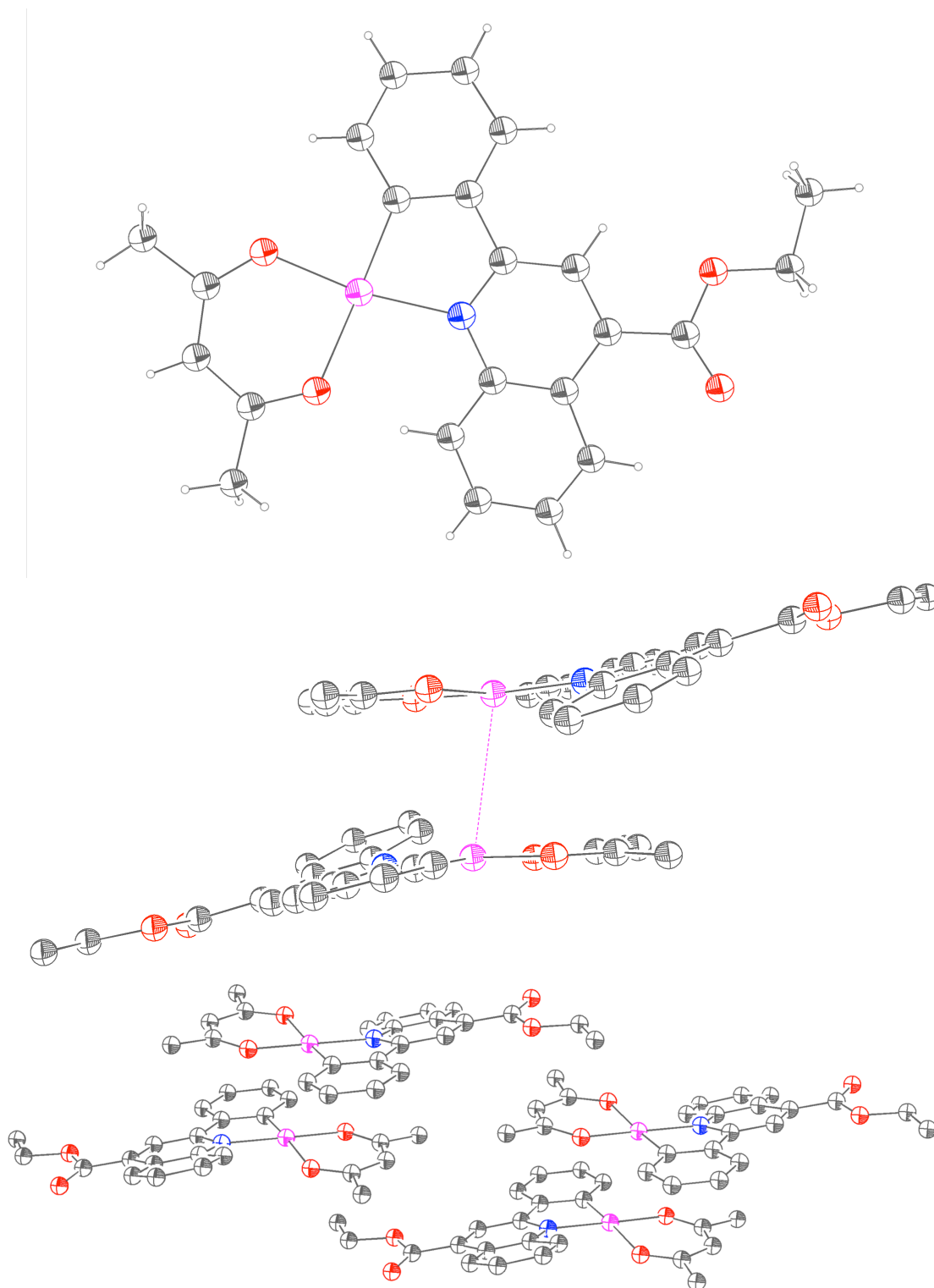


Figure 2.20 Ball and stick X-ray crystal structure of [Pt(L1)(acac)] (*top*), the Pt-Pt interaction (*middle*) and the unit cell packing (*bottom*).

2.3.7. X-ray crystal structure of [Pt(L1)(bpy)](PF₆)

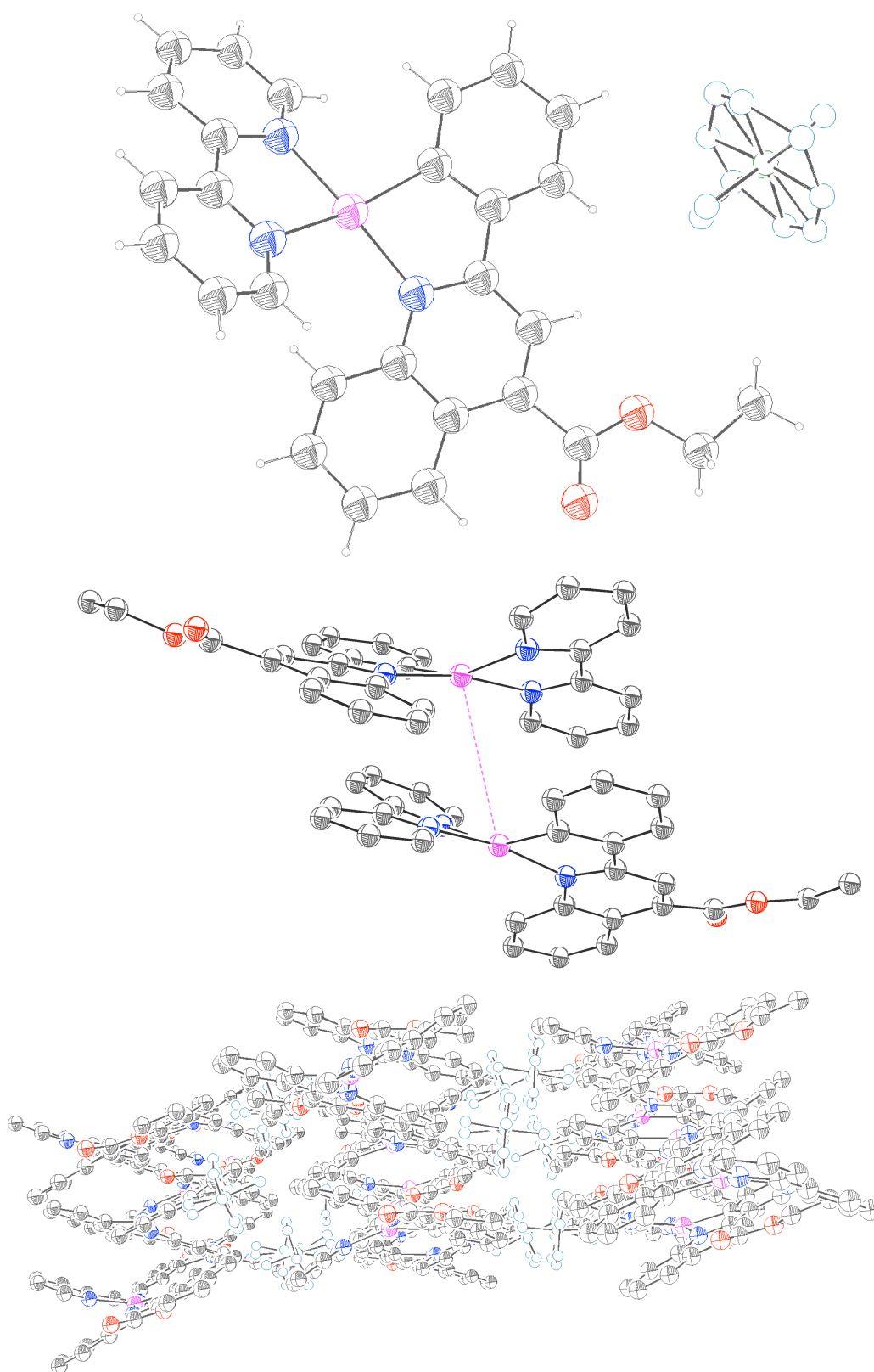


Figure 2.21 Ball and stick X-ray crystal structure of [Pt(L1)(bpy)](PF₆) (*top*), Pt-Pt interactions (*middle*) and the unit cell packing (*bottom*).

2.3.8. X-ray crystal structure data

	[Pt(L1)(DMSO)Cl]	[Pt(L1)(acac)]	[Pt(L1)(bpy)](PF ₆)
Empirical formula	C ₂₀ H ₂₀ ClNO ₃ PS	C ₂₃ H ₂₁ NO ₄ Pt	C ₂₈ H ₂₂ F ₆ N ₃ O ₂ PPt
Formula weight	584.97	570.50	772.54
Temperature	100(2) K	100(2) K	100(2) K
Wavelength	0.71075 Å	0.71075 Å	0.71075 Å
Crystal system	Triclinic	Triclinic	Monoclinic
Space group	<i>P</i> -1	<i>P</i> -1	<i>I</i> 2/a
Unit cell dimensions	<i>a</i> = 9.8021(7) Å <i>a</i> = 115.732(5)° <i>b</i> = 10.3147(7) Å <i>b</i> = 107.041(5)° <i>c</i> = 11.2998(7) Å <i>c</i> = 96.348(4)°	<i>a</i> = 10.1757(4) Å <i>a</i> = 75.248(2)° <i>b</i> = 10.2522(3) Å <i>b</i> = 73.403(3)° <i>c</i> = 10.5639(2) Å <i>c</i> = 69.265(3)°	<i>a</i> = 24.9815(10) Å <i>a</i> = 90° <i>b</i> = 7.2648(3) Å <i>b</i> = 102.905(4)° <i>c</i> = 28.8575(11) Å <i>c</i> = 90°
Volume	945.74(12) Å ³	973.14(6) Å ³	5104.9(4) Å ³
<i>Z</i>	2	2	8
Density (calculated)	2.054 Mg / m ³	1.947 Mg / m ³	2.010 Mg / m ³
Absorption coefficient	7.691 mm ⁻¹	7.240 mm ⁻¹	5.638 mm ⁻¹
<i>F</i> (000)	564	552	2992
Crystal	Cut Block; Red	Cut Block; Dark Red	Needle; Orange
Crystal size	0.110 × 0.070 × 0.030 mm ³	0.100 × 0.060 × 0.010 mm ³	0.060 × 0.010 × 0.010 mm ³
θ range for data collection	3.045 - 27.483°	3.214 - 27.485°	2.445 - 29.948°
Index ranges	-12 ≤ <i>h</i> ≤ 12, -13 ≤ <i>k</i> ≤ 13, -14 ≤ <i>l</i> ≤ 14	-13 ≤ <i>h</i> ≤ 13, -13 ≤ <i>k</i> ≤ 13, -13 ≤ <i>l</i> ≤ 12	-34 ≤ <i>h</i> ≤ 33, -9 ≤ <i>k</i> ≤ 10, -38 ≤ <i>l</i> ≤ 39
Reflections collected	16283	15013	31626
Independent reflections	4325 [<i>R</i> _{int} = 0.0277]	4458 [<i>R</i> _{int} = 0.0379]	6799 [<i>R</i> _{int} = 0.1164]
Completeness to θ = 25.242°	99.70%	99.8 %	99.9 %
Absorption correction	Semi-empirical from equivalents	Semi-empirical from equivalents	Semi-empirical from equivalents
Max. and min. transmission	1.000 and 0.820	1.00000 and 0.76530	1.000 and 0.80453
Refinement method	Full-matrix least-squares on <i>F</i> ²	Full-matrix least-squares on <i>F</i> ²	Full-matrix least-squares on <i>F</i> ²
Data / restraints / parameters	4325 / 0 / 247	4458 / 0 / 265	6799 / 339 / 435
Goodness-of-fit on <i>F</i> ²	1.044	1.009	0.984
Final R indices [<i>F</i> ₂ > 2s(<i>F</i> ₂)]	<i>R</i> = 0.0167, <i>wR</i> = 0.0442	<i>R</i> = 0.0312, <i>wR</i> = 0.0797	<i>R</i> = 0.0531, <i>wR</i> = 0.0900
<i>R</i> indices (all data)	<i>R</i> = 0.0168, <i>wR</i> = 0.0443	<i>R</i> = 0.0317, <i>wR</i> = 0.0802	<i>R</i> = 0.0988, <i>wR</i> = 0.1034
Extinction coefficient	n/a	n/a	n/a
Largest diff. peak and hole	0.783 and -1.207 e Å ⁻³	3.873 and -2.815 e Å ⁻³	1.491 and -1.362 e Å ⁻³

Table 2.2 Crystal structure data for [Pt(L1)(DMSO)Cl], [Pt(L1)(acac)] and [Pt(L1)(bpy)](PF₆).

2.3.9. Electronic absorption spectroscopy and DFT calculations

The absorption properties of the complexes were measured in chloroform except for [Pt(L4)(acac)], which was measured in methanol, and [Pt(L1)(bpy)](PF₆), which was measured in acetonitrile. They were all pale yellow solutions and absorbed below 550 nm.

Compound	λ_{max} / nm
[Pt(L1)(acac)]	253, 292, 300, 363, 427
[Pt(L2)(acac)]	258, 297, 343, 360, 415
[Pt(L3)(acac)]	300, 342, 363, 442
[Pt(L4)(acac)] ^a	282, 334, 348, 382
[Pt(L1)(hmacac)]	253, 291, 301, 357, 437
[Pt(L1)(hfacac)]	253, 293, 370, 400, 442
[Pt(L1)(DMSO)Cl]	257, 293, 366, 420
[Pt(L1)(py)Cl]	255, 285, 367, 450
[Pt(L1)(8-Q)]	257, 284, 370, 455
[Pt(L1)(bpy)](PF ₆) ^b	281, 318, 355, 368, 395, 448

^a recorded in methanol. ^b recorded in acetonitrile.

Table 2.3 Absorption maxima (λ_{max}) for complexes in Chapter 2.

The spectra all reveal strong absorption between 250 and 350 nm corresponding to intraligand $^1\text{IL}(\pi \rightarrow \pi^*)$ transitions. Lower energy transitions from around 350 nm, tailing off beyond 500 nm, can be classified as a combination of metal-to-ligand charge transfer ($^1\text{MLCT}$) and ligand-to-ligand charge transfer ($^1\text{LLCT}$). The observed ML or LL transitions are red-shifted compared to UV-vis data in the literature for [Pt(ppy)(acac)] and [Pt(ppy)(hfacac)] where the lowest energy absorption maxima lie around 350 to 370 nm.^{34, 93} UV-vis data for [Pt(pq)(acac)] and [Pt(isoquinoline)(acac)], as expected, match the data recorded far more closely with low energy transitions at 400 to 420 nm.^{27, 93} This red-shift was a result of the lower lying π^* orbitals on the cyclometallated ligand owing to the extended conjugation around the aromatic system.

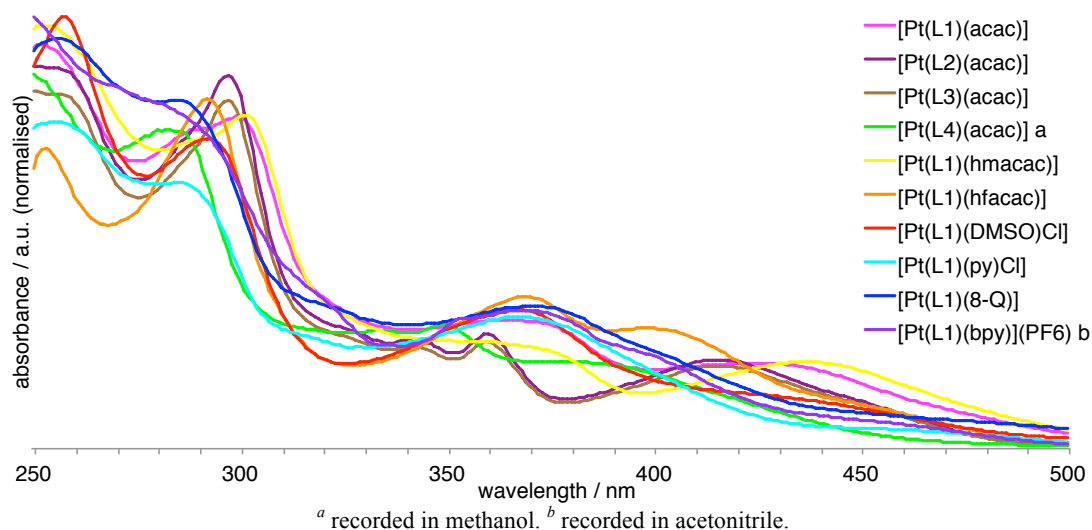


Figure 2.22 Absorption profiles (normalised) for complexes in chloroform.

The change in functionalisation from ester to amide appears to invoke a minor change in the absorption profile, especially around 340 – 400 nm, whilst altering the nature of the amide appears to have very little influence at all. Interestingly, the absorption is much greater affected by the nature of the ancillary ligand: between the β -diketonates, there is a subtle shift in absorption maxima *ca.* 430 – 440 nm. The intensities of the $^1\text{MLCT}$ band are also dramatically affected by the class of ancillary ligand incorporated: whilst the acac and hmacac ligands show a pronounced peak maxima, the pyridine, bipyridine and hydroxyquinoline ligands render the absorptions beyond 430 nm as nothing more than a shoulder of the higher energy absorption maxima *ca.* 380 nm.

Given the interest in tuning the photophysical properties and, therefore, the electronic properties of the cyclometallated Pt^{II} complexes, it was thought useful to carry out density functional theory (DFT) calculations in order to ascertain how the different ancillary ligands were influencing the electronics and, in particular, which transitions might be occurring in the lower energy absorptions and whether any possible explanations could be found for the changes in absorption profile. Time dependent DFT calculations were carried out by Dr. Jamie Platts.

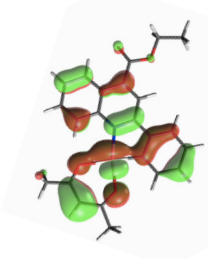
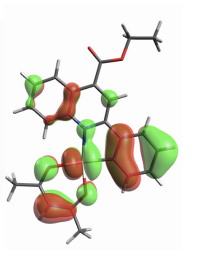
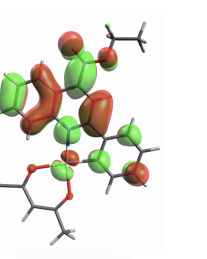
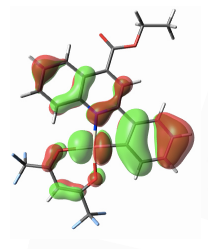
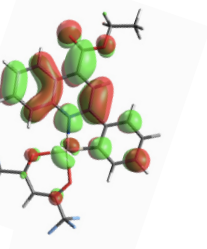
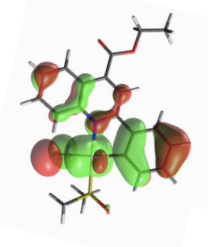
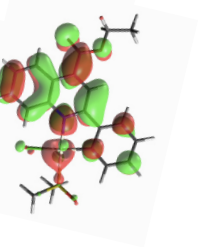
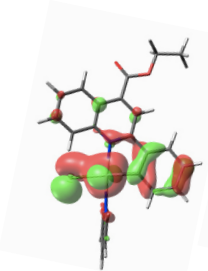
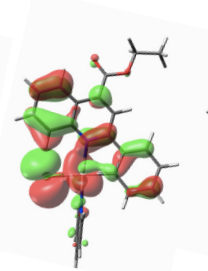
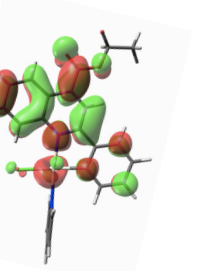
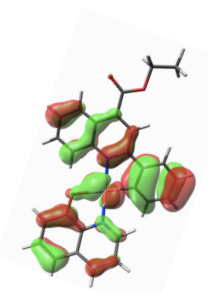
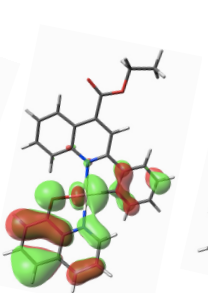
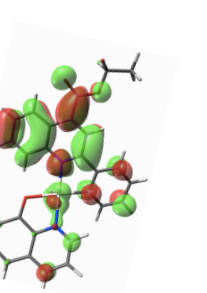
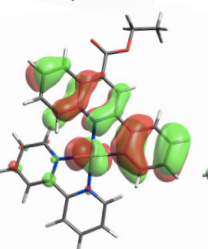
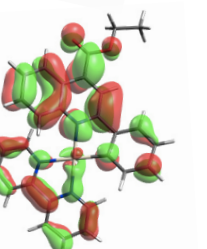
Compound	HOMO -1	HOMO	LUMO	Band Gap
[Pt(L1)(acac)]				2.49 eV 498 nm
[Pt(L1)(hfacac)]				2.61 eV 474 nm
[Pt(L1)(DMSO)Cl]				2.55 eV 487 nm
	HOMO-2	HOMO-1	LUMO	
[Pt(L1)(py)Cl]				2.66 eV 466 nm
	HOMO-1	HOMO	LUMO	
[Pt(L1)(8-Q)]				2.63 eV 472 nm
[Pt(L1)(bpy)](PF ₆)				2.53 eV 490 nm

Table 2.4 Calculated representations for the HOMO-1s (and HOMO-2s) (*left*), HOMOs (and HOMO-1s) (*middle*) and LUMOs (*right*) of a series of Pt^{II} complexes along with the band gaps.

Theoretical calculations revealed that most low energy transitions occurred from the HOMO-1 and HOMO to the LUMO although, for [Pt(**L1**)(py)Cl] and [Pt(**L1**)(8-Q)], the transitions predicted at 510 and 610 nm respectively are not found experimentally and so the next lowest possible transition was visualised. The second excited state for [Pt(**L1**)(8-Q)] involved only HOMO → LUMO transitions as did the first excited state predicted for [Pt(**L1**)(DMSO)Cl]. The LUMOs for all complexes, regardless of ancillary ligand, appear through DFT to be very similar and it is the HOMO and HOMO-1 (and HOMO-2 for the pyridine analogue) that affects the absorption.

In all cases, the majority of the electron density in the HOMO lies across both the ancillary ligand and the phenyl moiety of the cyclometallated ligand as well as the *d*-orbitals of the platinum. The percentage contribution to the energy levels for the Pt^{II}'s *d*-orbitals were calculated from the theoretical data and allowed the relative contribution of LLCT and MLCT to be investigated for each class of compound.

Compound	HOMO -2	% <i>d</i> -orbital character		
		HOMO-1	HOMO	LUMO
[Pt(L1)(acac)]	41.81%	35.51%	40.29%	2.00%
[Pt(L1)(hfacac)]	37.52%	19.01%	24.83%	0.96%
[Pt(L1)(DMSO)Cl]	11.54%	16.38%	23.29%	0.32%
[Pt(L1)(py)Cl]	7.10%	11.25%	26.48%	1.00%
[Pt(L1)(8-Q)]	31.13%	14.12%	4.25%	0.47%
[Pt(L1)(bpy)](PF ₆)	15.54%	24.88%	6.47%	0.25%

Table 2.5 Percentage *d*-orbital character predicted for the HOMO-2, HOMO-1, HOMO and LUMO, where the orbitals involved in observable transitions in the UV-vis spectra are highlighted in bold.

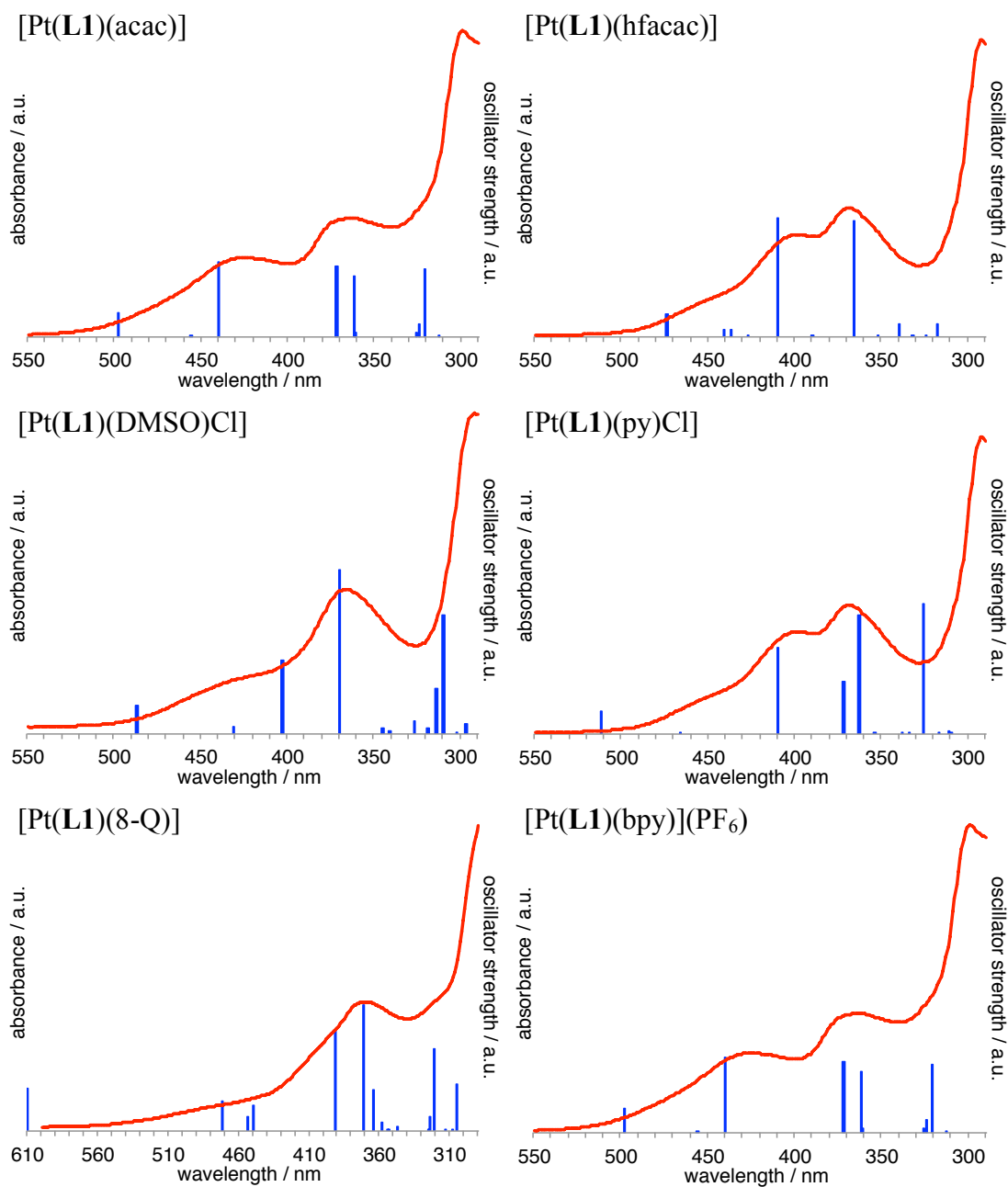


Figure 2.23 Absorption profiles (normalised) against excitation bands predicted using DFT.

2.3.9.1. Luminescence spectroscopy

Steady state luminescence and lifetime data were acquired for all complexes and were obtained in chloroform, except for [Pt(**L4**)(acac)] and [Pt(**L1**)(bpy)](PF₆), which were carried out in methanol and acetonitrile, respectively. Shoulders *ca.* 660 nm are a result of an artefact associated with the spectrometer and should be disregarded.

Compound	λ_{em}^a / nm	τ^a / ns	Φ^a
[Pt(L1)(acac)]	639	331 ^b	0.2%
[Pt(L2)(acac)]	615	427 ^b	
[Pt(L3)(acac)]	629	368 ^b	
[Pt(L4)(acac)]	605 ^d	182 ^{c,d}	
	605 ^e	249 ^{c,e}	
[Pt(L1)(hmacac)]	641	318 ^b	
[Pt(L1)(hfacac)]	616	262 ^b	
[Pt(L1)(DMSO)Cl]	610	113 ^c	0.1%
[Pt(L1)(py)Cl]	626	365 ^c	0.4%
[Pt(L1)(8-Q)]	620	59 ^b	
[Pt(L1)(bpy)](PF ₆)	630	155 ^c	

^a in chloroform unless stated otherwise. ^b excited at 295 nm. ^c excited at 372 nm. ^d in H₂O. ^e in methanol.

Table 2.6 Photophysical properties of the complexes synthesised in Chapter 2.

The data show that by altering the ancillary ligand and nature of the cyclometallated ligand, it is possible to tune the lifetime, excitation profile and emission maxima of cyclometallated Pt^{II} complexes. Even excluding the emission of the water-soluble complex at 605 nm, so as to rule out any influence of solvatochromism, the emission maxima span a range of over 30 nm. The effect on the lifetime is even more pronounced with lifetimes of some species almost an order of magnitude greater than others.

The excitation spectra for the complexes' emission between 600 and 640 nm vary dramatically. Whilst they all exhibit strong emission when excited between 250 and 300 nm, the relative intensity of emission from excitation of lower energy, 400 to 450 nm, varies between the complexes.

The emission profiles show subtle shifts in maxima with the highest energy emission for [Pt(**L4**)(acac)] and the lowest energy maximum for [Pt(**L1**)(acac)]. As [Pt(**L4**)(acac)] was carried out in a much more polar solvent, it is possible that the higher energy emission is a result of positive solvatochromism whereby either the

ground state is stabilised by the solvent, or the excited state destabilised. Interestingly, no compounds displayed any effective solvatochromic shifts when assessed, with shifts of no more than a few nanometres, which is within error.

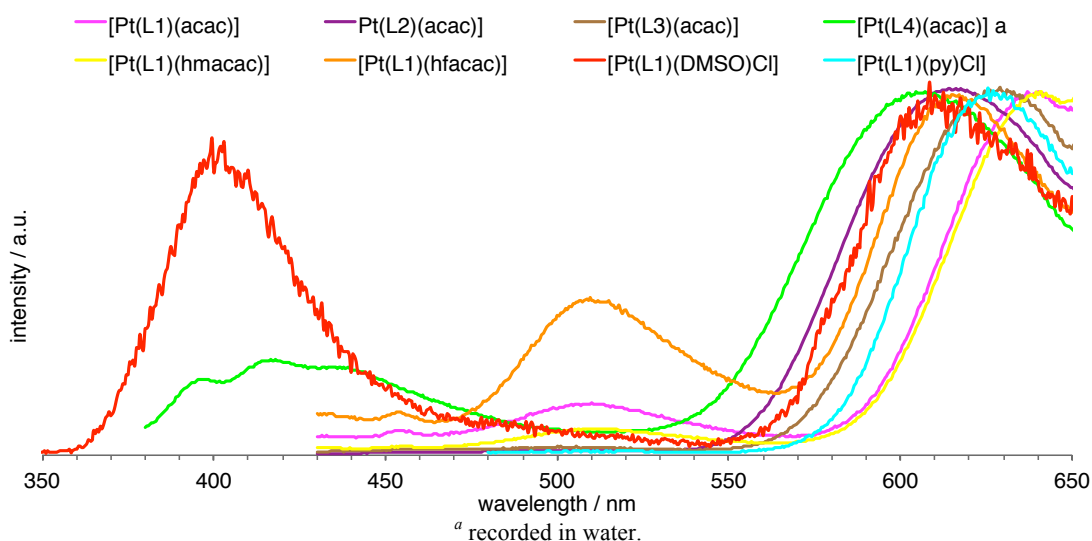


Figure 2.24 Normalised emission profiles of a selection of complexes from Chapter 2.

Given the extent to which the functionalisation of the cyclometallated ligand can influence the emission, it is possible that changing the solvent is not inducing the largest effect on the energy of the emission. Switching from an ester and an amide, and even altering the functionality of the amide, appears to have a strong influence on the emission, so it seems likely that deprotection of the ester to a carboxylic acid would play more of a role in influencing the emission than the solvent.

Altering the functionality of the β -diketonate also appears capable of influencing both the lifetime and emission maxima. Whilst there is very little difference between the acac and hmacac complexes, the hfacac complex shows both a reduction in lifetime by almost 20% and a blueshift in the emission by more than 20 nm, displaying a contradictory trend to the Energy Gap Law. Interestingly, in contrast to results published by both Ghedini *et al.* and Spencer *et al.*, the presence of the hfacac does not result in the quenching of emission.^{34, 35} The DFT calculations for this complex reveal that the electron density lies across the ancillary ligand only in the LUMO+1. This is most likely due to the fact that the added aromaticity in the cyclometallating ligand has lowered energy of the π^* orbitals on the phenylquinoline more than the affect of the CF_3 moieties have had on lowering the π^* orbitals on the ancillary ligand.

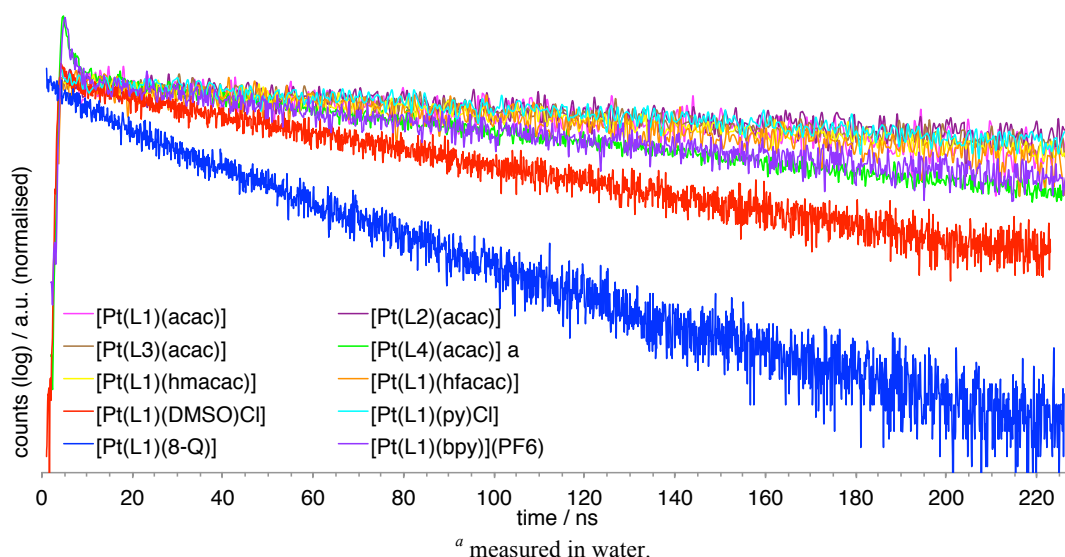


Figure 2.25 Normalised lifetime decay profiles.

The lifetimes are similar with all but $[\text{Pt}(\text{L1})(\text{DMSO})\text{Cl}]$, $[\text{Pt}(\text{L1})(8\text{-Q})]$, $[\text{Pt}(\text{L1})(\text{hfacac})]$ and $[\text{Pt}(\text{L1})(\text{bpy})](\text{PF}_6)$ lying between 427 and 318 ns in aerated solvent. The presence of the CF_3 groups again influence the photophysical properties and results in a quenching effect on the lifetime, reducing it from 331 to 262 ns. More interesting, however, is the difference of *ca.* 60 ns between the *t*-butyl and *p*-fluorobenzene functionalised amides. It appears that altering the functionalisation of the cyclometallated ligand has a profound influence on the lifetime and opens up the possibility to tune the lifetime, and emission, through simple alteration of substituents.

Also of interest is the apparent quenching of the emission at 610 nm in $[\text{Pt}(\text{L1})(\text{DMSO})\text{Cl}]$. The effect is such that fluorescent emission from the ligand at 400 nm, which is usually no more than a small indent in the baseline, appears equally intense in the emission profile.

2.4. Conclusion

This chapter summarises the synthetic routes to a series of cyclometallated Pt^{II} complexes *via* μ -dichloro-bridged dimer intermediates. Despite initial failings in the synthesis, a methodology was adopted which led to the successful formation of the μ -dichloro-bridged dimers from tetrachloroplatinate (II). The dimers were split using DMSO to give [Pt(L)(DMSO)Cl] complexes, which could be purified for use as a final product or further reacted with ancillary ligands. These included several β -diketonates or β -diketones, 8-hydroxyquinoline, pyridine and 2,2'-bipyridine in order to give a breadth of spectral variation and to alter the physical properties of the complexes. Altering the functionality of the cyclometallated phenylquinoline ligand and the type of ancillary ligand were both found to perturb the emissive wavelength and lifetime of the complexes in aerated solvents at room temperature. Crystal structures of [Pt(L1)(acac)] and [Pt(L1)(bpy)](PF₆) reveal Pt-Pt interactions, albeit weak interactions for the bpy complex, whilst [Pt(L1)(DMSO)Cl] shows a very distorted square planar geometry resulting in no Pt-Pt interactions in the solid state.

2.5. Experimental

2.5.1. General physical measurements

^1H NMR spectra were recorded on a Bruker Avance dpx 400 or 250 MHz spectrometer, $^{13}\text{C}\{^1\text{H}\}$ NMR spectra on a Joel Eclipse 300 MHz or Bruker Avance dpx 500 MHz spectrometer and ^{195}Pt NMR spectra on Bruker Avance dpx 500 MHz spectrometer, and were recorded in CDCl_3 , D_2O , CD_3OD or d_6 -DMSO solutions. ^1H , $^{13}\text{C}\{^1\text{H}\}$ and ^{195}Pt NMR spectroscopies' chemical shifts (δ) were determined relative to internal tetramethylsilane, $\text{Si}(\text{CH}_3)_4$ and are given in ppm. Low-resolution mass spectra were obtained by the staff at Cardiff University. High-resolution mass spectra were carried out by the staff at Cardiff University and the EPSRC National Mass Spectrometry Service at Swansea University, UK. All photophysical data were obtained on a JobinYvon-Horiba Fluorolog-3 spectrometer fitted with a JY TBX picosecond photodetection module in CHCl_3 , MeOH or H_2O solutions. Emission spectra were uncorrected and excitation spectra were instrument corrected. The pulsed source was a Nano-LED configured for 295, 372 or 459 nm output operating at 500 kHz or 1 MHz. Luminescence lifetime profiles were obtained using the JobinYvon-Horiba FluoroHub single photon counting module and the data fits yielded the lifetime values using the provided DAS6 deconvolution software. IR spectra were recorded on an ATR equipped Shimadzu IRAffinity-1 spectrophotometer. UV-vis data were recorded in solution on a Perkin Elmer Lambda20 spectrophotometer.

2.5.2. Density functional theory

Scalar relativistic DFT calculations were carried out using GAUSSIAN09,⁹⁴ with relativistic effects incorporated via use of appropriate effective core potentials (ECPs). Geometry optimisations of both singlet ground and triplet excited states were performed at the B3LYP level,^{95, 96} with a basis set consisting of Stuttgart-Dresden basis set plus ECP on Pt and 6-31+G(d,p) on all remaining atoms.⁹⁷⁻¹⁰⁰ Time-dependent DFT (TD-DFT) calculations also employed B3LYP. As shown by Vlček *et al.*,¹⁰¹ solvent effects can be crucial for obtaining satisfactory agreement between experiment and TD-DFT. Solvent was therefore modeled using the polarisable continuum model,¹⁰² with the molecular cavity defined by a united atom model that incorporates hydrogen into the parent heavy atom, and included in both geometry optimisations and TD-DFT calculations. Triplet states were confirmed not to suffer

from significant spin contamination *via* the expectation value of the S^2 operator, which in all cases were less than 2.01. Thus, effects of spin-contamination on energy differences and optimised structures are expected to be negligible. Emission energies were predicted at the triplet-optimised geometry using TD-DFT and were calculated vertically, *i.e.* without geometry relaxation.

2.5.3. X-ray crystallography

A small sample of pure product was dissolved in chloroform to give a concentrated solution. Toluene was added and the solution was left to evaporate slowly to yield brightly coloured crystals. X-ray crystallography measurements were carried out by Dr Peter Horton at the EPSRC National Crystallography Service at the University of Southampton, UK.¹⁰³ The diffractometer was a Rigaku AFC12 goniometer equipped with an enhanced sensitivity (HG) Saturn724+ detector mounted at the window of an FR-E+ SuperBright molybdenum rotating anode generator with HF Varimax optics (100 μm focus). The cell was determined and defined, the data reduced and the absorption corrected using CystalClear-SM Expert 3.1 b27 (Rigaku, 2012). The structure was solved using SUPERFLIP and refined using SHELXL-2013.^{104, 105} The graphics were obtained using ORTEP3 for Windows.¹⁰⁶

2.5.4. Ligand synthesis

Synthesis of LH1: was prepared by literature methodology.⁸⁰ 2-phenyl-4-quinolinecarboxylic acid (2.000 g) and H_2SO_4 (1 mL, excess) were heated in ethanol (100 mL) at reflux for 16 h under dinitrogen. The solvent was removed *in vacuo* and the residue dissolved in dichloromethane and washed with NaHCO_3 (sat. soln, 50 mL), water (20 mL) and brine (20 mL). The organic phase was dried over MgSO_4 , filtered and dried *in vacuo* to afford the product as a yellow semi-solid. Yield = 2.180 g, (98%). ^1H NMR (400 MHz, CDCl_3): δ_{H} 8.75 (1H, dd, $^3J_{\text{HH}} = 8.4$ Hz, $^4J_{\text{HH}} = 0.8$ Hz), 8.40 (1H, s), 8.34 (1H, d, $^3J_{\text{HH}} = 8.4$ Hz), 8.22 – 8.19 (2H, m), 7.84 – 7.80 (1H, m), 7.69 – 7.64 (1H, m), 7.60 – 7.50 (3H, m), 4.56 (2H, q, $^3J_{\text{HH}} = 7.2$ Hz), 1.51 (3H, t, $^3J_{\text{HH}} = 7.2$ Hz) ppm.

General procedure for the synthesis of 2-phenyl-4-quinolinecarboxamides: Based on a modified literature methodology.⁷⁹ Thionyl chloride (excess) was added, dropwise, to a stirring suspension of 2-phenyl-4-quinolinecarboxylic acid (1.1 eq) in

chloroform (10 mL). The reaction was heated at reflux for 16 h under dinitrogen. The solvent was removed *in vacuo* and the yellow solid redissolved in chloroform (10 mL) before RR'NH / RRNH / RNH₂ (1 eq) was added slowly to the stirring solution. EtNiPr₂ (excess) was added dropwise and the mixture was stirred for 16 h at room temperature under dinitrogen. The solvent was removed *in vacuo* before being redissolved in dichloromethane (20 mL). The crude mixture was washed with NaHCO₃ (sat. soln, 2 x 20 mL), water (1 x 20 mL) and brine (1 x 20 mL). The organic phase was dried over MgSO₄ and filtered before the solvent was removed *in vacuo*.

Synthesis of LH2: Following the general procedure for the synthesis of 2-phenyl-4-quinolinecarboxamides using 2-phenyl-4-quinolinecarboxylic acid (0.233 g, 0.935 mmol) and *tert*-butylamine (0.062 g, 0.850 mmol). Yield = 0.235 g, (91%). ¹H NMR (400 MHz, CDCl₃): δ_H 8.14 (1H, d, ³J_{HH} = 8.0 Hz), 8.10 – 8.05 (3H, m), 7.75 (1H, s), 7.74 – 7.70 (1H, m), 7.54 – 7.47 (4H, m), 6.09 (1H, br. s), 1.56 (9H, s) ppm.

Synthesis of LH3: Following the general procedure for the synthesis of 2-phenyl-4-quinolinecarboxamides using 2-phenyl-4-quinolinecarboxylic acid (0.233 g, 0.935 mmol) and 4-fluoroaniline (0.094 g, 0.850 mmol). Yield = 0.250 g, (86%). ¹H NMR (400 MHz, CDCl₃): δ_H 8.18 (1H, d, ³J_{HH} = 8.4 Hz), 8.13 (2H, d, ³J_{HH} = 8.0 Hz), 8.10 – 8.08 (2H, m), 7.90 (1H, s), 7.78 – 7.72 (3H, m), 7.55 – 7.48 (4H, m), 7.16 – 7.11 (2H, m) ppm.

2.5.5. Complex synthesis

General procedure for the synthesis of platinum dimers: Based on a modified literature methodology.⁸² A solution of potassium tetrachloroplatinate (II) (1 eq) in water (2 mL) was added to a stirring solution of **LH** (1 eq) in 2-ethoxyethanol (6 mL) under dinitrogen and heated to 80 °C for 16 h in a foil-wrapped flask. Brine (10 mL) was added to the cooled solution and the resultant precipitate was collected on a sinter and washed with water (2 x 10 mL) and dried. The solid was used without purification.

Synthesis of [Pt(L1)Cl]₂: Following the general procedure for the synthesis of platinum dimers using potassium tetrachloroplatinate (II) (0.084 g, 0.201 mmol) and **LH1** (0.056 g, 0.201 mmol). Yield = 0.049 g, (48%). ¹⁹⁵Pt (107.5 MHz, CDCl₃): δ_{Pt} -3219 ppm.

Synthesis of [Pt(L2)Cl]₂: Following the general procedure for the synthesis of platinum dimers using potassium tetrachloroplatinate (II) (0.261 g, 0.629 mmol) and **LH3** (0.191 g, 0.629 mmol). Yield = 0.265 g, (79%).

Synthesis of [Pt(L3)Cl]₂: Following the general procedure for the synthesis of platinum dimers using potassium tetrachloroplatinate (II) (0.171 g, 0.412 mmol) and **LH4** (0.141 g, 0.412 mmol). Yield = 0.151 g, (64%).

General procedure for splitting platinum dimers: Based on a modified literature methodology.¹⁰⁷ Crude [Pt(L)Cl]₂ was dissolved in a minimum volume of DMSO before being precipitated with brine (10 mL), filtered on a sinter and washed with water (2 x 20 mL). The solid was dried and purified if necessary.

Synthesis of [Pt(L1)(DMSO)Cl]: Following the general procedure for splitting platinum dimers using [Pt(L1)Cl]₂ (0.049 g, 0.048 mmol). Obtained as a brown/green solid. Yield = 0.053 g, (94%). ¹H NMR (400 MHz, CDCl₃): δ_H 9.07 (1H, d, ³J_{HH} = 8.4 Hz), 8.58 (1H, dd, ³J_{HH} = 8.4 Hz, ⁴J_{HH} = 1.2 Hz), 8.40 – 8.35 (1H, m), 8.29 (1H, s), 7.78 – 7.74 (1H, m), 7.71 – 7.68 (1H, m), 7.65 – 7.61 (1H, m), 7.31 – 7.25 (2H, m), 4.59 (2H, q, ³J_{HH} = 7.2 Hz), 3.67 (6H, s (with satellites ³J_{HPt} = 22 Hz)), 1.53 (3H, t, ³J_{HH} = 7.2 Hz). ¹³C{¹H} NMR (75.6 MHz, CDCl₃): δ_C 166.5, 165.3, 147.6, 145.7, 143.0, 139.9, 133.9, 130.9, 129.8, 128.6, 128.3, 126.1, 125.5, 125.2, 125.0, 117.6, 62.7, 46.3 (satellites 46.7 & 45.9), 14.4 ppm. ¹⁹⁵Pt (107.5 MHz, CDCl₃): δ_{Pt} -3662 ppm. UV-vis (CHCl₃): λ_{max} (ε / dm³ mol⁻¹ cm⁻¹) 257 (28100), 293 (20100), 366 (9050) nm. IR (thin film): ν_{max} 3048, 2976, 2918, 1715, 1597, 1578, 1543, 1514, 1466, 1451, 1397, 1375, 1348, 1292, 1271, 1248, 1233, 1194, 1130, 1018, 758 cm⁻¹.

Synthesis of [Pt(L2)(DMSO)Cl]: Following the general procedure for splitting the platinum dimers using [Pt(L2)Cl]₂ (0.265 g, 0.249 mmol). Obtained as a yellow/green solid. Yield = 0.283 g, (93%). ¹⁹⁵Pt (107.5 MHz, CDCl₃): δ_{Pt} -3675 ppm.

Synthesis of [Pt(L3)(DMSO)Cl]: Following the general procedure for splitting the platinum dimers using [Pt(L4)Cl]₂ (0.151 g, 0.132 mmol). Obtained as a brown/green solid. Yield = 0.156 g (91%). ¹⁹⁵Pt (107.5 MHz, CDCl₃): δ_{Pt} -3673 ppm.

General procedure for coordinating β-diketonates to platinum complexes: Based on a modified literature methodology.¹⁰⁸ [Pt(L)(DMSO)Cl] (1 eq) was dissolved in 3-

pentanone (5 mL), to which, the β -diketonate (1 – 10 eq) was added. The reaction was stirred at room temperature for 16 h under dinitrogen. The solvent was removed *in vacuo* and the crude product dissolved in dichloromethane (10 mL) and filtered to remove any insoluble salts. The yellow solution was dried *in vacuo*. The crude products were purified by column chromatography (silica, dichloromethane) and were eluted as the first yellow band with dichloromethane and dried *in vacuo*.

General procedure for preparing sodium salts of β -diketonates: Based on a literature methodology.³⁵ The β -diketonate (1.1 eq) was added slowly to a stirring suspension of NaH (1 eq) in petroleum ether (50 mL) under dinitrogen. The suspension was stirred at room temperature until the effervescence had subsided and was then heated at reflux for 3 h. The suspension was cooled and the product was obtained through filtration and washing with copious amounts of petroleum ether.

Synthesis of sodium acetylacetonate monohydrate: 2,4-pentanedione (1.000 g, 10.000 mmol), NaH (60% dispersion in mineral oil) (0.400 g, 9.091 mmol). Yield = 1.235 g, (97%).

Synthesis of the sodium hexamethylacetylacetonate monohydrate: 2,2,6,6,-tetramethyl-3,5-heptanedione (1.000 g, 5.435 mmol), NaH (60% dispersion in mineral oil) (0.217 g, 4.941 mmol). Yield = 1.051 g, (95%).

Synthesis of [Pt(L1)(acac)]: Following the general procedure for coordinating β -diketonates to platinum complexes using [Pt(L1)(DMSO)Cl] (0.053 g, 0.091 mmol) and sodium acetylacetonate monohydrate (0.111 g, 0.910 mmol). Obtained as a dark orange solid. Yield = 0.042 g, (81%). ¹H NMR (400 MHz, CDCl₃): δ_{H} 9.59 (1H, dd, ³J_{HH} = 8.0 Hz, ⁴J_{HH} = 0.4 Hz), 8.69 (1H, dd, ³J_{HH} = 8.4 Hz, ⁴J_{HH} = 1.2 Hz), 8.24 (1H, s), 7.81 – 7.75 (2H, m), 7.65 – 7.60 (2H, m), 7.29 – 7.25 (1H, m), 7.21 – 7.17 (1H, m), 5.58 (1H, s), 4.56 (2H, q, ³J_{HH} = 7.2 Hz), 2.06 (3H, s), 2.05 (3H, s), 1.52 (3H, t, ³J_{HH} = 7.2 Hz) ppm. ¹³C{¹H} NMR (75.6 MHz, CDCl₃): δ_{C} 185.7, 184.2, 169.4, 165.7, 149.9, 145.7, 140.3, 137.4, 130.8, 130.0, 129.7, 127.7, 126.9, 125.4, 125.2, 125.1, 124.0, 118.1, 101.8, 62.3, 28.5, 27.2, 14.4 ppm. ¹⁹⁵Pt (107.5 MHz, CDCl₃): δ_{Pt} -2765 ppm. UV-vis (CHCl₃): λ_{max} (ϵ / dm³ mol⁻¹ cm⁻¹) 253 (17500), 292 (13900), 300 (14400), 363 (5570), 427 (3720) nm. IR (thin film): ν_{max} 3115, 3053, 2980, 2920, 1723, 1580, 1541, 1522, 1452, 1393, 1375, 1298, 1267, 1238, 1196, 1146, 1028, 762 cm⁻¹.

Synthesis of [Pt(L1)(hmacac)]: Following the general procedure for coordinating β -diketonates to platinum complexes using [Pt(L1)(DMSO)Cl] (0.023 g, 0.039 mmol) and sodium hexamethylacetylacetonate monohydrate (0.009 g, 0.043 mmol). Yield = 0.024, (93%). ^1H NMR (400 MHz, CDCl_3): δ_{H} 9.70 (1H, d, $^3J_{\text{HH}} = 9.2$ Hz), 8.71 (1H, dd, $^3J_{\text{HH}} = 8.4$ Hz, $^4J_{\text{HH}} = 0.8$ Hz), 8.26 (1H, s), 7.88 (1H, dd (with satellites), $^3J_{\text{HH}} = 7.6$ Hz, $^4J_{\text{HH}} = 0.8$ Hz), 7.81 – 7.77 (1H, m), 7.67 – 7.61 (2H, m), 7.32 – 7.28 (1H, m), 7.23 – 7.19 (1H, m), 5.94 (1H, s), 4.58 (2H, q, $^3J_{\text{HH}} = 7.2$ Hz), 1.54 (3H, t, $^3J_{\text{HH}} = 7.2$ Hz), 1.35 (9H, s), 1.30 (9H, s) ppm. $^{13}\text{C}\{^1\text{H}\}$ NMR (75.6 MHz, CDCl_3): δ_{C} 195.7, 193.9, 169.5, 165.8, 150.0, 145.8, 141.1, 137.4, 131.0, 130.5, 129.7, 127.7, 127.5, 125.4, 125.1, 125.0, 123.9, 118.1, 92.8, 62.4, 42.3, 41.1, 28.8, 28.6, 14.4 ppm. ^{195}Pt (107.5 MHz, CDCl_3): δ_{Pt} -2733 ppm. UV-vis (CHCl_3): λ_{max} ($\epsilon / \text{dm}^3 \text{mol}^{-1} \text{cm}^{-1}$) 253 (18700), 291 (12300), 301 (13000), 357 (5220), 437 (3610) nm. IR (thin film): ν_{max} 3117, 3057, 2961, 2924, 2855, 1724, 1601, 1584, 1559, 1549, 1530, 1497, 1462, 1452, 1391, 1357, 1360, 1263, 1238, 1225, 1194, 1144, 1026, 791, 760 cm^{-1} .

Synthesis of [Pt(L1)(hfacac)]: Following the general procedure for coordinating β -diketonates to platinum complexes using [Pt(L1)(DMSO)Cl] (0.022 g, 0.057 mmol), Na_2CO_3 (0.007 g, 0.063 mmol) and hexafluoroacetylacetonate (0.013 g, 0.063 mmol). Obtained as a yellow solid. Yield = 0.036 g, (92%). ^1H NMR (400 MHz, CDCl_3): δ_{H} 8.97 (1H, dd, $^3J_{\text{HH}} = 9.2$ Hz, $^4J_{\text{HH}} = 0.8$ Hz), 8.75 (1H, dd, $^3J_{\text{HH}} = 8.4$ Hz, $^4J_{\text{HH}} = 1.2$ Hz), 7.95 (1H, s), 7.64 – 7.60 (1H, m), 7.57 – 7.52 (1H, m), 7.37 – 7.35 (1H, m), 7.24 – 7.22 (1H, m), 7.10 – 7.08 (2H, m), 6.21 (1H, s), 4.55 (2H, q, $^3J_{\text{HH}} = 7.2$ Hz), 1.53 (3H, t, $^3J_{\text{HH}} = 7.2$ Hz) ppm. $^{13}\text{C}\{^1\text{H}\}$ NMR (125.8 MHz, CDCl_3): δ_{C} 184.6, 183.1, 168.4, 163.8, 148.6, 144.5, 142.7, 139.1, 130.1, 128.8, 128.7, 126.3, 125.8, 124.1, 124.0, 123.3, 122.9, 121.6, 115.0, 114.9, 113.3, 100.9, 27.4, 26.1 ppm. ^{195}Pt (107.5 MHz, CDCl_3): δ_{Pt} -2693 ppm. UV-vis (CHCl_3): λ_{max} ($\epsilon / \text{dm}^3 \text{mol}^{-1} \text{cm}^{-1}$) 253 (17700), 293 (12500), 370 (5370), 400 (2930) nm. IR (thin film): ν_{max} 2934, 2851, 1724, 1624, 1603, 1545, 1466, 1456, 1377, 1350, 1260, 1200, 1146, 1109, 1030, 735 cm^{-1} .

Synthesis of [Pt(L2)(acac)]: Following the general procedure for coordinating β -diketonates to platinum complexes using [Pt(L2)(DMSO)Cl] (0.050 g, 0.077 mmol) and sodium acetylacetonate monohydrate (0.094 g, 0.770 mmol). Obtained as a dark yellow solid. Yield = 0.046, (94%). ^1H NMR (400 MHz, CDCl_3): δ_{H} 9.28 (1H, d, $^3J_{\text{HH}} = 8.8$ Hz), 8.95 (1H, s), 7.86 (1H, d, $^3J_{\text{HH}} = 8.0$ Hz), 7.69 – 7.66 (2H, m), 7.49 – 7.45

(2H, m), 7.36 – 7.31 (2H, m), 7.11 – 6.98 (4H, m), 6.80 – 6.76 (1H, m), 5.47 (1H, s), 2.00 (3H, s), 1.81 (3H, s) ppm. $^{13}\text{C}\{^1\text{H}\}$ NMR (125.8 MHz, CDCl_3): δ_{C} 184.5, 183.1, 168.8, 165.3, 148.6, 144.8, 144.4, 139.2, 130.0, 129.0, 128.6, 126.2, 125.8, 124.0, 123.9, 123.4, 122.9, 112.9, 100.8, 51.9, 27.9, 27.3, 26.2 ppm. ^{195}Pt (107.5 MHz, CDCl_3): δ_{Pt} -2779 ppm. UV-vis (CHCl_3): λ_{max} ($\epsilon / \text{dm}^3 \text{mol}^{-1} \text{cm}^{-1}$) 258 (28800), 297 (28300), 343 (9200), 360 (6800), 415 (3130) nm. IR (thin film): ν_{max} 3300, 3057, 2963, 2924, 2853, 1721, 1647, 1595, 1572, 1549, 1516, 1456, 1393, 1366, 1302, 1263, 1219, 1161, 1092, 1028, 793, 762, 733, 702 cm^{-1} .

Synthesis of [Pt(L3)(acac)]: Following the general procedure for coordinating β -diketonates to platinum complexes using [Pt(L3)(DMSO)Cl] (0.050 g, 0.077 mmol) and sodium acetylacetonate monohydrate (0.094 g, 0.770 mmol). Obtained as a dark yellow solid. Yield = 0.046 g, (94%). ^1H NMR (400 MHz, CDCl_3): δ_{H} 9.28 (1H, d, $^3J_{\text{HH}} = 8.8$ Hz), 8.95 (1H, s), 7.86 (1H, d, $^3J_{\text{HH}} = 8.0$ Hz), 7.69 – 7.66 (2H, m), 7.49 – 7.45 (2H, m), 7.36 – 7.31 (2H, m), 7.11 – 6.98 (4H, m), 6.80 – 6.76 (1H, m), 5.47 (1H, s), 2.00 (3H, s), 1.81 (3H, s) ppm. $^{13}\text{C}\{^1\text{H}\}$ NMR (125.8 MHz, CDCl_3): δ_{C} 184.6, 183.1, 168.4, 163.8, 148.6, 144.5, 142.7, 139.1, 130.1, 128.8, 128.7, 126.3, 125.8, 124.1, 124.0, 123.3, 122.9, 121.6, 121.5, 115.0, 114.9, 113.3, 100.8, 27.4, 26.1 ppm. ^{195}Pt (107.5 MHz, CDCl_3): δ_{Pt} -2769 ppm. UV-vis (CHCl_3): λ_{max} ($\epsilon / \text{dm}^3 \text{mol}^{-1} \text{cm}^{-1}$) 300 (14860), 342 (9840), 363 (4650), 442 (2170) nm. IR (thin film): ν_{max} 3262, 3063, 2963, 2924, 2853, 1672, 1655, 1582, 1547, 1522, 1508, 1456, 1404, 1373, 1308, 1260, 1211, 1157, 1090, 1015, 939, 864, 833, 800, 760, 729, 698 cm^{-1} .

Synthesis of [Pt(L4)(acac)]: The deprotection of the ethyl ester was carried out based on a similar literature methodology.⁸¹ [Pt(L1)(acac)] (0.029 g, 0.051 mmol) was dissolved in acetone (5 mL) and potassium hydroxide (1 M soln, 5 mL) and stirred for 16 h at room temperature under dinitrogen. The acetone was removed *in vacuo* and the solution neutralised with hydrochloric acid (1 M soln). The water was removed *in vacuo* and the solid dissolved in methanol (5 mL) and filtered to remove inorganic salts. Yield = 0.024 g, (87%). ^1H NMR (400 MHz, CD_3OD): δ_{H} 9.58 (1H, d, $^3J_{\text{HH}} = 9.2$ Hz), 8.30 (1H, dd, $^3J_{\text{HH}} = 8.4$ Hz, $^4J_{\text{HH}} = 1.6$ Hz), 7.93 (1H, s), 7.73 – 7.69 (1H, m), 7.65 – 7.62 (1H, m), 7.58 – 7.53 (2H, m), 7.13 – 7.07 (2H, m), 5.48 (1H, s), 2.86 (3H, s), 1.81 (3H, s) ppm. $^{13}\text{C}\{^1\text{H}\}$ NMR (125.8 MHz, CD_3OD): δ_{C} 185.7, 183.9, 172.8, 169.9, 150.2, 149.6, 146.5, 139.1, 130.1, 129.5, 128.5, 127.4, 126.3, 126.0, 124.7, 124.4, 123.4, 113.2, 101.0, 26.9, 25.7 ppm. ^{195}Pt (107.5 MHz, CD_3OD): δ_{Pt} -

2781 ppm. MS(ES) found $m/z = 541.06$ for $[M - H]^-$. UV-vis (MeOH): λ_{\max} ($\epsilon / \text{dm}^3 \text{mol}^{-1} \text{cm}^{-1}$) 282 (4990), 334 (1850), 348 (1940), 382 (1360) nm. IR (thin film): ν_{\max} 3379, 2963, 2918, 2849, 1659, 1576, 1539, 1520, 1454, 1393, 1360, 1337, 1277, 1024, 764 cm^{-1} .

General procedure for coordinating 8-hydroxyquinoline to platinum complexes:

Based on a modified literature methodology.³⁶ $[\text{Pt}(\text{L})(\text{DMSO})\text{Cl}]$ (1 eq), Na_2CO_3 (1.1 eq) and 8-hydroxyquinoline (1.1 eq) were heated to 100 °C, with stirring under dinitrogen, in 2-methoxyethanol (5 mL) for 24 h. The solvent was removed *in vacuo* and the crude product purified by precipitation or column chromatography.

Synthesis of $[\text{Pt}(\text{L1})(8\text{-Q})]$: Following the general procedure for coordinating 8-hydroxyquinoline to platinum complexes using $[\text{Pt}(\text{L1})(\text{DMSO})\text{Cl}]$ (0.038 g, 0.065 mmol), Na_2CO_3 (0.008 g, 0.072 mmol) and 8-hydroxyquinoline (0.010 g, 0.072 mmol). The product was purified by column chromatography (silica, dichloromethane). The product was eluted as the first red band with dichloromethane and dried to yield a dark red solid. Yield = 0.035 g, (88%). ^1H NMR (400 MHz, CDCl_3): δ_{H} 9.93 (1H, d, $^3J_{\text{HH}} = 8.8$ Hz), 9.18 (1H, d (with satellites $^3J_{\text{HPt}} = 44$ Hz), $^3J_{\text{HH}} = 5.2$ Hz), 8.66 (1H, dd, $^3J_{\text{HH}} = 8.4$ Hz, $^4J_{\text{HH}} = 0.8$ Hz), 8.28 (1H, dd, $^3J_{\text{HH}} = 8.0$ Hz, $^4J_{\text{HH}} = 0.8$ Hz), 8.23 (1H, s), 7.94 – 7.91 (1H, m), 7.67 – 7.63 (2H, m), 7.56 – 7.49 (2H, m), 7.40 – 7.36 (1H, m), 7.28 – 7.25 (1H, m), 7.22 – 7.18 (1H, m), 7.15 (1H, dd, $^3J_{\text{HH}} = 8.0$ Hz, $^4J_{\text{HH}} = 0.8$ Hz), 6.92 (1H, dd, $^3J_{\text{HH}} = 8.0$ Hz, $^4J_{\text{HH}} = 0.8$ Hz), 4.57 (2H, q, $^3J_{\text{HH}} = 7.2$ Hz), 1.53 (3H, t, $^3J_{\text{HH}} = 7.2$ Hz) ppm. $^{13}\text{C}\{^1\text{H}\}$ NMR (75.6 MHz, CDCl_3): δ_{C} 168.3, 167.4, 165.7, 149.7, 148.1, 147.6, 145.25, 144.66, 138.78, 137.91, 132.90, 131.65, 131.02, 130.83, 129.80, 128.48, 128.0, 125.9, 125.2, 124.7, 123.6, 121.0, 117.9, 116.1, 111.5, 62.4, 14.4 ppm. ^{195}Pt (107.5 MHz, CDCl_3): δ_{Pt} -2922 ppm. UV-vis (CHCl_3): λ_{\max} ($\epsilon / \text{dm}^3 \text{mol}^{-1} \text{cm}^{-1}$) 257 (16700), 284 (15900), 370 (12400) nm. IR (thin film): ν_{\max} 3063, 2965, 2934, 2864, 1721, 1653, 1645, 1599, 1580, 1541, 1501, 1452, 1375, 1352, 1294, 1262, 1240, 1196, 1144, 1092, 1084, 1022, 795, 762, 733 cm^{-1} .

General procedure for coordinating a monodentate *N*-heterocycle to platinum complexes: Prepared by a modified literature methodology.³⁷ The *N*-heterocycle (1 – 1.1 eq) was added to $[\text{Pt}(\text{L})(\text{DMSO})\text{Cl}]$ (1 eq) in acetone (5 mL) and stirred for 16 h

under dinitrogen at room temperature. The solvent was removed *in vacuo* and the product purified according to the compound.

Synthesis of [Pt(L1)(py)Cl]: Following the general procedure for coordinating a monodentate *N*-heterocycle to platinum complexes using pyridine (0.007 g, 0.094 mmol) and [Pt(L1)(DMSO)Cl] (0.050 g, 0.086 mmol). The solvent was reduced in volume and diethyl ether (5 mL) was added to precipitate the desired product, which was filtered and washed with cold diethyl ether (2 x 5 mL). Yield = 0.043 g, (86%). ^1H NMR (400 MHz, CDCl_3): δ_{H} 9.80 (1H, dd, $^3J_{\text{HH}} = 8.8$ Hz, $^4J_{\text{HH}} = 0.8$ Hz), 9.01 (2H, d (with satellites $^3J_{\text{HPt}} = 48.0$ Hz)), 8.59 (1H, d, $^3J_{\text{HH}} = 8.4$ Hz), 8.23 (1H, s), 7.93 – 7.89 (1H, m), 7.83 – 7.79 (1H, m), 7.67 – 6.60 (2H, m), 7.47 – 7.44 (2H, m), 7.19 – 7.16 (1H, m), 7.03 – 6.98 (1H, m), 6.29 (1H, dd (with satellites $^3J_{\text{HPt}} = 42.4$ Hz), $^3J_{\text{HH}} = 8.0$ Hz, $^4J_{\text{HH}} = 0.8$ Hz), 4.57 (2H, q, $^3J_{\text{HH}} = 7.2$ Hz), 1.52 (3H, t, $^3J_{\text{HH}} = 7.2$ Hz) ppm. $^{13}\text{C}\{^1\text{H}\}$ NMR (125.8 MHz, CDCl_3): δ_{C} 168.1, 165.6, 154.1, 149.3, 146.0, 143.7, 138.5, 138.0, 131.0, 130.6, 130.3, 129.5, 128.1, 126.1, 125.7, 124.9, 124.7, 123.9, 117.6, 62.4, 14.3 ppm. ^{195}Pt (107.5 MHz, CDCl_3): δ_{Pt} -3158 ppm. UV-vis (CHCl_3): λ_{max} ($\epsilon / \text{dm}^3 \text{mol}^{-1} \text{cm}^{-1}$) 255 (31800), 285 (26000), 367 (12800), 450 (1990) nm. IR (thin film): ν_{max} 3096, 3053, 2980, 2924, 2224, 1723, 1717, 1580, 1541, 1451, 1373, 1292, 1267, 1240, 1196, 1144, 1024, 907, 864, 760, 727, 689 cm^{-1} .

General procedure for coordinating 2,2'-bipyridine to platinum complexes:

Prepared by a modified literature methodology.³⁹ 2,2'-bipyridine (1.1 eq) was added to [Pt(L)(DMSO)Cl] (1 eq) in DMF (5 mL) and stirred for 48 h under dinitrogen at 65 °C. Diethyl ether was added to precipitate the complex, which was filtered and washed with plenty of diethyl ether. The yellow solid was dissolved in acetonitrile before a saturated aqueous solution of potassium hexafluorophosphate was added drop wise to exchange the chloride counter-ion. The precipitate was dissolved in dichloromethane before being washed with water (2 x 50 mL) and dried over MgSO_4 , filtered and the solvent was reduced in volume. Diethyl ether was added to precipitate and the solid was collected by filtration, washed with diethyl ether and dried to yield a dark yellow solid.

Synthesis of [Pt(L1)(bpy)Cl]: Following the general procedure for coordinating a bipyridine to platinum complexes using 2,2'-bipyridine (0.031 g, 0.200 mmol) and [Pt(L1)(DMSO)Cl] (0.070 g, 0.182 mmol). Yield = 0.057 g, (73%). ^1H NMR (400

MHz, CDCl₃): δ_{H} 9.40 (1H, d (with satellites $^3J_{\text{HPt}} = 40.8$ Hz), $^3J_{\text{HH}} = 6.0$ Hz), 8.66 – 8.61 (2H, m), 8.39 – 8.34 (1H, m), 8.32 – 8.28 (3H, m), 8.17 – 8.13 (1H, m), 8.09 – 8.07 (1H, m), 7.81 – 7.73 (3H, m), 7.64 – 7.61 (1H, m), 7.43 – 7.36 (2H, m), 7.29 – 7.22 (2H, m), 4.60 (2H, m q, $^3J_{\text{HH}} = 7.2$ Hz), 1.53 (3H, t, $^3J_{\text{HH}} = 7.2$ Hz) ppm. $^{13}\text{C}\{^1\text{H}\}$ NMR (125.8 MHz, CD₃CN): δ_{C} 167.6, 164.9, 157.3, 155.0, 152.8, 150.9, 146.5, 146.1, 142.3, 140.5, 140.1, 140.0, 132.0, 131.3, 130.3, 128.6, 128.2, 127.0, 126.5, 126.3, 125.2, 124.9, 124.6, 124.0, 123.3, 118.1, 62.6, 13.3 ppm. ^{195}Pt (107.5 MHz, CD₃CN): δ_{Pt} -3097 ppm. UV-vis (CH₃CN): λ_{max} (ϵ / dm³ mol⁻¹ cm⁻¹) 281 (28600), 318 (12900), 355 (10900), 368 (11500), 395 (8200), 448 (2460) nm. IR (thin film): ν_{max} 3086, 3055, 2984, 2932, 1723, 1669, 1599, 1582, 1545, 1472, 1449, 1377, 1267, 1246, 1200, 1157, 1146, 1024, 839, 762, 731, 700 cm⁻¹.

2.6. References

1. FDA Approved Drugs Products, <http://www.accessdata.fda.gov/>, Accessed 29 July, 2014.
2. R. C. Todd and S. J. Lippard, *Metallomics*, 2009, **1**, 280-291.
3. C. E. Housecroft, *The Heavier d-Block Metals: Aspects of Inorganic and Coordination Chemistry*, Oxford University Press, Oxford, 1999.
4. M. W. G. deBolster, R. Cammack, D. N. Coucouvanis, J. Reedijk and C. Veeger, *J. Biol. Inorg. Chem.*, 1996, **1**, G1-G29.
5. J. Pranczk, D. Jacewicz, D. Wyrzykowski and L. Chmurzynski, *Curr. Pharm. Anal.*, 2014, **10**, 2-9.
6. C. J. Williams and J. M. A. Whitehouse, *Brit. Med. J.*, 1979, **1**, 1689-1691.
7. D. Wang and S. J. Lippard, *Nat. Rev. Drug Discov.*, 2005, **4**, 307-320.
8. F. I. Raynaud, F. E. Boxall, P. M. Goddard, M. Valenti, M. Jones, B. A. Murrer, M. Abrams and L. R. Kelland, *Clin. Cancer Res.*, 1997, **3**, 2063-2074.
9. T. C. Johnstone, J. J. Wilson and S. J. Lippard, *Inorg. Chem.*, 2013, **52**, 12234-12249.
10. C. J. Ziegler, A. P. Silverman and S. J. Lippard, *J. Biol. Inorg. Chem.*, 2000, **5**, 774-783.
11. P. D. Braddock, T. A. Connors, M. Jones, A. R. Khokhar, D. H. Melzack and M. L. Tobe, *Chem.-Biol. Interact.*, 1975, **11**, 145-161.
12. J. Holford, F. Raynaud, B. A. Murrer, K. Grimaldi, J. A. Hartley, M. Abrams and L. R. Kelland, *Anti-Cancer Drug Des.*, 1998, **13**, 1-18.
13. V. Balzani, P. Ceroni and A. Juris, *Photochemistry and Photophysics*, Wiley-VCH Verlag GmbH and Co., Weinheim, 2014.
14. M. Mauro, A. Aliprandi, D. Septiadi, N. S. Kehra and L. De Cola, *Chem. Soc. Rev.*, 2014, **43**, 4144-4166.
15. R. Valiente, J. M. Garcia-Lastra, P. Garcia-Fernandez, S. Garcia-Revilla and O. S. Wenger, *Eur. J. Inorg. Chem.*, 2007, 5735-5742.
16. H. Yersin, I. Hidvegi, G. Gliemann and M. Stock, *Phys. Rev. B*, 1979, **19**, 177-180.
17. A. Loosli, M. Wermuth, H. U. Gudel, S. Capelli, J. Hauser and H. B. Burgi, *Inorg. Chem.*, 2000, **39**, 2289-2293.
18. J. Brooks, Y. Babayan, S. Lamansky, P. I. Djurovich, I. Tsyba, R. Bau and M. E. Thompson, *Inorg. Chem.*, 2002, **41**, 3055-3066.

19. P. I. Djurovich, D. Murphy, M. E. Thompson, B. Hernandez, R. Gao, P. L. Hunt and M. Selke, *Dalton Trans.*, 2007, 3763-3770.
20. S. Lamansky, P. Djurovich, D. Murphy, F. Abdel-Razzaq, R. Kwong, I. Tsyba, M. Bortz, B. Mui, R. Bau and M. E. Thompson, *Inorg. Chem.*, 2001, **40**, 1704-1711.
21. S. Lamansky, P. Djurovich, D. Murphy, F. Abdel-Razzaq, H. E. Lee, C. Adachi, P. E. Burrows, S. R. Forrest and M. E. Thompson, *J. Am. Chem. Soc.*, 2001, **123**, 4304-4312.
22. J. Li, P. I. Djurovich, B. D. Alleyne, I. Tsyba, N. N. Ho, R. Bau and M. E. Thompson, *Polyhedron*, 2004, **23**, 419-428.
23. J. Li, P. I. Djurovich, B. D. Alleyne, M. Yousufuddin, N. N. Ho, J. C. Thomas, J. C. Peters, R. Bau and M. E. Thompson, *Inorg. Chem.*, 2005, **44**, 1713-1727.
24. G. A. Crosby, *Acc. Chem. Res.*, 1975, **8**, 231-238.
25. X. Mou, Y. Q. Wu, S. J. Liu, M. Shi, X. M. Liu, C. M. Wang, S. Sun, Q. Zhao, X. H. Zhou and W. Huang, *J. Mater. Chem.*, 2011, **21**, 13951-13962.
26. A. Bossi, A. F. Rausch, M. J. Leidl, R. Czerwieniec, M. T. Whited, P. I. Djurovich, H. Yersin and M. E. Thompson, *Inorg. Chem.*, 2013, **52**, 12403-12415.
27. Z. M. Hudson, B. A. Blight and S. N. Wang, *Org. Lett.*, 2012, **14**, 1700-1703.
28. O. J. Stacey and S. J. A. Pope, *RSC Adv.*, 2013, **3**, 25550-25564.
29. M. Selke, W. L. Karney, S. I. Khan and C. S. Foote, *Inorg. Chem.*, 1995, **34**, 5715-5720.
30. S. W. Lai, T. C. Cheung, M. C. W. Chan, K. K. Cheung, S. M. Peng and C. M. Che, *Inorg. Chem.*, 2000, **39**, 255-262.
31. A. D. McNaught and A. Wilkinson, *IUPAC. Compendium of Chemical Terminology (the "Gold book")*, Blackwell Scientific Publications, Oxford, 2nd edn., 1997.
32. C. Cornioleydeuschel and A. Vonzelewsky, *Inorg. Chem.*, 1987, **26**, 3354-3358.
33. N. Ghavale, A. Wadawale, S. Dey and V. K. Jain, *J. Organomet. Chem.*, 2010, **695**, 1237-1245.
34. M. Ghedini, T. Pugliese, M. La Deda, N. Godbert, I. Aiello, M. Amati, S. Belviso, F. Lelj, G. Accorsi and F. Barigelletti, *Dalton Trans.*, 2008, 4303-4318.
35. M. Spencer, A. Santoro, G. R. Freeman, A. Diez, P. R. Murray, J. Torroba, A. C. Whitwood, L. J. Yellowlees, J. A. G. Williams and D. W. Bruce, *Dalton Trans.*, 2012, **41**, 14244-14256.

36. N. M. Shavaleev, H. Adams, J. Best, R. Edge, S. Navaratnam and J. A. Weinstein, *Inorg. Chem.*, 2006, **45**, 9410-9415.
37. A. Esmaeilbeig, H. Samouei, S. Abedanzadeh and Z. Amirghofran, *J. Organomet. Chem.*, 2011, **696**, 3135-3142.
38. P. I. Kvam, M. V. Puzyk, K. P. Balashev and J. Songstad, *Acta Chem. Scand.*, 1995, **49**, 335-343.
39. D. M. Jenkins, J. F. Senn and S. Bernhard, *Dalton Trans.*, 2012, **41**, 8077-8085.
40. M. Panigati, M. Mauro, D. Donghi, P. Mercandelli, P. Mussini, L. De Cola and G. D'Alfonso, *Coord. Chem. Rev.*, 2012, **256**, 1621-1643.
41. P. T. Chou and Y. Chi, *Chem. Eur. J.*, 2007, **13**, 380-395.
42. M. S. Lowry, J. I. Goldsmith, J. D. Slinker, R. Rohl, R. A. Pascal, G. G. Malliaras and S. Bernhard, *Chem. Mater.*, 2005, **17**, 5712-5719.
43. W. P. To, T. Zou, R. W. Y. Sun and C. M. Che, *Philos. T. R. Soc. A*, 2013, **371**.
44. P. Ceroni and V. Balzani, in *The Exploration of Supramolecular Systems and Nanostructures by Photochemical Techniques*, ed. P. Ceroni, Springer, New York, NY, 2012.
45. A. Ruggi, F. W. B. van Leeuwen and A. H. Velders, *Coord. Chem. Rev.*, 2011, **255**, 2542-2554.
46. V. Fernandez-Moreira, F. L. Thorp-Greenwood and M. P. Coogan, *Chem. Commun.*, 2010, **46**, 186-202.
47. A. J. Hallett and J. E. Jones, *Dalton Trans.*, 2011, **40**, 3871-3876.
48. E. Baranoff, J. H. Yum, M. Graetzel and M. K. Nazeeruddin, *J. Organomet. Chem.*, 2009, **694**, 2661-2670.
49. S. W. Lai, Y. Liu, D. Zhang, B. Wang, C. N. Lok, C. M. Che and M. Selke, *Photochem. Photobiol.*, 2010, **86**, 1414-1420.
50. S. W. Botchway, M. Charnley, J. W. Haycock, A. W. Parker, D. L. Rochester, J. A. Weinstein and J. A. G. Williams, *Proc. Natl. Acad. Sci. U. S. A.*, 2008, **105**, 16071-16076.
51. A. Beeby, S. W. Botchway, I. M. Clarkson, S. Faulkner, A. W. Parker, D. Parker and J. A. G. Williams, *J. Photoch. Photobio. B*, 2000, **57**, 83-89.
52. B. M. Still, P. G. A. Kumar, J. R. Aldrich-Wright and W. S. Price, *Chem. Soc. Rev.*, 2007, **36**, 665-686.
53. A. Pidcock, R. E. Richards and L. M. Venanzi, *J. Chem. Soc. A*, 1968, 1970-1973.

54. A. V. Zelewsky, *Helv. Chim. Acta*, 1968, **51**, 803-807.
55. P. S. Pregosin, *Coord. Chem. Rev.*, 1982, **44**, 247-291.
56. B. E. Schwederski, H. P. D. Lee and D. W. Margerum, *Inorg. Chem.*, 1990, **29**, 3569-3578.
57. D. P. Bancroft, C. A. Lepre and S. J. Lippard, *J. Am. Chem. Soc.*, 1990, **112**, 6860-6871.
58. W. Freeman, P. S. Pregosin, S. N. Sze and L. M. Venanzi, *J. Magn. Reson.*, 1976, **22**, 473-478.
59. P. S. Pregosin, *Transition Metal Nuclear Magnetic Resonance*, Elsevier, Amsterdam, 1991.
60. C. Cutrin Prieto, E. Nieto Pol, A. Batalla Eiras, L. Casal Iglesias, E. Perez Becerra and V. Lorenzo Zuniga, *Med. Clin.*, 1991, **97**, 104-106.
61. W. J. Geldenhuys, S. R. Kuzenko and M. A. Simmons, *J. Med. Chem.*, 2010, **53**, 8080-8088.
62. F. E. Blaney, L. F. Raveglia, M. Artico, S. Cavagnera, C. Dartois, C. Farina, M. Grugni, S. Gagliardi, M. A. Luttmann, M. Martinelli, G. M. M. G. Nadler, C. Parini, P. Petrillo, H. M. Sarau, M. A. Scheideler, D. W. P. Hay and G. A. M. Giardina, *J. Med. Chem.*, 2001, **44**, 1675-1689.
63. G. A. M. Giardina, L. F. Raveglia, M. Grugni, H. M. Sarau, C. Farina, A. D. Medhurst, D. Graziani, D. B. Schmidt, R. Rigolio, M. Luttmann, S. Cavagnera, J. J. Foley, V. Vecchietti and D. W. P. Hay, *J. Med. Chem.*, 1999, **42**, 1053-1065.
64. W. H. Zhang, X. H. Zhang, A. L. Tan, M. A. Yong, D. J. Young and T. S. A. Hor, *Organometallics*, 2012, **31**, 553-559.
65. K. K. W. Lo, J. S. W. Chan, L. H. Lui and C. K. Chung, *Organometallics*, 2004, **23**, 3108-3116.
66. R. Tao, J. Qiao, G. L. Zhang, L. Duan, L. D. Wang and Y. Qiu, *J. Phys. Chem. C*, 2012, **116**, 11658-11664.
67. W. J. Xu, S. J. Liu, T. C. Ma, Q. Zhao, A. Pertegas, D. Tordera, H. J. Bolink, S. H. Ye, X. M. Liu, S. Sun and W. Huang, *J. Mater. Chem.*, 2011, **21**, 13999-14007.
68. C. Dragonetti, A. Valore, A. Colombo, S. Righetto and V. Trifiletti, *Inorg. Chim. Acta*, 2012, **388**, 163-167.
69. B. H. Tong, J. Y. Qiang, Y. Q. Xu, Q. B. Mei, T. K. Duan, Q. Chen and Q. F. Zhang, *Inorg. Chem. Commun.*, 2011, **14**, 1937-1939.
70. P. K. Lee, W. H. T. Law, H. W. Liu and K. K. W. Lo, *Inorg. Chem.*, 2011, **50**, 8570-8579.

71. Q. Zhao, F. Y. Li, S. J. Liu, M. X. Yu, Z. Q. Liu, T. Yi and C. H. Huang, *Inorg. Chem.*, 2008, **47**, 9256-9264.
72. K. K. W. Lo, C. K. Chung, T. K. M. Lee, L. H. Lui, K. H. K. Tsang and N. Y. Zhu, *Inorg. Chem.*, 2003, **42**, 6886-6897.
73. M. J. Li, P. C. Jiao, M. Lin, W. W. He, G. N. Chen and X. Chen, *Analyst*, 2011, **136**, 205-210.
74. M. J. Li, X. Liu, Y. Q. Shi, R. J. Xie, Q. H. Wei and G. N. Chen, *Dalton Trans.*, 2012, **41**, 10612-10618.
75. J. T. Yu, K. Q. He, Y. H. Li, H. Tan, M. X. Zhu, Y. F. Wang, Y. Liu, W. G. Zhu and H. B. Wu, *Dyes Pigm.*, 2014, **107**, 146-152.
76. G. Y. Zheng, D. P. Rillema, J. DePriest and C. Woods, *Inorg. Chem.*, 1998, **37**, 3588-3592.
77. E. Lalinde, M. T. Moreno, S. Ruiz and S. Sánchez, *Organometallics*, 2014, **33**, 3078-3090.
78. J. R. Berenguer, A. Diez, E. Lalinde, M. T. Moreno, S. Ruiz and S. Sanchez, *Organometallics*, 2011, **30**, 5776-5792.
79. J. D. Routledge, A. J. Hallett, J. A. Platts, P. N. Horton, S. J. Coles and S. J. A. Pope, *Eur. J. Inorg. Chem.*, 2012, 4065-4075.
80. L. Monti and G. Franchi, *Gazz. Chim. Ital.*, 1951, **81**, 544-547.
81. R. A. Smith, E. C. Stokes, E. E. Langdon-Jones, J. A. Platts, B. M. Kariuki, A. J. Hallett and S. J. A. Pope, *Dalton Trans.*, 2013, **42**, 10347-10357.
82. N. Godbert, T. Pugliese, I. Aiello, A. Bellusci, A. Crispini and M. Ghedini, *Eur. J. Inorg. Chem.*, 2007, 5105-5111.
83. J. Y. Cho, K. Y. Suponitsky, J. Li, T. V. Tirnoveeva, S. Barlow and S. R. Marder, *J. Organomet. Chem.*, 2005, **690**, 4090-4093.
84. H. Yersin and A. Volger, eds., *Photochemistry and Photophysics of Coordination Compounds*, Springer-Verlag, Berlin, 1987.
85. R. E. Cameron and A. B. Bocarsly, *Inorg. Chem.*, 1986, **25**, 2910-2913.
86. K. L. Mittal, ed., *Metallized Plastics 2*, Springer, 1991.
87. T. Okada, I. M. El-Mehasseb, M. Kodaka, T. Tomohiro, K. Okamoto and H. Okuno, *J. Med. Chem.*, 2001, **44**, 4661-4667.
88. C. P. Newman, K. Casey-Green, G. J. Clarkson, G. W. V. Cave, W. Errington and J. P. Rourke, *Dalton Trans.*, 2007, 3170-3182.
89. R. F. M. Elshaarawy and C. Janiak, *Eur. J. Med. Chem.*, 2014, **75**, 31-42.

90. L. Pazderski, T. Pawlak, J. Sitkowski, L. Kozerski and E. Szlyk, *Magn. Reson. Chem.*, 2009, **47**, 932-941.
91. D. Sooksawat, S. J. Pike, A. M. Z. Slawin and P. J. Lusby, *Chem. Commun.*, 2013, **49**, 11077-11079.
92. S. Alvarez, *Dalton Trans.*, 2013, **42**, 8617-8636.
93. D. Kourkoulos, C. Karakus, D. Hertel, R. Alle, S. Schmeding, J. Hummel, N. Risch, E. Holder and K. Meerholz, *Dalton Trans.*, 2013, **42**, 13612-13621.
94. M. J. Frisch, G. W. Trucks, H. B. Schlegel, G. E. Scuseria, M. A. Robb, J. R. Cheeseman, G. Scalmani, V. Barone, B. Mennucci, G. A. Petersson, H. Nakatsuji, M. Caricato, X. Li, H. P. Hratchian, A. F. Izmaylov, J. Bloino, G. Zheng, J. L. Sonnenberg, M. Hada, M. Ehara, K. Toyota, R. Fukuda, J. Hasegawa, M. Ishida, T. Nakajima, Y. Honda, O. Kitao, H. Nakai, T. Vreven, J. A. Montgomery Jr., J. E. Peralta, F. Ogliaro, M. J. Bearpark, J. Heyd, E. N. Brothers, K. N. Kudin, V. N. Staroverov, R. Kobayashi, J. Normand, K. Raghavachari, A. P. Rendell, J. C. Burant, S. S. Iyengar, J. Tomasi, M. Cossi, N. Rega, N. J. Millam, M. Klene, J. E. Knox, J. B. Cross, V. Bakken, C. Adamo, J. Jaramillo, R. Gomperts, R. E. Stratmann, O. Yazyev, A. J. Austin, R. Cammi, C. Pomelli, J. W. Ochterski, R. L. Martin, K. Morokuma, V. G. Zakrzewski, G. A. Voth, P. Salvador, J. J. Dannenberg, S. Dapprich, A. D. Daniels, Ö. Farkas, J. B. Foresman, J. V. Ortiz, J. Cioslowski and D. J. Fox, Gaussian, Inc., Wallingford, CT, USA, 2009.
95. A. D. Becke, *J. Chem. Phys.*, 1993, **98**, 5648-5652.
96. C. T. Lee, W. T. Yang and R. G. Parr, *Phys. Rev. B*, 1988, **37**, 785-789.
97. D. Andrae, U. Haussermann, M. Dolg, H. Stoll and H. Preuss, *Theor. Chim. Acta*, 1990, **77**, 123-141.
98. W. J. Hehre, Ditchfield and J. A. Pople, *J. Chem. Phys.*, 1972, **56**, 2257-2261.
99. M. M. Francl, W. J. Pietro, W. J. Hehre, J. S. Binkley, M. S. Gordon, D. J. Defrees and J. A. Pople, *J. Chem. Phys.*, 1982, **77**, 3654-3665.
100. T. Clark, J. Chandrasekhar, G. W. Spitznagel and P. V. Schleyer, *J. Comput. Chem.*, 1983, **4**, 294-301.
101. A. Vlcek and S. Zalis, *Coord. Chem. Rev.*, 2007, **251**, 258-287.
102. J. Tomasi, B. Mennucci and R. Cammi, *Chem. Rev.*, 2005, **105**, 2999-3093.
103. S. J. Coles and P. A. Gale, *Chem. Sci.*, 2012, **3**, 683-689.
104. G. M. Sheldrick, *Acta Cryst. A*, 2008, **64**, 112-122.
105. L. Palatinus and G. Chapuis, *J. Appl. Crystallogr.*, 2007, **40**, 786-790.
106. L. J. Farrugia, *J. Appl. Crystallogr.*, 2012, **45**, 849-854.

107. D. S. Black, G. B. Deacon and G. L. Edwards, *Aust. J. Chem.*, 1994, **47**, 217-227.
108. A. Santoro, A. C. Whitwood, J. A. G. Williams, V. N. Kozhevnikov and D. W. Bruce, *Chem. Mater.*, 2009, **21**, 3871-3882.

**Chapter 3: Adapting platinum (II) complexes towards
diagnostic and therapeutic applications**

3.1. Introduction

Chapter 3 aims to adapt the functionalisation of 2-phenylquinoline ligand architectures to increase the hydrophilicity of the subsequent complexes towards biologically relevant studies. Recent literature, outlined below, discusses the application of a class of cyclometallated Pt^{II} complexes in the fight against Alzheimer's disease. This chapter also aims to develop a macrocyclic ligand system capable of exploiting a coordination technique, utilised in Chapter 2, in order to form a dimetallic (Pt^{II} / Gd^{III}) bimodal imaging agent with potential application as a contrast agent in magnetic resonance imaging. Chapter 3 will also examine the photophysical properties of the dimetallic species to ascertain some of the physical attributes of the species by incorporating Yb^{III} .

3.1.1. Amyloid- β peptide and Alzheimer's disease – The amyloid hypothesis

Given that this chapter aims to develop compounds towards the potential detection and/or treatment of Alzheimer's, it is crucial that the disease be explained in some detail. Alzheimer's disease is one of the major causes of death in the developed world, after heart disease, cancer and strokes. It affects between 1 and 6% of those over the age of 65 and is an increasing problem with larger numbers of elderly people living for longer. The disease initially causes memory loss before worsening to leave patients bedridden, incontinent and with a personality completely unrecognisable to friends and family.¹

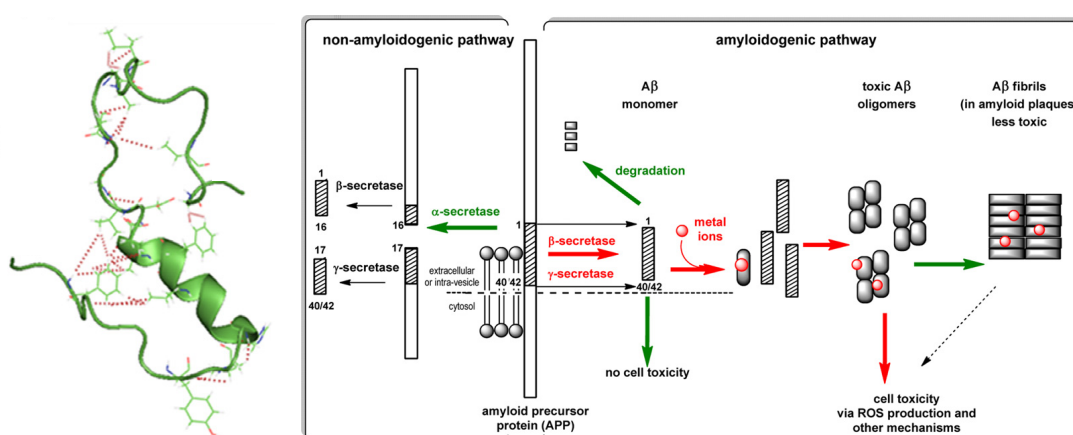


Figure 3.1 Structure of amyloid- β peptide in water determined by NMR spectroscopy (*left*)² and amyloid cascade process (*right*).³

The disease is thought to be linked to amyloid- β peptide ($A\beta$) (Figure 3.1).⁴ The peptide is a 38, 40 or 42 amino acid sequence in the amyloid precursor protein (APP), which is an integral membrane protein found in many structures, but especially in the neuronal synapses.⁵ The peptide is spliced from the protein by two enzymes (α - and γ -secretase).⁶ A possible defect in the splicing of the protein by the γ -secretase, or a mutation in the amino acid sequencing, has been found to result in an increase in the ‘sticky’ $A\beta_{42}$, which is thought to form fibrils which aggregate to form amyloid plaques.⁷ These plaques were thought to be toxic and cause damage to neurons, which leads to a repair mechanism causing an inflammatory response. The plaques were also thought to cause the formation of tau protein fibrils, which further the damage to the brain through cellular damage, leading to dementia however more recent evidence suggests that the plaques are a response to the formation of toxic soluble oligomers precipitating.^{4, 8}

More recently, interaction of Cu^{II} and Zn^{II} with $A\beta$ peptide have been linked to Alzheimer’s disease through their involvement in the amyloid cascade process.^{3, 9} Redox-active metals such as Zn^{II} are capable of forming reactive oxygen species (ROS), which are highly toxic and thought to be a key part of the pathology, along with the metals’ ability to induce amyloidogenic peptide aggregation.¹⁰

3.1.2. Peptide binding

Based on the knowledge that Alzheimer’s disease is intimately associated with $A\beta$ peptide, it is important to give some background information on peptide binding and, in particular, the binding of Pt^{II} complexes to $A\beta$ peptide and how this shows promise in the battle against Alzheimer’s disease.

There are many reports of metal interactions with peptides. Of great interest is the interaction of metal ions and complexes with $A\beta$ peptide because of its link to Alzheimer’s disease. Bathocuproine (Figure 3.2) had been shown to interact with $A\beta$ through NMR spectroscopy and,¹¹ in 2008, Barnham *et al.* found that an $L-PtCl_2$ complex (where L = 1,10-phenanthroline-type diimine, such as bathocuproine) coordinated to $A\beta$, inhibiting aggregation and neutralising the resultant toxicity. They found that cisplatin did not show any affect on the effects of $A\beta$, suggesting that the

planar aromatic nature of the ligand, L, is a key component in preventing aggregation and the subsequent neurological damage.¹²

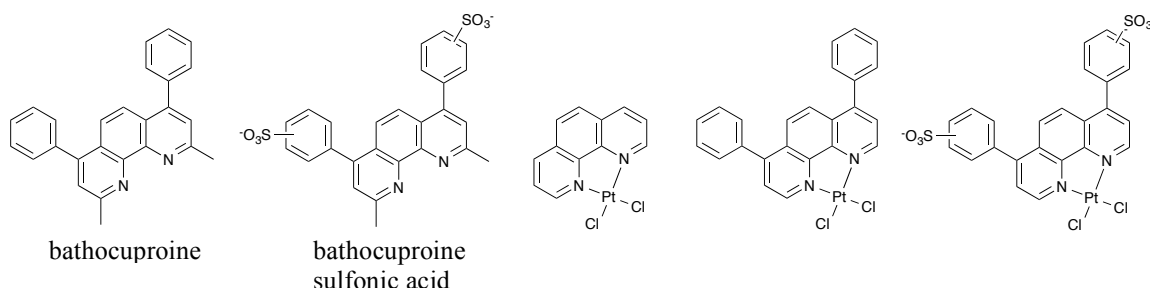


Figure 3.2 Structures (*left to right*) of bathocuproine, bathocuproine sulfonic acid and the three L-PtCl₂ complexes investigated by Barnham *et al.*¹²

The results found by Barnham *et al.* were further investigated to uncover the complex-peptide interactions. Using an A β_{1-16} oligomer, Ma *et al.* found that initial non-covalent interactions between the planar aromatic ligand and the peptide resulted in rapid platination of A β with multiple coordination modes (Figure 3.3). His6/His14 chelation was the major product but coordination was also found at Asp7, His13 and Lys16.¹³

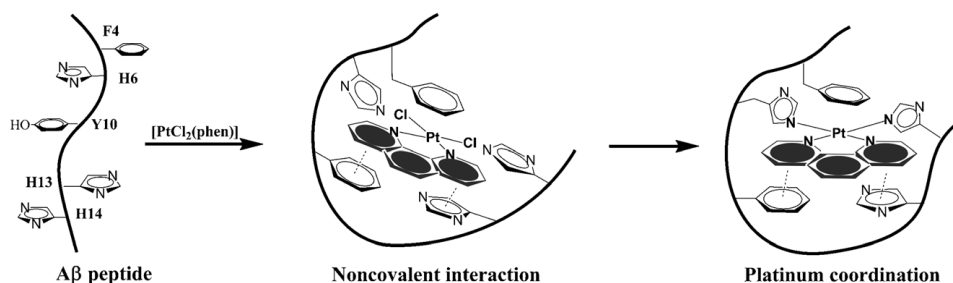
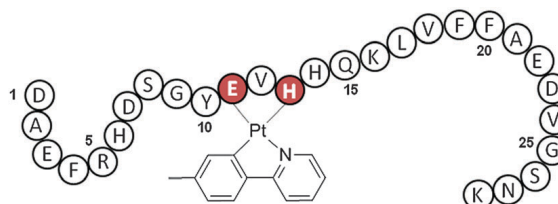


Figure 3.3 Interaction of [Pt(Cl)₂(phen)] with A β_{1-16} .¹³

In 2013, Collin *et al.* investigated the potential of five complexes to inhibit the coordination of copper and zinc to A β and thus prevent aggregation and the formation of ROS.¹⁴ Their research (Figure 3.4) revealed that, although the Cu(A β) could not be prevented by the coordination of the Pt^{II} complexes, Zn binding was completely precluded, which is important given the aggregation of Zn(A β), the high zinc concentrations around glutamatergic neurons and the preferential formation of the amyloid plaques at these sites.¹⁵⁻¹⁷

Figure 3.4 Binding of a cyclometallated Pt^{II} complex with $\text{A}\beta_{1-16}$.¹⁴

3.1.3. Magnetic resonance imaging

As mentioned in the opening remarks of this chapter, one of the reasons for increasing the hydrophilicity of the phosphorescent cyclometallated Pt^{II} moiety was to be able to append a Gd^{III} -containing architecture so that the subsequent relaxivity studies could be carried out. In order to develop a compound for these measurements, it is important that the basic principles behind magnetic resonance imaging and relaxivity are explained so that an appreciation for the parameters determining a compound's utility as a contrast agent are understood.

Magnetic resonance imaging (MRI) has become one of the most useful diagnostic techniques in modern medicine. It is a non-invasive tool that allows whole-body imaging with deep tissue penetration without the use of harmful ionising radiation like X-rays.^{18, 19} It can provide high definition three-dimensional images of soft tissue with millimetre accuracy by probing the environment of *in vivo* water protons *via* their relaxation rates.^{20, 21} The sensitivity can be enhanced through the introduction of a contrast agent, which are typically paramagnetic, superparamagnetic or ferromagnetic compounds capable of catalytically reducing the relaxation rate of proximal water molecules. The seven unpaired electrons on Gd^{III} result in a high magnetic moment and long electron spin relaxation time, making it an ideal candidate for use in contrast agents, which is the reason why it is the most widely used metal for increasing the contrast in MRI.²² Despite this, free Gd^{III} is highly toxic (LD_{50} of 0.2 mmol kg^{-1} in mice) and must be administered in the form of a stable chelate to prevent leaching of the metal ion *in vivo*.²³ Given the toxic nature of the Gd^{III} ion, the contrast agent is administered at a much lower concentration than that of water within the body so it is important that Gd-based contrast agents are able to coordinate and dissociate multiple water molecules in quick succession in order to increase the contrast effectively.²⁴

3.1.4. Relaxivity

MRI works by measuring the difference in the nuclear magnetic resonance properties of water protons imposed by the local environment. The nuclear spins of the protons are exposed to an external magnetic field, B_0 , which results in their alignment with the field. The nuclear spins are then realigned with the transverse plane by pulsed radio waves at 90° to B_0 . After the pulse sequence, the nuclei are allowed to relax back in line with B_0 .

Relaxation occurs through T_1 and T_2 processes, where T_1 is the spin-lattice (longitudinal) relaxation time and T_2 is the spin-spin (transverse) relaxation time.¹⁹ Contrast agents can reduce T_1 and T_2 to increase the number of relaxations in a given time frame, which allows for a greater contrast to be achieved in an MR image. How useful a compound is as a contrast agent is determined by the relaxivity, which can be defined as the relative increase in relaxation of bulk water protons by the agent at a given concentration. This can be observed through r_1 and r_2 , which are related to T_1 and T_2 , respectively. The effect of most interest in MRI is the longitudinal relaxation rate due to the slower rate of relaxation by the T_1 component.²⁵ Relaxivity, r_1 , is described in equation (18) where $(1/T_1)_{\text{obs}}$ is the inverse of the observed T_1 , $[\text{Gd}]$ is the concentration of Gd ions and $(1/T_1)_d$ is the diamagnetic contribution, which is the inherent relaxation of water.

$$r_1 = \frac{(1/T_1)_{\text{obs}}}{[\text{Gd}]} - \left(\frac{1}{T_1} \right)_d \quad (18)$$

The paramagnetic relaxation enhancement (Figure 3.5) of water molecules by gadolinium, and other paramagnetic species, is made up of two components: inner-sphere and outer-sphere.²³ Inner sphere relaxation relates to the enhanced relaxation of water molecules directly coordinated to the paramagnetic species (usually Gd^{III} ions), whilst outer-sphere relaxation is the relaxation enhancement of solvent molecules in the second coordination sphere and the bulk solvent. Inner-sphere and second-sphere water molecules are relaxed before exchanging rapidly with the bulk water, meaning that relaxation is dependent upon the number of coordination sites for water within the inner and second-sphere, their distances to the metal ion and the rate of exchange with the bulk solvent.²⁰

The inner-sphere contribution consists of q coordinated water molecules with a Gd-H distance r and a residency time of coordination τ_M , whilst second-sphere has q' water molecules with a Gd-H distance of r' and a residency time within the second-sphere of τ_M' . Relaxivity is also affected by the rotational motion of the contrast agent through the bulk solution, which gives a rotational correlation time, τ_R . The motion of bulk water is also a factor and is described by a translational diffusion correlation time, τ_D , which changes with factors such as viscosity.²³

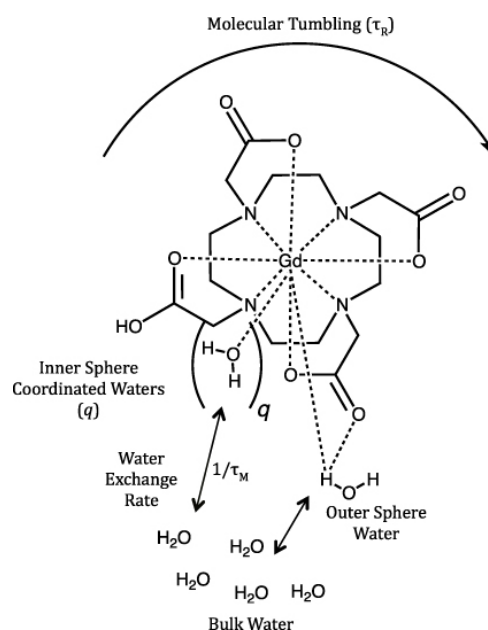
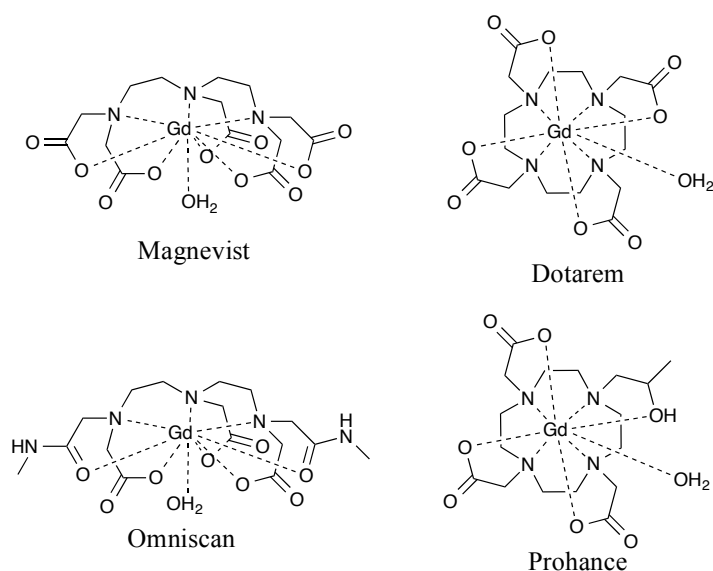


Figure 3.5 Graphical depiction of the factors influencing r_1 relaxation rates.²⁶

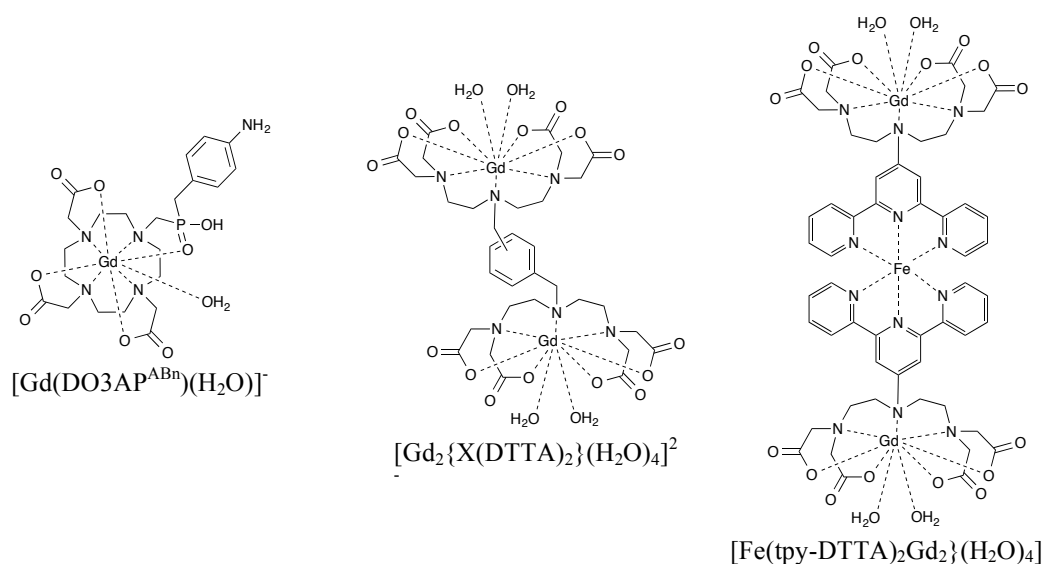
Appreciation of these components is critical in understanding how relaxation occurs and how contrast agents can be developed in order to provide greater image contrast by increasing water exchange rates, reducing tumbling by enhancing the molecular size and weight and increasing inner-sphere coordination.

3.1.5. Contrast agents

Contrast agents are administered intravenously and, as such, must be kinetically inert to prevent leaching of toxic Gd^{III} ions into the body, capable of rapid excretion from the body so as to only be prevalent for the time taken to perform the MRI scan and have good aqueous solubility to stay in solution under physiological conditions. For this reason, most commercial Gd^{III} -based contrast agents are based around polydentate cyclen or diethylenetriamine core structures with pendant coordinative ligands appended (Figure 3.6).

Figure 3.6 Commonly used Gd^{III} contrast agents.

These compounds have shown great utility in a wide number of MRI applications and can be used in high doses without complications (except to those with kidney disease), and are excreted in the urine with half-lives of 1 – 2 h.²³ They have to be used at relatively high concentrations ($> 0.01 \text{ mM}$) in order to obtain high contrast images and, as such, work has focussed on developing contrast agents with a higher sensitivity, thus requiring a lower dose. This can be done by increasing the relaxation rate by fine-tuning the parameters that affect T_1 and T_2 .

Figure 3.7 Structures of compounds with enhanced r_1 values.

Subtle changes in the functionalisation of commercially available contrast agents have been shown to be effective in increasing r_1 through modulating the values for q , τ_{M} and τ_{R} (Figure 3.7).²³ A Gd-DO3A-like complex, $[\text{Gd}(\text{DO3AP}^{\text{ABn}})]^-$, developed by

Rudovský *et al.* was found to have a much shorter water residency time, with a value for τ_M of just 16 ns (*cf.* 244 ns for $[\text{Gd}(\text{DOTA})(\text{H}_2\text{O})]^-$) due to the incorporation of a bulky phosphinate group creating steric crowding and creating a favourable arrangement of second-sphere water molecules.²⁷ Costa *et al.* developed several complexes where q was found to be 2, which all exhibited enhanced r_1 values compared to compounds where $q = 1$, such as Magnevist.²⁸ For $[\text{Gd}_2\{\text{X}(\text{dtta})_2\}(\text{H}_2\text{O})_4]^{2-}$ r_1 values $>11 \text{ mM}^{-1} \text{ s}^{-1}$ (20 MHz, 37 °C) were observed (*cf.* $4.0 \text{ mM}^{-1} \text{ s}^{-1}$ for Magnevist),²⁹ which were thought to be a result of an increase in q and, because of the increased molecular size and weight and the rigid linker, an increase in the rotational correlation time, τ_R .²⁸ Another paper by Costa outlined the development of a dimetallic complex where two Gd-DTTA groups were linked by a $[\text{Fe}(\text{tpy})_2]$ complex to give $[\text{Fe}(\text{tpy-DTTA})_2\text{Gd}_2\{\text{H}_2\text{O}\}_4]$.³⁰ They found that the increased size and rigidity of the molecule resulted in an r_1 value of $15.7 \text{ mM}^{-1} \text{ s}^{-1}$ (20 MHz, 37 °C), even greater than that found for $[\text{Gd}_2\{\text{X}(\text{DTTA})_2\}(\text{H}_2\text{O})_4]^{2-}$.

3.1.6. Photophysical properties of lanthanides

Ln^{III} ions display low molar absorption coefficients (where $\epsilon < 10 \text{ dm}^3 \text{ mol}^{-1} \text{ cm}^{-1}$) due to the Laporte forbidden nature of f - f transitions resulting in very weak emission upon direct excitation of lanthanide ions. The nature of the emission (UV/visible/near-IR and fluorescent/phosphorescent/both) varies depending upon the lanthanide ion.³¹

In order to combat the inherently weak absorption and, as a result, emission, it is possible to sensitise the lanthanide ion by introducing it into an organic matrix, which acts efficiently as a light harvester. This energy is transferred from the matrix, the ‘antenna’, to the metal ion which then emits from the excited Ln^{III} state.³² This results in large pseudo-Stokes’ shifts, where the excitation profile is completely independent of the Ln^{III} ion, making these compounds ideal candidates for biological imaging as the emission can be easily differentiated from autofluorescent biological systems. Intersystem crossing from the excited singlet (S_1) state results in an excited triplet (T_1) state, which is facilitated by spin-orbit coupling before energy transfer processes, such as Dexter- or Forster-type transfer, result in population of the excited state $4f$ orbitals, which relax to the ground state, resulting in emission (Figure 3.8).

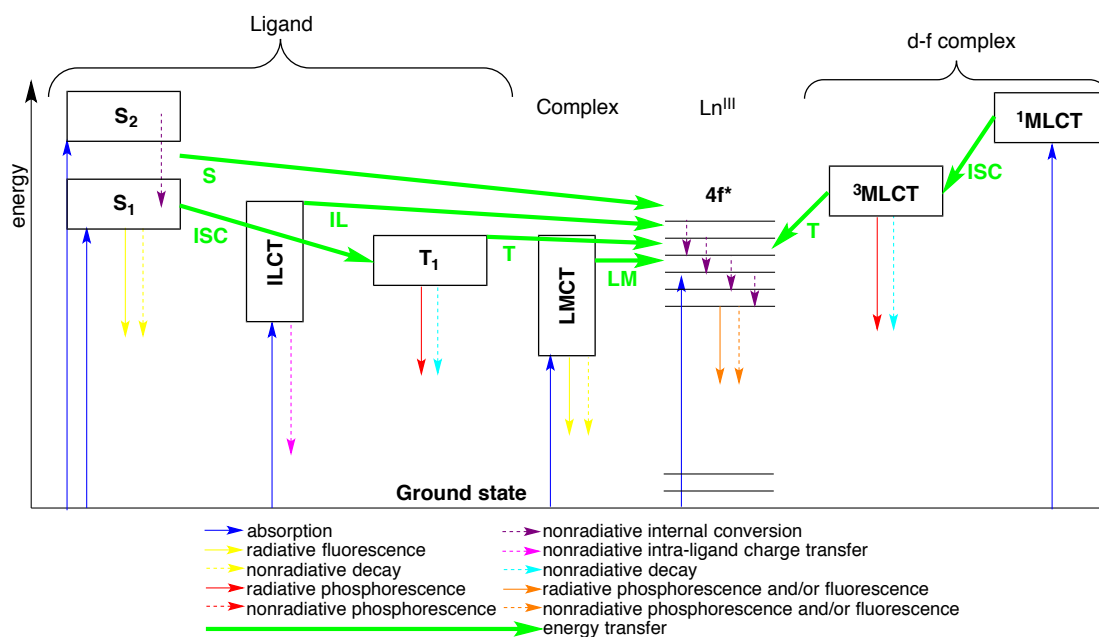


Figure 3.8 Schematic representation of the energy pathways within organically and inorganically sensitised lanthanide(III) complexes. S_n = excited singlet state, ILCT = intra-ligand charge transfer, T₁ = excited triplet state, LMCT = ligand-to-metal charge transfer, S = singlet energy transfer, ISC = intersystem crossing, IL = intra-ligand energy transfer, LM = ligand-metal energy transfer, 4f* = excited 4f electronic state. Back transfer processes are omitted for clarity.³³

Metal complexes, including those incorporating Pt^{II}, can also be utilised as antennae and often result in more efficient transfer, as emission from metal complexes is often longer-lived and lower energy than emission from organic species due to the spin-orbit coupling-facilitated intersystem crossing to the triplet state (Figure 3.8). This lower energy emission is especially important when trying to sensitise Ln^{III} ions, such as Nd, Yb and Er, which emit in the near-IR region at *ca.* 885, 980 and 1540 nm, respectively. Suitable sensitisers should emit around 750, 820 and 1200 nm for the three Ln^{III} ions in order to facilitate efficient energy transfer, which is too low in energy even for the excited T₁ state of most organic chromophores.

Complexes incorporating Re^I, Ru^{II}, Ir^{III}, Pt^{II}, amongst others, are all reported to be capable of sensitising Ln^{III} emission. A *d-f-d* complex (Re₂-Ln) (Figure 3.9) incorporating two [Re(diimine)(CO)₃Cl] units linked to a Ln-DTPA (DTPA = diethylenetriaminepentacetic acid) core was found to sensitise Nd, Yb and Er. A reduction in the emission of the ³MLCT state is in line with other reports that the sensitisation invokes quenching in the *d*-centred emissive state.³⁴ Similar photophysical properties were found in (Ru-Ln),³⁵ (Ir-Ln) and (Pt-Ln) (Figure 3.9),^{36, 37} where the *d*-centred excited triplet state undergoes energy transfer to Ln^{III}, resulting in emission from the excited *f*-orbitals.

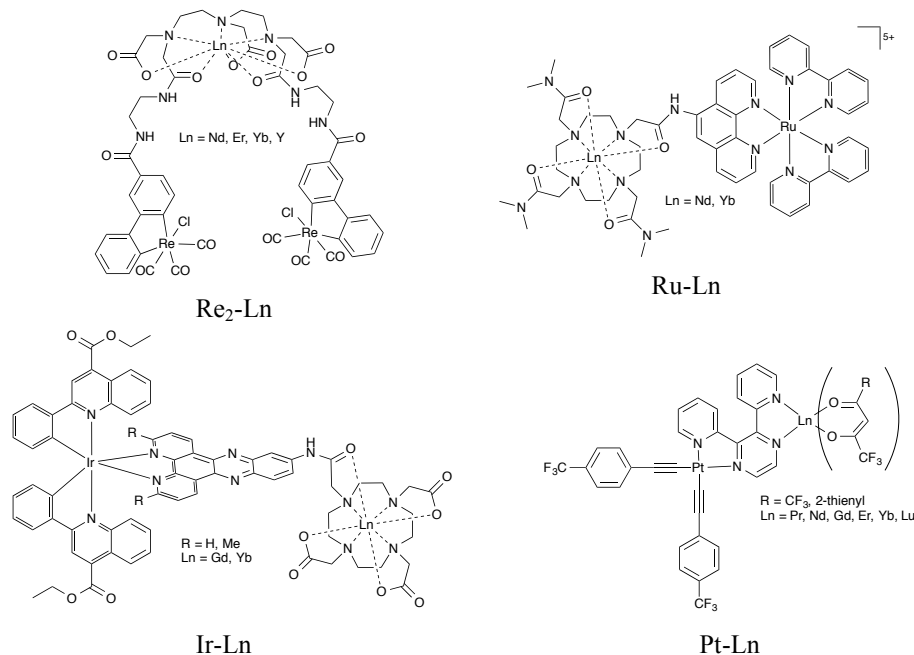


Figure 3.9 Structures of dimetallic complexes incorporating transition metals and a Ln^{III} ions.

3.1.7. Bimodal contrast agents

Given the need for Ln^{III} ions to be sensitised in order to display emissive properties, it seems logical that these compounds could possess bimodal imaging properties, especially if compounds with poly-acid functionalisation are involved as these are, for the most part, water soluble, which is often one of the major problems with many luminescent transition metal complexes. Jones *et al.* developed a water soluble Ir^{III}-Gd^{III} complex (Figure 3.9), whose structure shows promise as a contrast agent given the increased size by the introduction of a cyclometallated Ir^{III} core and the rigid nature of the diimine linker.³⁶ Despite this, relaxivity measurements were not carried out however, from an imaging perspective, the complex showed broad emission *ca.* 600 nm, making it possible to utilise the complex for cellular imaging.

Other research has focused on utilising an organic sensitizer with a metal binding site to detect metal ions, whilst incorporating a Gd^{III} ion to invoke greater relaxivity of water molecules in order to create more dynamic MR images. Jang *et al.* developed a complex (Figure 3.10), which shows enhanced MRI relaxivity and a diminished optical signal in the presence of Cu^{II} ions.³⁸ A cyclodextrin-based bimodal fluorescent contrast agent (Figure 3.10) has also been developed that shows excellent promise towards *T*₁ weighted MRI with *r*₁ values in excess of 20 mM⁻¹ s⁻¹ (20 MHz, 25 °C).

Cell imaging of mesenchymal stem cells also showed that the compound localised in intracellular spaces for long periods of time.³⁹

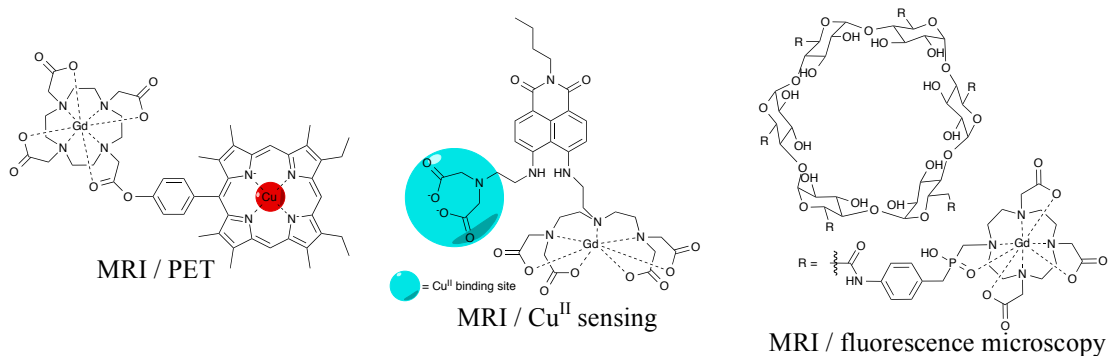


Figure 3.10 Three functionalised MRI contrast agents exhibiting bimodal properties.

As well as bimodal imaging with fluorescence and MRI contrast agents, there are also examples of bimodal medical imaging compounds that incorporate MRI with positron emission tomography (PET) imaging. Gros *et al.* linked a DO3A-Gd complex with a porphyrin moiety incorporating a ‘hot’ ^{64}Cu atom, a positron-emitting tracer for PET scans.⁴⁰ Incorporating the imaging agents for both techniques into one molecule would allow for successive scans using just one drug, which could reduce waiting times and costs to healthcare services.

3.2. Aims

Chapter 3 outlines the development of tuning the solubility of 2-phenylquinoline ligands in order to obtain Pt^{II} complexes that might show solubility in aqueous media and possess suitable amphoteric nature to be granted access inside cells by the lipophilic membranes. The synthesis of a series of alkyl-functionalised ligands is discussed as well as the problems associated coordinating the highly lipophilic ligands under aqueous conditions.

The development of more hydrophilic ligands is also discussed, along with the coordination to Pt^{II} to form a versatile $[\text{Pt}(\text{L})(\text{DMSO})\text{Cl}]$ with sufficient hydrophilic nature to perform subsequent chemistry in aqueous media for various applications. To exploit the chemistry, a pendant pyridine-appended DO3A analogue was synthesised in order to bind an encapsulated Ln^{III} ion to $[\text{Pt}(\text{L})(\text{DMSO})\text{Cl}]$ to give $[\text{Pt}(\text{L})(\text{L}'\text{-Gd})\text{Cl}]$ so that the Pt-based emissive state might act as an antenna to generate an electronically excited Ln^{III} ion.

3.3. Results and Discussion

3.3.1. Development and synthesis of 2-phenylquinoline ligand functionalisation

Given the facile coordination of functionalised 2-phenylquinolines to Pt^{II} , described in Chapter 2, and the interest towards the coordination of $[\text{Pt}(\text{ppy})(\text{DMSO})\text{Cl}]$ to amyloid- β peptide, the ligand functionalisation was focussed on developing suitable characteristics for biological application, including solubility.

Initially, investigations were based on increasing the amphoteric nature due to increased diffusion of more greasy compounds across cell membranes. To this end, 2-phenyl-4-quinolinecarboxylic acyl chloride was reacted with a series of n-alkyl amines, with C_8 , C_{12} and C_{16} chains, to give **LH5**, **LH6** and **LH7** (Figure 3.11), respectively. They were all prepared following the methodology outlined in Chapter 2 for the related amide-functionalised ligands. **LH5** is known and had previously been coordinated to Ir^{III} by Routledge *et al.* **LH6** and **LH7** are unreported and, as such, were fully characterised.

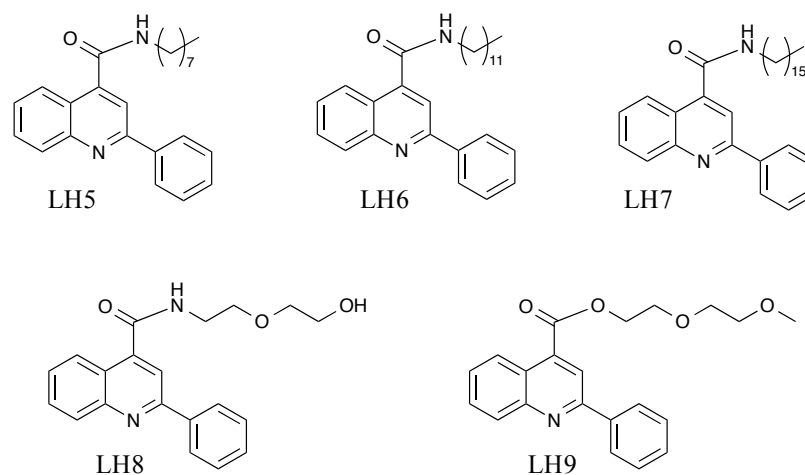


Figure 3.11 Structures of ligands **LH5** to **LH9**.

The need for high water solubility is also crucial if the interaction of the Pt^{II} complexes with peptides and DNA is to be investigated. For this reason, a polyethyleneglycol (PEG) derived reagent was used to functionalise the ligand to increase the water solubility. It is known that esters are not particularly stable to excessively high or low pHs, or to high temperatures so 2-(2-aminoethoxy)ethanol was used to form the corresponding amide upon reaction with the acyl chloride to give **LH8** (Figure 3.11), which was synthesised in the same way as the other amides and was fully characterised. Problems were encountered with the stability of the

complexes of **L8**, which were thought to be due to the primary alcohol and its intermolecular interaction with the Pt^{II} . To combat this, diethylene glycol monomethyl ether was used to synthesise the corresponding ester; despite esters' relatively low stability, the ester was thought to be stable enough to tolerate the conditions it would be exposed to. The ester, **LH9** (Figure 3.11), was synthesised following the same technique used for the synthesis of the amides but, instead, using an excess of the alcohol, which could be extracted into the aqueous phase during the workup.

3.3.2. Synthesis and characterisation of platinum (II) complexes

The complexes were all synthesised in the same manner as those in Chapter 2. The solubility of the ligands started to pose issues in the synthesis of the μ -dichloro-bridged dimers for **LH6** and **LH7** due to the added hydrophobicity of the longer alkyl chains in the aqueous reaction mixture. In order to combat this, extra 2-ethoxyethanol could be added to try to encourage greater solubility of the ligands. Despite this, the yields were lower for the dimer of **L7** than for those of **L5** and **L6**. Unreacted ligand was removed by washing the crude product with dichloromethane. The subsequent reactions to form $[\text{Pt}(\text{L})(\text{DMSO})\text{Cl}]$ complexes of **L5** – **L7** were successful and the compounds were obtained in high spectroscopic purity. The insolubility in aqueous media rendered the compounds unsuitable for investigations with peptides or DNA so the subsequent reactions with 2,4-pentanediketonate and 8-hydroxyquinoline were carried out based on the methods used in Chapter 2.

There were complications with the complexes of **L8**, as mentioned, presumed to be from the intermolecular interactions between the hydroxyl group and Pt^{II} metal centre in the presence of the labile DMSO ligand. Despite attempts to synthesise $[\text{Pt}(\text{L8})(\text{acac})]$ from the dimer, avoiding the DMSO precursor, the compound was still unobtainable so efforts were focussed on the altered PEG-type ligand, **L9**. This compound was purified through removal of an unknown brown impurity by precipitating it from dichloromethane with diethyl ether. The product was then triturated with diethyl ether to give the pure $[\text{Pt}(\text{L9})(\text{DMSO})\text{Cl}]$ as an orange solid.

Unfortunately, despite the more hydrophilic PEG-type functionalisation, $[\text{Pt}(\text{L9})(\text{DMSO})\text{Cl}]$ was not soluble in water and only soluble in $\text{H}_2\text{O}/\text{DMSO}$ (9:1) at

low concentrations (50 μM) for short periods of time. Due to the synthetic route used to obtain the complexes, excessively hydrophilic compounds would be unable to be isolated due to the need to precipitate them from solution using aqueous media. Despite this, micromolar concentrations are still useful for analysis by NMR and UV spectroscopies and luminescence so this compound was targeted as being the most likely to show promise in subsequent studies with bioactive compounds. The β -diketonate complex, $[\text{Pt}(\text{L9})(\text{acac})]$ was also formed so that the photophysical characteristics of these classes of compounds could be assessed and compared to related compounds synthesised in Chapter 2.

^{195}Pt NMR spectra of the complexes revealed very similar results to those observed in Chapter 2. Altering the alkyl chain length had very little effect on the electronic distribution at the Pt^{II} centre. The $[\text{Pt}(\text{L})(\text{acac})]$ complexes all showed a shift of around -2775 ppm.

3.3.3. X-ray crystal structures

The bond lengths around the Pt centre for [Pt(**L5**)(acac)] were found to be 1.952(6) and 2.041(5) Å for the Pt-C and Pt-N bonds, respectively, and 2.006(4) and 2.089(4) Å for the Pt-O bond lengths (where the shorter bond is *trans* to the coordinated N atom). These are very similar to the [Pt(**L1**)(acac)] complex and the [Pt(ppy)(acac)] complex recorded by Bossi *et. al.* in 2013.⁴¹ These findings further support those in Chapter 2 that alterations within the ligand have very minor implications on the bond length, especially when comparing the two acac complexes of **L1** and **L5**, where the differences in ligand are very subtle and removed from the immediate coordination sphere. The formation of dyads through Pt-Pt interactions is also evident with a distance between two Pt atoms of around 3.3 Å, almost identical to that found in the analogous complex of **L1** (and therefore also below the sum of van der Waal's radii). As seen with other complexes, there is a head-to-tail packing arrangement within the crystal.

The X-ray crystal structure of [Pt(**L9**)(DMSO)Cl] has a similarly distorted arrangement as was found for [Pt(**L1**)(DMSO)Cl]. The bond lengths of 2.003(3), 2.078(2), 2.4135(7) and 2.2141(8) Å, corresponding to the Pt-C, Pt-N, Pt-Cl and Pt-S bonds, are all very similar to the comparable complex of **L1**. As with the analogous structure, there is a large out of plane twist by both the chloride and the naphthyl moiety; this results in more than a 45° angle between the plane of the quinoline (specifically the carbon atoms in the 5- to 8-positions on the quinoline ring) and the plane of the Pt-Cl bond. This, again, appears to be as a result of the close proximity of the proton's proximity to the chloride. No Pt-Pt contacts are observed, however π - π interactions are still present due to the head-to-tail packing arrangement within in the solid state.

3.3.4. X-ray crystal structure of [Pt(L5)(acac)]

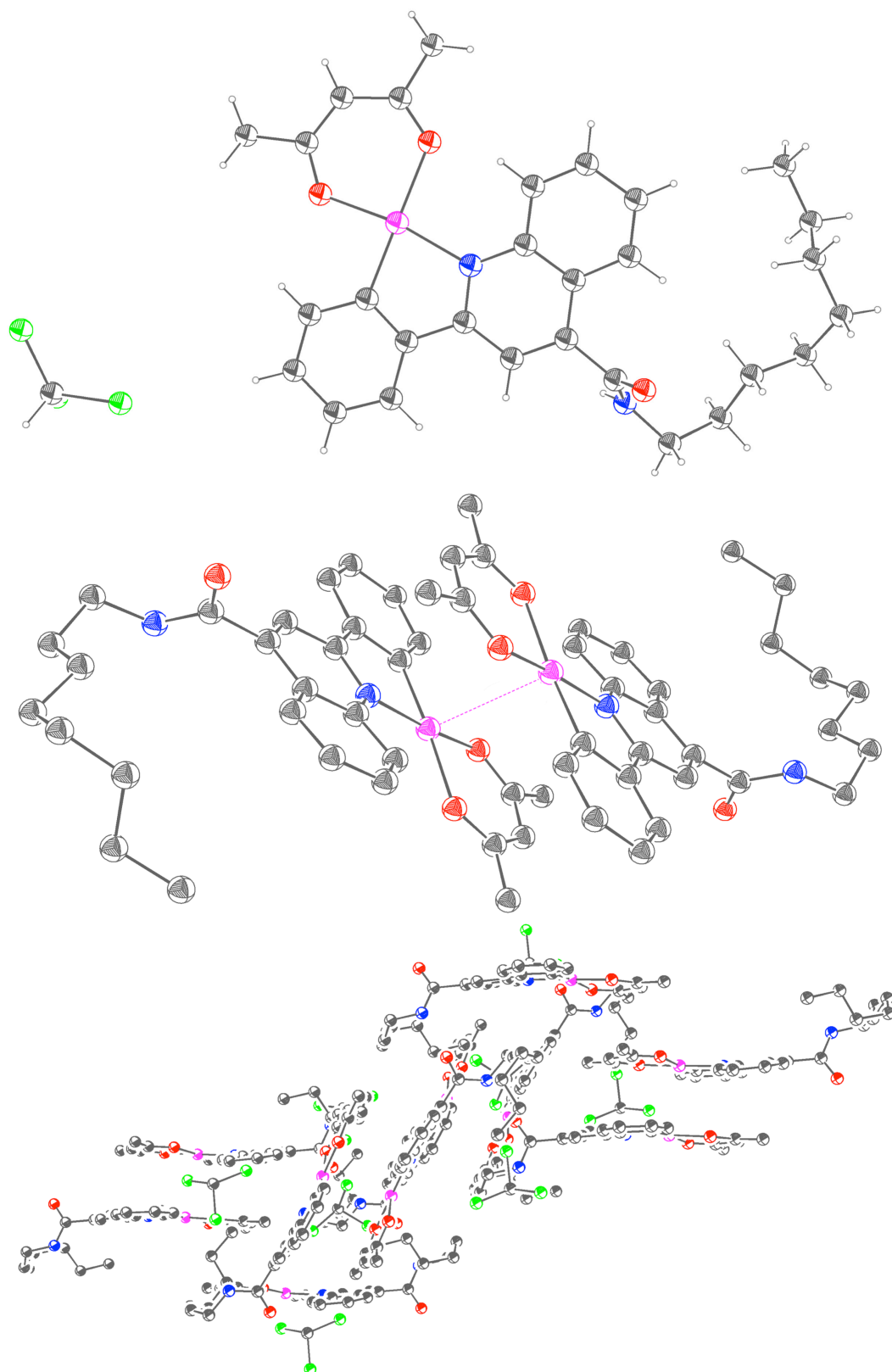


Figure 3.12 Ball and stick X-ray crystal structure of [Pt(L5)(acac)] (*top*), the Pt-Pt interaction (*middle*) and the unit cell packing (*bottom*).

3.3.5. X-ray crystal structure of [Pt(L9)(DMSO)Cl]

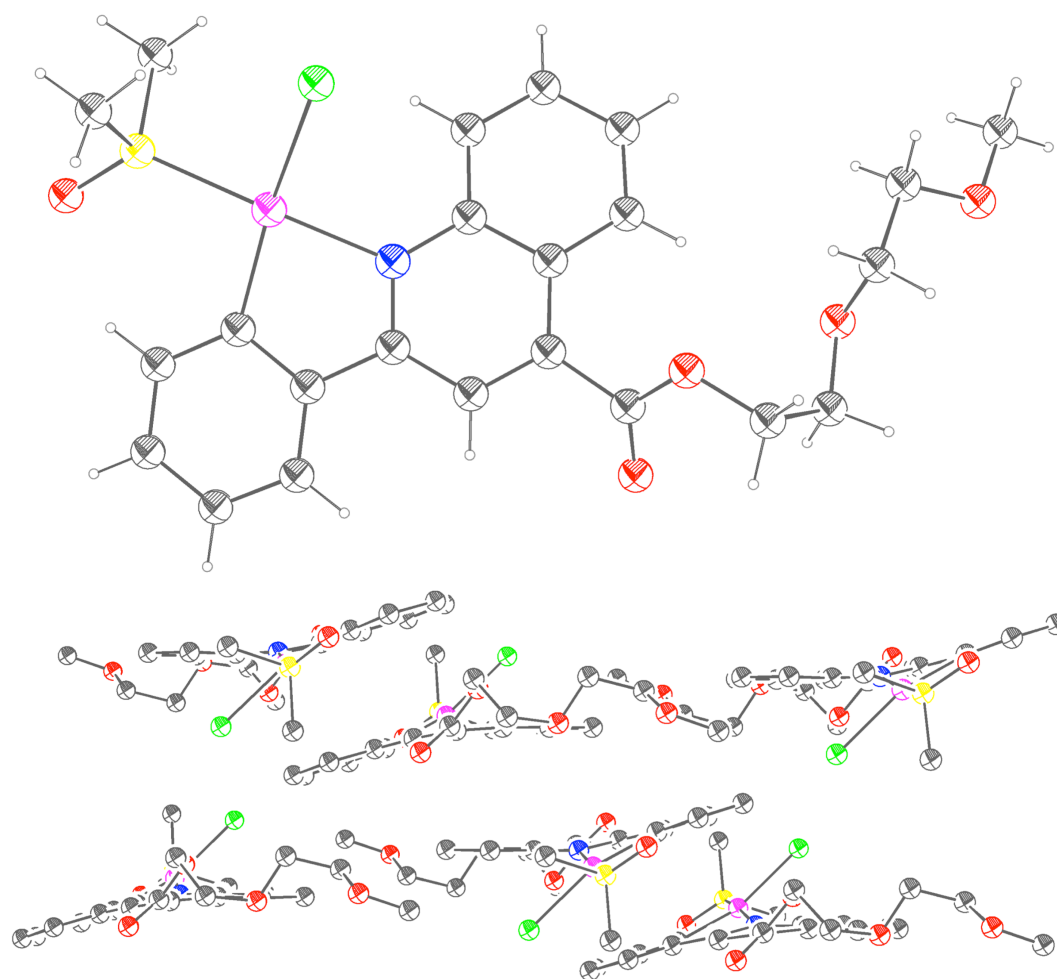


Figure 3.13 Ball and stick X-ray crystal structure of [Pt(L9)(DMSO)Cl] (*top*) and the unit cell packing (*bottom*).

3.3.6. Crystal structure data

	[Pt(L5)(acac)]	[Pt(L9)(DMSO)Cl]
Empirical formula	C ₃₀ H ₃₅ Cl ₃ N ₃ O ₃ Pt	C ₂₃ H ₂₆ ClNO ₅ PtS
Formula weight	773.04	659.05
Temperature	120(2) K	100(2) K
Wavelength	0.71075 Å	0.71075 Å
Crystal system	Monoclinic	Triclinic
Space group	<i>P</i> 2 ₁ / <i>n</i>	<i>P</i> -1
Unit cell dimensions	<i>a</i> = 14.0542(10) Å, <i>a</i> = 90° <i>b</i> = 8.3288(5) Å, <i>b</i> = 93.606(2)° <i>c</i> = 25.6474(18) Å, <i>g</i> = 90°	<i>a</i> = 9.5830(7) Å, <i>α</i> = 104.643(4)° <i>b</i> = 9.8654(7) Å, <i>β</i> = 95.718(3)° <i>c</i> = 14.2517(10) Å, <i>γ</i> = 114.866(4)°
Volume	2996.2(3) Å ³	1149.74(15) Å ³
<i>Z</i>	4	2
Density (calculated)	1.714 Mg / m ³	1.904 Mg / m ³
Absorption coefficient	4.985 mm ⁻¹	6.345 mm ⁻¹
<i>F</i> (000)	1528	644
Crystal	Plate; Red	Blade; Dark Orange
Crystal size	0.410 × 0.240 × 0.090 mm ³	0.170 × 0.100 × 0.040 mm ³
θ range for data collection	2.918 - 27.484°	3.035 - 27.485°
Index ranges	-18 ≤ <i>h</i> ≤ 18, -10 ≤ <i>k</i> ≤ 10, -31 ≤ <i>l</i> ≤ 33	-12 ≤ <i>h</i> ≤ 10, -12 ≤ <i>k</i> ≤ 12, -18 ≤ <i>l</i> ≤ 16
Reflections collected	30031	15635
Independent reflections	6837 [<i>R</i> _{int} = 0.1338]	5262 [<i>R</i> _{int} = 0.0403]
Completeness to θ = 25.242°	99.40%	99.80%
Absorption correction	Semi-empirical from equivalents	Semi-empirical from equivalents
Max. and min. transmission	1.000 and 0.397	1.000 and 0.700
Refinement method	Full-matrix least-squares on <i>F</i> ²	Full-matrix least-squares on <i>F</i> ²
Data / restraints / parameters	6837 / 0 / 355	5262 / 0 / 292
Goodness-of-fit on <i>F</i> ²	0.802	1.061
Final <i>R</i> indices [<i>F</i> ² > 2σ(<i>F</i> ²)]	<i>R</i> = 0.0448, <i>wR</i> 2 = 0.0784	<i>R</i> = 0.0237, <i>wR</i> 2 = 0.0619
<i>R</i> indices (all data)	<i>R</i> = 0.0713, <i>wR</i> 2 = 0.0825	<i>R</i> = 0.0245, <i>wR</i> 2 = 0.0623
Extinction coefficient	n/a	n/a
Largest diff. peak and hole	2.068 and -3.427 e Å ⁻³	1.529 and -1.257 e Å ⁻³

Table 3.1 Crystal structure data for [Pt(L5)(acac)] and [Pt(L9)(DMSO)Cl].

3.3.7. Photophysical properties of complexes

Compound	$\lambda_{\text{abs}} / \text{nm}$	$\lambda_{\text{em}} / \text{nm}$	τ / ns
[Pt(L5)(DMSO)Cl]	272, 281, 341, 368, 422	609	24
[Pt(L5)(acac)]	300, 349, 368, 417	618	380
[Pt(L5)(8-Q)]	263, 370, 505	606	211
[Pt(L6)(DMSO)Cl]	281, 363, 430	615	54
[Pt(L6)(acac)]	284, 345, 368, 415	617	406
[Pt(L6)(8-Q)]	265, 269, 368, 502	606	238
[Pt(L7)(DMSO)Cl]	365, 284, 265, 426	592	28
[Pt(L7)(acac)]	259, 286, 295, 344, 361, 414	617	439
[Pt(L7)(8-Q)]	283, 346, 362, 429, 496	593	227
[Pt(L9)(DMSO)Cl]	253, 291, 362, 424	625	116
[Pt(L9)(acac)]	253, 300, 365, 431	639	316

^a excited at 372 nm. ^b excited at 459 nm.

Table 3.2 Photophysical properties, in chloroform solutions, of the complexes synthesised in Chapter 3.

The data show similar characteristics to the complexes in Chapter 2; they all exhibit ¹MLCT absorption at *ca.* 420 nm (although some are not defined enough to assign an absorption maxima), emission from the ³MLCT state occurs *ca.* 590 – 640 nm and the lifetimes of the [Pt(**L**)(DMSO)Cl] and [Pt(**L1**)(8-Q)] complexes are notably shorter than the corresponding [Pt(**L**)(acac)] complexes. Of interest is the red-shifted ¹MLCT absorption for the 8-Q complexes, which was not observed to such an extent in the complex for **L1**. There do not appear to be any trends in the photophysical properties as the chain length is extended from C₈ to C₁₂ and C₁₆, except for the apparent increase in lifetimes of 380, 406 and 439, respectively. This could be due to the longer chain's increased ability to reduce the quenching by dissolved oxygen through some means.

3.3.8. Development of a bimodal contrast agent incorporating platinum (II)

3.3.8.1. Macrocyclic ligand synthesis and incorporation of lanthanide (III) ions

The facile coordination reported by Esmaeilbeig *et al.* for appending *N*-heterocycles to [Pt(L)(DMSO)Cl] complexes and the work by Koullourou *et al.* in the development of a DO3A-type macrocycle with a pendant pyridine outlined a simple method for forming a dimetallic complex with bimodal imaging properties.^{42, 43} Despite this, there is only one report of dimetallic Pt^{II}–Ln^{III} complexes being developed for their paramagnetic relaxation properties and, within the patent, there is no information about the relaxivity measurements, including r_1 values.⁴⁴ A handful of papers facilitate Ln^{III} emission through using a Pt antenna but have not investigated their utility as a contrast agent for MRI.^{37, 45-49}

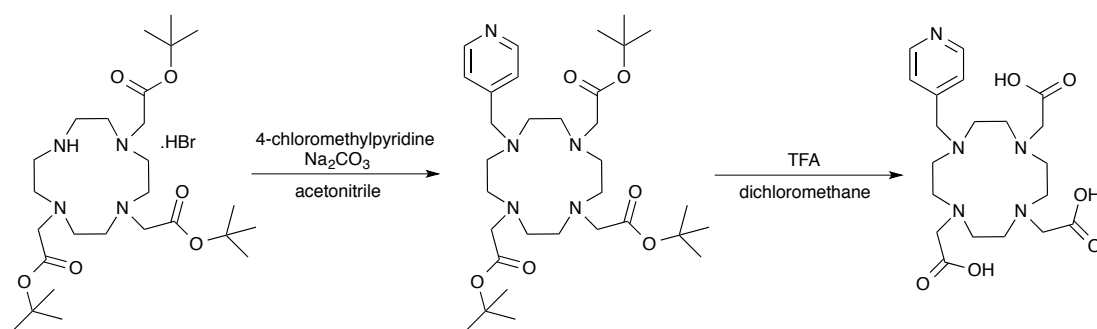


Figure 3.14 Synthetic route for a pyridine functionalised DO3A as used by Koullourou *et al.*⁴³

To this end, attempts were made to resynthesise (Figure 3.14) the ligand outlined by Koullourou *et al.*, which had been coordinated to Re^I as the axial ligand. Strangely, despite various attempts, the reaction of 2-, 3- and 4-chloromethylpyridine, with the triester, were unsuccessful and yielded a dark red solution, which was thought to be due to intermolecular reaction of chloride moiety with the pyridine-*N* to form the cationic pyridonium salt. After numerous failed attempts, a new route was utilised based on the methods of Crich and Andre *et al.* who utilised an ethylene diimine linker to give biologically relevant functionalisation.^{50, 51} The *N*-terminus was alkylated with ethyl bromoacetate to give the ethyl protected ester (Figure 3.15). This was then deprotected *in situ* with ethylene diamine to give the corresponding ethylamine amide. Subsequent reaction with 4-pyridinecarboxaldehyde using a reductive amination and deprotection of the *t*-butyl esters with trifluoroacetic acid (TFA) yielded the target compound (**L10**) in high purity and good yield. The synthesis of precursors (**P1** – **P2**) was confirmed by comparison of ¹H NMR spectra

with the literature. **P3** and **L10** were fully characterised by ^1H and ^{13}C NMR spectroscopies as well as MS.

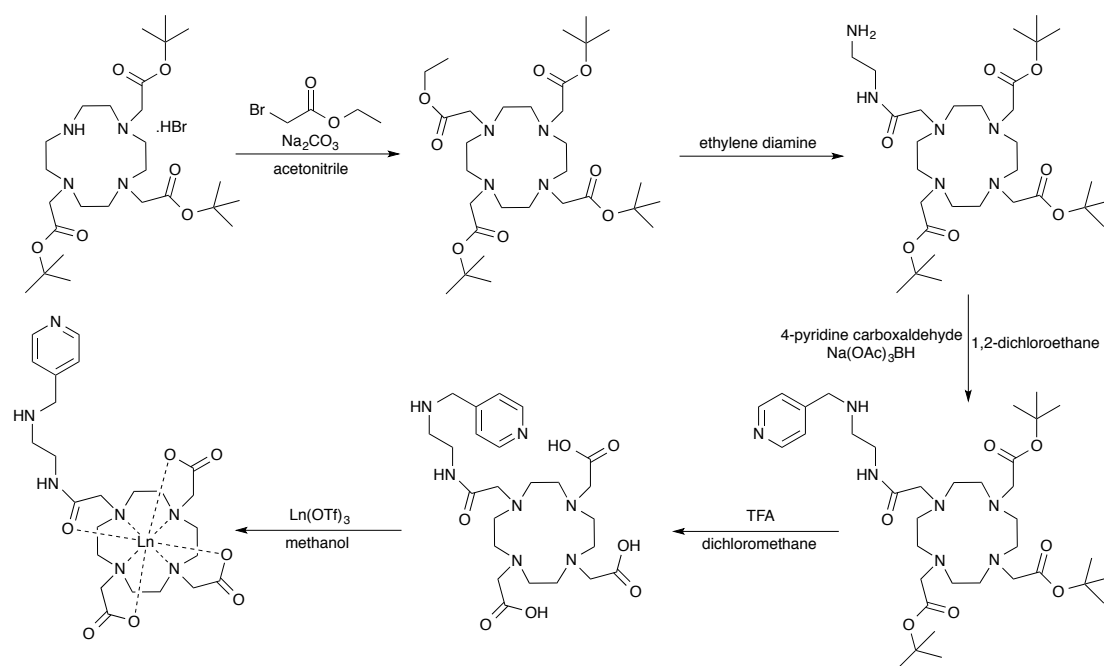


Figure 3.15 Synthetic route to **L10** based on work by Crich and Andre *et al.*^{50, 51}

L10 was then reacted with $\text{Gd}(\text{OTf})_3$ and $\text{Yb}(\text{OTf})_3$ in methanol at 50 °C overnight, cooled and precipitated with diethyl ether to give the $[\text{Gd}(\text{L10})]$ and $[\text{Yb}(\text{L10})]$ complexes as white powders, which were characterised by UV-vis and IR spectroscopy as well as by HR-MS.

3.3.8.2. Synthesis and characterisation of platinum (II) / lanthanide (III) dyads

The two complexes, $[\text{Ln}(\text{L10})]$ and $[\text{Pt}(\text{L9})(\text{DMSO})\text{Cl}]$ were dissolved in a minimum volume of acetone and reacted at 40 °C for 48 h to ensure complete coordination. Diethyl ether was used to precipitate the complexes from acetonitrile, which were filtered and washed with dichloromethane to remove any unreacted Pt^{II} complex. Comparison of $[\text{Pt}(\text{L9})(\text{DMSO})\text{Cl}]$ and $[\text{Pt}(\text{L9})\{\text{Ln}(\text{L10})\}\text{Cl}]$ revealed a shift in the absorption maxima at 253 and 291 nm to 247 and 286 nm, respectively. This slight blue-shift, along with the reduced extinction coefficient of the $^1\text{MLCT}$ absorption, the MS data, IR spectra and the water solubility confirm the successful synthesis of the $\text{Pt}^{\text{II}}\text{--Ln}^{\text{III}}$ complexes, which were obtained as extremely hygroscopic orange powders.

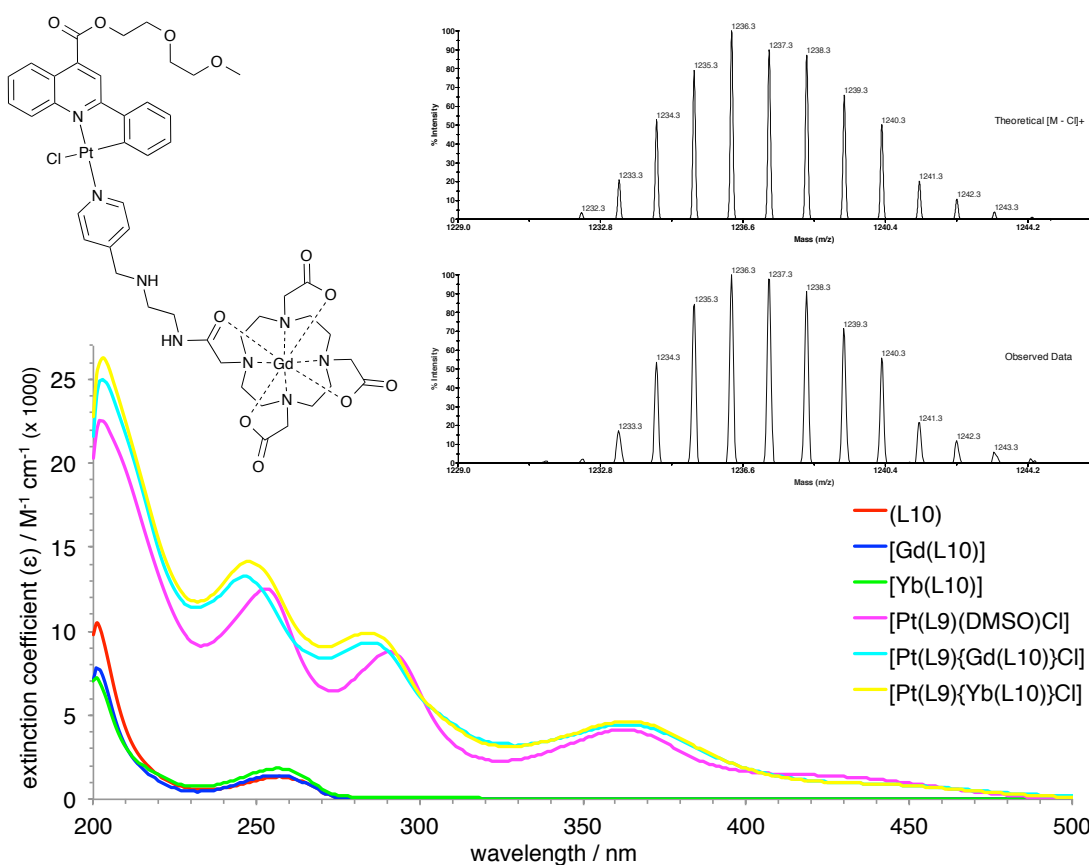


Figure 3.16 Structure (top left) and MALDI-TOF MS spectrum (top right) of [Pt(L9){(L10)Gd}] and the UV-vis spectra of (L10), [Gd(L10)], [Yb(L10)], [Pt(L9)(DMSO)Cl], [Pt(L9){Gd(L10)}Cl] and [Pt(L9){Yb(L10)}Cl] (bottom).

The steady state luminescence of [Pt(L9){Yb(L10)}Cl] displayed dual emission upon excitation at 360 nm comprised of ³MLCT character at *ca.* 630 nm and Yb^{III} radiative decay in the near-IR region around 1000 nm, corresponding to (²F_{5/2} → ²F_{7/2}) transitions sensitised by emission from the Pt^{II} component.

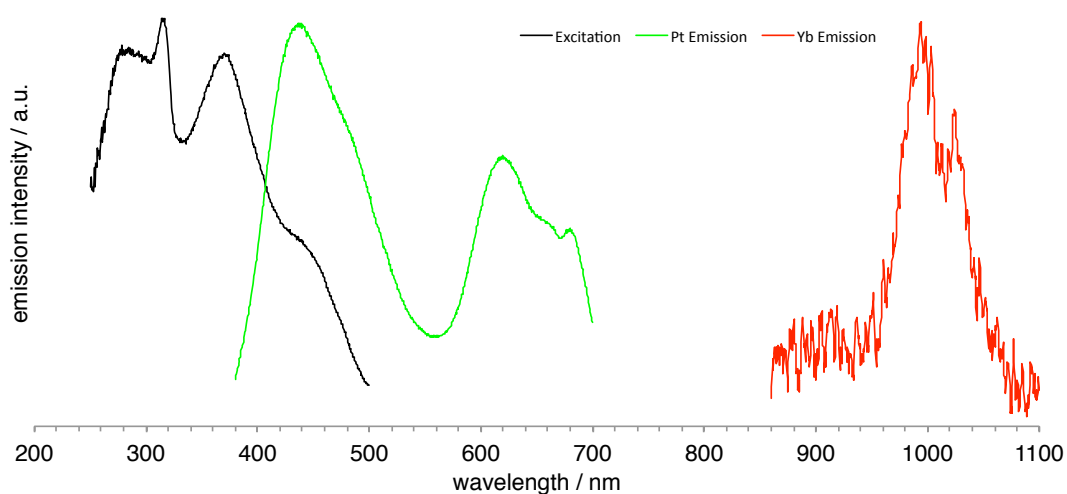


Figure 3.17 Excitation and emission profiles for [Pt(L9){Yb(L10)}Cl] where excitation is in black, ³MLCT emission is in green and ²F_{5/2} → ²F_{7/2} Yb^{III} emission is in red.

The lifetime measurements of the two dimetallic complexes were recorded in order to ascertain values for the Pt \rightarrow Yb energy-transfer rates, k_{ET} , using equation (19), and the inner sphere hydration, q , using equation (20). k_{ET} was calculated by obtaining the lifetime of the donor component ($^3\text{MLCT}$) emission in the quenched system (where Ln is Yb^{III}) and an ‘unquenched’ analogue (where Ln is Gd^{III}). The value for k_{ET} was calculated to be $3 \times 10^6 \text{ s}^{-1}$, which is similar to the rate of $2 \times 10^6 \text{ s}^{-1}$ reported by Ronson *et al.* for a Pt^{II}–Yb^{III} complex.⁴⁶ The rate for the energy transfer is relatively low due to the weak overlap of the tail of the emission profile of the $^3\text{MLCT}$ component and the absorption spectrum of the Yb^{III} acceptor, which has one f - f absorption at around 980 nm.

Compound	λ_{em} / nm	τ / ns	λ_{em} / nm	$\tau (\text{H}_2\text{O}) / \mu\text{s}$	$\tau (\text{D}_2\text{O}) / \mu\text{s}$	q
[Pt(L9){Gd(L10)Cl}]	617	59	-	-	-	-
[Pt(L9){Yb(L10)Cl}]	619	50	<i>ca.</i> 1000	0.90	5.46	0.8

Table 3.3 Photophysical data for the Pt^{II} / Ln^{III} complexes.

q can be calculated by comparing the lifetime of the Yb^{III} emission in H₂O and D₂O due to the inefficient vibronic quenching of the excited state by deuterium oxide compared to water (D₂O is more than 200 times less effective than H₂O).^{52, 53} The data from the lifetime measurements gave a value for q of 0.8, which is consistent for an octadentate Yb^{III} complex, suggesting that the amide carbonyl participates in the coordination to the Ln^{III}, which has also been observed in other lanthanide complexes with mono-amide DO3A analogues.³⁶

$$k_{ET} = \frac{1}{\tau_q} - \frac{1}{\tau_u} \quad (19)$$

$$q = 1\{(k_{\text{H}_2\text{O}} - k_{\text{D}_2\text{O}}) - 0.1\} \quad (20)$$

3.3.8.3. Relaxivity studies of compounds containing gadolinium (III)

^1H nuclear magnetic relaxation dispersion (NMRD) plots were obtained for $[\text{Pt}(\text{L9})\{\text{Gd}(\text{L10})\}\text{Cl}]$ and $[\text{Gd}(\text{L10})]$. The plots (Figure 3.18) illustrate the relationship between the field strength ($1 \times 10^{-2} - 3 \times 10^1$ MHz) and r_1 , the relaxation rate of water *per* mM of complex *per* second.

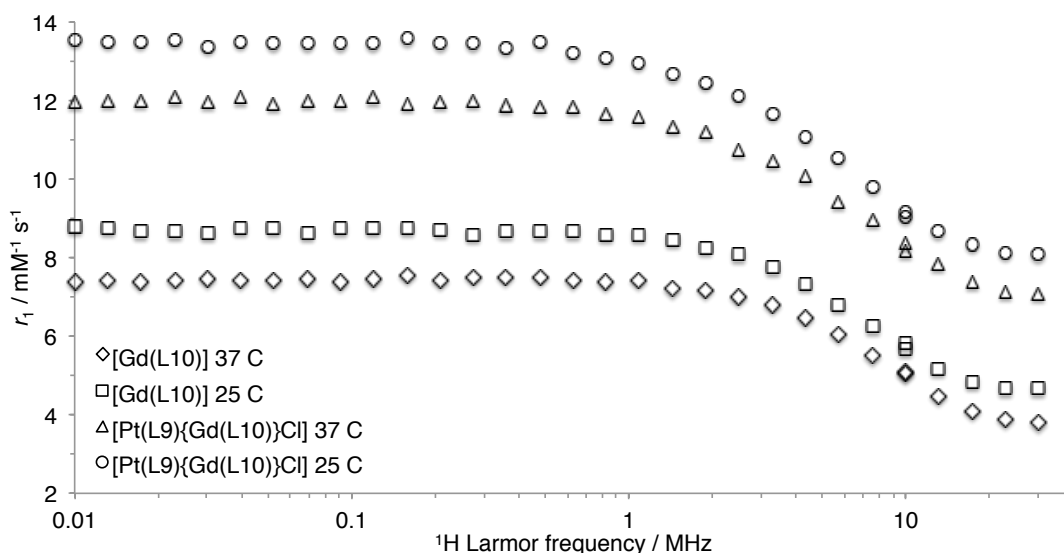


Figure 3.18 Fitted ^1H NMRD plots of $[\text{Gd}(\text{L10})]$ and $[\text{Pt}(\text{L9})\{\text{Gd}(\text{L10})\}\text{Cl}]$.

The relaxivity of $[\text{Gd}(\text{L10})]$ was $3.8 \text{ mM}^{-1} \text{ s}^{-1}$ (30 MHz, 37 °C), which is in accordance with literature values for $[\text{Gd}(\text{DOTA})(\text{H}_2\text{O})]^{-1}$, a commonly used contrast agent (marketed as Dotarem), where r_1 was recorded as $3.8 \text{ mM}^{-1} \text{ s}^{-1}$ (20 MHz, 37 °C).²⁸ Interestingly, the r_1 value for $[\text{Pt}(\text{L9})\{\text{Gd}(\text{L10})\}\text{Cl}]$ was $7.1 \text{ mM}^{-1} \text{ s}^{-1}$ (30 MHz, 37 °C), which shows that, upon formation of the dimetallic species, the r_1 almost doubles; (values for r_1 had an error of $< 2\%$ and results were reproducible within 5% error). This could be due to the increase in the molecular size and weight resulting in a reduced tumbling rate, τ_R , which would lead to an elongated r_1 . The plots also demonstrate the temperature dependence of r_1 in the case of both compounds, with relaxivities at 25 °C approximately 10 – 25% greater at the lower temperature across field strengths between 1×10^{-2} and 3×10^1 MHz.

3.4. Conclusion

Three n-alkyl functionalised phenylquinoline ligands were synthesised with C₈, C₁₂ and C₁₆ chain lengths. The solubility in the solvent system used for coordination was poor for the longer chain ligands so the ratio of 2-ethoxyethanol was increased from 3:1 to 4:1 however, the yield of the C₁₆ dimer was noticeably lower than the complexes of the C₈ and C₁₂ chains due to the insoluble nature of the long chain in aqueous media. In order to increase the hydrophilic nature of the ligand, a PEG-like moiety was introduced however, due to the interaction of the primary alcohol with the Pt^{II} centre, complexes using this ligand were unobtainable. A methyl ether functionalised moiety was introduced in order to combat the proposed problem with the primary alcohol, which led to the successful coordination but the complexes were still found to be poorly soluble in aqueous media. The ligands and complexes were all fully characterised and X-ray crystal structures of [Pt(**L5**)(acac)] and [Pt(**L9**)(DMSO)Cl] were obtained.

[Pt(**L9**)(DMSO)Cl] was reacted with a pendant pyridine-functionalised DO3A ligand (**L10**) containing Gd^{III} and Yb^{III} to form two dimetallic complexes, [Pt(**L9**){Gd(**L10**)}Cl] and [Pt(**L9**){Yb(**L10**)}Cl], which were characterised by UV-vis and IR spectroscopy and MS. The ¹H NMRD data for both Gd^{III} complexes were obtained to give *r*₁ values of 3.8 and 7.1 mM⁻¹ s⁻¹ (30 MHz, 37 °C) for [Gd(**L10**)] and the Gd^{III} / Pt^{II} dyad, respectively.

3.5. Experimental

3.5.1. General physical measurements

All physical measurements were carried out as outlined in Chapter 2.

Relaxivity measurements were recorded on a Stelar Spinmaster FFC-2000 relaxometer, typically covering magnetic fields from 2.3×10^{-4} to 7.1×10^{-1} T (corresponding to a proton Larmor frequency range 1×10^{-2} – 3×10^1 MHz). A Spinmaster Variable Temperature Controller allowed the setting and monitoring of the sample temperature to 25 and 37 °C with a resolution of 0.1 °C. For field strengths less than 10 MHz, a pre-polarising field sequence was used with the sample polarised at 30 MHz before being allowed to relax at the field of interest.

3.5.2. Precursor synthesis

Synthesis of P1: Prepared from literature methodology.⁵⁰ K_2CO_3 (0.788 g, 5.710 mmol) was added to a solution of the HBr salt of tris-1,4,7-*tert*-butoxycarbonylmethyl-1,4,7,10-tetraazacyclododecane (0.500 g, 0.841 mmol) in acetonitrile (7 mL) and the mixture was stirred for 1 h at room temperature under dinitrogen. The suspension was cooled in an ice bath and ethyl bromoacetate (0.157 g, 0.940 mmol) in acetonitrile (3 mL) was added dropwise over 1 h. The reaction was stirred overnight at room temperature before the suspended salts were removed by filtration and the solvent evaporated under reduced pressure. Yield = 0.424 g, (84%). ^1H NMR (400 MHz, CDCl_3): δ_{H} 4.26 – 4.11 (2H, br. m), 3.62 – 1.95 (18H, br. m), 1.77 – 1.67 (2H, br. m), 1.46, 1.45 (27H, s), 1.28 (3H, t, $^3J_{\text{HH}} = 7.2$ Hz) ppm.

Synthesis of P2: Prepared from literature methodology.⁵¹ **P1** (0.410 g, 0.683 mmol) was dissolved in ethylenediamine (3 mL, excess) and stirred under dinitrogen for 72 h. The solvent was removed *in vacuo*. Yield = 0.378 g, (90%). ^1H NMR (400 MHz, CDCl_3): δ_{H} 8.74 (1H, br. m), 3.65 – 1.68 (30H, br. m), 1.45 – 1.42 (27H, m) ppm.

Synthesis of P3: 4-pyridinecarboxaldehyde (0.083 g, 0.779 mmol) was added to a stirring solution of **P2** (0.476 g, 0.779 mmol) in 1,2-dichloroethane (8 mL) and was stirred under dinitrogen. After 16 h, $\text{Na}(\text{OAc})_3\text{BH}$ (0.500 g, excess) was added and the reaction was left stirring for 16 h. NaHCO_3 (sat. soln, 10 mL) was added and the product was extracted with dichloromethane (20 mL). The organic phase was washed

with water (2 x 20 mL) and brine (20 mL) before being dried over MgSO_4 , filtered and dried *in vacuo*. Yield = 0.505 g, (92%). ^1H NMR (400 MHz, CDCl_3): δ_{H} 8.99 (1H, m), 8.47 (2H, d, $^3J_{\text{HH}} = 6.0$ Hz), 7.46 (2H, d, $^3J_{\text{HH}} = 6.0$ Hz), 4.80 – 4.69 (2H, br. m), 3.97 – 3.86 (2H, br. m), 3.67 – 1.87 (27H, br. m), 1.39, 1.36 (27H, s) ppm. $^{13}\text{C}\{^1\text{H}\}$ NMR (125.8 MHz, CDCl_3): δ_{C} 171.3, 171.1, 148.7, 145.6, 123.1, 81.0, 81.0, 55.1, 54.8, 54.7, 50.3, 46.8, 37.1, 27.2, 27.0, 27.0 ppm. MS(ES) found $m/z = 728.45$ for $[\text{M} + \text{Na}]^+$.

3.5.3. Ligand synthesis

Synthesis of LH5: Following the general procedure outlined in Chapter 2 for the synthesis of 2-phenyl-4-quinolinecarboxamides using 2-phenyl-4-quinolinecarboxylic acid (0.465 g, 1.869 mmol) and 1-octylamine (0.219 g, 1.699 mmol). Yield = 0.434 g, (71%). ^1H NMR (400 MHz, CDCl_3): δ_{H} 7.98 (1H, d, $^3J_{\text{HH}} = 8.4$ Hz), 7.94 - 7.91 (2H, m), 7.84 (1H, d, $^3J_{\text{HH}} = 8.0$ Hz), 7.60 – 7.56 (1H, m), 7.51 (1H, s), 7.42 - 7.40 (3H, m), 7.33 – 7.29 (1H, m), 6.93 (1H, br. t, $^3J_{\text{HH}} = 4.4$ Hz), 3.35 - 3.30 (2H, m), 1.59 – 1.52 (2H, m), 1.34 – 1.19 (10H, m), 0.90 (3H, t, $^3J_{\text{HH}} = 6.4$ Hz) ppm.

Synthesis of LH6: Following the general procedure outlined in Chapter 2 for the synthesis of 2-phenyl-4-quinolinecarboxamides using 2-phenyl-4-quinolinecarboxylic acid (0.370 g, 1.486 mmol) and 1-dodecylamine (0.250 g, 1.351 mmol). Yield = 0.416 g, (74%). ^1H NMR (400 MHz, CDCl_3): δ_{H} 8.13 (1H, d, $^3J_{\text{HH}} = 8.0$ Hz), 8.09 – 8.06 (3H, m), 7.77 (1H, s), 7.73 – 7.69 (1H, m), 7.52 – 7.46 (4H, m), 6.37 (1H, br. t, $^3J_{\text{HH}} = 4.4$ Hz), 3.54 – 3.49 (2H, m), 1.71 – 1.63 (2H, m), 1.42 – 1.22 (18H, m), 0.88 (3H, t, $^3J_{\text{HH}} = 6.4$ Hz) ppm.

Synthesis of LH7: Following the general procedure outlined in Chapter 2 for the synthesis of 2-phenyl-4-quinolinecarboxamides using 2-phenyl-4-quinolinecarboxylic acid (0.454 g, 1.826 mmol) and 1-hexadecylamine (0.400 g, 1.660 mmol). Yield = 0.572 g, (73%). ^1H NMR (400 MHz, CDCl_3): δ_{H} 8.12 – 8.04 (4H, m), 7.75 (1H, s), 7.72 – 7.68 (1H, m), 7.51 – 7.45 (4H, m), 6.50 (1H, br. t, $^3J_{\text{HH}} = 4.4$ Hz), 3.52 – 3.46 (2H, m), 1.69 – 1.61 (2H, m), 1.41 – 1.19 (24H, m), 0.87 (3H, t, $^3J_{\text{HH}} = 6.8$ Hz) ppm. $^{13}\text{C}\{^1\text{H}\}$ NMR (75.6 MHz, CDCl_3): δ_{C} 167.6, 156.6, 148.5, 143.3, 138.7, 130.1, 129.9, 129.8, 128.9, 127.6, 127.5, 127.2, 125.1, 123.4, 116.3, 53.5, 40.3, 32.0, 29.8, 29.7, 29.5, 29.1, 27.1, 22.8, 14.2 ppm. MS(ES) found $m/z = 473.34$ for $[\text{M} + \text{H}]^+$.

UV-vis (CHCl_3): λ_{max} ($\epsilon / \text{dm}^3 \text{mol}^{-1} \text{cm}^{-1}$) 257 (76000), 324 (28500) nm. IR (thin film): ν_{max} 3306, 1633, 1531 cm^{-1} .

Synthesis of LH8: Following the general procedure outlined in Chapter 2 for the synthesis of 2-phenyl-4-quinolinecarboxamides using 2-phenyl-4-quinolinecarboxylic acid (0.521 g, 2.095 mmol) and 2-(2-aminoethoxy)ethanol (0.200 g, 1.905 mmol). Yield = 0.416 g, (65%). ^1H NMR (400 MHz, CDCl_3): δ_{H} 8.10 (1H, d, $^3J_{\text{HH}} = 8.8$ Hz), 8.06 – 8.03 (3H, m), 7.76 (1H, s), 7.69 – 7.66 (1H, m), 7.50 – 7.43 (4H, m), 7.14 (1H, br. t, $^3J_{\text{HH}} = 4.4$ Hz), 3.71 – 3.64 (6H, m), 3.56 – 3.54 (2H, m), 2.77 (1H, br. s) ppm. $^{13}\text{C}\{^1\text{H}\}$ NMR (75.6 MHz, CDCl_3): δ_{C} 167.7, 156.6, 148.2, 143.0, 138.4, 130.9, 130.3, 129.9, 129.6, 128.9, 127.5, 127.3, 125.1, 123.4, 72.4, 69.6, 61.7, 39.9 ppm. MS(ES) found $m/z = 359.14$ for $[\text{M} + \text{H}]^+$. UV-vis (CHCl_3): λ_{max} ($\epsilon / \text{dm}^3 \text{mol}^{-1} \text{cm}^{-1}$) 261 (30500), 329 (69900) nm. IR (thin film): ν_{max} 3404, 3273, 1643, 1546 cm^{-1} .

Synthesis of LH9: Following a modified procedure outlined in Chapter 2 for the synthesis of 2-phenyl-4-quinolinecarboxamides using 2-phenyl-4-quinolinecarboxylic acid chloride (0.200 g, 0.748 mmol) and diethylene glycol monomethyl ether (0.135 g, 1.121 mmol). Yield = 0.252 g, (96%). ^1H NMR (400 MHz, CDCl_3): δ_{H} 8.75 (1H, dd, $^3J_{\text{HH}} = 8.4$ Hz, $^4J_{\text{HH}} = 1.2$ Hz), 8.42 (1H, s), 8.24 – 8.19 (3H, m), 7.80 – 7.75 (1H, m), 7.65 – 7.61 (1H, m), 7.57 – 7.48 (3H, m), 4.66 (2H, m), 3.93 (2H, m), 3.74 (2H, m), 3.60 (2H, m), 3.39 (3H, s) ppm. $^{13}\text{C}\{^1\text{H}\}$ NMR (125.8 MHz, CDCl_3): δ_{C} 166.5, 156.8, 149.3, 138.8, 135.9, 130.3, 129.9, 129.7, 128.9, 128.8, 127.8, 127.6, 127.5, 125.5, 124.0, 120.4, 72.0, 70.7, 69.1, 64.8, 59.1 ppm. HR-MS: calcd. for $[\text{C}_{24}\text{H}_{40}\text{N}_7\text{O}_7]^+$ 538.2984, found 538.2974 and calcd. for $[\text{C}_{24}\text{H}_{39}\text{N}_7\text{O}_7]^+$ 560.2803, found 560.2792. UV-vis (CHCl_3): λ_{max} ($\epsilon / \text{dm}^3 \text{mol}^{-1} \text{cm}^{-1}$) 265 (29900), 339 (7680) nm. IR (thin film): ν_{max} 3061, 2876, 1723, 1591, 1549, 1495, 1447, 1343, 1246, 1231, 1194, 1107, 1020, 770, 692 cm^{-1} .

Synthesis of L10: Trifluoroacetic acid (3 mL, excess) was added to a stirring solution of **P3** (0.505 g, 0.717 mmol) in dichloromethane (3 mL). The reaction was stirred for 48 h before the solvent was removed *in vacuo*. The residue was dissolved in a minimal acetonitrile and added, dropwise, to a vigorously stirred vessel of cold diethyl ether (20 mL). The resultant precipitate was filtered under dinitrogen to yield a white solid. Yield = 0.350 g, (91%). ^1H NMR (500 MHz, D_2O): δ_{H} 8.87 (2H, d, $^3J_{\text{HH}} = 7.0$ Hz), 8.21 (2H, br. m), 4.70 (2H, s), 3.97 – 2.88 (28H, br. m) ppm. $^{13}\text{C}\{^1\text{H}\}$

NMR (125.8 MHz, D₂O): δ_C 162.2, 161.9, 150.8, 141.1, 126.7, 116.7, 114.4, 54.2, 48.4, 47.3, 34.6 ppm. HR-MS: calcd. for [C₃₅H₃₇N₂O]⁺ 501.2900, found 501.2889

3.5.4. Synthesis of platinum (II) complexes

Synthesis of [Pt(L5)Cl]₂: Following the general procedure outlined in Chapter 2 for the synthesis of platinum dimers using potassium tetrachloroplatinate (II) (0.057 g, 0.137 mmol) and **LH5** (0.050 g, 0.139 mmol). The precipitate was washed with dichloromethane to remove any unreacted ligand. Yield = 0.070 g, (87%).

Synthesis of [Pt(L6)Cl]₂: Following the general procedure outlined in Chapter 2 for the synthesis of platinum dimers using potassium tetrachloroplatinate (II) (0.050 g, 0.120 mmol) and **LH6** (0.050 g, 0.120 mmol). The solvent ratio was adjusted to 4:1 by using 8 mL of 2-ethoxyethanol. The precipitate was washed with dichloromethane to remove any unreacted ligand. Yield = 0.068 g, (87%).

Synthesis of [Pt(L7)Cl]₂: Following the general procedure outlined in Chapter 2 for the synthesis of platinum dimers using potassium tetrachloroplatinate (II) (0.097 g, 0.233 mmol) and **LH7** (0.100 g, 0.212 mmol). The solvent ratio was adjusted to 4:1 by using 8 mL of 2-ethoxyethanol. The precipitate was washed with dichloromethane to remove any unreacted ligand. Yield = 0.095 g, (64%).

Synthesis of [Pt(L9)Cl]₂: Following the general procedure outlined in Chapter 2 for the synthesis of platinum dimers using potassium tetrachloroplatinate (II) (0.100 g, 0.241 mmol) and **LH9** (0.064 g, 0.182 mmol). Yield = 0.062 g, (59%).

Synthesis of [Pt(L5)(DMSO)Cl]: Following the general procedure outlined in Chapter 2 for splitting platinum dimers using [Pt(L5)Cl]₂ (0.070 g, 0.059 mmol). Yield = 0.044 g (55 %). ¹H NMR (400 MHz, CDCl₃): δ_H 8.95 (1H, d, ³J_{HH} = 8.8 Hz), 8.29 – 8.27 (1H, m (with satellites)), 7.94 (1H, d, ³J_{HH} = 8.0 Hz), 7.75 (1H, s), 7.71 – 7.47 (1H, m), 7.58 – 7.56 (1H, m), 7.51 – 7.47 (1H, d), 7.21 – 7.19 (2H, m), 6.51 (1H, br. t, ³J_{HH} = 5.6 Hz), 3.60 (6H, s (with satellites), 3.55 – 3.50 (2H, m), 1.72–1.65 (2H, m), 1.43 – 1.25 (10H, m), 0.89 (3H, t, ³J_{HH} = 7.2 Hz) ppm. ¹³C{¹H} NMR (75.6 MHz, CDCl₃): δ_C 166.7, 166.2, 147.1, 146.7, 145.6, 142.8, 133.7, 130.8, 130.0, 128.6, 127.9, 126.1, 125.5, 124.8, 124.5, 114.3, 46.2, 41.0, 40.4, 31.9, 29.6, 29.3, 27.1, 22.7, 14.2 ppm. ¹⁹⁵Pt NMR (107.51 MHz, CDCl₃): δ_{Pt} -2672 ppm. MS(ES) found m/z =

306.18 for $[M + Cl - DMSO + MeOH + MeOH]^-$. UV-vis ($CHCl_3$): λ_{max} ($\epsilon / dm^3 mol^{-1} cm^{-1}$) 272 (1844), 281 (1698), 368 (419), nm. IR (thin film): ν_{max} 3281, 1647 cm^{-1} .

Synthesis of $[Pt(L6)(DMSO)Cl]$: Following the general procedure outlined in Chapter 2 for splitting platinum dimers using $[Pt(L6)(Cl)]_2$ (0.068 g, 0.026 mmol). Yield = 0.035 g, (93%). 1H NMR (400 MHz, $CDCl_3$): δ_H 8.92 (1H, d, $^3J_{HH} = 8.8$ Hz), 8.28 – 8.25 (1H, m), 7.91 (1H, d, $^3J_{HH} = 8.0$ Hz), 7.70 (1H, s), 7.68 – 7.64 (1H, m), 7.55 – 7.53 (1H, m), 7.47 – 7.43 (1H, m), 7.19 – 7.17 (2H, m), 6.66 (1H, br. t, $^3J_{HH} = 5.6$ Hz), 3.59 (6H, s (with satellites)), 3.52 – 3.47 (2H, m), 1.71 – 1.64 (2H, m), 1.43 – 1.22 (18H, m), 0.87 (3H, t, 6.8 Hz) ppm. $^{13}C\{^1H\}$ NMR (75.6 MHz, $CDCl_3$): δ_C 207.1, 166.6, 166.1, 147.0, 146.6, 145.6, 142.5, 129.9, 128.5, 127.8, 126.1, 125.4, 124.8, 114.2, 53.5, 46.2, 41.0, 40.3, 31.0, 29.7, 29.6, 29.6, 29.4, 29.3, 14.2 ppm. MS(ES) found $m/z = 683.3$ for $[M - DMSO - Cl + MeCN + MeOH]^+$. UV-vis ($CHCl_3$): λ_{max} ($\epsilon / dm^3 mol^{-1} cm^{-1}$) 281 (2000), 363 (548) nm. IR (thin film): ν_{max} 3283, 1645, 1543 cm^{-1} .

Synthesis of $[Pt(L7)(DMSO)Cl]$: Following the general procedure outlined in Chapter 2 for splitting platinum dimers using $[Pt(L7)Cl]_2$ (0.095 g, 0.068 mmol). Yield = 0.071 g, (67%). 1H NMR (400 MHz, $CDCl_3$): δ_H 8.91 (1H, d, $^3J_{HH} = 8.8$ Hz), 8.27 – 8.25 (1H, m), 7.91 (1H, d, $^3J_{HH} = 8.4$ Hz), 7.71 (1H, s), 7.68 – 7.64 (1H, m), 7.55 – 7.53 (1H, m), 7.47 – 7.43 (1H, m), 7.19 – 7.17 (2H, m), 6.90 (1H, br. t, $^3J_{HH} = 6.0$ Hz), 3.58 (6H, s (with satellites)), 3.51 – 3.46 (2H, m), 1.70 – 1.63 (2H, m), 1.42 – 1.18 (26H, m), 0.86 (3H, t, $^3J_{HH} = 6.8$ Hz) ppm. MS(ES) found $m/z = 739.4$ for $[M - DMSO - Cl + MeCN + MeOH]^-$. UV-vis ($CHCl_3$): λ_{max} ($\epsilon / dm^3 mol^{-1} cm^{-1}$) 265 (1013), 284 (964), 365 (446) nm. IR (thin film): ν_{max} 3283, 1639, 1543 cm^{-1} .

Synthesis of $[Pt(L9)(DMSO)Cl]$: Following the general procedure outlined in Chapter 2 for splitting platinum dimers using $[Pt(L9)Cl]_2$ (0.062 g, 0.053 mmol). The dark brown compound was purified by dissolving in a minimum volume of dichloromethane and precipitating dark brown impurities by slow addition of diethyl ether. The filtrate was then dried and triturated with diethyl ether until the sticky oil formed a bright orange precipitate. Yield = 0.049 g, (70%). 1H NMR (400 MHz, $CDCl_3$): δ_H 9.06 (1H, d, $^3J_{HH} = 8.8$ Hz), 8.58 (1H, dd, $^3J_{HH} = 8.8$ Hz, $^4J_{HH} = 1.2$ Hz), 8.37 – 8.34 (1H, m), 8.32 (1H, s), 7.78 – 7.73 (1H, m), 7.71 – 7.69 (1H, m), 7.65 – 7.61 (1H, m), 7.29 – 7.26 (2H, m), 4.70 – 4.67 (2H, m), 3.95 – 3.92 (2H, m), 3.76 –

3.74 (2H, m), 3.67 (6H, s (with satellites $^3J_{\text{HPt}} = 21.2$ Hz)), 3.62 – 3.60 (2H, m), 3.41 (3H, s) ppm. $^{13}\text{C}\{^1\text{H}\}$ NMR (125.8 MHz, CDCl_3): δ_{C} 166.5, 165.2, 147.6, 145.6, 143.0, 139.7, 133.8, 130.8, 129.7, 128.5, 128.3, 126.0, 125.4, 125.2, 124.9, 117.7, 72.0, 70.7, 68.9, 65.3, 59.1, 46.2 ppm. ^{195}Pt (107.5 MHz, CDCl_3): δ_{Pt} -3665 ppm. MS(ES) found $m/z = 586.08$ for $[\text{M} - \text{SO}(\text{CH}_3)_2 - \text{Cl} + \text{CH}_3\text{CN}]^+$ and 627.10 for $[\text{M} - \text{SO}(\text{CH}_3)_2 - \text{Cl} + 2\text{CH}_3\text{CN}]^+$. HR-MS: calcd. for $[\text{C}_{25}\text{H}_{26}\text{N}_3\text{O}_4^{194}\text{Pt}]^+$ 626.1550, found 626.1567. UV-vis (CHCl_3): λ_{max} ($\epsilon / \text{dm}^3 \text{mol}^{-1} \text{cm}^{-1}$) 253, (12500), 291 (8790), 362 (4130), 424 (1410) nm. IR (thin film): ν_{max} 2876, 1728, 1597, 1580, 1545, 1454, 1379, 1294, 1275, 1250, 1198, 1138, 1022, 766, 731 cm^{-1} .

Synthesis of [Pt(L5)(acac)]: Following the general procedure outlined in Chapter 2 for coordinating β -diketonates to platinum complexes using $[\text{Pt}(\text{L5})(\text{DMSO})\text{Cl}]$ (0.044 g, 0.066 mmol) and sodium acetylacetonate monohydrate (0.080 g, 0.660 mmol). Obtained as a dark yellow solid. Yield = 0.038 g, (89%). ^1H NMR (400 MHz, CDCl_3): δ_{H} 9.43 (1H, d, $^3J_{\text{HH}} = 8.8$ Hz), 8.00 (1H, dd, $^3J_{\text{HH}} = 8.4$ Hz, $^4J_{\text{HH}} = 1.2$ Hz), 7.70 – 7.64 (2H, m), 7.57 (1H, s), 7.51 – 7.47 (1H, m), 7.33 (1H, dd, $^3J_{\text{HH}} = 8.0$ Hz, $^4J_{\text{HH}} = 1.2$ Hz), 7.17 – 7.13 (1H, m), 7.02 – 6.98 (1H, m), 6.66 (1H, br. t, $^3J_{\text{HH}} = 6.0$ Hz), 5.57 (1H, s), 3.55 – 3.50 (2H, m), 2.04 (3H, s), 2.03 (3H, s), 1.75 – 1.67 (2H, m), 1.45 – 1.28 (10H, m), 0.91 (3H, t, $^3J_{\text{HH}} = 6.8$ Hz) ppm. $^{13}\text{C}\{^1\text{H}\}$ NMR (75.6 MHz, CDCl_3): δ_{C} 185.7, 184.0, 169.3, 166.8, 149.4, 145.7, 144.7, 139.8, 131.0, 129.7, 129.6, 127.1, 126.5, 125.2, 125.1, 124.5, 124.0, 114.2, 101.9, 40.3, 31.9, 29.8, 29.4, 28.5, 27.3, 27.2, 22.8, 14.2 ppm. ^{195}Pt NMR (107.51 MHz, CDCl_3): -2776 ppm. MS(ES) found $m/z = 652.2$ for $[\text{M} - \text{H}]^-$. UV-vis (CHCl_3): λ_{max} ($\epsilon / \text{dm}^3 \text{mol}^{-1} \text{cm}^{-1}$) 300 (9920), 349 (2810), 368 (3126), 423 (2420) nm. IR (thin film): ν_{max} 3268, 1738, 1643, 1582 cm^{-1} .

Synthesis of [Pt(L6)(acac)]: Following the general procedure outlined in Chapter 2 for coordinating β -diketonates to platinum complexes using $[\text{Pt}(\text{L6})(\text{DMSO})\text{Cl}]$ (0.035 g, 0.048 mmol) and sodium acetylacetonate monohydrate (0.059 g, 0.484 mmol). Obtained as a dark yellow solid. Yield = 0.031 g, (90%). ^1H NMR (500 MHz, CDCl_3): δ_{H} 9.48 (1H, d, $^3J_{\text{HH}} = 9.0$ Hz), 8.03 (1H, d, $^3J_{\text{HH}} = 8.0$ Hz), 7.72 – 7.67 (2H, m), 7.63 (1H, s), 7.53 – 7.50 (1H, m), 7.40 – 7.38 (1H, d, $^3J_{\text{HH}} = 7.5$ Hz), 7.19 – 7.16 (1H, m), 7.05 – 7.02 (1H, m), 6.48 (1H, br. t, $^3J_{\text{HH}} = 6.0$ Hz), 5.57 (1H, s), 3.56 – 3.52 (2H, m), 2.04 (3H, s), 2.03 (3H, s), 1.73 – 1.67 (2H, m), 1.35 – 1.22 (18H, m), 0.83 –

0.89 (3H, t, $^3J_{\text{HH}} = 7.5$ Hz) ppm. $^{13}\text{C}\{^1\text{H}\}$ NMR (75.6 MHz, CDCl_3): δ_{C} 185.7, 184.1, 169.5, 166.8, 149.5, 145.7, 144.7, 139.9, 131.1, 129.8, 129.6, 127.2, 126.6, 125.2, 125.1, 124.5, 124.0, 114.2, 101.9, 40.4, 32.0, 29.7, 29.4, 28.5, 27.3, 27.2, 22.8, 14.2 ppm. ^{195}Pt NMR (107.51 MHz, CDCl_3): -2779 ppm. MS(ES) found $m/z = 708.46$ for $[\text{M} - \text{H}]^-$. UV-vis (CHCl_3): λ_{max} ($\epsilon / \text{dm}^3 \text{mol}^{-1} \text{cm}^{-1}$) 284 (418), 368 (291) nm. IR (thin film): ν_{max} 3306, 1668, 1523 cm^{-1} .

Synthesis of [Pt(L7)(acac)]: Following the general procedure outlined in Chapter 2 for coordinating β -diketonates to platinum complexes using $[\text{Pt}(\text{L7})(\text{DMSO})\text{Cl}]$ (0.071 g, 0.091 mmol) and sodium acetylacetonate monohydrate (0.111 g, 0.911 mmol). Yield = 0.034 g, (49%). ^1H NMR (400 MHz, CDCl_3): δ_{H} 9.53 (1H, d, $^3J_{\text{HH}} = 8.8$ Hz), 8.07 (1H, d, $^3J_{\text{HH}} = 8.4$ Hz), 7.77 – 7.70 (3H, m), 7.57 – 7.53 (1H, m), 7.47 (1H, dd, $^3J_{\text{HH}} = 7.2$ Hz, $^4J_{\text{HH}} = 1.2$ Hz), 7.24 – 7.20 (1H, m), 7.12 – 7.08 (1H, m), 6.29 (1H, br. t, $^3J_{\text{HH}} = 5.6$ Hz), 5.58 (1H, s), 3.59 – 3.54 (2H, m), 2.05 (3H, s), 2.04 (3H, s), 1.74 – 1.67 (2H, m), 1.46 – 1.24 (26H, m), 0.88 (3H, t, $^3J_{\text{HH}} = 7.2$ Hz) ppm. MS(ES) found $m/z = 764.4$ for $[\text{M} - \text{H}]^-$. UV-vis (CHCl_3): λ_{max} ($\epsilon / \text{dm}^3 \text{mol}^{-1} \text{cm}^{-1}$) 263 (795), 293 (758), 348 (241), 357 (272), 421 (156) nm. IR (thin film): ν_{max} 3300, 1669, 1548 cm^{-1} .

Synthesis of [Pt(L9)(acac)]: Following the general procedure outlined in Chapter 2 for coordinating β -diketonates to platinum complexes using $[\text{Pt}(\text{L9})(\text{DMSO})\text{Cl}]$ (0.049 g, 0.075 mmol) and sodium acetylacetonate monohydrate (0.091 g, 0.748 mmol). Obtained as a dark yellow solid. Yield = 0.042 g, (88%). ^1H NMR (400 MHz, CDCl_3): δ_{H} 9.58 (1H, d, $^3J_{\text{HH}} = 9.2$ Hz), 8.68 (1H, dd, $^3J_{\text{HH}} = 8.4$ Hz, $^4J_{\text{HH}} = 1.6$ Hz), 8.27 (1H, s), 7.81 – 7.75 (2H, m), 7.65 – 7.59 (2H, m), 7.28 – 7.25 (1H, m), 7.20 – 7.16 (1H, m), 5.58 (1H, s), 4.67 – 4.65 (2H, m), 3.95 – 3.92 (2H, m), 3.76 – 3.74 (2H, m), 3.62 – 3.60 (2H, m), 3.40 (3H, s), 2.06 (3H, s), 2.04 (3H, s) ppm. $^{13}\text{C}\{^1\text{H}\}$ NMR (125.8 MHz, CDCl_3): δ_{C} 185.7, 184.2, 169.5, 165.7, 149.9, 145.7, 140.3, 137.3, 130.8, 130.0, 129.7, 127.6, 126.8, 125.4, 125.2, 125.0, 124.0, 118.2, 101.8, 72.0, 70.7, 68.9, 65.1, 59.1, 28.4, 27.2 ppm. ^{195}Pt NMR (107.51 MHz, CDCl_3): δ_{Pt} -2770 ppm. UV-vis (CHCl_3): λ_{max} ($\epsilon / \text{dm}^3 \text{mol}^{-1} \text{cm}^{-1}$) 252 (42800), 301 (36300), 366 (11500), 431 (9980) nm. IR (thin film): ν_{max} 2905, 1721, 1578, 1522, 1383, 1240, 1267, 1194, 1136, 1024, 760 cm^{-1} .

Synthesis of [Gd(L10)]: Gadolinium(III) triflate (0.112 g, 0.186 mmol) and **L10** (0.100 g, 0.186 mmol) were dissolved in methanol (10 mL) and heated to 50 °C for 24 h under dinitrogen. The solution was cooled and diethyl ether (20 mL) was added. The precipitate was filtered under dinitrogen to yield an off-white solid. Yield = 0.112 g, (87%). HR-MS: calcd. for $[\text{C}_{24}\text{H}_{37}^{152}\text{GdN}_7\text{O}_7]^+$ 687.1947 found 687.1941. UV-vis (CHCl_3): λ_{max} ($\epsilon / \text{dm}^3 \text{mol}^{-1} \text{cm}^{-1}$) 201 (7240), 256 (1840) nm. IR (thin film): ν_{max} 3397, 1582, 1402, 1244, 1225, 1165, 1082, 1026, 635 cm^{-1} .

Synthesis of [Yb(L10)]: Ytterbium(III) triflate (0.115 g, 0.186 mmol) and **L10** (0.100 g, 0.186 mmol) were dissolved in methanol (10 mL) and heated to 50 °C for 24 h under dinitrogen. The solution was cooled and diethyl ether (20 mL) was added. The precipitate was filtered under dinitrogen to yield an off-white solid. Yield = 0.121 g, (92%). HR-MS: calcd. for $[\text{C}_{24}\text{H}_{37}\text{N}_7\text{O}_7^{170}\text{Yb}]^+$ 705.2102 found 705.2110. UV-vis (CHCl_3): λ_{max} ($\epsilon / \text{dm}^3 \text{mol}^{-1} \text{cm}^{-1}$) 201 (7800), 256 (1430) nm. IR (thin film): ν_{max} 3408, 1601, 1410, 1258, 1167, 1084, 1026, 800, 640 cm^{-1} .

Synthesis of [Pt(L9){Gd(L10)}Cl]: [Pt(L9)(DMSO)Cl] (0.052 g, 0.079 mmol) and **GdL10** (0.050 g, 0.072 mmol) were dissolved in acetone and heated to 40 °C for 48 h under dinitrogen. The solvent was removed *in vacuo* and the solid dissolved in minimal acetonitrile and precipitated with diethyl ether. The solid was filtered and washed with dichloromethane to yield a bright orange solid. Yield = 0.062 g, (68%). HR-MS: calcd. for $[\text{C}_{45}\text{H}_{56}\text{N}_8\text{O}_{11}^{155}\text{Gd}^{194}\text{Pt}]^+$ 1233.2922 found 1233.2953. UV-vis (CHCl_3): λ_{max} ($\epsilon / \text{dm}^3 \text{mol}^{-1} \text{cm}^{-1}$) 203 (25000), 246 (13300), 285 (9320), 364 (4450) nm. IR (thin film): ν_{max} 3433, 1732, 1591, 1456, 1404, 1246, 1167, 1084, 1028, 941, 903, 841, 762, 723, 637 cm^{-1} .

Synthesis of [Pt(L9){Yb(L10)}Cl]: [Pt(L9)(DMSO)Cl] (0.051 g, 0.078 mmol) and **YbL10** (0.050 g, 0.071 mmol) were dissolved in acetone and heated to 40 °C for 48 h under dinitrogen. The solvent was removed *in vacuo* and the solid dissolved in minimal acetonitrile and precipitated with diethyl ether. The solid was filtered and washed with dichloromethane to yield a bright orange solid. Yield = 0.072 g, (79%). HR-MS: calcd. for $[\text{C}_{45}\text{H}_{56}\text{N}_8\text{O}_{11}^{171}\text{Yb}^{194}\text{Pt}]^+$ 1249.3059 found 1249.3076. UV-vis (CHCl_3): λ_{max} ($\epsilon / \text{dm}^3 \text{mol}^{-1} \text{cm}^{-1}$) 203 (26300), 248 (14100), 284 (9920), 364 (4640) nm. IR (thin film): ν_{max} 3408, 1730, 1595, 1458, 1400, 1389, 1248, 1165, 1084, 1028, 943, 909, 843, 762, 727, 638 cm^{-1} .

Synthesis of [Pt(L5)(8-Q)]: Following the general procedure outlined in Chapter 2 for coordinating 8-hydroxyquinoline to platinum complexes using [Pt(L5)(DMSO)Cl] (0.033 g, 0.049 mmol), Na₂CO₃ (0.010 g, 0.099 mmol) and 8-hydroxyquinoline (0.008 g, 0.054 mmol). The red solution was dried *in vacuo* and diethyl ether (5 mL) was added to remove excess 8-hydroxyquinoline. The precipitate was filtered, washed with diethyl ether (2 x 10 mL) and methanol (1 x 5 mL). The solid was dissolved in dichloromethane and dried *in vacuo* to afford a red solid. Yield = 0.026 g, (76%). ¹H NMR (400 MHz, CDCl₃): δ_H 9.64 (1H, d, ³J_{HH} = 8.4 Hz), 8.95 (1H, m (with satellites)), 8.32 (1H, d, ³J_{HH} = 8.4 Hz), 7.90 (1H, d, ³J_{HH} = 8.0 Hz), 7.75 – 7.71 (1H, m), 7.57 – 7.52 (2H, m), 7.43 – 7.38 (2H, m), 7.30 – 7.25 (2H, m), 7.18 – 7.12 (2H, m), 7.07 – 7.04 (1H, m), 6.97 (H, d, ³J_{HH} = 7.6 Hz), 6.88 – 6.85 (1H, m), 3.58 – 3.48 (2H, m), 1.81 – 1.72 (2H, m), 1.49 – 1.25 (10H, m), 0.92 (3H, t, ³J_{HH} = 6.8 Hz) ppm. MS(ES) found m/z = 753.25 for [M + MeOH + Na]⁺. UV-vis (CHCl₃): λ_{max} (ε / dm³ mol⁻¹ cm⁻¹) 280 (1023), 370 (253), 505 (75) nm. IR (thin film): ν_{max} 3257, 1645, 1539 cm⁻¹.

Synthesis of [Pt(L6)(8-Q)]: Following the general procedure outlined in Chapter 2 for coordinating 8-hydroxyquinoline to platinum complexes using [Pt(L6)(DMSO)Cl] (0.052 g, 0.072 mmol), Na₂CO₃ (0.038 g, 0.360 mmol) and 8-hydroxyquinoline (0.021 g, 0.145 mmol). The red solution was dried *in vacuo* and diethyl ether (5 mL) was added to remove excess 8-hydroxyquinoline. The precipitate was filtered, washed with diethyl ether (2 x 10 mL) and methanol (1 x 5 mL). The solid was dissolved in dichloromethane and dried *in vacuo*. Yield = 0.033 g, (61%). ¹H NMR (400 MHz, CDCl₃): δ_H 9.61 (1H, d, ³J_{HH} = 8.4 Hz), 8.94 – 8.88 (1H, m (with satellites)), 8.31 (1H, d, ³J_{HH} = 8.0 Hz), 7.86 (1H, d, ³J_{HH} = 8.0 Hz), 7.71 – 7.67 (1H, m), 7.56 – 7.50 (3H, m), 7.39 – 7.35 (2H, m), 7.27 – 7.24 (1H, m) 7.14 – 6.97 (4H, m), 6.82 – 6.79 (1H, m), 3.57 - 3.49 (2H, m), 1.81 – 1.75 (2H, m), 1.48 – 1.25 (18H, m), 0.89 (3H, t, ³J_{HH} = 6.8 Hz) ppm. UV-vis (CHCl₃): λ_{max} (ε / dm³ mol⁻¹ cm⁻¹) 265 (864), 368 (264), 506 (75) nm. IR (thin film): ν_{max} 3289, 1646, 1539 cm⁻¹.

Synthesis of [Pt(L7)(8-Q)]: Following the general procedure outlined in Chapter 2 for coordinating 8-hydroxyquinoline to platinum complexes using [Pt(L7)(DMSO)Cl] (0.029 g, 0.037 mmol), Na₂CO₃ (0.020 g, 0.186 mmol) and 8-hydroxyquinoline (0.011 g, 0.074 mmol). The red solution was dried *in vacuo* and diethyl ether (5 mL) was added to remove excess 8-hydroxyquinoline. The precipitate was filtered, washed

with diethyl ether (2 x 10 mL) and methanol (1 x 5 mL). The solid was dissolved in dichloromethane and dried *in vacuo* to obtain a red solid. Yield = 0.021 g, (68%). ^1H NMR (400 MHz, CDCl_3): δ_{H} 9.64 (1H, d, $^3J_{\text{HH}} = 8.8$ Hz), 8.93 (1H, d (with satellites), $^3J_{\text{HH}} = 3.2$ Hz), 8.31 (1H, d, $^3J_{\text{HH}} = 8.0$ Hz), 7.88 (1H, d, $^3J_{\text{HH}} = 8.0$ Hz), 7.74 – 7.70 (1H, m), 7.56 – 7.52 (2H, m), 7.41 – 7.36 (3H, m), 7.29 – 7.24 (1H, m), 7.14 – 7.13 (2H, m), 7.06 – 7.03 (1H, m), 6.97 (1H, d, $^3J_{\text{HH}} = 7.6$ Hz), 6.85 – 6.82 (1H, m), 3.56 – 3.45 (2H, m), 1.80 – 1.71 (2H, m), 1.45 – 1.19 (26H, m), 0.88 (3H, t, $^3J_{\text{HH}} = 7.2$ Hz) ppm. UV-vis (CHCl_3): λ_{max} ($\epsilon / \text{dm}^3 \text{mol}^{-1} \text{cm}^{-1}$) 504 (119), 438 (108), 369 (259), 352 (275) nm. IR (thin film): ν_{max} 3292, 1670, 1597 cm^{-1} .

3.6. References

1. J. Hardy and D. Allsop, *Trends Pharmacol. Sci.*, 1991, **12**, 383-388.
2. S. Vivekanandan, J. R. Brender, S. Y. Lee and A. Ramamoorthy, *Biochem. Biophys. Res. Commun.*, 2011, **411**, 312-316.
3. C. Hureau, *Coord. Chem. Rev.*, 2012, **256**, 2164-2174.
4. A. Khan, *The Journal of Quality Research in Dementia*, 2007.
5. C. Priller, T. Bauer, G. Mitteregger, B. Krebs, H. A. Kretschmar and J. Herms, *J. Neurosci.*, 2006, **26**, 7212-7221.
6. J. Hardy and D. J. Selkoe, *Science*, 2002, **297**, 353-356.
7. J. P. Taylor, J. Hardy and K. H. Fischbeck, *Science*, 2002, **296**, 1991-1995.
8. S. T. Ferreira, M. N. N. Vieira and F. G. De Felice, *IUBMB Life*, 2007, **59**, 332-345.
9. C. Migliorini, E. Porciatti, M. Luczkowski and D. Valensin, *Coord. Chem. Rev.*, 2012, **256**, 352-368.
10. C. Hureau and P. Faller, *Biochimie*, 2009, **91**, 1212-1217.
11. S. G. Yao, R. A. Cherny, A. I. Bush, C. L. Masters and K. J. Barnham, *J. Pept. Sci.*, 2004, **10**, 210-217.
12. K. J. Barnham, V. B. Kenche, G. D. Ciccotosto, D. P. Smith, D. J. Tew, X. Liu, K. Perez, G. A. Cranston, T. J. Johanssen, I. Volitakis, A. I. Bush, C. L. Masters, A. R. White, J. P. Smith, R. A. Cherny and R. Cappai, *Proc. Natl. Acad. Sci. U. S. A.*, 2008, **105**, 6813-6818.
13. G. L. Ma, F. Huang, X. W. Pu, L. Y. Jia, T. Jiang, L. Z. Li and Y. Z. Liu, *Chem. Eur. J.*, 2011, **17**, 11657-11666.
14. F. Collin, I. Sasaki, H. Eury, P. Faller and C. Hureau, *Chem. Commun.*, 2013, **49**, 2130-2132.
15. C. J. Frederickson, J. Y. Koh and A. I. Bush, *Nat. Rev. Neurosci.*, 2005, **6**, 449-462.
16. J. Y. Lee, T. B. Cole, R. D. Palmiter, S. W. Suh and J. Y. Koh, *Proc. Natl. Acad. Sci. U. S. A.*, 2002, **99**, 7705-7710.
17. A. I. Bush, W. H. Pettingell, G. Multhaup, M. D. Paradis, J. P. Vonsattel, J. F. Gusella, K. Beyreuther, C. L. Masters and R. E. Tanzi, *Science*, 1994, **265**, 1464-1467.
18. P. A. Rinck, ed., *Magnetic Resonance in Medicine*, Blackwell Scientific Publications, Oxford, UK, 1993.

19. D. D. Stark and W. G. Bradley, eds., *Magnetic Resonance Imaging*, The V.C. Mosby Company, St. Louis, US, 1988.
20. P. Caravan, *Chem. Soc. Rev.*, 2006, **35**, 512-523.
21. P. Caravan, *Acc. Chem. Res.*, 2009, **42**, 851-862.
22. M. Wagner, R. Schilling, P. Doeblin, A. Huppertz, R. Lühr, C. Schwenke, M. Maurer, B. Hamm, M. Taupitz and T. Durmus, *Eur. Radiol.*, 2013, **23**, 108-114.
23. E. J. Werner, A. Datta, C. J. Jocher and K. N. Raymond, *Angew. Chem. Int. Edit.*, 2008, **47**, 8568-8580.
24. A. S. Merbach, L. Helm and É. Tóth, *The Chemistry of Contrast Agents in Medical Magnetic Resonance Imaging*, Wiley, Chichester, 2013.
25. S. Aime, M. Botta, M. Fasano, S. G. Crich and E. Terreno, *Coord. Chem. Rev.*, 1999, **185-6**, 321-333.
26. M. A. Bruckman, X. Yu and N. F. Steinmetz, *Nanotechnology*, 2013, **24**.
27. J. Rudovsky, J. Kotek, P. Hermann, I. Lukes, V. Mainero and S. Aime, *Org. Biomol. Chem.*, 2005, **3**, 112-117.
28. J. Costa, E. Toth, L. Helm and A. E. Merbach, *Inorg. Chem.*, 2005, **44**, 4747-4755.
29. D. H. Powell, O. M. NiDhubhghaill, D. Pubanz, L. Helm, Y. S. Lebedev, W. Schlaepfer and A. E. Merbach, *J. Am. Chem. Soc.*, 1996, **118**, 9333-9346.
30. J. Costa, R. Ruloff, L. Burai, L. Helm and A. E. Merbach, *J. Am. Chem. Soc.*, 2005, **127**, 5147-5157.
31. S. V. Eliseeva and J. C. G. Bunzli, *Chem. Soc. Rev.*, 2010, **39**, 189-227.
32. S. I. Weissman, *J. Chem. Phys.*, 1942, **10**, 214-217.
33. J.-C. G. Bünzli and S. V. Eliseeva, in *Lanthanide Luminescence: Photophysical, Analytical and Biological Aspects*, eds. P. Hänninen and H. Härmä, Springer-Verlag, Berlin, 2010.
34. A. M. Nonat, C. Allain, S. Faulkner and T. Gunnlaugsson, *Inorg. Chem.*, 2010, **49**, 8449-8456.
35. K. Senechal-David, S. J. A. Pope, S. Quinn, S. Faulkner and T. Gunnlaugsson, *Inorg. Chem.*, 2006, **45**, 10040-10042.
36. J. E. Jones, R. L. Jenkins, R. S. Hicks, A. J. Hallett and S. J. A. Pope, *Dalton Trans.*, 2012, **41**, 10372-10381.
37. F. Kennedy, N. M. Shavaleev, T. Koullourou, Z. R. Bell, J. C. Jeffery, S. Faulkner and M. D. Ward, *Dalton Trans.*, 2007, 1492-1499.

38. J. H. Jang, S. Bhuniya, J. Kang, A. Yeom, K. S. Hong and J. S. Kim, *Org. Lett.*, 2013, **15**, 4702-4705.
39. Z. Kotkova, J. Kotek, D. Jirak, P. Jendelova, V. Herynek, Z. Berkova, P. Hermann and I. Lukes, *Chem. Eur. J.*, 2010, **16**, 10094-10102.
40. C. P. Gros, A. Eggenpilller, A. Nonat, J. M. Barbe and F. Denat, *Med. Chem. Commun.*, 2011, **2**, 119-125.
41. A. Bossi, A. F. Rausch, M. J. Leidl, R. Czerwieniec, M. T. Whited, P. I. Djurovich, H. Yersin and M. E. Thompson, *Inorg. Chem.*, 2013, **52**, 12403-12415.
42. A. Esmaeilbeig, H. Samouei, S. Abedanzadeh and Z. Amirghofran, *J. Organomet. Chem.*, 2011, **696**, 3135-3142.
43. T. Koullourou, L. S. Natrajan, H. Bhavsar, S. J. A. Pope, J. H. Feng, J. Narvainen, R. Shaw, E. Scales, R. Kauppinen, A. M. Kenwright and S. Faulkner, *J. Am. Chem. Soc.*, 2008, **130**, 2178-2179.
44. *US Pat.*, WO2002096417, 2002.
45. H. B. Xu, L. Y. Zhang, Z. H. Chen, L. X. Shi and Z. N. Chen, *Dalton Trans.*, 2008, 4664-4670.
46. T. K. Ronson, T. Lazarides, H. Adams, S. J. A. Pope, D. Sykes, S. Faulkner, S. J. Coles, M. B. Hursthouse, W. Clegg, R. W. Harrington and M. D. Ward, *Chem. Eur. J.*, 2006, **12**, 9299-9313.
47. N. M. Shavaleev, G. Accorsi, D. Virgili, D. R. Bell, T. Lazarides, G. Calogero, N. Armaroli and M. D. Ward, *Inorg. Chem.*, 2005, **44**, 61-72.
48. N. M. Shavaleev, L. P. Moorcraft, S. J. A. Pope, Z. R. Bell, S. Faulkner and M. D. Ward, *Chem. Eur. J.*, 2003, **9**, 5283-5291.
49. N. M. Shavaleev, L. P. Moorcraft, S. J. A. Pope, Z. R. Bell, S. Faulkner and M. D. Ward, *Chem. Commun.*, 2003, 1134-1135.
50. S. G. Crich, D. Alberti, I. Szabo, S. Aime and K. Djanashvili, *Angew. Chem. Int. Edit.*, 2013, **52**, 1161-1164.
51. J. P. Andre, C. Geraldies, J. A. Martins, A. E. Merbach, M. I. M. Prata, A. C. Santos, J. J. P. de Lima and E. Toth, *Chem. Eur. J.*, 2004, **10**, 5804-5816.
52. A. Beeby, I. M. Clarkson, R. S. Dickins, S. Faulkner, D. Parker, L. Royle, A. S. de Sousa, J. A. G. Williams and M. Woods, *J. Chem. Soc., Perkin Trans. 2*, 1999, 493-503.
53. Y. Haas and G. Stein, *J. Phys. Chem.*, 1972, **76**, 1093-1104.

**Chapter 4: Examining the photophysical properties of
chromophore appended platinum (II) complexes**

4.1. Introduction

Chapter 4 discusses the development of ligands incorporating pendant chromophores in order to assess the impact of the chromophores on the $^3\text{MLCT}$ -derived emission. Given previous examples in the literature, as outlined below, the chromophore of greatest interest in this investigation is pyrene and, in order to discuss the results, it is important to have an appreciation of the physical and photophysical properties of pyrene and its prior utility in transition metal complexes.

4.1.1. Photophysical properties of pyrene monomers

Due to the planar aromatic nature of pyrene, it readily interacts with other pyrene moieties through π -stacking. It is, however, important to have an appreciation of the monomeric properties before discussing the properties of excimers.

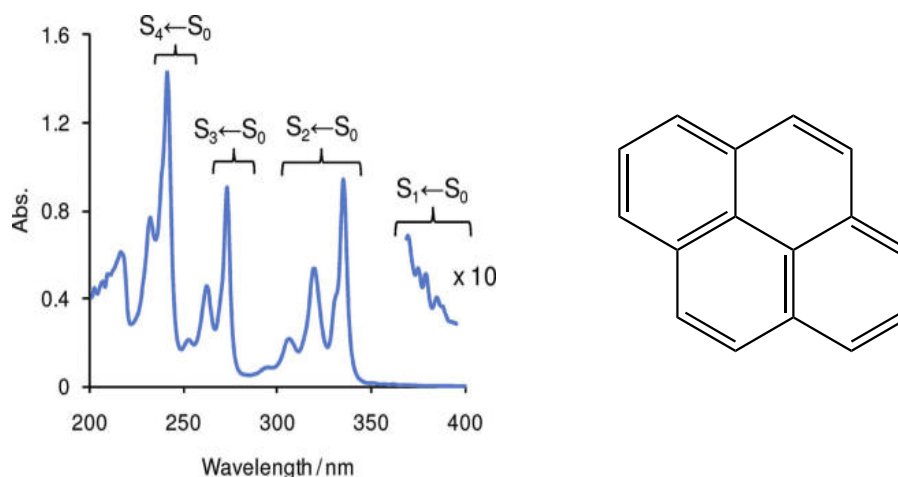


Figure 4.1 Absorption spectrum of pyrene in cyclohexane with transitional assignments (*left*)¹ and structure of pyrene (*right*).

Monomeric pyrene shows four bands in the absorption spectrum (Figure 4.1) between 200 and 400 nm, which can be assigned to ($S_4 \leftarrow S_0$), ($S_3 \leftarrow S_0$), ($S_2 \leftarrow S_0$) and ($S_1 \leftarrow S_0$) transitions.¹ Vibrations from $v'' = 0$ to $v' = 1, 2, 3, 4, \dots$ results in the vibronic structure observed within each $S_n \leftarrow S_0$ excitation. The emission also exhibits this characteristic structure due to the mirror-image rule and Franck-Condon factors and emits predominantly in the region *ca.* 370 nm.² The fluorescence from pyrene (pyr) compounds can possess extraordinarily long fluorescence lifetimes due to the symmetry of the molecule. This can often be in the hundreds of ns range, which is of the same magnitude as many coordination complexes' phosphorescent lifetime.¹ As well as desirable fluorescent properties, pyrene can also undergo intersystem crossing

Chapter 4: Examining the photophysical properties of chromophore appended platinum (II) complexes from the S_1 to the T_1 state. The emission of the triplet can be observed at *ca.* 600 nm at low temperature (77 K) in frozen solvent mixtures.³

4.1.2. Photophysical properties of pyrene excimers

Excimers, or excited state dimers, of pyrene readily form through the favourable interaction between the two planar aromatic ‘sheets’ leading to the formation of charge transfer complexes. The interaction results in π -stacking that perturbs both the emission wavelength and lifetime without affecting the absorption profile.⁴ The reduced energy of the excimers’ emission leads to a shift in λ_{max} from *ca.* 380 nm for the monomer to nearly 500 nm. The excimer emission does not exhibit the vibronic structure of its parental monomer. The formation of excimers usually results in faster relaxation of the excited state, resulting in shortened lifetimes compared to that of the monomeric compound. This is the case with pyrene, as lifetimes for excimer species are reported *ca.* 90 ns.⁵ Despite the reduction in lifetime, this is still much longer than the emissive decay of most organic chromophores, rendering it extremely useful as a biological tool.

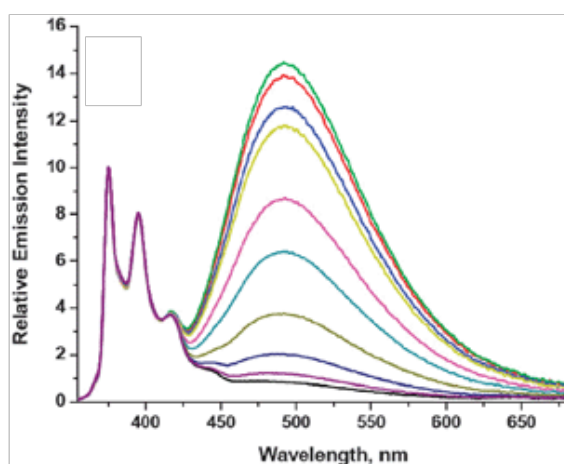


Figure 4.2 Pyrene excimer emission ($\lambda_{\text{em}} = 492$ nm).⁶

4.1.3. Pyrene in biological imaging

Pyrene-based systems have been well studied for many years due to their important photophysical properties. The long-lived fluorescence lifetimes and capacity to readily form excimers in solution and solid state have resulted in a plethora of applications. They have seen use in determining the concentration of dissolved oxygen in biological studies,^{7, 8} as biological labelling applications,^{9, 10} as probes for the intracellular delivery of molecules and as labels on nucleotide bases to study DNA

Chapter 4: Examining the photophysical properties of chromophore appended platinum (II) complexes charge transfer, non-covalent interactions between nucleotides and the detection of defects.¹¹⁻¹⁶

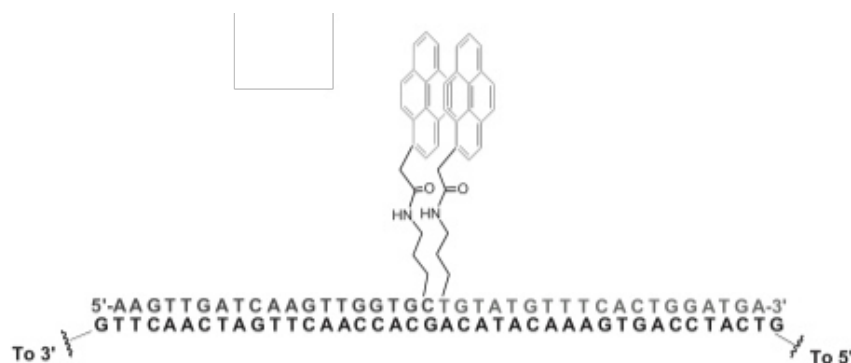
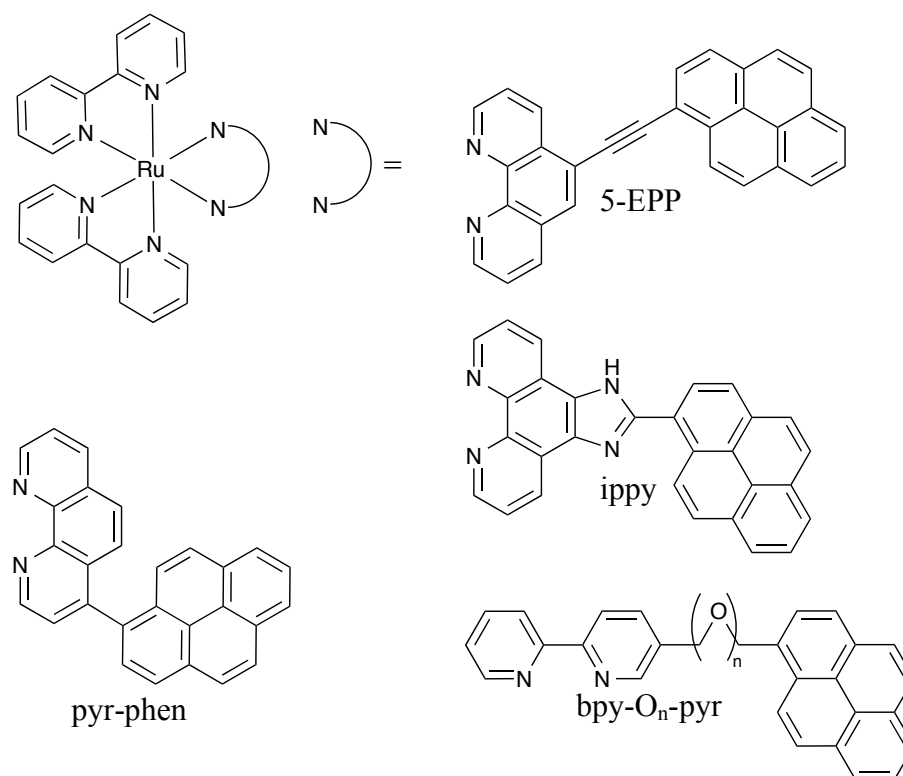


Figure 4.3 Pyrene-labelled mRNA bases leading to the formation of pyrene excimers.¹⁷

Excimers have also been utilised in biological imaging due to their long lifetimes and the ability to differentiate between excimer and monomer emission through time-gated fluorescence mapping and time-resolved emission spectra.¹⁷ Marti *et al.*'s technique allows for the detection of specific mRNA *in vivo* so that the onset of molecular interactions by stimuli can be studied.¹⁸

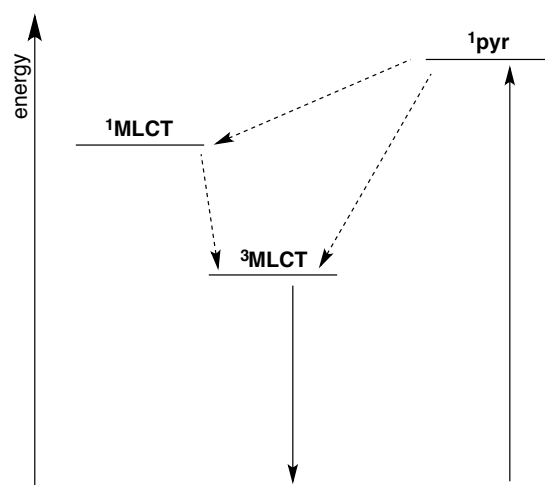
4.1.4. Development of long lifetime complexes using pyrene

Pyrene has long been incorporated into metal complexes for various applications. The majority of these complexes centre on Ru^{II} due to the good energetic matching of the two emissive triplet states (*ca.* 600 nm). This has led to a wide range of investigations into extending the lifetime of the ³MLCT emissive state for applications in photodynamic therapy (PDT), where extended lifetimes of the emission tend to lend themselves to greater quantum yields of singlet oxygen.

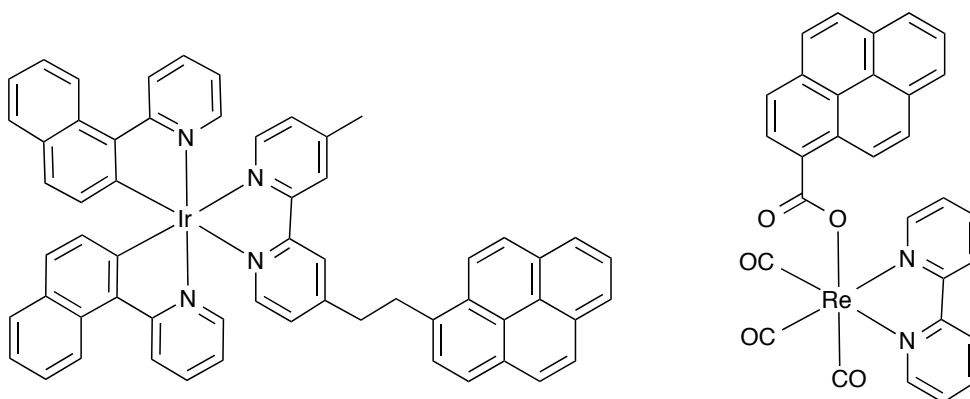
Figure 4.4 Ru^{II} complexes incorporating pyrene functionalisation.

Lincoln *et al.* recently developed a Ru^{II} trisimine complex ($[\text{Ru}(\text{bpy})_2(5\text{-EPP})]^{2+}$) with an ethynyl pyrene unit appended and investigated the change in photophysical properties when the pyrene unit was moved to different positions on the coordinated 1,10-phenanthroline moiety. They found that, at room temperature, emissive lifetimes could be tuned between 22 and 220 μs depending upon the position of attachment of the chromophore.¹⁹ Similar Ru^{II} pyrene dyads ($[\text{Ru}(\text{bpy})_2(\text{ippy})]^{2+}$) have also displayed long-lived lifetimes and have consequently shown promise as photosensitizers. Stephenson *et al.* quote lifetimes in excess of 80 μs , 100 times longer than lifetimes of polypyridyl Ru^{II} complexes lacking pyrene association.²⁰

These examples have all shown relatively short distances between the Ru^{II} and pyrene moieties. Morales *et al.* investigated whether the extended lifetimes could be observed across larger distances and probed whether the antenna effects (Figure 4.5) are affected by the nature of the connectors.²¹ They found that, even with a separation distance of up to 21 Å, excitation of the ^1pyr state results only in emission from the $^3\text{MLCT}$ state in their trisimine complex ($[\text{Ru}(\text{bpy})_2(\text{bpy-O}_6\text{-pyr})]^{2+}$), which was put down to a Förster-type step where energy is transferred through non-radiative dipole-dipole coupling.²² The long lifetimes were found to be a result of energy equilibration between the $^3\text{MLCT}$ and ^3pyr states.

Figure 4.5 Energy pathways associated with pyrene acting as an antenna.²³

Pyrene has also been incorporated in Ir^{III} and Re^I complexes. Ragone *et al.* found that the Re^I pyrene dyad showed promise as a photosensitizer for singlet oxygen. The Re^I complex does not display equilibration of states as was seen in the Ru^{II} complexes due to the raised energy of the ³MLCT. It does, however, display ³LC emission from intersystem crossing of the pyrene excited state. The T₁ state was found to be extremely efficient at generating singlet oxygen with quantum yields close to unity.²⁴ The Ir^{III} complex displays electronic energy transfer between the metal-centred and pyrene excited states, much like [Ru(bpy)₂(pyr-phen)], resulting in lifetimes exceeding 200 μs, compared to a lifetime of < 10 μs for the analogous compound without pyrene.²⁵ This is, as with the Ru^{II} complexes, due to the energy overlap of the two T₁ energy states and demonstrates that the equilibration of the ³pyr and ³MLCT states is not limited to Ru^{II}-based complexes.

Figure 4.6 Ir^{III} and Re^I complexes incorporating pyrene functionalised ligands.

4.1.5. Pyrene in platinum (II) complexes

Hissler *et al.* developed pyr-ethynylene-Ru and pyr-Pt-Ru (Figure 4.7) complexes to study the equilibration of the Ru^{II} and pyr triplet excited states. The platinum centre was utilised to compare the efficiency of electronic conductivity from the pyrene to the Ru^{II} compared to a simple ethynylene linker. They found that, in the presence of the Pt^{II} , the emissive lifetime was nearly three times shorter than was observed for the monometallic species, which has a lifetime of more than $40\ \mu\text{s}$.²⁶ They subsequently investigated the monometallic pyr-Pt-bpy complex (Pt-pyr-3) (Figure 4.7) and found that there was no interplay between the ^3pyr and $^3\text{MLCT}$ states.²⁷

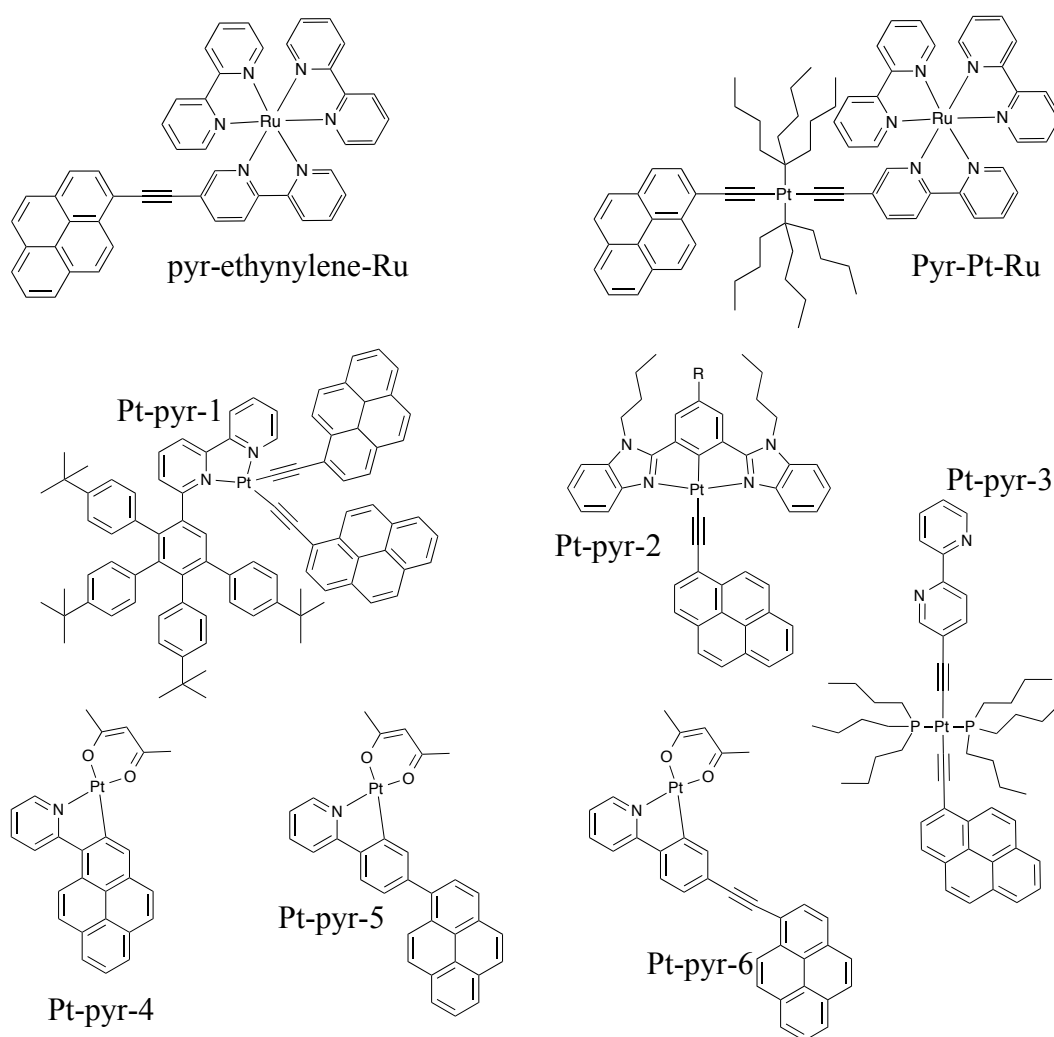


Figure 4.7 Examples of pyrene incorporated into Pt^{II} complexes for photophysical investigations.

Observations of various other platinum complexes incorporating pyrene all suggest that low energy emission (*ca.* 600 nm) is a result of phosphorescence associated with emission from the pyrene triplet state.²⁸⁻³⁰ There appear to be no examples in the

literature of Pt^{II}-based ³MLCT equilibration with the ³pyr excited state, unlike those found for Ir^{III} and Ru^{II}. Despite this, the Pt^{II} pyrene dyads have shown promise for applications in organic light emitting diodes (OLEDs) (Pt-pyr-2) and as photosensitizers (Pt-pyr-1) due to the long-lived emission of the ³pyr state, in the region of 5 μs for the ³IL emission.²⁸ Wu *et al.* tried to cyclometallate pyrene directly (Pt-pyr-4) in the hope of visualising ³pyr emission at room temperature. They found that this could be achieved and also presented the first observable pyrene phosphorescence at room temperature without direct cyclometallation (Pt-pyr-5).²⁹

4.2. Aims

Chapter 4 outlines the development of a series of Pt^{II} complexes with pendant chromophores attached. The ligands were based on the 2-phenylquinoline structure utilised in previous chapters. Naphthyl, anthracenyl and pyrenyl moieties were incorporated in the hope that there might be observable changes to the photophysical properties due to interplay between the excited states of the metal centre and chromophore. In depth photophysical studies, including low temperature and degassed measurements were utilised to reveal the relevant energies of the various states in order to link observable trends with the relative energy levels.

4.3. Results and Discussion

4.3.1. Ligand development and synthesis

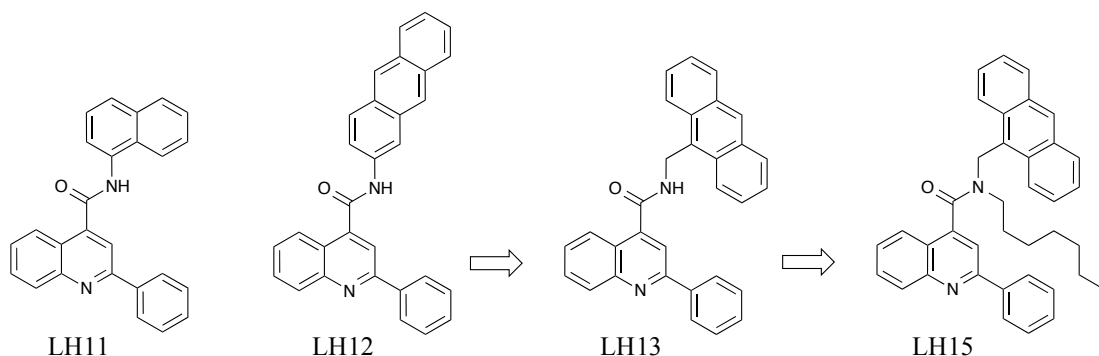


Figure 4.8 Structure of **LH11** (*left*) and the development of a suitably soluble ligand with an appended anthracene chromophore from **LH12** to eventually give **LH15** (*right*).

To append a chromophore in close proximity to the metal centre, 1-naphthylamine and 2-aminoanthracene were reacted with the acid chloride of 2-phenyl-4-quinolinecarboxylic acid using the methodology outlined in Chapter 2. **LH11** (Figure 4.8) is commercially available from small suppliers, however there is no literature associated with the compound and, as such, it was characterised by ^1H and ^{13}C NMR spectroscopies as well as mass spectrometry in order to confirm its synthesis. Whilst **LH11** showed good levels of solubility, **LH12** (Figure 4.8) was found to be insoluble in all common solvents except for DMSO. Attempts to synthesise the Pt^{II} dimer incorporating **L12** were unsuccessful using the methodologies outlined in Chapter 2, which is most likely due to the highly insoluble nature of the ligand in the solvent system used for the synthesis.

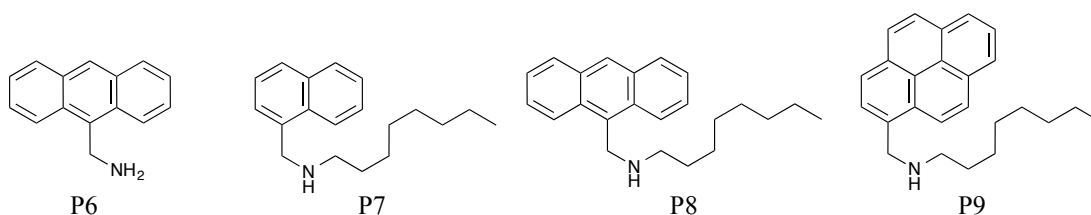


Figure 4.9 Structures of the precursors, **P6 – P9**.

In order to accommodate the larger chromophore, the ligand structure was altered by replacing 2-aminoanthracene with 9-aminomethylantracene, **P6**, hopefully reducing the insolubility, which was thought to be a result of the increased π -stacking interactions formed upon addition of extra planar aromatic character. This was achieved through a Gabriel synthesis from 9-anthracenemethanol.^{31, 32} Reaction

Chapter 4: Examining the photophysical properties of chromophore appended platinum (II) complexes conditions were based on previous synthesis of the target compound by Mallard *et al.* and Sun *et al.*^{33, 34} Despite the successful synthesis of the ligand by reacting **P6** with the acid chloride, the reaction with tetrachloroplatinate (II) was non-yielding.

The incorporation of an alkyl chain was thought to help with solubility, which would hopefully overcome the difficulties in isolating a chromophore-appended ligand coordinated to Pt^{II}. A means of incorporating an octyl chain into the ligand system was developed, given the utility of the C₈ chain in Chapter 3 at generating highly soluble complexes.

Secondary amines were formed in a two-step synthesis from the aldehyde of the corresponding chromophore and octylamine. Initial attempts using a reductive amination process adopted for other similar reactions were unsuccessful as the imine proved to be too stable to be reduced by the trisacetoxyborohydride salt (Na(OAc)₃BH),³⁵ presumably through the stability presented by extension of the conjugated aromatic systems. A different method was then found which had been used previously for the synthesis of the alkylated anthracene precursor, **P8**.³⁶ The immines were formed in refluxing ethanol before sodium borohydride (NaBH₄) was used to reduce the intermediates to give **P7** – **P9**.

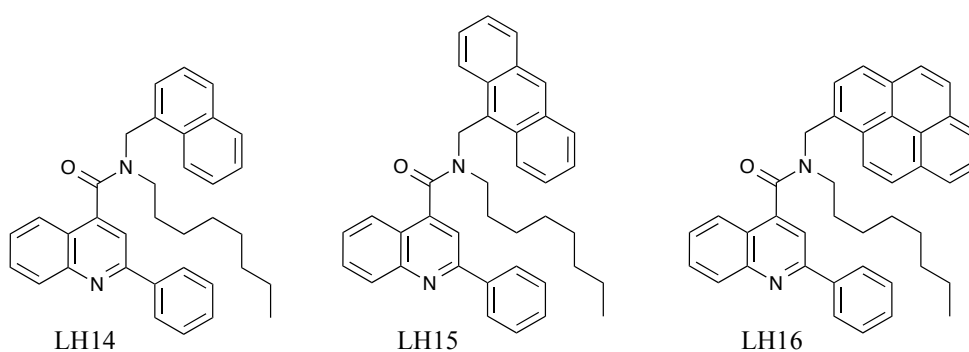


Figure 4.10 Structures of **LH14**, **LH15** and **LH16**.

The secondary amines were then reacted with the acid chloride, in the same manner as the primary amines in Chapters 2 and 3, to form ligands **LH14**, **LH15** and **LH16** (Figure 4.10) in good yields. Although **LH15** was isolated as a spectroscopically pure product, the compounds incorporating naphthalene and pyrene were found to contain more than one product. It was not until coordination to Pt^{II} and characterisation of the corresponding β -diketonate complexes that the cause for the impurity was discovered: both ligands contained a mixture of two isomers in *ca.* 3:1 ratio. Despite various

Chapter 4: Examining the photophysical properties of chromophore appended platinum (II) complexes purification techniques, including recrystallisation, column chromatography and precipitation, separation of the two forms was unsuccessful. Ligands **LH14** and **LH16** were used as the mixtures with the hope that they might become isolatable in a coordinated state.

Analysis of the ^1H NMR spectrum of **LH16** (Figure 4.11) reveals that the CH_2 group adjacent to the chromophore in both isomers is diastereotopic, suggesting that there is a degree of fixed rotation, which results in the coupling of one proton to the other. The major product appears to have a much greater inequivalence than the minor as the separation of the two environments is much larger. The major product displays two distinct doublets with a coupling constant of $^2J_{\text{HH}} = 14.4 \text{ Hz}$, whilst the minor isomer is not clearly defined enough to assign any multiplicity or coupling constants.

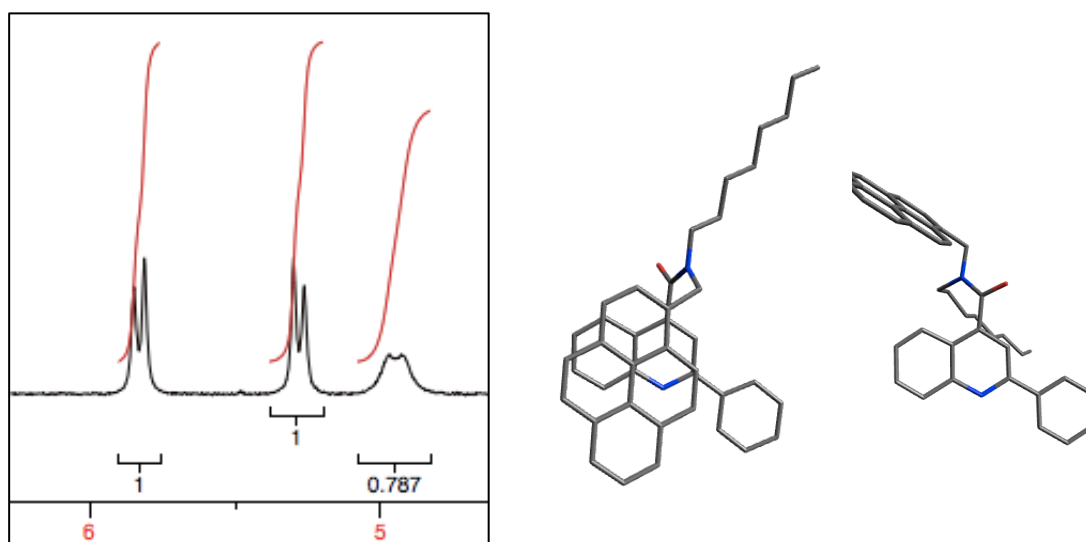


Figure 4.11 5 – 6 ppm region of the ^1H NMR spectrum of **LH16** demonstrating the inequivalence of the protons on the methyl linker between the amide and the pyrene chromophore (*left*). Geometrically optimised structures for the two isomers of **LH16** (*right*).

Avogadro was used to build structures of **LH16** so that the two structural isomers could be optimised using Universal force field (UFF).^{37, 38} The structures (Figure 4.11) suggest that a degree of π -stacking between the pyrene and phenylquinoline moieties is probable in one arrangement, whilst the other structure displays no possibility of intramolecular interaction between the two aromatic units. Whilst the reason for the restricted movement, preventing the equilibration to one isomer, is unclear, the spectroscopic data all suggest this is a possibility.

4.3.2. Synthesis and characterisation of cyclometallated platinum (II) complexes

[Pt(**L11**)(acac)] was successfully accessed using the methodology described in Chapter 2 through synthesis of the dimer, [Pt(**L11**)(μ -Cl)]₂, followed by the DMSO adduct, [Pt(**L11**)(DMSO)Cl], which was then reacted with the β -diketonate. After competing against the decreased solubility associated with the larger chromophores, complexes [Pt(**L14**)(acac)], [Pt(**L15**)(acac)] and [Pt(**L16**)(acac)] were all synthesised in the same manner.

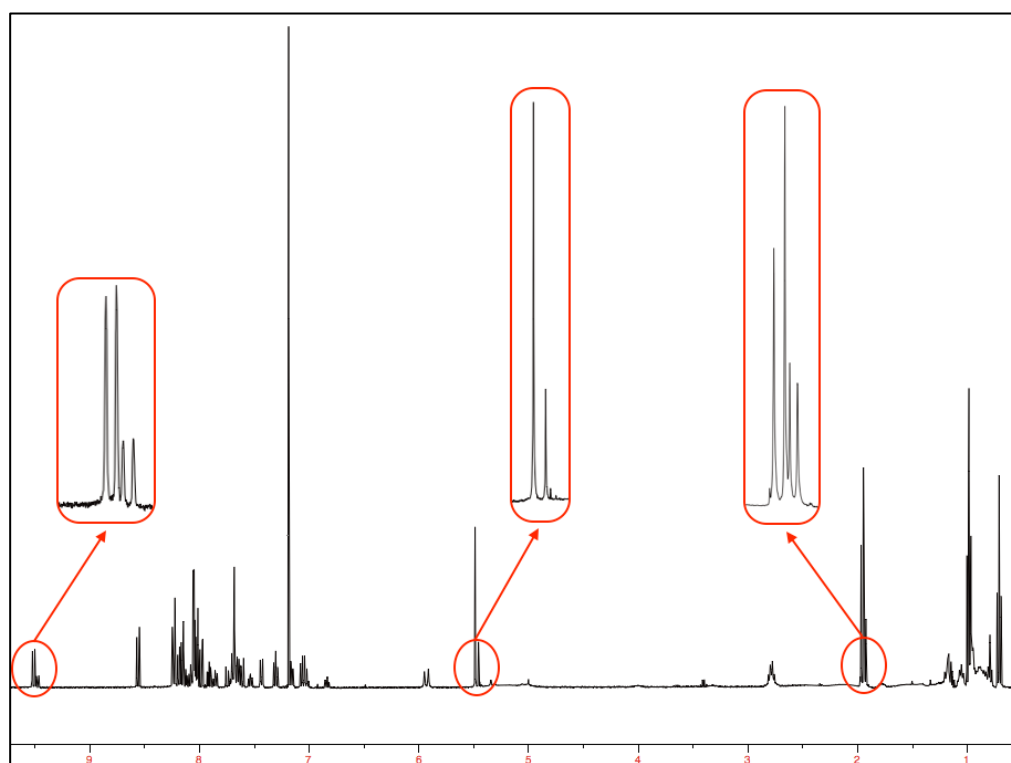


Figure 4.12 ¹H NMR spectrum of [Pt(**L16**)(acac)] highlighting evidence of the two isomers.

The complexes incorporating **L14** and **L16** were still found to contain a mixture of two isomers. This was clear, mostly through analysis by ¹H NMR spectroscopy (Figure 4.12), which showed the presence of two singlets at *ca.* 5.5 ppm for the proton in the 3-position of the 2,4-pentanediketonate. This was strengthened by the doubling up of the two singlets for the acac methyl groups, in the 1- and 5-positions, at *ca.* 2.0 ppm and the two downfield doublets at *ca.* 9.5 ppm corresponding to the phenylquinoline ligand. The most telling indicator was that all three sets of peaks had a major and minor component, which integrated to the major and minor component of each of the other peaks.

These isomers were again inseparable using the purification techniques available however, despite the mixture, the compounds were obtained in high purity. Variable temperature (VT) NMR spectroscopy was also employed to see whether the signals converged at higher temperatures (up to 90°C in d₈-toluene) but the only apparent effect this had on the spectrum was the broadening of signals.

The ¹⁹⁵Pt NMR spectra for the acac complexes of **L14**, **L15** and **L16** revealed a δ_{Pt} at -2784, -2786 and -2788 ppm, respectively. This is consistent with the data found in Chapter 2 for functionalised cyclometallated 2-phenylquinoline Pt^{II} complexes with an appended acetylacetonate ancillary ligand (*cf.* -2779 ppm for [Pt(**L2**)(acac)]).

4.3.3. X-ray crystal structures

The X-ray crystal structure of [Pt(**L15**)(acac)] has inner-sphere coordination bond lengths of 1.962(3) and 2.0551(16) Å for the Pt-C and Pt-N bonds and 2.0031(17) and 2.1057(18) Å for the Pt-O bonds, where the shorter length is *trans* to the coordinated N atom. As with the other acac structures, the coordinative bond lengths are comparable to the [Pt(ppy)(acac)] complex.³⁹ The anthracene moiety is almost perpendicular to the plane of the phenylquinoline providing a very organised packing arrangement. This head-to-tail formation results in both π - π and Pt-Pt interactions, with a Pt-Pt bond length of just 3.2365(2) Å, the shortest of all the Pt-Pt distances reported in this thesis. This compares to a bond distance of nearly 3.7 Å for the [Pt(ppy)(acac)] complex, which is greater in length by more than 10%. This may be as a result of the bulky anthracenyl component forcing the overlap to be more aligned than has been observed in other structures, where the two molecules have been slightly offset from one another. The resultant structure is far less out of plane than has been observed in the other phenylquinoline complexes and is much more like the planar nature of the [Pt(ppy)(acac)] complex.

In contrast, the X-ray structure of [Pt(**L16**)(acac)] displays a packing arrangement resulting in very little π -stacking interactions between phenylquinoline units and none between pyrene, which is unexpected given the large planar aromatic pyrene substituent. This is probably due to the bulky nature of the pyrenyl ligand in combination with the octyl chain, which can be seen lying between the pyrene units. Unlike the other complexes, there is also no formation of dimer substructures from metallophilic interactions, presumably due to the bulk of the ligand preventing such interactions. As with the other structures, bond lengths of 1.970(3), 2.056(3), 1.998(2) and 2.098(2) Å for Pt-C, Pt-N and Pt-O are all comparable to [Pt(ppy)(acac)].

4.3.4. X-ray crystal structure of [Pt(L15)(acac)]

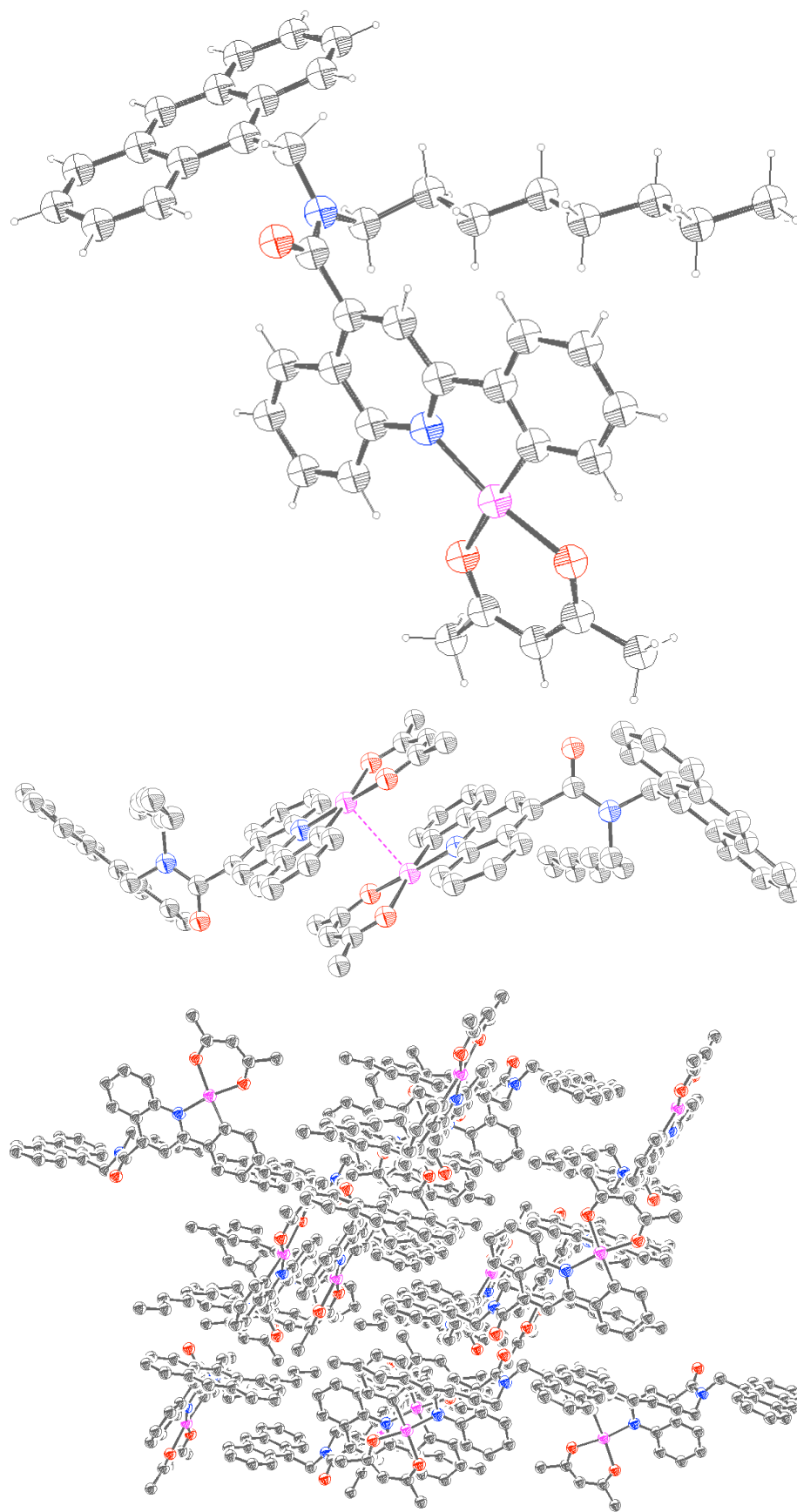


Figure 4.13 Ball and stick X-ray crystal structure of [Pt(L15)(acac)] (*top*), the Pt-Pt interaction (*middle*) and the packing arrangement (*bottom*).

4.3.5. X-ray crystal structure of [Pt(L16)(acac)]

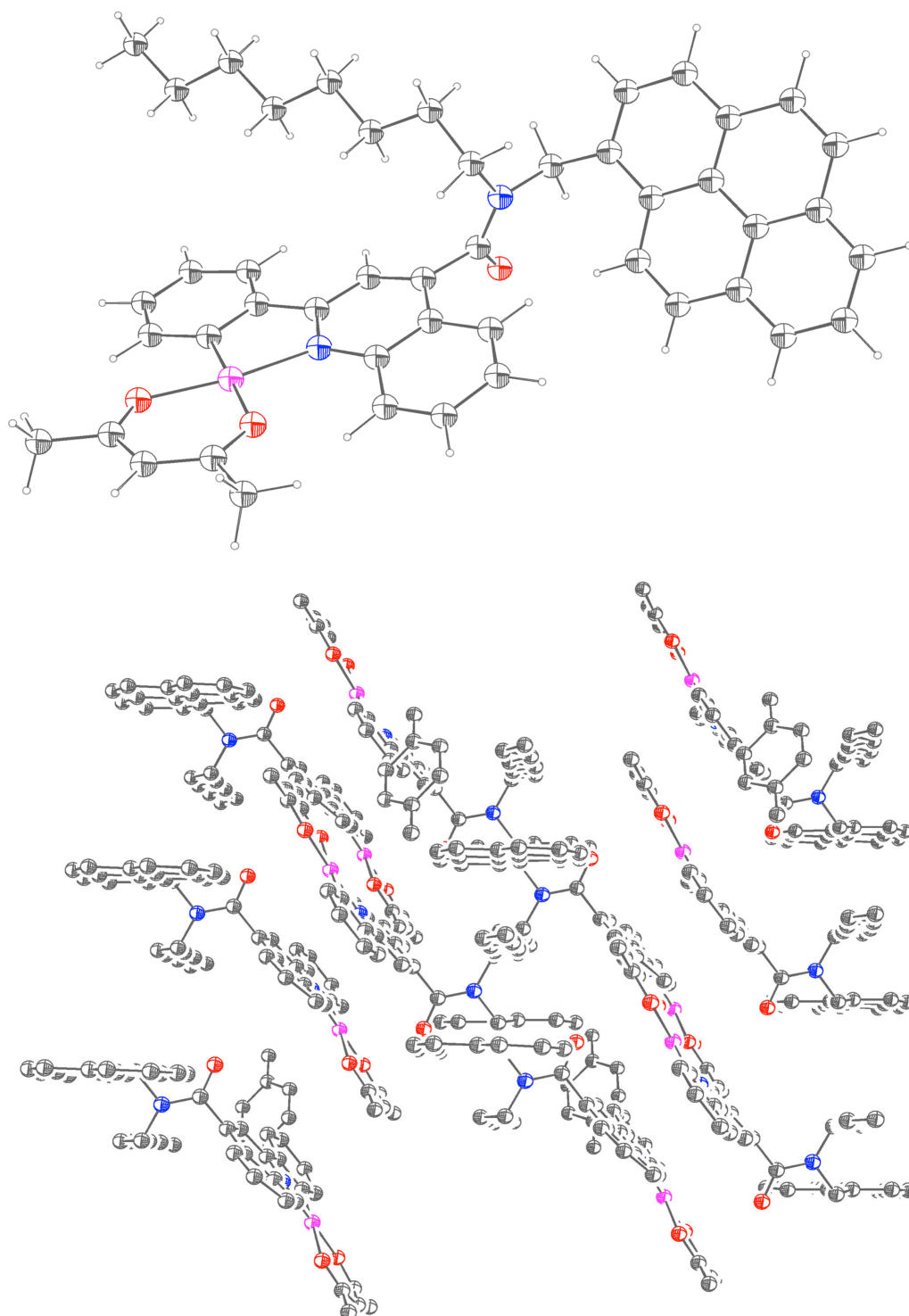


Figure 4.14 Ball and stick X-ray crystal structure of [Pt(**L16**)(acac)] (*top*) and the packing arrangement (*bottom*).

4.3.6. X-ray crystal data

	[Pt(L15)(acac)]	[Pt(L16)(acac)]
Empirical formula	C ₄₄ H ₄₄ N ₂ O ₃ Pt	C _{49.50} H ₄₈ N ₂ O ₃ Pt
Formula weight	843.90	913.99
Temperature	120(2) K	100(2) K
Wavelength	0.71075 Å	0.71075 Å
Crystal system	Monoclinic	Triclinic
Space group	<i>P</i> 2 ₁ / <i>c</i>	<i>P</i> -1
Unit cell dimensions	<i>a</i> = 17.5181(11) Å, <i>a</i> = 90° <i>b</i> = 14.2716(10) Å, <i>b</i> = 117.1440(5)° <i>c</i> = 16.0586(11) Å, <i>c</i> = 90°	<i>a</i> = 8.9153(5) Å, <i>α</i> = 77.279(3)° <i>b</i> = 12.6111(9) Å, <i>β</i> = 83.655(3)° <i>c</i> = 18.5893(13) Å, <i>γ</i> = 76.145(3)°
Volume	3572.6(4) Å ³	1975.7(2) Å ³
<i>Z</i>	4	2
Density (calculated)	1.569 Mg / m ³	1.536 Mg / m ³
Absorption coefficient	3.971 mm ⁻¹	3.597 mm ⁻¹
<i>F</i> (000)	1696	922
Crystal	Plate; Red	Plate; Orange
Crystal size	0.090 × 0.060 × 0.010 mm ³	0.240 × 0.140 × 0.020 mm ³
θ range for data collection	2.911 - 27.481°	3.004 - 27.485°
Index ranges	-22 ≤ <i>h</i> ≤ 22, -18 ≤ <i>k</i> ≤ 18, -19 ≤ <i>l</i> ≤ 20	-11 ≤ <i>h</i> ≤ 11, -15 ≤ <i>k</i> ≤ 16, -24 ≤ <i>l</i> ≤ 24
Reflections collected	62732	26783
Independent reflections	8186 [<i>R</i> _{int} = 0.0502]	9026 [<i>R</i> _{int} = 0.0484]
Completeness to θ = 25.242°	99.8%	99.6%
Absorption correction	Semi-empirical from equivalents	Semi-empirical from equivalents
Max. and min. transmission	1.000 and 0.819	1.000 and 0.642
Refinement method	Full-matrix least-squares on <i>F</i> ²	Full-matrix least-squares on <i>F</i> ²
Data / restraints / parameters	8186 / 0 / 454	9026 / 92 / 536
Goodness-of-fit on <i>F</i> ²	1.044	1.053
Final <i>R</i> indices [<i>F</i> ² > 2σ(<i>F</i> ²)]	<i>R</i> = 0.0235, <i>wR</i> = 0.0592	<i>R</i> = 0.0302, <i>wR</i> = 0.0846
<i>R</i> indices (all data)	<i>R</i> = 0.0264, <i>wR</i> = 0.0611	<i>R</i> = 0.0313, <i>wR</i> = 0.0856
Extinction coefficient	n/a	n/a
Largest diff. peak and hole	1.576 and -0.591 e Å ⁻³	1.712 and -1.336 e Å ⁻³

Table 4.1 Crystal structure data for [Pt(L15)(acac)] and [Pt(L16)(acac)].

4.3.7. Electronic absorption spectroscopy

The ligands appear as colourless solutions in chloroform and absorb between 250 and 400 nm. The complexes are all pale yellow solutions, absorbing between 250 and 450 nm in chloroform.

Compound	$\lambda_{\text{max}} / \text{nm}$
LH14	263, 282, 293, 312, 325, 336
LH15	258, 333, 350, 368, 389
LH16	259, 264, 277, 302, 314, 328, 345
[Pt(L14)(acac)]	261, 273, 284, 294, 342, 359, 378, 406
[Pt(L15)(acac)]	257, 298, 350, 362, 368, 389, 413
[Pt(L16)(acac)]	256, 266, 278, 297, 314, 329, 345, 361, 408

Table 4.2 Absorption maxima (λ_{max}) for ligands and complexes.

The ligands all exhibit absorption assigned to $^1\text{IL}(\pi \rightarrow \pi^*)$ transitions of the phenylquinoline at shorter wavelengths *ca.* 250 – 300 nm. The naphthyl component of **LH14** and [Pt(**L14**)(acac)] absorbs between around 300 and 350 nm and can be assigned as $^1\text{IL}(\pi \rightarrow \pi^*)$. The anthracenyl absorption in **LH15** and [Pt(**L15**)(acac)] occurs between 350 and 400 nm, again assigned as $^1\text{IL}(\pi \rightarrow \pi^*)$ and exhibits vibronic structure with the lowest energy absorption at 389 nm corresponding to ($S_1 \leftarrow S_0$). The pyrenyl moiety absorbs between 250 and 350 nm for **LH16** and [Pt(**L16**)(acac)], again expressing vibronic structure relating to excitation into different vibronic energy levels. The complexes all absorb relatively weakly between 400 and 480 nm, which corresponds to spin-allowed $^1\text{MLCT}(d \rightarrow \pi^*)$ excitation.

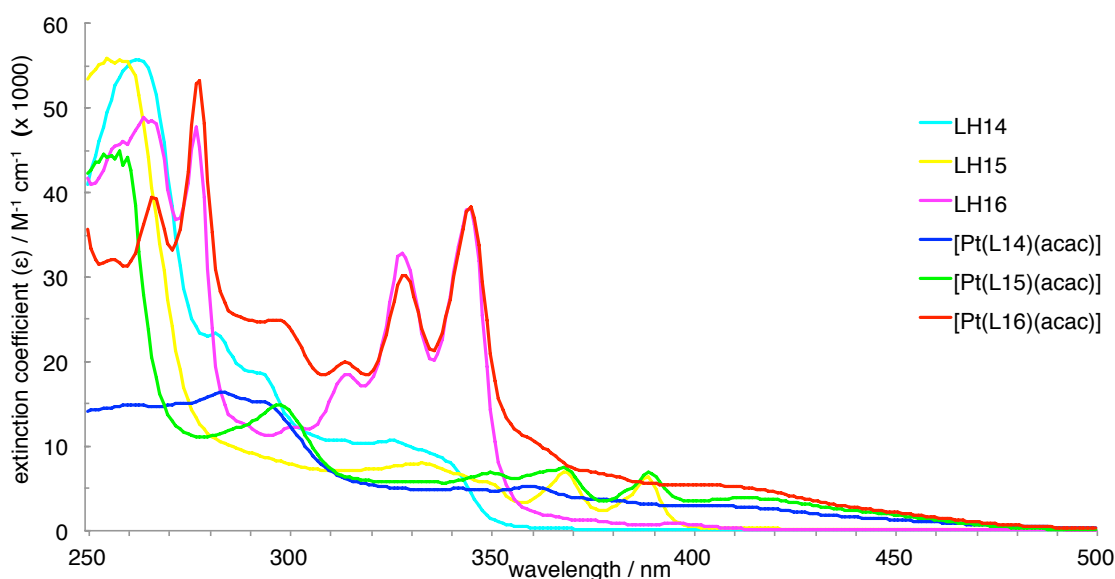


Figure 4.15 Absorption profiles for the ligands and complexes in chloroform.

4.3.8. Luminescence spectroscopy

Compound	λ_{ex}^a / nm	$^1\text{IL } \lambda_{\text{em}}^a$ / nm	$^1\text{IL } \tau^b$ / ns	$^3\text{IL } \lambda_{\text{em}}^c$ / nm
LH14	273, 327	377	1.1 ^d	483, 518, 556
LH15	354, 369, 388	392, 414, 438	1.9 ^e	487, 529
LH16	251, 271, 284, 317, 334, 353	392, 412 754, 774, 793	2.8 (50%), 7.2 (50%) ^e	602, 616, 632, 649, 665
[Pt(L14)(acac)]	-	357, 391	< 1 ^d	485, 520, 571
[Pt(L15)(acac)]	-	393, 414, 438	3.3 ^e	453, 488, 529, 578
[Pt(L16)(acac)]	-	400	3.9 (95%), 0.3 (5%) ^e	601, 616, 652, 666

^a in 1:1 chloroform and ethanol. ^b in chloroform. ^c 1:1 chloroform and ethanol glass at 77 K. ^d excited at 295 nm. ^e excited at 372 nm.

Table 4.3 Excitation, emission and lifetime data for the ^1IL and ^3IL components of the ligands and complexes. Excited at 350 nm unless otherwise stated.

Compound	λ_{ex}^a / nm	$^3\text{MLCT } \lambda_{\text{em}}^b$ / nm	$^3\text{MLCT } \tau^b$ / ns	$^3\text{MLCT } \tau^c$ / μs
[Pt(L5)(acac)]	337, 403, 466	618	380 ^d	3.4
[Pt(L14)(acac)]	281, 299, 342, 363, 413	603	543 ^d	6.6
[Pt(L15)(acac)]	281, 319, 341, 361, 380, 428	606	356 ^e	2.9
[Pt(L16)(acac)]	272, 288, 305, 320, 338, 365, 405	603	258 ^d	42 (95%), 3.7 (5%)

^a in 1:1 chloroform and ethanol. ^b in chloroform. ^c excited at 355 nm in degassed chloroform. ^d excited at 459 nm. ^e excited at 295 nm. ^f not strongly emissive enough for reliable data to be obtained.

Table 4.4 Excitation, emission and lifetime data for the $^3\text{MLCT}$ component of the complexes. Excited at 350 nm unless otherwise stated.

The excitation profiles for complexes of **L14** to **L16** all exhibit excitation of both the chromophore and the $^1\text{MLCT}$ band. This suggests that the $^3\text{MLCT}$ is of chromophoric parentage as well as the expected $^1\text{MLCT}$ component. This indicates that, upon excitation to S_1 , all the ligands undergo a degree of energy transfer to the $^1\text{MLCT}$.

4.3.8.1. Naphthyl system

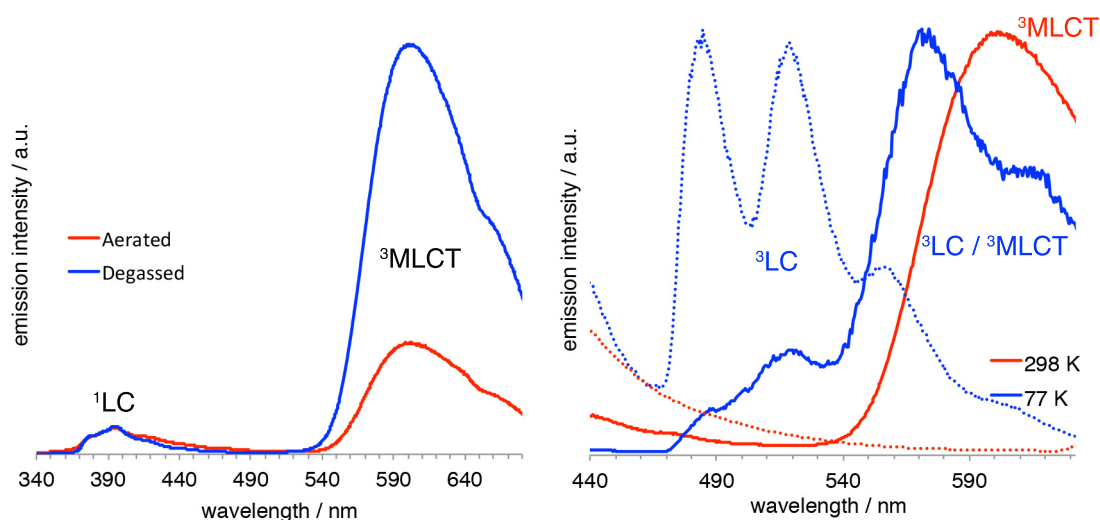


Figure 4.16 Comparison of the aerated and degassed emission in chloroform (*left*) and room temperature and low temperature emission in 1:1 chloroform and ethanol (*right*) of [Pt(**L14**)(acac)]. Room temperature and low temperature emission of **LH14** is also included with dashed lines (*right*).

The photophysical data for [Pt(**L14**)(acac)] and **LH14** reveal the presence of triplet emission from the naphthyl moiety in both the complex and the ligand between 470 and 630 nm at low temperature. The emissive energy from the ^3nap state just overlaps that of the $^3\text{MLCT}$ state. Both room and low temperature measurements show very weakly emissive ^1nap states even in contrast to the $^3\text{MLCT}$ in aerated chloroform. The lifetime of the emission in aerated chloroform is in excess of 540 ns, which is much longer than the lifetimes of the **L5**, **L15** and **L16** complexes, which do not exceed 380 ns. The degassed lifetime is almost double that of [Pt(**L5**)(acac)], at 6.6 μs .

4.3.8.2. Anthracenyl system

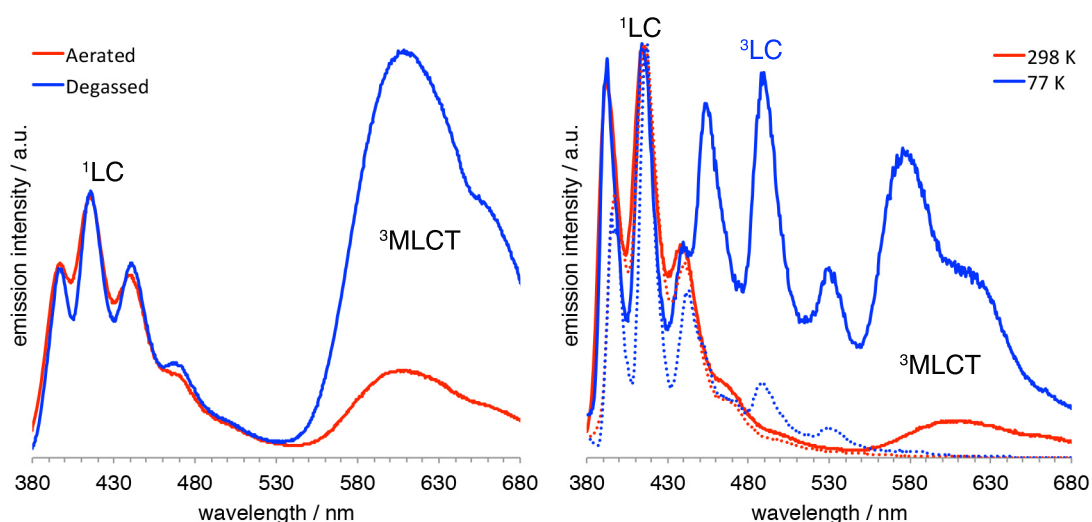


Figure 4.17 Comparison of the aerated and degassed emission in chloroform (*left*) and room temperature and low temperature emission in 1:1 chloroform and ethanol (*right*) of [Pt(**L15**)(acac)]. Room temperature and low temperature emission of **LH15** is also included with dashed lines (*right*).

[Pt(**L15**)(acac)] exhibits emission from both the anthracene and the $^3\text{MLCT}$ in chloroform at room temperature. The degassed solution shows the expected increase in intensity of the $^3\text{MLCT}$ emission, due to the lack of quenching by dissolved oxygen, but still shows emission from the anthracenyl component. Most literature reports anthracene phosphorescence at around 700 nm.³ Despite the literature, there is no visible emission beyond the emission *ca.* 600 nm from the $^3\text{MLCT}$ state. In order to be sure that the anthracenyl triplet state was not masked by the $^3\text{MLCT}$, the low temperature measurements were run on both **P8** and **LH15**. They both confirmed a lack of emission at 700 nm and suggest that the triplet state has a much higher energy, which was also found by Melo *et al.* for 9-(methylaminomethyl)anthracene.⁴⁰ The lifetimes in aerated and degassed solvents are 356 ns and 2.9 μs , respectively, which are both very similar to that of [Pt(**L5**)(acac)].

4.3.8.3. Pyrenyl system

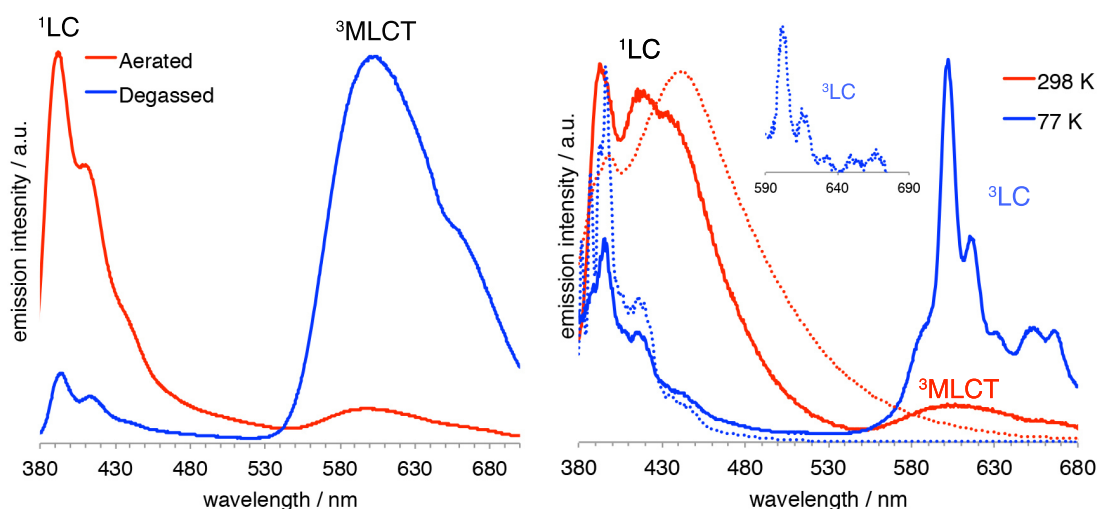


Figure 4.18 Comparison of the aerated and degassed emission in chloroform (*left*) and room temperature and low temperature emission in 1:1 chloroform and ethanol (*right*) of [Pt(**L16**)(acac)]. Room temperature and low temperature emission of **LH16** is also included with dashed lines (*right*).

Insert: Expanded section of **LH16** at low temperature to show evidence of ^3IL emission.

Measurements at 77 K of [Pt(**L16**)(acac)] and **LH16** reveal emission from ^3pyr from 590 to 680 nm, which is in accordance with literary values for the pyrene triplet state. The ^3pyr state for the free ligand is barely visible compared to ^1pyr emission, in contrast to the dominating ^3pyr emission in the presence of the heavy platinum atom. The $^3\text{MLCT}$ emission is more quenched in aerated solvent than is observed for the naphthyl and anthracenyl complexes. The lifetime in aerated solvent was significantly shorter than the other aerated lifetimes, at just 258 ns, whilst the degassed solution exhibits a lifetime in chloroform of 42 μs , which is over an order of magnitude longer than that observed for the anthracenyl complex.

4.3.8.4. Energy pathways

The very weakly emissive ^1nap state in $[\text{Pt}(\text{L14})(\text{acac})]$ suggests that there is a high degree of energy transfer from the ^1nap to the $^1\text{MLCT}$ state. The extended lifetime in aerated chloroform is most likely due to population of the $^3\text{MLCT}$ state by partial energy transfer from ^3nap , although much of the ^3nap state is likely to be quenched by oxygen so the two deactivation pathways to S_0 are competitive. The extended lifetime of the $^3\text{MLCT}$ in degassed chloroform is likely a result of partial equilibration of the ^3nap and $^3\text{MLCT}$ states due to limited overlying of the two T_1 states, resulting in an energy pathway as shown in Figure 4.19.

There is very little overlap of the $^3\text{anthr}$ and $^3\text{MLCT}$ states in $[\text{Pt}(\text{L15})(\text{acac})]$, which gives rise to the shortest degassed lifetime observed for the three complexes. The lifetime is similar to that of $[\text{Pt}(\text{L5})(\text{acac})]$ where there is no appended chromophore suggesting no equilibration is occurring between the triplet states and each of the two systems is unaffected by the other, as shown in Figure 4.20. Having said this, the graphs show that intersystem crossing to the $^3\text{anthr}$ state is much more dominant in the complex than the free ligand, due to the spin orbit coupling facilitated by the presence of the heavy Pt^{II} atom. The lack of quenched anthracenyl emission further suggests that energy transfer from the $^1\text{anthr}$ to the $^1\text{MLCT}$ state is not efficient.

There is strong spectral overlap of the $^3\text{MLCT}$ state emission and the ^3pyr state emission for $[\text{Pt}(\text{L16})(\text{acac})]$, which suggests that interplay between the two states may be possible. The dramatically augmented lifetime suggests that, given the proximate energies of the ^3pyr and $^3\text{MLCT}$ states, interplay between the two states is resulting in the equilibration of the energies, which is leading to a much longer lifetime of 42 μs . The aerated system appears much shorter due to energy transfer into the ^3pyr state from the $^3\text{MLCT}$ state, which is then rapidly quenched by dissolved oxygen. The resultant interplay between the states can be seen in the energy diagram in Figure 4.21.

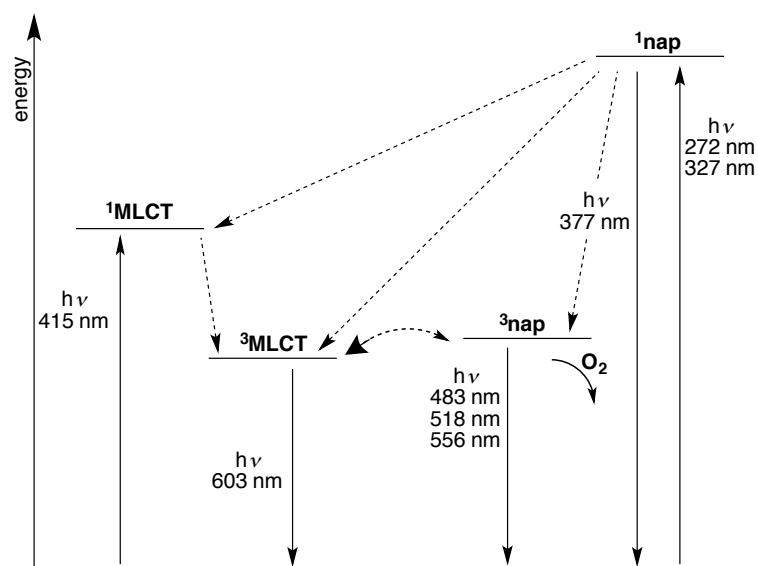


Figure 4.19 Energy level diagram of the relevant excited states of [Pt(L14)(acac)]

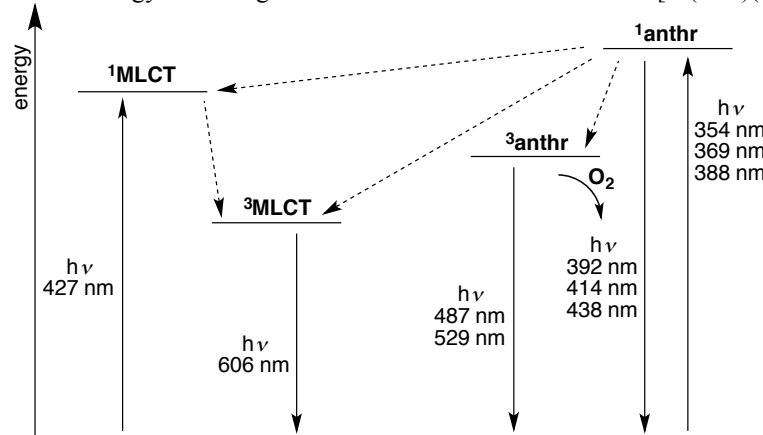


Figure 4.20 Energy level diagram of the relevant excited states of [Pt(**L15**)(acac)]

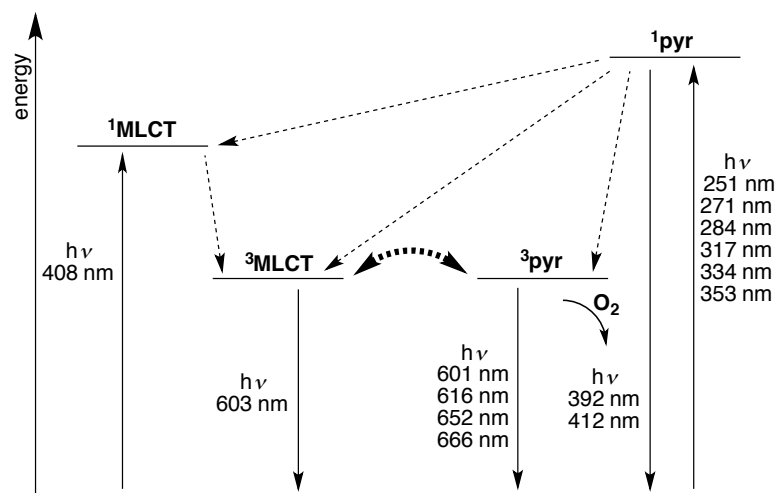


Figure 4.21 Energy level diagram of the relevant excited states of [Pt(**L16**)(acac)]

4.4. Conclusion

A novel set of ligands with an appended chromophore were developed with adequate solubility to successfully cyclometallate to Pt^{II}. The ligands incorporating pyrene and naphthalene exhibited evidence for two structural isomers, which were believed to form one where the chromophore interacts with the phenylquinoline through π -stacking interactions and one in which there is no intramolecular interactions of this type. The abundance of these isomers was found to be roughly 3:1 whilst the anthracenyl ligand was found to be dominated by one structural isomer with an abundance of > 95%.

The β -diketonate complexes were synthesised to give [Pt(L)(acac)] systems to aid solubility and stability so that the photophysical properties could be measured. The complexes of **L14** and **L16** were again found to possess two isomers, which was confirmed through the presence of two coordinated acac species. This was visible both in the ¹H and ¹³C NMR spectra and, although ¹⁹⁵Pt NMR spectra were acquired, the broadness of the signals prevented observation of two ¹⁹⁵Pt environments.

Photophysical studies revealed that there is interplay between the chromophoric and metal-based excitation and emission pathways. Energy transfer from the S₁ state of the chromophore to the ^{1/3}MLCT excited state was observed, as well as deactivation from the S₁ state of the chromophores as fluorescence. Low temperature (77 K) measurements revealed the T₁ states of the naphthyl, anthracenyl and pyrenyl moieties, with the ³pyr and ³nap states being close in energy to ³MLCT. Aerated and degassed lifetime data revealed equilibration of the ³pyr and ³MLCT states, resulting in a lifetime of 42 μ s, partial interplay between ³nap and ³MLCT and no observable energy transfer between ³anthr and ³MLCT.

4.5. Experimental

4.5.1. General physical measurements

All physical measurements were carried out as outlined in Chapter 2.

The μs lifetimes were collected using a Hamamatsu R5509-73 detector (cooled to -80°C using a C9940 housing). The pulsed laser source was a Continuum Minilite Nd:YAG configured for 355 nm output. All lifetime data were collected using the JY-Horiba FluoroHub single photon counting module in multi-channel scalar mode. Lifetimes were obtained using the provided software, DAS6.

4.5.2. Molecular structure calculations

The two proposed structures were refined in Avogadro using the UFF optimisation.^{37, 38}

4.5.3. Precursor synthesis

Synthesis of P4: Based on a modified literature methodology.³³ To a stirring suspension of anthracene methanol (0.500 g, 2.404 mmol) in chloroform (50 mL) was added, dropwise, thionyl chloride (0.35 mL, 4.808 mmol) and DMF (1 drop). The reaction was heated at reflux for 3 h under dinitrogen before being cooled and the solvent and volatile reagents removed *in vacuo*. The residue was dissolved in dichloromethane (20 mL) and washed with water (2 x 10 mL) and brine (1 x 10 mL) before being dried over MgSO_4 and dried *in vacuo*. Yield 0.516, (95%). ^1H NMR (400 MHz, CDCl_3): δ_{H} 8.47 (1H, s), 8.31 (2H, dd, $^3J_{\text{HH}} = 8.8$ Hz, $^4J_{\text{HH}} = 0.8$ Hz), 8.02 (2H, d, $^3J_{\text{HH}} = 8.4$ Hz), 7.62 (2H, ddd, $^3J_{\text{HH}} = 9.2$ Hz, $^3J_{\text{HH}} = 6.8$ Hz, $^4J_{\text{HH}} = 1.6$ Hz), 7.51 (2H, ddd, $^3J_{\text{HH}} = 8.4$ Hz, $^3J_{\text{HH}} = 6.8$ Hz, $^4J_{\text{HH}} = 1.2$ Hz), 5.97 (2H, s) ppm.

Synthesis of P5: Based on a literature methodology.³⁴ **P4** (0.500 g, 2.208 mmol) and potassium phthalimide (0.450 g, 2.432 mmol) were dissolved in DMF (10 mL) and heated to 100°C for 48 h under dinitrogen. The solution was cooled in the freezer, yielding a light yellow precipitate, which was filtered and washed with cold DMF (2 mL) and water (2 x 20 mL). The resulting precipitation in the filtrate was collected separately and treated in the same manner. The second crop was combined with the first if it was found to be spectroscopically pure. Yield = 0.618 g, (83%). ^1H NMR

(400 MHz, CDCl₃): δ_{H} 8.66 (2H, dd, $^3J_{\text{HH}} = 8.8$ Hz, $^4J_{\text{HH}} = 0.8$ Hz), 8.49 (1H, s), 8.02 (2H, dd, $^3J_{\text{HH}} = 8.4$ Hz, $^4J_{\text{HH}} = 0.4$ Hz), 7.78 – 7.74 (2H, m), 7.77 – 7.63 (2H, m), 7.60 (2H, ddd, $^3J_{\text{HH}} = 6.8$ Hz, $^3J_{\text{HH}} = 9.2$ Hz, $^4J_{\text{HH}} = 1.6$ Hz), 7.48 (2H, ddd, $^3J_{\text{HH}} = 6.4$ Hz, $^3J_{\text{HH}} = 8.4$ Hz, $^4J_{\text{HH}} = 0.8$ Hz), 5.87 (2H, s) ppm.

Synthesis of P6: Based on a literature methodology.³⁴ **P5** (0.230 g, 0.682 mmol) was dissolved in ethanol (17 mL) to which, hydrazine monohydrate (0.17 mL, 3.410 mmol) was added dropwise. The solution was heated at reflux for 24 h under dinitrogen before being cooled to give a white precipitate. The solid was filtered and water (10 mL) was added to the filtrate. The ethanol was removed *in vacuo* leaving an aqueous solution to which dichloromethane (2 x 20 mL) and sodium hydroxide (2 M soln, 10 mL) were added. The organic layer was collected and acidified with hydrochloric acid (1 M soln, 2 x 10 mL). The aqueous layer was collected and neutralised with sodium hydroxide (2 M soln). The product was extracted into dichloromethane (2 x 20 mL), which was washed with brine (10 mL) and dried over MgSO₄. The solvent was removed *in vacuo*. Yield = 0.136 g, (96%). ¹H NMR (400 MHz, CDCl₃): δ_{H} 8.31 (1H, s), 8.25 (2H, d, $^3J_{\text{HH}} = 8.8$ Hz), 7.94 (2H, d, $^3J_{\text{HH}} = 8.0$ Hz), 7.48 – 7.45 (2H, m), 7.41 – 7.38 (2H, m), 4.74 (2H, s), 1.60 (2H, br. s) ppm.

General procedure for reductive alkylations: Based on a modified literature methodology.³⁶ The aldehyde (1 eq) and octylamine (1 eq) were dissolved in ethanol (20 mL) and heated at reflux for 16 h under dinitrogen. The reaction was cooled and NaBH₄ (excess) was added in portions. The reaction was stirred for a further 16 h before being diluted with dichloromethane (20 mL) and washed with water (2 x 20 mL) and brine (20 mL). The organic phase was dried over MgSO₄ before the solvent was removed *in vacuo*.

Synthesis of P7: Following the general procedure for reductive alkylations using 1-naphthaldehyde (0.254 g, 1.628 mmol), 1-octylamine (0.210 g, 1.628 mmol) and NaBH₄ (0.124 g, 3.256 mmol). Obtained as a light yellow oil. Yield = 0.358 g, (82%). ¹H NMR (400 MHz, CDCl₃): δ_{H} 8.04 (1H, d, $^3J_{\text{HH}} = 8.0$ Hz), 7.85 (1H, dd, $^3J_{\text{HH}} = 8.0$ Hz, $^4J_{\text{HH}} = 1.6$ Hz), 7.77 (1H, dd, $^3J_{\text{HH}} = 7.6$ Hz, $^4J_{\text{HH}} = 1.6$ Hz), 7.54 – 7.39 (4H, m), 4.21 (2H, s), 2.70 (2H, t, $^3J_{\text{HH}} = 7.2$ Hz), 1.56 – 1.49 (2H, m), 1.33 – 1.19 (10H, m), 0.86 (3H, t, $^3J_{\text{HH}} = 7.2$ Hz) ppm.

Synthesis of P8: Following the general procedure for reductive alkylations using 9-anthraldehyde (0.163 g, 0.789 mmol), 1-octylamine (0.102 g, 0.789 mmol) and NaBH₄ (0.060 g, 1.577 mmol). The product was purified by column chromatography (silica, dichloromethane) and was eluted with dichloromethane/methanol (9:1). Yield = 0.242 g, (96%). ¹H NMR (400 MHz, CDCl₃): δ_H 8.41 (1H, s), 8.34 (2H, dd, ³J_{HH} = 8.8 Hz, ⁴J_{HH} = 0.8 Hz), 8.01 (2H, d, ³J_{HH} = 8.4 Hz), 7.54 (2H, ddd, ³J_{HH} = 8.8 Hz, ³J_{HH} = 6.4 Hz), ⁴J_{HH} = 1.2 Hz), 7.47 (2H, m), 4.73 (2H, s), 2.87 (2H, t, ³J_{HH} = 7.2 Hz), 1.62 – 1.55 (2H, m), 1.35 – 1.23 (10H, m), 0.88 (3H, t, ³J_{HH} = 1.6 Hz) ppm.

Synthesis of P9: Following the general procedure for reductive alkylations using 1-pyrenecarboxaldehyde (0.169 g, 0.733 mmol), 1-octylamine (0.095 g, 0.733 mmol) and NaBH₄ (0.056 g, 1.466 mmol). The product was purified by column chromatography (silica, dichloromethane) and was eluted with dichloromethane/methanol (9:1). Yield = 0.246 g, (98%). ¹H NMR (400 MHz, CDCl₃): δ_H 8.35 (1H, d, ³J_{HH} = 9.2 Hz), 8.20 – 8.16 (2H, m), 8.15 – 8.12 (2H, m), 8.04 – 7.98 (4H, m), 4.49 (2H, s), 2.79 (2H, t, ³J_{HH} = 7.2 Hz), 1.62 – 1.54 (2H, m), 1.35 – 1.22 (10H, m), 0.88 (3H, t, ³J_{HH} = 6.8 Hz) ppm. ¹³C{¹H} NMR (125.8 MHz, CDCl₃): δ_C 131.3, 130.9, 130.8, 129.2, 127.9, 127.5, 127.4, 127.4, 127.3, 125.9, 125.2, 125.1, 124.7, 122.9, 50.9, 49.3, 31.8, 29.4, 29.3, 29.2, 27.3, 22.6, 14.1 ppm. MS(ES) found m/z = 344.2 for [M + H]⁺. UV-vis (CHCl₃): λ_{max} (ε / dm³ mol⁻¹ cm⁻¹) 266 (23400), 277 (39600), 300 (4720), 314 (11400), 327 (26700), 344 (39000) nm. IR (thin film): ν_{max} 3040, 2953, 2928, 2855, 2816, 1603, 1587, 1458, 1443, 1184, 1096, 841, 802, 710 cm⁻¹.

4.5.4. Ligand synthesis

Synthesis of LH11: Following the general procedure outlined in Chapter 2 for the synthesis of 2-phenyl-4-quinolinecarboxamides using 2-phenyl-4-quinolinecarboxylic acid (0.479 g, 1.923 mmol) and 1-naphthylamine (0.250 g, 1.748 mmol). Obtained as an off-white solid. Yield = 0.588 g, (90%). ¹H NMR (400 MHz, CDCl₃): δ_H 8.24 (1H, d, ³J_{HH} = 8.4 Hz), 8.20 – 8.17 (2H, m), 8.12 – 8.09 (3H, m), 8.06 (1H, s), 7.87 – 7.84 (1H, m), 7.81 – 7.79 (1H, m), 7.75 – 7.71 (2H, m), 7.54 – 7.41 (7H, m) ppm. ¹³C{¹H} NMR (125.8 MHz, CDCl₃): δ_C 166.3, 156.9, 148.9, 142.8, 138.8, 134.2, 131.8, 130.4, 130.3, 129.9, 129.0, 127.6, 127.5, 127.1, 126.7, 126.3, 125.8, 124.9, 123.3, 121.2, 120.5, 116.6 ppm.

Synthesis of LH12: Following a modified procedure outlined in Chapter 2 for the synthesis of 2-phenyl-4-quinolinecarboxamides using 2-phenyl-4-quinolinecarbonyl chloride (0.280 g, 1.047 mmol) and 2-aminoanthracene (0.200 g, 1.036 mmol) were heated to reflux in chloroform (20 mL) under dinitrogen for 16 h before being cooled and the product collected by filtration. The solid was washed with water (2 x 20 mL) and dried to obtain an off-white solid. Yield = 0.588 g, (90%). ^1H NMR (400 MHz, $\text{d}_6\text{-DMSO}$): δ_{H} 8.79 (1H, s), 8.58 – 8.55 (2H, m), 8.44 (1H, s), 8.39 (2H, d, $^3J_{\text{HH}} = 7.2$ Hz), 8.25 (1H, d, $^3J_{\text{HH}} = 8.0$ Hz), 8.20 (1H, d, $^3J_{\text{HH}} = 8.8$ Hz), 8.14 (1H, d, $^3J_{\text{HH}} = 9.2$ Hz), 8.10 – 8.07 (2H, m), 7.90 – 7.86 (1H, m), 7.76 (1H, d, $^3J_{\text{HH}} = 9.2$ Hz), 7.72 – 7.68 (1H, m), 7.62 – 7.48 (5H, m) ppm. $^{13}\text{C}\{^1\text{H}\}$ NMR (125.8 MHz, $\text{d}_6\text{-DMSO}$): δ_{C} 165.7, 155.9, 148.0, 145.8, 142.9, 138.1, 135.9, 131.8, 130.7, 130.3, 130.0, 129.7, 128.9, 128.8, 128.1, 127.8, 127.5, 127.4, 126.0, 125.7, 125.4, 125.2, 125.1, 123.2, 121.3, 116.9, 115.3 ppm. UV-vis (CHCl_3): λ_{max} ($\epsilon / \text{dm}^3 \text{mol}^{-1} \text{cm}^{-1}$) 263 (90200), 333 (15100), 370 (6760), 391 (4940) nm. IR (thin film): ν_{max} 2916, 1724, 1688, 1641, 1586, 1512, 1445, 1346, 1306, 1277, 1250, 1177, 750, 691 cm^{-1} .

Synthesis of LH13: Following the general procedure outlined in Chapter 2 for the synthesis of 2-phenyl-4-quinolinecarboxamides using 2-phenyl-4-quinolinecarboxylic acid (0.114 g, 0.457 mmol) and **P6** (0.086 g, 0.415 mmol). Yield = 0.162 g, (89%). ^1H NMR (400 MHz, CDCl_3): δ_{H} 8.51 (1H, s), 8.44 (2H, d, $^3J_{\text{HH}} = 9.2$ Hz), 8.20 (1H, dd, $^3J_{\text{HH}} = 8.4$ Hz, $^4J_{\text{HH}} = 0.4$ Hz), 8.10 – 8.05 (3H, m), 8.02 – 7.99 (2H, m), 7.80 (1H, s), 7.71 – 7.62 (3H, m), 7.54 – 7.41 (6H, m), 6.37 (1H, br. s), 5.78 (2H, d, $^3J_{\text{HH}} = 5.2$ Hz) ppm. $^{13}\text{C}\{^1\text{H}\}$ NMR (125.8 MHz, $\text{d}_6\text{-DMSO}$): δ_{C} 167.4, 156.7, 148.7, 142.5, 138.7, 131.6, 130.5, 130.1, 129.6, 129.4, 128.8, 128.6, 127.7, 127.4, 127.3, 127.0, 125.3, 124.9, 123.6, 123.3, 116.5, 36.7 ppm. HR-MS: calcd. for $[\text{C}_{31}\text{H}_{23}\text{N}_2\text{O}]^+$ 439.1805, found 439.1803. UV-vis (CHCl_3): λ_{max} ($\epsilon / \text{dm}^3 \text{mol}^{-1} \text{cm}^{-1}$) 257 (78500), 332 (8960), 346 (8270), 367 (8520), 388 (7720) nm. IR (thin film): ν_{max} 3285, 1626, 1587, 1518, 1493, 1445, 1344, 1275, 1260, 1179, 1153, 1080, 1022, 893, 885, 799, 766, 750, 745, 689 cm^{-1} .

Synthesis of LH14: Following the general procedure outlined in Chapter 2 for the synthesis of 2-phenyl-4-quinolinecarboxamides using 2-phenyl-4-quinolinecarboxylic acid (0.235 g, 0.941 mmol) and **P7** (0.231 g, 0.855 mmol. Column chromatography (silica) was used with various mobile phases to attempt separation of a mixture of

structural isomers however this was unsuccessful and resulted in a pure mixture of the product's two isomeric forms. Yield = 0.268 g, (89%). ^1H NMR (400 MHz, CDCl_3): δ_{H} 8.42 (1H, d, $^3J_{\text{HH}} = 8.4$ Hz), 8.19 – 7.32 (33H, m), 5.72 (1H, d, $^2J_{\text{HH}} = 14.4$ Hz), 5.18 (1H, d, $^2J_{\text{HH}} = 14.4$ Hz), 4.92 – 4.72 (2H, br. m), 3.38 – 3.16 (1H, br. m), 2.94 – 2.80 (2H, m), 4.31 – 4.11 (1H, br. m), 1.92 – 1.79 (2H, br. m), 1.47 – 0.86 (25H, m), 0.79 (3H, t, $^3J_{\text{HH}} = 6.8$ Hz) ppm. $^{13}\text{C}\{^1\text{H}\}$ NMR (125.8 MHz, CDCl_3): δ_{C} 167.7, 155.8, 147.4, 142.7, 138.1, 130.5, 130.4, 129.2, 129.1, 128.6, 128.5, 127.9, 127.7, 126.4, 126.4, 126.1, 125.8, 124.3, 123.7, 123.1, 122.2, 114.9, 45.7, 38.0, 30.4, 28.1, 27.6, 27.4, 25.2, 21.4, 13.0 ppm. HR-MS: calcd. for $[\text{C}_{35}\text{H}_{37}\text{N}_2\text{O}]^+$ 501.2900, found 501.2889. UV-vis (CHCl_3): λ_{max} ($\epsilon / \text{dm}^3 \text{mol}^{-1} \text{cm}^{-1}$) 263 (46500), 282 (19400), 293 (15600), 312 (8980), 325 (8880), 336 (7570) nm. IR (thin film): ν_{max} 3059, 2926, 2853, 1638, 1597, 1549, 1510, 1466, 1460, 1406, 1377, 1348, 1248, 1028, 793, 772, 760, 741, 694, 665 cm^{-1} .

Synthesis of LH15: Following the general procedure outlined in Chapter 2 for the synthesis of 2-phenyl-4-quinolinecarboxamides using 2-phenyl-4-quinolinecarboxylic acid (0.163 g, 0.656 mmol) and **P8** (0.190 g, 0.596 mmol). Yield = 0.282 g, (86%). ^1H NMR (400 MHz, CDCl_3): δ_{H} 8.58 – 8.54 (3H, s), 8.17 – 8.08 (5H, m), 7.84 (1H, s), 7.80 (1H, d, $^3J_{\text{HH}} = 7.2$ Hz), 7.71 – 7.65 (3H, m), 7.58 – 7.46 (5H, m), 7.39 (1H, m), 6.28 (1H, d, $^2J_{\text{HH}} = 15.2$ Hz), 5.82 (1H, d, $^2J_{\text{HH}} = 15.2$ Hz), 1.39 – 1.25 (2H, m), 1.08 – 1.00 (2H, m), 0.92 – 0.73 (8H, m), 0.68 – 0.53 (3H, m) ppm. $^{13}\text{C}\{^1\text{H}\}$ NMR (125.8 MHz, $\text{d}_6\text{-DMSO}$): δ_{C} 167.7, 155.8, 147.4, 142.7, 138.1, 130.5, 130.4, 130.2, 129.2, 129.1, 128.6, 128.5, 128.0, 127.9, 127.7, 126.6, 126.4, 126.4, 126.2, 126.1, 125.8, 125.6, 124.3, 124.0, 123.7, 123.1, 122.2, 114.9, 45.7, 38.0, 30.6, 30.4, 28.1, 27.9, 27.8, 27.6, 27.4, 26.9, 25.8, 25.2, 21.5, 21.4, 13.1, 12.9 ppm. HR-MS: calcd. for $[\text{C}_{39}\text{H}_{39}\text{N}_2\text{O}]^+$ 551.3057, found 551.3051. UV-vis (CHCl_3): λ_{max} ($\epsilon / \text{dm}^3 \text{mol}^{-1} \text{cm}^{-1}$) 258 (55700), 333 (7980), 350 (5680), 6960 (368), 389 (6320) nm. IR (thin film): ν_{max} 3057, 2955, 2924, 2855, 1628, 1593, 1549, 1495, 1462, 1447, 1431, 1406, 1373, 1343, 1263, 1240, 1180, 1159, 1123, 1028, 889, 767, 759 cm^{-1} .

Synthesis of LH16: Following the general procedure outlined in Chapter 2 for the synthesis of 2-phenyl-4-quinolinecarboxamides using 2-phenyl-4-quinolinecarboxylic acid (0.235 g, 0.941 mmol) and **P9** (0.231 g, 0.855 mmol). Column chromatography (silica) was used with various mobile phases to attempt separation of a mixture of

structural isomers however this was unsuccessful and resulted in a pure mixture of the product's two isomeric forms. Yield = 0.268 g, (89%). ^1H NMR (400 MHz, CDCl_3): δ_{H} 8.42 (1H, d, $^3J_{\text{HH}} = 8.4$ Hz), 8.19 – 7.32 (33H, m), 5.72 (1H, d, $^2J_{\text{HH}} = 14.4$ Hz), 5.18 (1H, d, $^2J_{\text{HH}} = 14.4$ Hz), 4.92 – 4.72 (2H, br. m), 3.38 – 3.16 (1H, br. m), 2.94 – 2.80 (2H, m), 4.31 – 4.11 (1H, br. m), 1.92 – 1.79 (2H, br. m), 1.47 – 0.86 (25H, m), 0.79 (3H, t, $^3J_{\text{HH}} = 6.8$ Hz) ppm. HR-MS: calcd. for $[\text{C}_{41}\text{H}_{39}\text{N}_2\text{O}]^+$ 575.3057, found 575.3046. UV-vis (CHCl_3): λ_{max} ($\epsilon / \text{dm}^3 \text{mol}^{-1} \text{cm}^{-1}$) 259 (46000), 264 (49000), 277 (47800), 302 (12200), 314 (18600), 328 (32800), 345 (38100) nm. IR (thin film): ν_{max} 3045, 2926, 2855, 1634, 1628, 1593, 1549, 1435, 1406, 1373, 1344, 1296, 1263, 1238, 1198, 1184, 1155, 1123, 1028, 889, 847, 768, 733, 694 cm^{-1} .

4.5.5. Synthesis of platinum (II) complexes

Synthesis of $[\text{Pt}(\text{L11})\text{Cl}]_2$: Following the general procedure outlined in Chapter 2 for the synthesis of platinum dimers using potassium tetrachloroplatinate (II) (0.055 g, 0.133 mmol) and **LH11** (0.050 g, 0.134 mmol). Yield = 0.062 g, (77%).

Synthesis of $[\text{Pt}(\text{L14})\text{Cl}]_2$: Following the general procedure outlined in Chapter 2 for the synthesis of platinum dimers using potassium tetrachloroplatinate (II) (0.030 g, 0.072 mmol) and **LH14** (0.040 g, 0.070 mmol). Yield = 0.050 g, (86%).

Synthesis of $[\text{Pt}(\text{L15})\text{Cl}]_2$: Following the general procedure outlined in Chapter 2 for the synthesis of platinum dimers using potassium tetrachloroplatinate (II) (0.074 g, 0.176 mmol) and **LH15** (0.085 g, 0.177 mmol). Yield = 0.099 g, (72%).

Synthesis of $[\text{Pt}(\text{L16})\text{Cl}]_2$: Following the general procedure outlined in Chapter 2 for the synthesis of platinum dimers using potassium tetrachloroplatinate (II) (0.030 g, 0.072 mmol) and **LH16** (0.040 g, 0.070 mmol). Yield = 0.050 g, (86%).

Synthesis of $[\text{Pt}(\text{L11})(\text{DMSO})\text{Cl}]$: Following the general procedure outlined in Chapter 2 for splitting platinum dimers using $[\text{Pt}(\text{L11})\text{Cl}]_2$ (0.062 g, 0.051 mmol). Yield = 0.063 g, (91%).

Synthesis of $[\text{Pt}(\text{L14})(\text{DMSO})\text{Cl}]$: Following the general procedure outlined in Chapter 2 for splitting platinum dimers using $[\text{Pt}(\text{L14})\text{Cl}]_2$ (0.047 g, 0.032 mmol). Yield = 0.041 g, (78%).

Synthesis of [Pt(L15)(DMSO)Cl]: Following the general procedure outlined in Chapter 2 for splitting platinum dimers using [Pt(L15)(Cl)]₂ (0.099 g, 0.064 mmol). Yield = 0.095 g, (87%).

Synthesis of [Pt(L16)(DMSO)Cl]: Following the general procedure outlined in Chapter 2 for splitting platinum dimers using [Pt(L16)Cl]₂ (0.050 g, 0.031 mmol). Yield = 0.050 g, (91%).

Synthesis of [Pt(L11)(acac)]: Following the general procedure outlined in Chapter 2 for coordinating β -diketonates to platinum complexes using [Pt(L11)(DMSO)Cl] (0.063 g, 0.093 mmol) and sodium acetylacetonate monohydrate (0.113 g, 0.928 mmol). The product was purified by column chromatography (silica, dichloromethane) and was eluted as the first yellow band with dichloromethane and dried to yield a dark yellow solid. Yield = 0.056 g, (91%). ¹H NMR (400 MHz, CDCl₃): δ_{H} 9.47 (1H, d, ³J_{HH} = 8.8 Hz, ⁴J_{HH} = 0.4 Hz), 9.07 (1H, br. s), 8.17 (1H, dd, ³J_{HH} = 8.4 Hz, ⁴J_{HH} = 1.2 Hz), 8.05 (1H, d, ³J_{HH} = 8.0 Hz), 7.99 (1H, d, ³J_{HH} = 7.2 Hz), 7.92 (1H, dd, ³J_{HH} = 7.6 Hz, ⁴J_{HH} = 1.6 Hz), 7.85 – 7.82 (2H, m), 7.74 – 7.70 (1H, m), 7.62 – 7.53 (5H, m), 7.28 (1H, d ³J_{HH} = 7.6 Hz), 7.15 – 7.11 (1H, m), 6.93 – 6.89 (1H, m), 5.30 (1H, s), 1.97 (3H, s), 1.51 (3H, s) ppm. ¹³C{¹H} NMR (151.2 MHz, CDCl₃): δ_{C} 185.6, 184.2, 169.5, 165.6, 152.8, 149.6, 145.4, 144.1, 139.4, 137.4, 134.2, 131.2, 129.8, 128.9, 127.4, 127.0, 126.8, 126.3, 125.8, 125.2, 124.0, 122.0, 120.9, 114.5, 101.8, 30.9, 28.4 ppm. 3239, 2922, 2853, 1674, 1655, 1597, 1580, 1543, 1522, 1497, 1464, 1454, 1435, 1391, 1377, 1344, 1296, 1277, 1198, 1148, 1020, 795, 762, 735 cm⁻¹. IR (thin film): ν_{max} 2922, 2853, 1674, 1655, 1597, 1580, 1543, 1522, 1497, 1391, 1377, 1344, 1296, 1277, 1198, 1148, 1020, 941, 795, 762, 735 cm⁻¹.

Synthesis of [Pt(L14)(acac)]: Following the general procedure outlined in Chapter 2 for coordinating β -diketonates to platinum complexes using [Pt(L14)(DMSO)Cl] (0.041 g, 0.051 mmol) and sodium acetylacetonate monohydrate (0.062 g, 0.508 mmol). The product was purified by column chromatography (silica, dichloromethane) and was eluted as the first yellow band with dichloromethane and dried to yield a dark yellow solid. Subsequent columns to isolate the two isomers of the product were attempted with no success. The products were isolated as a mixture (roughly 1:2). Yield = 0.034 g, (85%). ¹H NMR (400 MHz, CDCl₃): δ_{H} 9.59 (1H, d, ³J_{HH} = 8.4 Hz), 9.56 (1H, d, ³J_{HH} = 8.8 Hz), 8.39 (1H, d, ³J_{HH} = 8.0 Hz), 7.97 (1H, d,

$^3J_{\text{HH}} = 7.6$ Hz), 7.91 (1H, d, $^3J_{\text{HH}} = 8.0$ Hz), 7.90 (1H, d, $^3J_{\text{HH}} = 8.4$ Hz), 7.82 – 7.36 (21H, m), 7.27 – 7.23 (1H, m), 7.17 – 7.11 (3H, m), 7.03 – 7.00 (1H, m), 5.71 (1H, d, $^2J_{\text{HH}} = 14.8$ Hz), 5.57 (1H, s), 5.53 (1H, s), 5.15 (1H, d, $^2J_{\text{HH}} = 14.8$ Hz), 4.89 – 4.78 (2H, br. m), 4.22 – 4.05 (1H, br. m), 3.35 – 3.20 (1H, m), 2.92 – 2.80 (2H, m), 2.05 (3H, s), 2.03 (3H, s), 2.01 (3H, s), 2.00 (3H, s), 1.91 – 1.77 (2H, br. m), 1.50 – 0.90 (22H, m), 0.89 (3H, t, $^3J_{\text{HH}} = 6.8$ Hz), 0.80 (3H, t, $^3J_{\text{HH}} = 7.2$ Hz) ppm. $^{13}\text{C}\{^1\text{H}\}$ NMR (151.2 MHz, CDCl_3): δ_{C} 184.5, 184.4, 183.2, 183.1, 168.8, 168.6, 167.3, 166.7, 148.5, 148.5, 144.8, 144.7, 144.6, 143.8, 139.1, 133.1, 132.8, 130.9, 130.8, 130.3, 130.2, 130.2, 129.7, 129.0, 128.9, 128.6, 128.5, 128.2, 128.0, 128.0, 127.9, 127.9, 127.7, 127.2, 126.5, 126.2, 126.1, 126.0, 125.9, 125.6, 125.4, 123.9, 123.8, 123.7, 123.3, 123.1, 123.0, 123.0, 122.8, 121.0, 114.8, 112.6, 112.1, 100.8, 100.7, 49.1, 46.1, 44.8, 43.9, 34.4, 30.8, 30.6, 28.3, 28.2, 27.9, 27.9, 27.3, 27.3, 27.0, 26.6, 26.2, 26.1, 25.4, 21.6, 21.5, 13.1, 13.0 ppm. ^{195}Pt (107.51 MHz, CDCl_3): δ_{Pt} -2784 ppm. UV-vis (CHCl_3): λ_{max} ($\epsilon / \text{dm}^3 \text{mol}^{-1} \text{cm}^{-1}$) 261 (12500), 273 (12500), 284 (13600), 294 (12700), 342 (4140), 359 (4370), 378 (3070), 406 (2450) nm. IR (thin film): ν_{max} 3059, 2953, 2926, 2855, 1638, 1580, 1541, 1522, 1470, 1433, 1393, 1373, 1296, 1277, 1202, 1159, 1030, 1022, 937, 883, 791, 779, 765, 729 cm^{-1} .

Synthesis of [Pt(L15)(acac)]: Following the general procedure outlined in Chapter 2 for coordinating β -diketonates to platinum complexes using [Pt(L15)(DMSO)Cl] (0.095 g, 0.111 mmol) and sodium acetylacetonate monohydrate (0.135 g, 1.109 mmol). The product was purified by column chromatography (silica, dichloromethane). The product was eluted as the first yellow band with dichloromethane and dried to yield a dark yellow solid. Yield = 0.068 g, (73%). ^1H NMR (400 MHz, CDCl_3): δ_{H} 9.58 (1H, d, $^3J_{\text{HH}} = 8.8$ Hz), 8.56 – 8.54 (3H, m), 8.11 (2H, dd, $^3J_{\text{HH}} = 8.4$ Hz, $^4J_{\text{HH}} = 0.8$ Hz), 7.74 – 7.65 (6H, m), 7.59 – 7.55 (2H, m), 7.49 (1H, dd, $^3J_{\text{HH}} = 7.6$ Hz, $^4J_{\text{HH}} = 0.8$ Hz), 7.38 – 7.34 (1H, m), 7.26 – 7.23 (1H, m), 7.17 – 7.14 (1H, m), 6.27 (1H, d, $^2J_{\text{HH}} = 15.2$ Hz), 5.81 (1H, d, $^2J_{\text{HH}} = 15.2$ Hz), 5.56 (1H, s), 2.56 (2H, t, $^3J_{\text{HH}} = 8.0$ Hz), 2.04 (3H, s), 2.02 (3H, s), 1.42 – 1.22 (2H, m), 1.13 – 1.04 (2H, m), 0.99 – 0.82 (6H, m), 0.77 (3H, t, $^3J_{\text{HH}} = 7.2$ Hz), 0.75 – 0.68 (2H, m), 0.65 – 0.55 (2H, m) ppm. $^{13}\text{C}\{^1\text{H}\}$ NMR (125.8 MHz, CDCl_3): δ_{C} 184.5, 184.4, 183.2, 183.1, 168.8, 168.7, 167.2, 166.7, 148.5, 144.8, 144.6, 144.5, 144.0, 139.1, 138.9, 130.6, 130.3, 130.2, 130.2, 130.1, 129.9, 129.5, 129.0, 128.8, 128.7, 128.6, 128.5, 128.4, 127.5, 127.4, 126.9, 126.8, 126.3, 126.2, 126.0, 125.8, 125.3, 125.1,

124.6, 124.6, 124.5, 124.3, 123.9, 123.8, 123.8, 123.7, 123.6, 123.5, 123.4, 123.2, 122.9, 122.7, 122.4, 120.2, 112.7, 112.3, 100.8, 100.7, 49.2, 46.0, 44.7, 43.9, 30.7, 30.5, 28.7, 28.3, 28.2, 27.9, 27.9, 27.3, 27.0, 26.5, 26.2, 26.1, 25.4, 21.6, 21.5, 13.1, 13.0 ppm. ^{195}Pt (107.51 MHz, CDCl_3): δ_{Pt} -2786 ppm. HR-MS: calcd. for $[\text{C}_{44}\text{H}_{44}\text{N}_2\text{O}_4^{194}\text{Pt}]^+$ 859.3001, found 859.3009. UV-vis (CHCl_3): λ_{max} ($\epsilon / \text{dm}^3 \text{mol}^{-1} \text{cm}^{-1}$) 257 (44000), 298 (14800), 350 (6870), 362 (6930), 368 (7440), 389 (6850), 413 (3860) nm. IR (thin film): ν_{max} 2959, 2924, 2855, 2369, 1734, 1674, 1636, 1582, 1524, 1458, 1433, 1391, 1302, 1279, 1262, 1024, 939, 885, 806, 760, 731 cm^{-1} .

Synthesis of [Pt(L16)(acac)]: Following the general procedure outlined in Chapter 2 for coordinating β -diketonates to platinum complexes using $[\text{Pt}(\text{L16})(\text{DMSO})\text{Cl}]$ (0.050 g, 0.057 mmol) and sodium acetylacetonate monohydrate (0.069 g, 0.568 mmol). The product was purified by column chromatography (silica, dichloromethane) and was eluted as the first yellow band with dichloromethane and dried to yield a dark yellow solid. Subsequent columns to isolate the two isomers of the product were attempted with no success. The products were isolated as a mixture (roughly 1:2). Yield = 0.068 g, (73%). ^1H NMR (400 MHz, CDCl_3): δ_{H} 9.59 (1H, d, $^3J_{\text{HH}} = 8.4$ Hz), 9.55 (1H, d, $^3J_{\text{HH}} = 8.8$ Hz), 8.63 (1H, d, $^3J_{\text{HH}} = 9.2$ Hz), 8.32 – 7.67 (24H, m), 7.63 – 7.59 (2H, m), 7.51 (1H, dd, $^3J_{\text{HH}} = 7.6$ Hz, $^4J_{\text{HH}} = 1.2$ Hz), 7.40 – 7.36 (1H, m), 7.26 – 7.22 (1H, m), 7.16 – 7.08 (3H, m), 6.93 – 6.89 (1H, m), 6.01 (1H, d, $^2J_{\text{HH}} = 14.4$ Hz), 5.56 (1H, s), 5.53 (1H, s), 5.40 (1H, d, $^2J_{\text{HH}} = 14.8$ Hz), 5.16 – 5.05 (2H, br. m), 4.13 – 4.02 (1H, br. m), 3.44 – 3.33 (1H, br. m), 2.89 – 2.83 (2H, m), 2.04 (3H, s), 2.02 (3H, s), 2.01 (3H, s), 2.00 (3H, s), 1.90 – 1.80 (2H, br. m), 1.56 – 1.46 (2H, m), 1.41 – 0.90 (20H, m), 0.87 (3H, t, $^3J_{\text{HH}} = 7.2$ Hz), 0.78 (3H, t, $^3J_{\text{HH}} = 7.2$ Hz) ppm. $^{13}\text{C}\{^1\text{H}\}$ NMR (125.8 MHz, CDCl_3): δ_{C} 184.5, 184.4, 183.2, 183.1, 168.8, 168.7, 167.2, 166.7, 148.5, 144.8, 144.6, 144.5, 144.0, 139.1, 130.6, 130.3, 130.2, 130.2, 130.1, 129.9, 129.5, 129.0, 128.8, 128.7, 128.6, 128.5, 128.4, 127.5, 127.5, 127.4, 127.4, 126.9, 126.8, 126.3, 126.2, 126.0, 125.8, 125.3, 125.1, 124.6, 124.6, 124.5, 124.3, 123.9, 123.9, 123.8, 123.8, 123.7, 123.6, 123.5, 123.4, 123.2, 122.9, 122.7, 122.4, 120.3, 112.7, 112.4, 100.8, 100.7, 49.3, 46.1, 44.7, 43.9, 30.8, 30.5, 28.3, 28.2, 27.9, 27.9, 27.3, 27.1, 26.5, 26.2, 25.4, 21.6, 21.5, 13.1, 13.0 ppm. ^{195}Pt (107.51 MHz, CDCl_3): δ_{Pt} -2788 ppm. HR-MS: calcd. for $[\text{C}_{46}\text{H}_{45}\text{N}_2\text{O}_4^{194}\text{Pt}]^+$ 883.3001, found 883.3010. UV-vis (CHCl_3): λ_{max} ($\epsilon / \text{dm}^3 \text{mol}^{-1} \text{cm}^{-1}$) 256 (32100), 266 (39400), 278 (48200), 297 (25000), 314 (19900), 329(30300), 345 (38300), 361

(10600), 408 (5330) nm. IR (thin film): ν_{max} 3080, 3046, 2951, 2924, 2853, 2245, 1634, 1601, 1580, 1559, 1520, 1470, 1456, 1435, 1393, 1371, 1277, 1198, 1184, 1157, 1022, 907, 847, 762, 731 cm^{-1} .

4.6. References

1. A. G. Crawford, A. D. Dwyer, Z. Q. Liu, A. Steffen, A. Beeby, L. O. Palsson, D. J. Tozer and T. B. Marder, *J. Am. Chem. Soc.*, 2011, **133**, 13349-13362.
2. J. R. Lakowicz, *Principles of Fluorescence Spectroscopy*, Springer, New York, 3rd edn., 2006.
3. D. F. Evans, *J. Chem. Soc.*, 1957, 1351-1357.
4. M. Y. Berezin and S. Achilefu, *Chem. Rev.*, 2010, **110**, 2641-2684.
5. J. B. Birks, I. H. Munro and D. J. Dyson, *Proc. R. Soc. A*, 1963, **275**, 575.
6. C. Yu and V. W. W. Yam, *Chem. Commun.*, 2009, 1347-1349.
7. A. C. Ribou, J. Vigo and J. M. Salmon, *Photochem. Photobiol.*, 2004, **80**, 274-280.
8. W. M. Vaughn and G. Weber, *Biochemistry*, 1970, **9**, 464-473.
9. M. Flamm and D. Schachter, *Nature*, 1982, **298**, 290-292.
10. D. Sugahara, J. Amano and T. Irimura, *Anal. Sci.*, 2003, **19**, 167-169.
11. A. E. Jablonski, T. Kawakami, A. Y. Ting and C. K. Payne, *J. Phys. Chem. Lett.*, 2010, **1**, 1312-1315.
12. P. Kaden, E. Mayer-Enthart, A. Trifonov, T. Fiebig and H. A. Wagenknecht, *Angew. Chem. Int. Edit.*, 2005, **44**, 1637-1639.
13. R. Huber, T. Fiebig and H. A. Wagenknecht, *Chem. Commun.*, 2003, 1878-1879.
14. E. T. Kool, J. C. Morales and K. M. Guckian, *Angew. Chem. Int. Edit.*, 2000, **39**, 990-1009.
15. A. Okamoto, K. Kanatani and I. Saito, *J. Am. Chem. Soc.*, 2004, **126**, 4820-4827.
16. H. Kashida, H. Asanuma and M. Komiyama, *Chem. Commun.*, 2006, 2768-2770.
17. A. A. Marti, X. X. Li, S. Jockusch, Z. M. Li, B. Raveendra, S. Kalachikov, J. J. Russo, I. Morozova, S. V. Puthanveetil, J. Y. Ju and N. J. Turro, *Nucleic Acids Res.*, 2006, **34**, 3161-3168.
18. J. Y. Hu, X. Meng and S. Schacher, *J. Neurosci.*, 2002, **22**, 2669-2678.
19. R. Lincoln, L. Kohler, S. Monro, H. M. Yin, M. Stephenson, R. F. Zong, A. Chouai, C. Dorsey, R. Hennigar, R. P. Thummel and S. A. McFarland, *J. Am. Chem. Soc.*, 2013, **135**, 17161-17175.

20. M. Stephenson, C. Reichardt, M. Pinto, M. Wächtler, T. Sainuddin, G. Shi, H. Yin, S. Monro, E. Sampson, B. Dietzek and S. A. McFarland, *J. Phys. Chem. A*, 2014.
21. A. F. Morales, G. Accorsi, N. Armaroli, F. Barigelletti, S. J. A. Pope and M. D. Ward, *Inorg. Chem.*, 2002, **41**, 6711-6719.
22. T. Forster, *Discuss. Faraday Soc.*, 1959, 7-17.
23. D. S. Tyson, K. B. Henbest, J. Bialecki and F. N. Castellano, *J. Phys. Chem. A*, 2001, **105**, 8154-8161.
24. F. Ragone, H. H. M. Saavedra, P. M. D. Gara, G. T. Ruiz and E. Wolcan, *J. Phys. Chem. A*, 2013, **117**, 4428-4435.
25. S. A. Denisov, Y. Cudre, P. Verwilt, G. Jonusauskas, M. Marin-Suarez, J. F. Fernandez-Sanchez, E. Baranoff and N. D. McClenaghan, *Inorg. Chem.*, 2014, **53**, 2677-2682.
26. M. Hissler, A. Harriman, A. Khatyr and R. Ziessel, *Chem. Eur. J.*, 1999, **5**, 3366-3381.
27. A. Harriman, M. Hissler and R. Ziessel, *Phys. Chem. Chem. Phys.*, 1999, **1**, 4203-4211.
28. D. Nolan, B. Gil, L. S. Wang, J. Z. Zhao and S. M. Draper, *Chem. Eur. J.*, 2013, **19**, 15615-15626.
29. W. T. Wu, W. H. Wu, S. M. Ji, H. M. Guo and J. Z. Zhao, *Eur. J. Inorg. Chem.*, 2010, 4470-4482.
30. E. S. H. Lam, D. P. K. Tsang, W. H. Lam, A. Y. Y. Tam, M. Y. Chan, W. T. Wong and V. W. W. Yam, *Chem. Eur. J.*, 2013, **19**, 6385-6397.
31. S. Gabriel, *Berichte der deutschen chemischen Gesellschaft*, 1887, **20**, 2224-2236.
32. M. S. Gibson and R. W. Bradshaw, *Angew. Chem. Int. Edit.*, 1968, **7**, 919-930.
33. I. Mallard, D. Landy, N. Bouchemal and S. Fourmentin, *Carbohydr. Res.*, 2011, **346**, 35-42.
34. Y. Sun, C. Zhong, R. Gong, H. Mu and E. Fu, *J. Org. Chem.*, 2009, **74**, 7943-7946.
35. L. A. Mullice, R. H. Laye, L. P. Harding, N. J. Buurma and S. J. A. Pope, *New J. Chem.*, 2008, **32**, 2140-2149.
36. M. Jaseer and E. Prasad, *J. Photochem. Photobiol., A*, 2010, **214**, 248-256.
37. M. D. Hanwell, D. E. Curtis, D. C. Lonie, T. Vandermeersch, E. Zurek and G. R. Hutchison, *J. Cheminform.*, 2012, **4**.

38. A. K. Rappe, C. J. Casewit, K. S. Colwell, W. A. Goddard and W. M. Skiff, *J. Am. Chem. Soc.*, 1992, **114**, 10024-10035.
39. A. Bossi, A. F. Rausch, M. J. Leidl, R. Czerwieniec, M. T. Whited, P. I. Djurovich, H. Yersin and M. E. Thompson, *Inorg. Chem.*, 2013, **52**, 12403-12415.
40. J. S. de Melo, A. J. F. N. Sobral, A. M. D. R. Gonsalves and H. D. Burrows, *J. Photochem. Photobiol. A*, 2005, **172**, 151-160.

**Chapter 5: Development of anthraquinone-derived scaffolds
for lanthanide (III) ion coordination**

5.1. Introduction

This chapter discusses the development of anthraquinone-based polydentate ligand architectures for the incorporation of Ln^{III} ions in order to study the photophysical properties and assess the relaxivity of the compounds towards potential bimodal contrast agents.

5.1.1. Anthraquinone

It is important to firstly understand some fundamental properties of anthraquinones and their prior incorporation into metal complexes. Anthraquinones (AQs) are naturally occurring products, which can be found in both plants and animals.¹⁻³ Anthraquinone (AQ) is a polycyclic compound made up of two benzene rings fused together by carbonyl groups at the 9- and 10-positions (Figure 5.1). It is usually synthesised through the oxidation of anthracene although it can be prepared *via* a Friedel-Crafts reaction using benzene and phthalic anhydride with AlCl_3 .⁴ AQs have long been functionalised and studied for a plethora of applications ranging from dyes and pigments through to biological and medicinal uses.

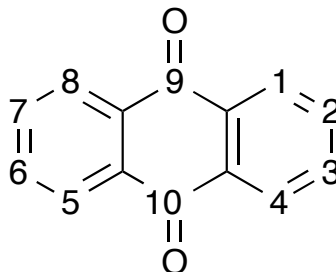


Figure 5.1 Structure and numbering of anthraquinone.

Their utility is made more appealing by the facile functionalisation and a large variety of commercially available starting materials, which lend themselves to the development of more complicated species with various functionalities for a breadth of applications. They can undergo functionalisation through nucleophilic substitution at the 1-, 4-, 5- and 8-positions to give the amino- derivatives of the chloro- precursors, alkoxyl formation from the fluoro- derivatives and Sonogashira couplings from iodo-derivatives to give alkynyl functionality, amongst others.⁵⁻⁹

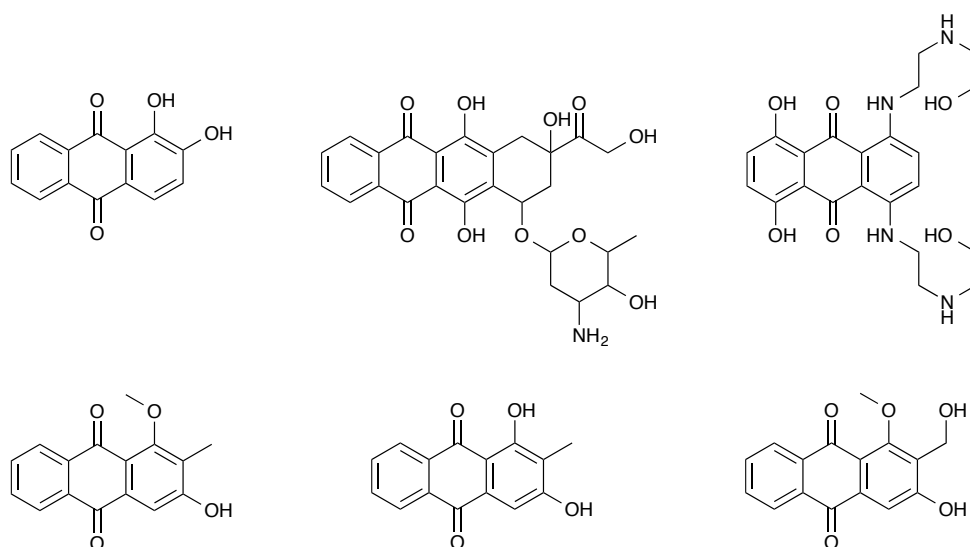


Figure 5.2 Structures of some naturally occurring (*top*) and commercially available (*bottom*) AQs.¹⁰

Their functionalisation can result in dramatic shifts in the absorption and emission properties of the compounds: 2-hydroxy-AQ absorbs and emits at 368 and 472/500 nm whilst 1,4-diamino-AQ absorbs and emits at 592 and 614/641 nm, respectively.¹¹ This means the compounds can be tuned to emit close to the near-IR region, which makes them potential candidates for bioimaging and therapeutics.

The facility to readily functionalise AQ and the ability to tune the photophysical properties have led to the incorporation of AQs into transition metal and lanthanide ion coordination chemistry. One of the simplest AQ complexes incorporates alizarin into a Ru(bpy)₂ complex, where the AQ coordination mode varies depending on the conditions (Figure 5.3).¹² Upon heating, the complex coordinates to both alkoxide moieties in the 1- and 2-positions; in the presence of acid this configuration alters to give coordination through the 1-position and to the carbonyl in the 9-position, leaving the 2-position as the alcohol, whilst in the presence of base, the alcohol deprotonates which can revert back to the 1,2- coordination mode again upon heating. Ruthenium complexes have also incorporated AQs to form diimines such as AQ-phen (Figure 5.3) in order to exploit the redox potential of the quinone core.¹³ Ji *et al.* found that, in the quinone form, a similar complex was non-emissive, whilst the quinol species emitted at *ca.* 600 nm with a long-lived lifetime (> 800 ns) suggestive of a ³MLCT-based emissive state.¹⁴

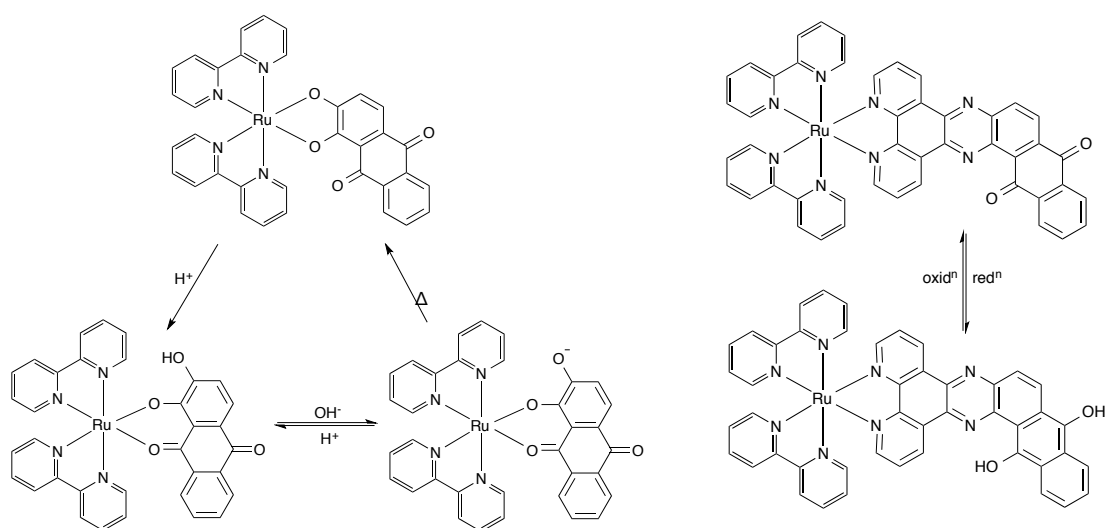


Figure 5.3 Structures of a Ru-AQ (alizarin) complex under different conditions (*left*) and the redox products of Ru-dppzAQ (*right*).

Nishihara *et al.* utilised the facile synthesis of alkynyl anthraquinones to develop a complex with two Pt^{II} tpy (2,2';6',2''-terpyridine) moieties in the 1- and 8-position.¹⁵ They proposed the presence of Pt-Pt interactions leading to an MMLCT excited state giving a low energy emission.

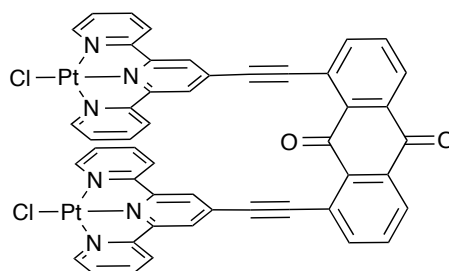


Figure 5.4 Pt_2 -AQ complex, which exhibits Pt-Pt interactions resulting in low energy emission.

As well as their incorporation into *d*-block metal complexes, AQs have also shown promise as antennas for sensitising near-IR emitting Ln^{III} ions due to their tunable visible light absorbing properties. Jones *et al.* developed a series of monometallic and dimetallic complexes by functionalising amino-AQs to incorporate DO3A-type macrocycles, within which Ln^{III} ions were coordinated to give water soluble AQ- Ln complexes.¹⁶ These were all found to both fluoresce, from AQ-centred emission, and phosphoresce from the Ln -centred near-IR emission. Yb^{III} gave a structured emission at 975 nm ($^2F_{5/2} \rightarrow ^2F_{7/2}$), Nd^{III} was found to emit at 1058 nm ($^4F_{3/2} \rightarrow ^4I_{11/2}$) with a weakly emitting peak at 1340 nm ($^4F_{3/2} \rightarrow ^4I_{13/2}$) and Er^{III} emitted weakly at 1540 nm for the ($^4I_{13/2} \rightarrow ^3H_4$) transition. The dimetallic complexes, with 1,4- and 1,5-substitution, were found to bind to calf thymus DNA with a binding constant of *ca.* 2

$\times 10^4 \text{ mol}^{-1} \text{ dm}^3$ for the 1,4-substituted derivative.¹⁷ The Gd^{III} complexes were also assessed for their utility as contrast agents by obtaining the ^1H NMRDs for the complexes in water and also in the presence of DNA. The spectra revealed a reduced rotational correlation time upon DNA binding, resulting in an increased value for r_1 , which is consistent with the binding of the AQ- Gd_2 complexes to the DNA.

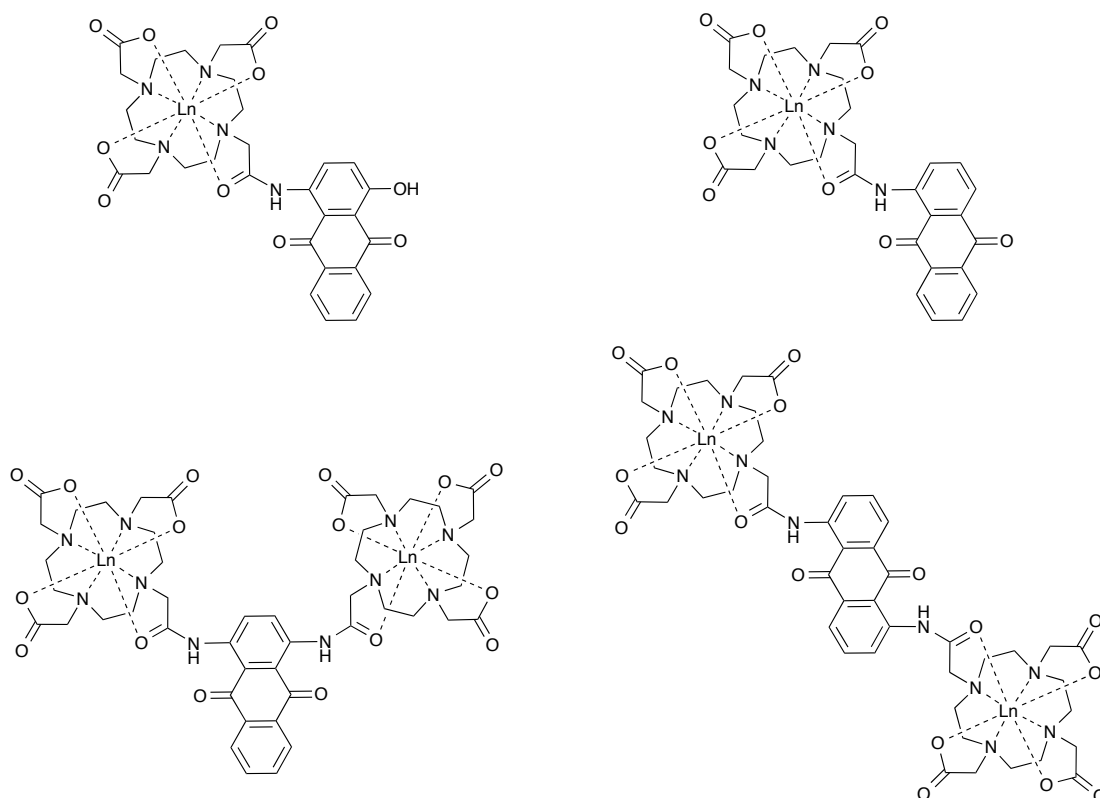


Figure 5.5 Structures of AQ- Ln complexes where AQ acts as a sensitizer for near-IR Ln^{III} metal ion emission.

AQ- Yb complexes have also been developed to act as responsive probes for Hg^{II} by incorporating a dipicolylamine-type linker between the AQ core and the macrocyclic component; the addition of Hg^{II} was found to modulate the AQ-centred emission and perturb the emissive state of Yb^{III} and quench the lifetime from 11 to 8 μs .¹⁸

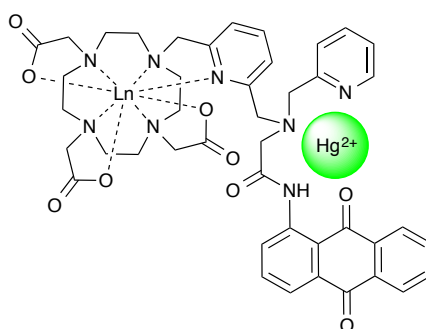


Figure 5.6 Hg^{II} sensitive AQ- Ln probe with a multidentate Hg^{II} binding site (highlighted in green).

5.2. Aims

Chapter 5 discusses the development of novel anthraquinone-based polypyridyl ligand architectures for the incorporation of Ln^{III} metal ions (Gd, Yb, Nd, Er). The synthetic procedures are outlined along with the characterisation of the ligands and complexes. The photophysical analysis of both the ligands and complexes is detailed, along with a proposed inner coordination sphere of the Ln^{III} ion for each ligand based on calculations of q . The relaxivities of the Gd^{III} complexes are assessed in $\text{H}_2\text{O}/\text{DMSO}$ mixtures, which are compared to free GdCl_3 in the same solvent systems to give an insight into the effectiveness of the complexes as contrast agents.

5.3. Results and Discussion

5.3.1. Precursor and ligand synthesis

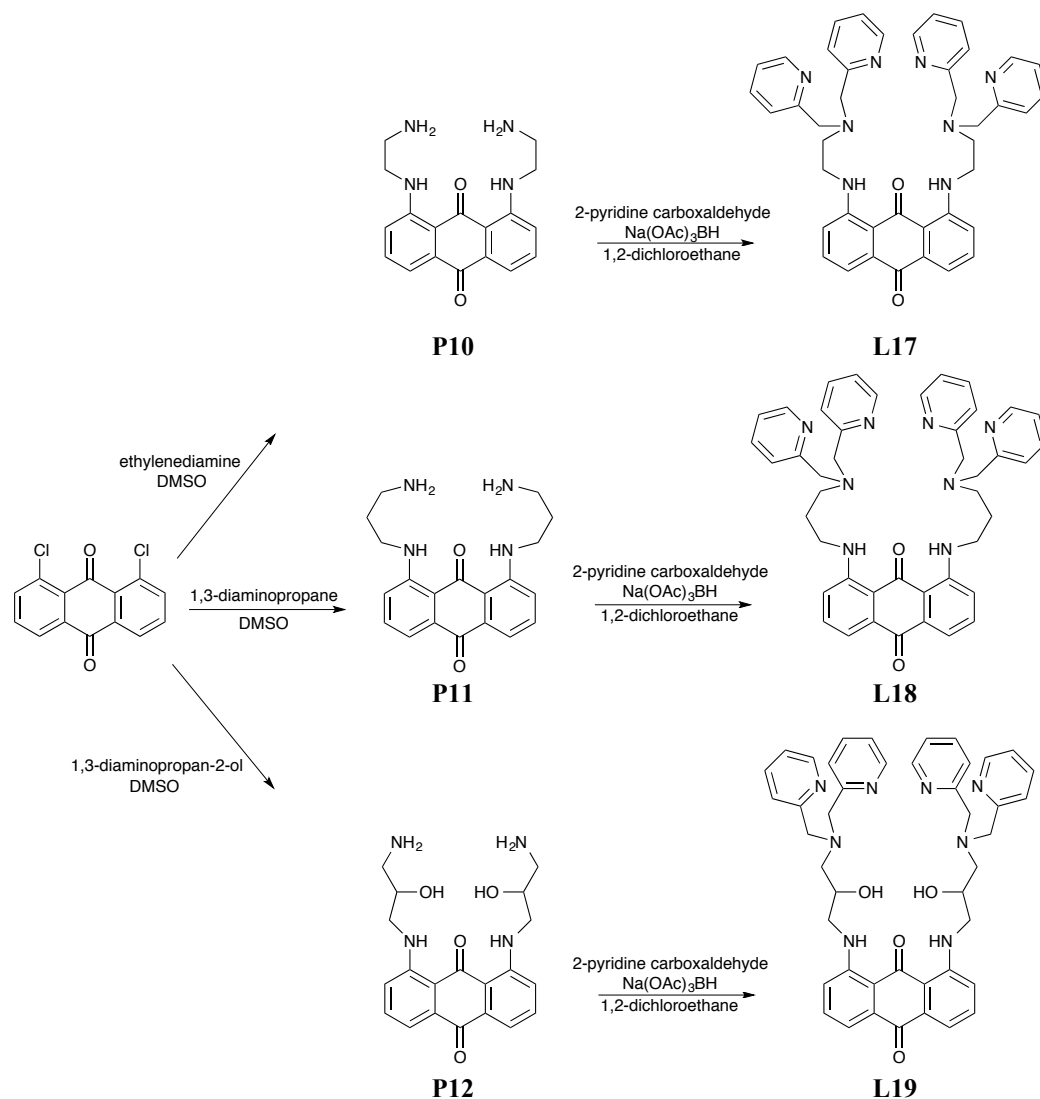


Figure 5.7 Synthetic pathway to the synthesis of **L17**, **L18** and **L19** via **P10**, **P11** and **P12**, respectively, from 1,8-dichloroanthraquinone (*left*).

The chromophoric ligands were developed by alkylating 1,8-dichloroanthraquinone with an excess of ethylenediamine, 1,3-diaminopropane or 1,3-diaminopropan-2-ol in refluxing DMSO based on a similar literature method.¹⁹ A colour change from yellow to red indicated formation of the monosubstituted compound, followed by a further change to purple, indicating the progression of the reaction to the disubstituted product. The solution was cooled and precipitated with iced water to yield the disubstituted amino intermediates. The sticky precipitate was then dissolved in methanol and precipitated with diethyl ether to give the products as highly coloured solids.

The precursors were characterised by ^1H NMR and IR spectroscopies, however the compounds were not soluble enough (especially in the case of **P12**, which was almost completely insoluble in all common solvents other than DMSO) to obtain ^{13}C NMR spectra. Attempts to obtain MS data were unsuccessful and, as such, the compounds were used in the following steps without full characterisation. Subsequent treatment with four equivalents of 2-pyridinecarboxaldehyde under reductive amination reaction conditions yielded the three multidentate ligands, **L17** – **L19**. The ligands all possess good solubility in a range of common organic solvents and were characterised using the usual spectroscopic and analytical techniques. The complexes were characterised by ^1H and ^{13}C NMR spectroscopy as well as HR-MS and UV-vis and IR spectroscopies. Of particular note in the ^1H NMR spectra are the characteristic NH resonances that indicate formation of the amino-substituted anthraquinone ligands, which appear as broadened triplets.

5.3.2. Complex synthesis

The complexes were obtained as dark purple coloured solids upon reaction with $\text{Ln}(\text{OTf})_3$ in methanol in the same manner as the Ln^{III} complexes in Chapter 3. The stoichiometry of the complexes was quantitatively confirmed using elemental analyses suggesting a 1:1 ($\text{Ln}:\text{L}$) ratio, where $\text{Ln} = \text{Nd}$ and Er (Gd and Yb complexes revealed incomplete combustion as indicated by low C, H and N values). MS(LD) revealed the appropriate isotopic patterns for the monometallic Ln^{III} species in all cases.

5.3.3. Electronic absorption spectroscopy

The UV-vis absorption spectra of the free ligands were obtained from acetonitrile solutions, revealing absorbing bands throughout the visible and UV regions. The anthraquinone $^1\text{IL}(\pi \rightarrow \pi^*)$ transitions contribute between 260 – 350 nm with pyridine-centred absorptions at shorter wavelengths, below 300 nm. The lowest energy absorption band peaked at 550, 547 and 542 nm for **L17**, **L18** and **L19** respectively, with corresponding molar absorptivity of *ca.* $10^4 \text{ dm}^3 \text{ mol}^{-1} \text{ cm}^{-1}$. These can be assigned to a charge transfer (CT) dominated transition that is anthraquinone-centred and derived from significant $^1\text{IL}(n \rightarrow \pi^*)$ character due to the donor-substituted chromophore.

5.3.4. Luminescence spectroscopy

Following irradiation of the lowest energy band, each of the ligands were visibly fluorescent *ca.* 630 nm as indicated by a modest Stokes' shift and short lifetime ($\tau = 1 - 2$ ns). Corresponding excitation spectra revealed a dominant feature at *ca.* 540 nm. Upon complexation of the Ln^{III} , subtle hypsochromic shifts were noted for this transition. Luminescence studies on the Gd^{III} complexes revealed a bathochromic energy shift of the ligand-based fluorescence to around 670 nm. To assess the effectiveness of the ligands as sensitising chromophores, anticipating the most common mechanism to involve energy transfer from the triplet state of the chromophore to the Ln^{III} excited state, additional low temperature measurements were obtained on solvent glasses (ethanol/methanol 5:1) at 77 K (Figure 5.8). In this manner, estimation of the ligand-centred triplet energies of the anthraquinone chromophores was possible from the onsets of the spectral profiles. It was noted that the peak position at 77K resided at higher energy relative to the room temperature fluorescence peak, with a subtle hint of vibronic structure suggesting that the lowest lying excited state at 77K was $^3\pi \rightarrow \pi^*$. The onset was recorded at *ca.* 560 nm for all three ligand types, and therefore deemed to be of sufficient energy to sensitise the near-IR emitting Nd^{III} , Er^{III} and Yb^{III} ions.

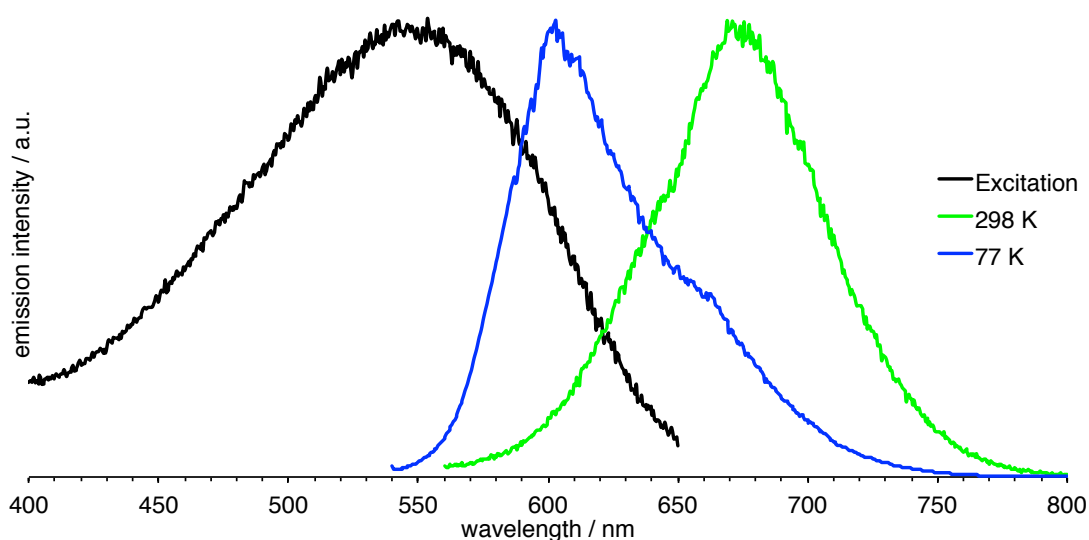


Figure 5.8 Excitation and emission (room temperature and low temperature) of $[\text{Gd}(\text{L18})](\text{OTf})_3$.

For the Ln^{III} complexes, the emission characteristics are ascribed to two processes: one anthraquinone-centred and one lanthanide-centred. Each of these complexes

retained the anthraquinone-based fluorescence at *ca.* 670 nm, together with additional weaker bands in the near-IR region associated with the lanthanide-centred transitions consistent with the inclusion of the respective Ln^{III} ion (Figure 5.9). It was possible to obtain lifetime-decay profiles for all examples using a cut-off filter (< 850 nm) to eliminate ligand-based fluorescence. Time-resolved measurements on the complexes confirmed the long-lived nature of the emission and also allowed a qualitative insight into the likely binding mode of the ligand with Ln^{III}.

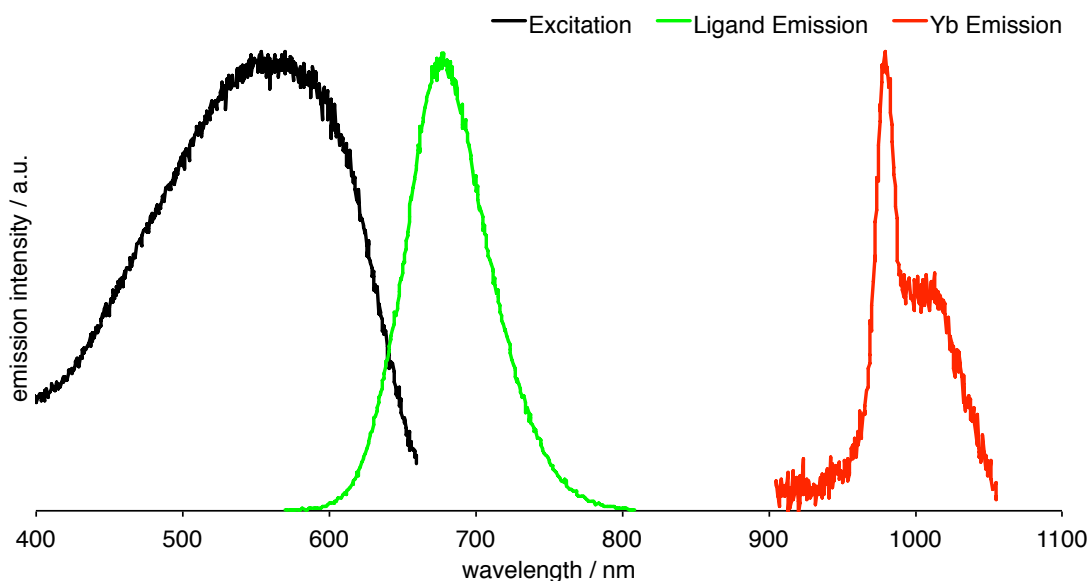


Figure 5.9 Excitation and emission profiles for [Yb(**L19**)](OTf)₃, where excitation is in black, ligand emission is in green and ²F_{5/2} → ²F_{7/2} Yb^{III} emission is in red.

The values in methanol for the Yb^{III} complexes showed a large increase in lifetime from **L18** to **L17** to **L19**. Using the values obtained in CD₃OD/CH₃OH allowed the determination of *q*, the number of Ln^{III}-bound solvents (Table 5.1). For Yb^{III}, *q* reduces from *ca.* 4 (**L18**) to *ca.* 1 (**L19**) using equation (21). This suggests that for [Yb(**L18**)](OTf)₃ the coordination sphere is probably six coordinate and likely to comprise both dipicolyl amine units and not the anthraquinone core (*cf.* very minor changes in the UV-vis spectra of the ligand) (Figure 5.11). For [Yb(**L19**)](OTf)₃ the low *q* value suggests an effective exclusion of solvent and an eight-coordinate ligand encapsulating Yb^{III}. This is attributed to the coordinative participation of the alcohol donors of the propan-2-ol moiety (Figure 5.11). For the analogous parameters obtained from the Nd^{III} species, using equation (22), the trend is the same with respect to the obtained *q* values although they are generally larger, as expected for ionic radii.

$$q = 2\{(k_{\text{MeOH}} - k_{\text{MeOD}}) - 0.05\} \quad (21)$$

$$q = 290(k_{\text{MeOH}} - k_{\text{MeOD}}) - 0.4 \quad (22)^{20}$$

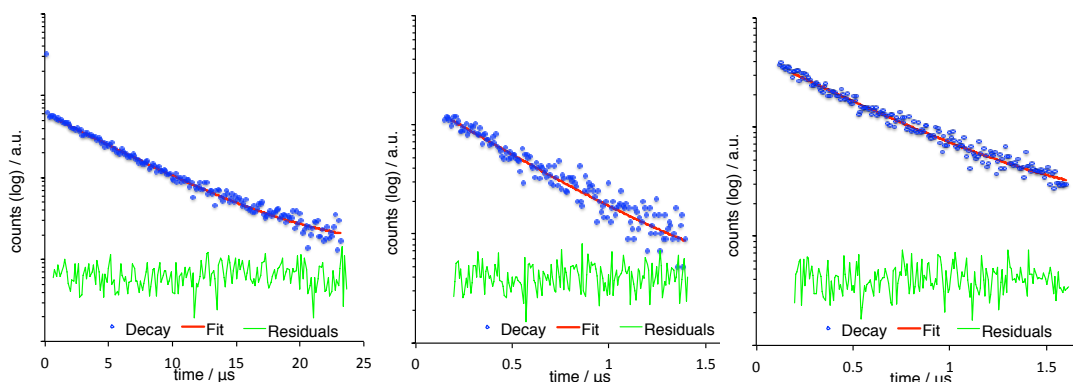
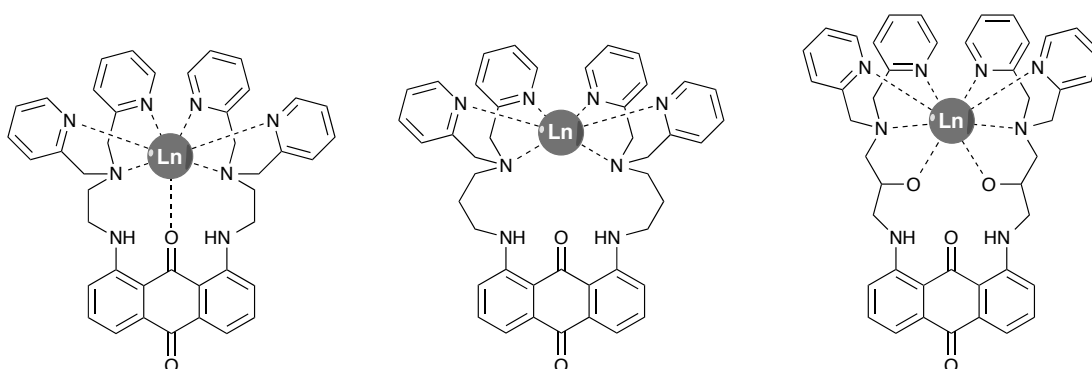


Figure 5.10 Decay profiles, with fit residuals, for Yb^{III} (*left*), Nd^{III} (*middle*) and Er^{III} (*right*) complexes in CD₃OD, λ_{ex} at 355 nm.

Compound	λ_{ex} / nm ($n \rightarrow \pi^*$)	λ_{em} / nm ($n \rightarrow \pi^*$)	Near-IR τ / ns		q
			MeOH	CD ₃ OD	
L17	547	636	-	-	-
[Gd(L17)](OTf) ₃	538	664	-	-	-
[Yb(L17)](OTf) ₃	539	-	699	5680	2.4
[Nd(L17)](OTf) ₃	539	-	60	409	3.7
[Er(L17)](OTf) ₃	540	-	-	448	-
L18	550	632	-	-	-
[Gd(L18)](OTf) ₃	546	679	-	-	-
[Yb(L18)](OTf) ₃	543	-	441	6350	4.1
[Nd(L18)](OTf) ₃	545	-	48	378	4.9
[Er(L18)](OTf) ₃	548	-	-	597	-
L19	542	633	-	-	-
[Gd(L19)](OTf) ₃	535	672	-	-	-
[Yb(L19)](OTf) ₃	534	-	1300	5360	1.1
[Nd(L19)](OTf) ₃	532	-	65	415	3.4
[Er(L19)](OTf) ₃	535	-	-	567	-

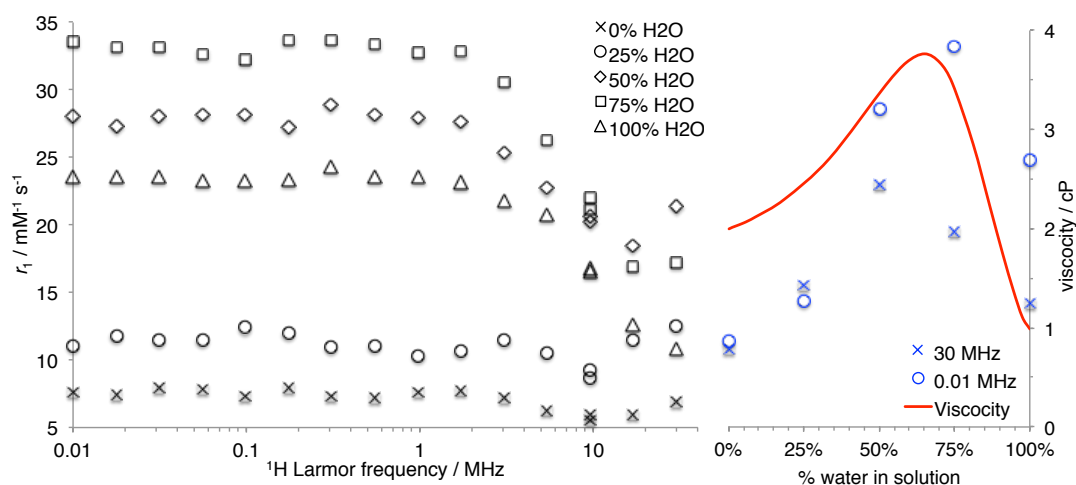
Table 5.1 Summary of the photophysical data for the ligands and complexes in Chapter 5.

Near-IR steady state spectra were unobtainable for the complexes of **L17** and **L18** with the Ln^{III} peaks appearing as extremely weak and often superimposed by the tail of the anthraquinone fluorescence. However, for the complexes of **L19**, which possessed a lower q value, the Ln^{III}-based peaks were more easily observed. The Nd^{III} complex revealed near-IR emission with a peak at 1058 nm ($^4F_{3/2} \rightarrow ^4I_{11/2}$) with a much weaker feature at *ca.* 1340 nm, corresponding to ($^4F_{3/2} \rightarrow ^4I_{13/2}$). The steady state emission spectra of [Yb(**L19**)](OTf)₃ gave a spectral profile typical of Yb^{III} with a structured peak at 975 nm ($^2F_{5/2} \rightarrow ^2F_{7/2}$), whilst [Er(**L19**)](OTf)₃ gave a very weak broad emission feature centred around 1540 nm assigned to the ($^4I_{13/2} \rightarrow ^3H_4$) transition.

Figure 5.11 Proposed coordination modes of $[\text{Ln}(\text{L17-L19})](\text{OTf})_3$ based on q values.

5.3.5. Relaxivity

The solubility of the cationic complexes was not sufficient to allow for relaxometric ^1H NMRD studies to be completed in water. However, a suitable solvent system was obtained from a $\text{H}_2\text{O}/\text{DMSO}$ 50/50 mixture. For reference purposes, a number of comparative spectra were undertaken on GdCl_3 in various $\text{H}_2\text{O}/\text{DMSO}$ mixtures.

Figure 5.12 ^1H NMRD profiles for GdCl_3 in various $\text{H}_2\text{O}/\text{DMSO}$ ratios at 37°C with various field strengths (*left*) and change in relaxivity at 30 and 0.01 MHz and the change in viscosity of a water/DMSO solution at solvent ratios (*right*).²¹

The data from the measurements in various $\text{H}_2\text{O}/\text{DMSO}$ mixtures suggest that the viscosity of the solvent mixture plays a vital role in the relaxivities of GdCl_3 . Whilst the viscosities of water and DMSO are 0.89 and 1.99 cP, respectively, the viscosity of a mixture of the two solvents is as much as 3.73 cP with around 33% DMSO (Figure 5.12).²² This means that the molar ratio at the maximum viscosity for $\text{H}_2\text{O}/\text{DMSO}$ is 2:1, which has been proposed by Cowie *et al.* to be due to a strong association complex of the two components and a complicated network of resultant hydrogen bonding, leading to a much greater viscosity than the sum of the two component parts.^{21, 23} High viscosities lend themselves to faster rates of relaxation due to the

reduced rotational correlation time τ_R , however they also make movement of water around the system more difficult resulting in a potentially longer residency time, τ_M , which would have the opposite effect on the relaxation rate. The Gd-H distances, r and r' , are also different due to the presence of both Gd-H_{H₂O} and Gd-H_{DMSO}, again affecting the relaxation rates of protons. These factors make it extremely difficult to calculate exactly what is happening in the binary systems, and prevented fitting of the NMRD data to obtain parameters such as residency times and rotational correlation times. The only comparison that can be made is the relaxivity of GdCl₃ in the two solvent systems: r_1 value of *ca.* 10.9 mM⁻¹ s⁻¹ (30 MHz, 37 °C, H₂O) compared to 21.4 mM⁻¹ s⁻¹ (30 MHz, 37 °C, 1:1 H₂O/DMSO).

Compound	r_1 (mM ⁻¹ s ⁻¹) (30 MHz, 25 °C)
GdCl ₃ (H ₂ O)	10.9
GdCl ₃	21.4
[Gd(L17)]	16.7
[Gd(L18)]	13.7
[Gd(L19)]	19.3

Table 5.2 r_1 values for GdCl₃ in water and GdCl₃ and the anthraquinone complexes in a 1:1 mixture of H₂O/DMSO.

The values for the anthraquinone-based Gd^{III} complexes all lie below the value for GdCl₃ (Table 5.2); this is to be expected, given that r_1 for the free gadolinium is much higher than the anticipated values would be for multidentate Gd^{III} complexes. The complex of **L19** has the highest relaxation rate, which was suggested to be from the interaction of the –OH groups facilitating a more effective second coordination sphere, and potentially reducing the residency time of coordinated solvent molecules as was seen for the phosphinate group in Rudovsky *et al*'s [Gd(DO3AP^{ABn})]⁻ complex.²⁴ The value for r_1 of [Gd(**L17**)] was greater than that of [Gd(**L18**)], despite the latter having a greater q value; this was thought to be due to the more polar coordination sphere with the proposed participation of the carbonyl moiety and, therefore, the closer proximity of the –NH groups, facilitating hydrogen bonding in the second sphere, invoking a similar effect to that of **L19**. It is assumed that the inner-sphere solvation is the same across the complexes for these proposals, although it is likely that the solvation around the different complexes is different and, as such, the data are not comparable.

It would not be logical to apply the relative difference in the relaxivity found from the two solvent systems for GdCl_3 to the AQ systems as this would wrongly assume that the parameters for these species are the same for those of the free Gd^{III} ion. It does, however, act as a guide to suggest how efficient the novel systems are at generating greater relaxation rates compared to the known standard.

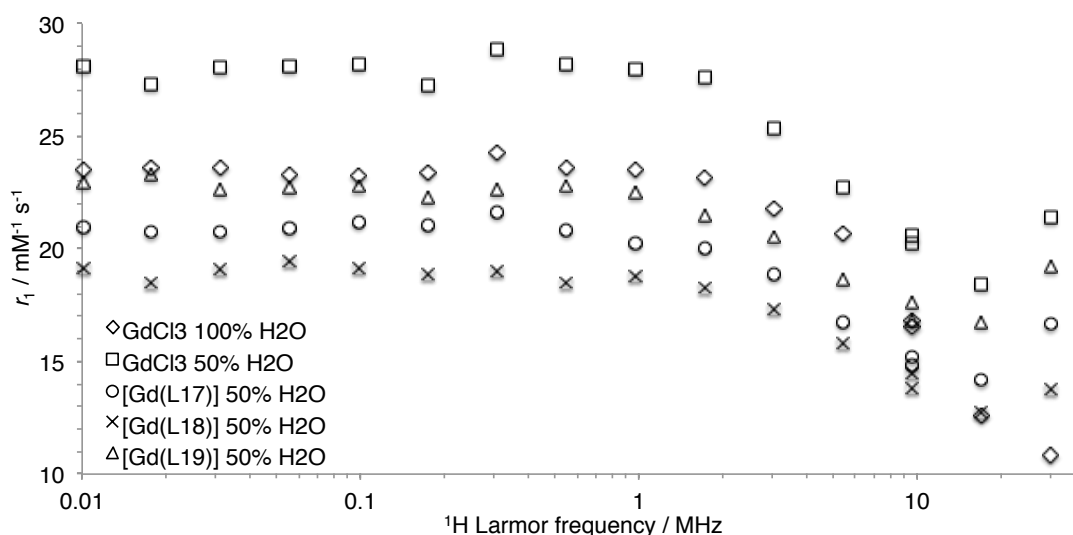


Figure 5.13 ^1H NMRD profiles of GdCl_3 in H_2O and $\text{H}_2\text{O}/\text{DMSO}$ (1:1) and $[\text{Gd}(\text{L17-L19})](\text{OTf})_3$ in $\text{H}_2\text{O}/\text{DMSO}$ (1:1) at 37°C .

The ^1H NMRD profile (Figure 5.13) of the binary system compared to H_2O for GdCl_3 shows that, whilst the relaxivity at high field strengths is much greater in the binary system, the relative difference at lower field strengths is considerably smaller due to a significant inflexion of the binary solvent profile. This inflexion is also observed in the anthraquinone species in the two-solvent mixture.

5.4. Conclusion

Chapter 5 summarises the synthesis of a series of novel polydentate ligands with an anthraquinone backbone, along with the subsequent coordination chemistry with a series of Ln^{III} metal ions (Gd, Nd, Yb and Er). The characterisation of precursors, ligands and complexes is detailed along with a detailed photophysical study on the emissive properties of the ligands and complexes. The lifetimes of the Yb and Nd complexes were recorded in both methanol and CD_3OD in order to ascertain the inner-sphere coordination value, q , in order to give a greater understanding of the coordination modes of each of the three ligands.

A relaxometric investigation was also carried out, despite the insolubility of the anthraquinone complexes in aqueous media. Comparative studies on GdCl_3 are detailed in a range of ratios of $\text{H}_2\text{O}:\text{DMSO}$ before measurements were taken on $[\text{Gd}(\text{L17})]$ to $[\text{Gd}(\text{L19})]$ in order to determine values for r_1 of the three complexes, relative to GdCl_3 .

5.5. Experimental

5.5.1. General physical measurements

All physical measurements were carried out as outlined in previous chapters.

5.5.2. Precursor synthesis

General procedure for diaminoanthraquinone alkylations: Based on a modified literature methodology.¹⁹ The amine (10 eq) was added to a stirring suspension of 1,8-dichloroanthraquinone (1 eq) in DMSO (5 mL). Cold water was added to the hot solution and the resultant suspension was stirred for 1 h before the product was collected by filtration.

Synthesis of P10: Following the general procedure for diaminoanthraquinone alkylations using ethylene diamine (4.5 mL, 18.1 mmol) and 1,8-dichloroanthraquinone (0.500 g, 1.81 mmol). The product was purified by column chromatography (silica, dichloromethane) and was eluted as the purple band with dichloromethane/ethyl acetate (9:1). The solvent was removed *in vacuo* and the product was re-precipitated from methanol/diethyl ether, filtered and dried to give a dark purple solid. Yield = 0.79 g, (34%). ¹H NMR (250 MHz, CDCl₃): δ_{H} 9.68 (2H, t, ³*J*_{HH} = 5.0 Hz), 7.50 – 7.36 (4H, m), 6.98 (2H, m), 3.35 (4H, q, ³*J*_{HH} = 5.8 Hz), 3.00 (4H, t, ³*J*_{HH} = 6.3 Hz) ppm. IR (solid): ν_{max} 3271, 1736, 1657, 1612, 1566, 1512, 1379, 1298, 1277, 1260, 1209, 1177, 1076, 1020, 745 cm⁻¹.

Synthesis of P11: Following the general procedure for diaminoanthraquinone alkylations using 1,3-diaminopropane (1.5 mL, 18.1 mmol) and 1,8-dichloroanthraquinone (0.500 g, 1.81 mmol). The precipitate was re-dissolved in methanol before being precipitated with ether and collected by filtration to afford a dark purple solid. Yield = 0.15 g (23%). ¹H NMR (400 MHz, CDCl₃): δ_{H} 7.46 – 7.44 (2H, m), 7.38 – 7.34 (m, 2H), 7.01 – 6.97 (m, 2H), 3.23 (4H, q, ³*J*_{HH} = 5.2 Hz), 2.64 (4H, t, ³*J*_{HH} = 6.8 Hz), 1.89 (4H, m) ppm. IR (solid): ν_{max} 3275, 1661, 1612, 1591, 1564, 1508, 1450, 1395, 1342, 1296, 1215, 1198, 1173, 1076, 1030, 833, 819, 741 cm⁻¹.

Synthesis of P12: Following the general procedure for diaminoanthraquinone alkylations using 1,3-diamino-2-propanol (1.63 g, 18.1 mmol) and 1,8-

dichloroanthraquinone (0.500 g, 1.81 mmol). The precipitate was re-precipitated from methanol/diethyl ether, before being collected by filtration and dried to afford a dark purple solid (yield 0.54 g, 78 %). ^1H NMR (250 MHz, DMSO): δ_{H} 9.72 (2H, t, $^3J_{\text{HH}} = 5.05$ Hz), 7.56 (2H, m), 7.37 (2H, d, $^3J_{\text{HH}} = 7.1$ Hz), 7.25 (2H, d, $^3J_{\text{HH}} = 8.5$ Hz), 3.68 (2H, br. m), 3.46 (4H, m), 3.22 (4H, m) ppm. IR (solid): ν_{max} 3262, 1736, 1655, 1612, 1553, 1501, 1449, 1400, 1366, 1296, 1207, 1177, 1138, 1069, 1016 cm^{-1} .

5.5.3. Ligand synthesis

General procedure for reductive aminations: Following the general procedure outlined in Chapter 3 for the reduction of pyridine carboxaldehyde onto an amine (reductive amination). 2-pyridine carboxaldehyde (4 eq) and the alkylated anthraquinone precursor (1 eq) was added to a stirring solution of $\text{Na}(\text{OAc})_3\text{BH}$ (6 eq) in 1,2-dichloroethane (3.5 mL). The suspension was stirred under dinitrogen for 48 h before being neutralised with NaHCO_3 (sat. soln, 10 mL) and extracted into ethyl acetate (20 mL). The product was washed with water (2 x 20 mL) and brine (1 x 20 mL) before the solvent was removed *in vacuo*.

Synthesis of L17: Following the general procedure for reductive aminations using **P10** (0.230 g, 0.710 mmol), 2-pyridine carboxaldehyde (0.27 mL, 2.84 mmol) and $\text{Na}(\text{OAc})_3\text{BH}$ (0.900 g, 4.25 mmol). Obtained as a dark purple viscid solid. Yield = 0.41 g, (83%). ^1H NMR (400 MHz, CDCl_3): δ_{H} 9.75 (2H, t, $^3J_{\text{HH}} = 5.1$ Hz), 8.41 (4H, d, $^3J_{\text{HH}} = 4.8$ Hz), 7.56 – 7.30 (12H, m), 7.01 (4H, m), 6.85 (2H, m), 3.85 (8H, s), 3.41 (4H, q, $^3J_{\text{HH}} = 6.3$ Hz), 2.87 (4H, t, $^3J_{\text{HH}} = 6.5$ Hz) ppm. $^{13}\text{C}\{^1\text{H}\}$ NMR (75.6 MHz, CDCl_3): δ_{C} 40.8, 52.8, 60.6, 114.5, 115.1, 117.9, 122.0, 122.2, 123.1, 134.2, 136.5, 149.0, 151.0, 159.2, 184.6, 189.4 ppm. HR-MS: calcd. for $[\text{C}_{40}\text{H}_{41}\text{N}_8\text{O}_2]^+$ 689.3347, found 689.3344. UV-vis (MeCN): λ_{max} ($\epsilon / \text{dm}^3 \text{mol}^{-1} \text{cm}^{-1}$) 260 (17600), 304 (4500), 550 (7000) nm. IR (MeCN): ν_{max} 3288, 1661, 1612, 1589, 1568, 1512, 1472, 1433, 1400, 1364, 1298, 1206, 1148, 1076, 1047, 1024, 995 cm^{-1} .

Synthesis of L18: Following the general procedure for reductive aminations using **P11** (0.153 g, 0.431 mmol), 2-pyridine carboxaldehyde (0.16 mL, 1.67 mmol) and $\text{Na}(\text{OAc})_3\text{BH}$ (0.542 g, 2.56 mmol). Obtained as a dark purple oil. Yield = 0.15 g (48%). ^1H NMR (250 MHz, CDCl_3): δ_{H} 9.32 (2H, t, $^3J_{\text{HH}} = 5.2$ Hz), 8.40 (4H, d, $^3J_{\text{HH}} = 4.8$ Hz), 7.50–7.31 (12H, m), 6.98 (4H, m), 6.88 (2H, d, $^3J_{\text{HH}} = 8.4$ Hz), 3.76 (8H, s,

$^3J_{\text{HH}} = 14.4$ Hz), 3.22 (4H, q, $^3J_{\text{HH}} = 6.7$ Hz), 2.67 (4H, t, $^3J_{\text{HH}} = 6.8$ Hz), 1.90 (4H, q, $^3J_{\text{HH}} = 6.9$ Hz) ppm. $^{13}\text{C}\{^1\text{H}\}$ NMR (75.6 MHz, CDCl_3): δ_{C} 26.7, 40.8, 43.5, 51.5, 114.3, 114.8, 117.7, 122.0, 123.0, 134.1, 134.3, 136.46, 136.72, 148.89, 151.04, 159.52, 184.72, 188.62 ppm. HR-MS: calcd. for $[\text{C}_{44}\text{H}_{45}\text{N}_8\text{O}_2]^+$ 717.3660, found 717.3659. UV-vis (MeCN): λ_{max} ($\epsilon / \text{dm}^3 \text{mol}^{-1} \text{cm}^{-1}$) 238 (38900), 325 (5800), 547 (9400) nm. IR (MeCN): ν_{max} 3279, 1659, 1612, 1589, 1568, 1512, 1472, 1431, 1398, 1364, 1298, 1236, 1213, 1202, 1150, 1076, 1047, 1024, 993, 745 cm^{-1} .

Synthesis of L19: Following the general procedure for reductive aminations using **P12** (0.352 g, 0.912 mmol), 2-pyridine carboxaldehyde (0.35 mL, 3.66 mmol) and $\text{Na}(\text{OAc})_3\text{BH}$ (1.15 g, 5.45 mmol). Obtained as a dark purple oil, which solidified upon standing. Yield = 0.460 g, (67%). ^1H NMR (400 MHz, CDCl_3): δ_{H} 9.32 (2H, m), 8.40 (4H, d, $^3J_{\text{HH}} = 4.6$ Hz), 7.50 – 7.31 (12H, m), 6.98 (4H, m), 6.88 (2H, m), 4.06 (4H, m), 3.76 (8H, m), 3.22 (4H, br. m), 2.87 – 2.70 (2H, m) ppm. $^{13}\text{C}\{^1\text{H}\}$ NMR (75.6 MHz, CDCl_3): δ_{C} 43.6, 47.0, 59.2, 67.8, 114.6, 114.9, 117.9, 122.3, 123.3, 134.0, 134.3, 136.5, 136.7, 149.0, 151.2, 159.0, 184.7, 188.6 ppm. HR-MS: calcd. for $[\text{C}_{44}\text{H}_{44}\text{N}_8\text{O}_4]^+$ 749.3558, found 749.3570. UV-vis (MeCN): λ_{max} ($\epsilon / \text{dm}^3 \text{mol}^{-1} \text{cm}^{-1}$) 237 (60100), 313 (10300), 542 (12900) nm. IR (MeCN): ν_{max} 3281, 1659, 1615, 1595, 1570, 1515, 1475, 1435, 1300, 1265, 1210, 1069, 1047, 1020, 744 cm^{-1} .

5.5.4. Synthesis of Complexes

General procedure for complexation of lanthanides: Following the general procedure outlined in Chapter 3 for the complexation of lanthanides. The ligand (1 eq) and $\text{Ln}(\text{OTf})_3$ (1 eq) were dissolved in methanol (5 mL) and heated to reflux overnight. The reaction mixture was dried *in vacuo* and re-dissolved in a minimum volume of acetonitrile before being precipitated with diethyl ether.

Synthesis of $[\text{Gd}(\text{L17})](\text{OTf})_3$: Following the general procedure for complexation of lanthanides using **L17** (0.105 g, 0.147 mmol) and $\text{Gd}(\text{OTf})_3$ (0.089 g, 0.147 mmol). Obtained as a dark purple solid. Yield = 0.177 g, (91%). MS(LD) found $m/z = 880.0$ for $[\text{M} - 3\text{OTf} - 2\text{H} + 2\text{H}_2\text{O}]^+$. UV-vis (MeCN): λ_{max} ($\epsilon / \text{dm}^3 \text{mol}^{-1} \text{cm}^{-1}$) 238 (54969), 268 (52234), 546 (12266) nm. IR (MeCN): ν_{max} 1654, 1614, 1570, 1514, 1442, 1400, 1263, 1234, 1215, 1163, 1026, 731 cm^{-1} .

Synthesis of [Yb(L17)](OTf)₃: Following the general procedure for complexation of lanthanides using **L17** (0.081 g, 0.113 mmol) and Yb(OTf)₃ (0.072 g, 0.113 mmol). Obtained as a dark purple solid. Yield = 0.118 g, (78%). MS(LD) found m/z = 896.1 for $[M - 3OTf - 2H + 2H_2O]^+$. UV-vis (MeCN): λ_{\max} (ϵ / dm³ mol⁻¹ cm⁻¹) 236 (35900), 543 (7500) nm. IR (MeCN): ν_{\max} 1736, 1655, 1614, 1595, 1568, 1512, 1472, 1437, 1398, 1371, 1238, 1225, 1167, 1028, 746 cm⁻¹.

Synthesis of [Nd(L17)](OTf)₃: Following the general procedure for complexation of lanthanides using **L17** (0.068 g, 0.095 mmol) and Nd(OTf)₃ (0.066 g, 0.095 mmol). Obtained as a dark purple solid. Yield = 0.104 g, (84%). MS(LD) found m/z = 886.0 for $[M - 3OTf - 2H + 2H_2O]^+$. UV-vis (MeCN): λ_{\max} (ϵ / dm³ mol⁻¹ cm⁻¹) 236 (37800), 545 (8200) nm. IR (MeCN): ν_{\max} 1736, 1612, 1595, 1570, 1508, 1431, 1371, 1275, 1227, 1217, 1161, 1053, 1032, 1016, 748 cm⁻¹. Calculated for C₄₂H₄₀N₈O₂Nd(CF₃SO₃)₃: C, 42.22; H, 3.15; N, 8.75; Found C, 42.13; H, 3.09; N, 8.81 %.

Synthesis of [Er(L17)](OTf)₃: Following the general procedure for complexation of lanthanides using **L17** (0.060 g, 0.084 mmol) and Er(OTf)₃ (0.052 g, 0.084 mmol). Obtained as a dark purple solid. Yield = 0.097 g, (87%). MS(LD) found m/z = 890.0 for $[M - 2OTf - H]^+$. UV-vis (MeCN): λ_{\max} (ϵ / dm³ mol⁻¹ cm⁻¹) 238 (42500), 272 (54700), 548 (8000) nm. IR (MeCN): ν_{\max} 1722, 1612, 1595, 1568, 1512, 1435, 1400, 1371, 1248, 1225, 1157, 1078, 1047, 1029, 746 cm⁻¹. Calculated for C₄₂H₄₀N₈O₂Er(CF₃SO₃)₃: C, 41.47; H, 3.09; N, 8.60; Found C, 41.38; H, 3.03; N, 8.59 %.

Synthesis of [Gd(L18)](OTf)₃: Following the general procedure for complexation of lanthanides using **L18** (0.050 g, 0.073 mmol) and Gd(OTf)₃ (0.044 g, 0.073 mmol). Obtained as a dark purple solid. Yield = 0.081 g, (86%). MS(LD) found m/z = 876.1 for $[M - 3OTf - 2H + 2H_2O]^+$. UV-vis (MeCN): λ_{\max} (ϵ / dm³ mol⁻¹ cm⁻¹) 259 (29900), 314 (5600), 538 (9800) nm. IR (MeCN): ν_{\max} 1615, 1573, 1515, 1271, 1225, 1157, 1032, 770, 745 cm⁻¹.

Synthesis of [Yb(L18)](OTf)₃: Following the general procedure for complexation of lanthanides using **L18** (0.051 g, 0.074 mmol) and Yb(OTf)₃ (0.047 g, 0.074 mmol). Obtained as a dark purple solid. Yield = 0.040 g, (42%). MS(LD) found m/z = 893.1

for $[M - 3OTf - 2H + 2H_2O]^+$. UV-vis (MeCN): λ_{\max} ($\epsilon / \text{dm}^3 \text{mol}^{-1} \text{cm}^{-1}$) 258 (27100), 315 (5500), 539 (10100) nm. IR (MeCN): ν_{\max} 1615, 1573, 1515, 1270, 1225, 1157, 1032, 766 cm^{-1} .

Synthesis of [Nd(L18)](OTf)₃: Following the general procedure for complexation of lanthanides using **L18** (0.050 g, 0.073 mmol) and Nd(OTf)₃ (0.051 g, 0.073 mmol). Obtained as a dark purple solid. Yield = 0.074 g, (80%). MS(LD) found m/z = 864.0 for $[M - 3OTf - 2H + 2H_2O]^+$. UV-vis (MeCN): λ_{\max} ($\epsilon / \text{dm}^3 \text{mol}^{-1} \text{cm}^{-1}$) 259 (42000), 315 (7700), 539 (13400) nm. IR (MeCN): ν_{\max} 1615, 1515, 1273, 1225, 1159, 1032 cm^{-1} . Calculated for C₄₂H₄₀N₈O₂Nd(CF₃SO₃)₃: C, 42.22; H, 3.15; N, 8.75; Found C, 42.13; H, 3.09; N, 8.81 %.

Synthesis of [Er(L18)](OTf)₃: Following the general procedure for complexation of lanthanides using **L18** (0.050 g, 0.073 mmol) and Er(OTf)₃ (0.045 g, 0.073 mmol). Obtained as a dark purple solid. Yield = 0.062 g, (65%). MS(LD) found m/z = 889.0 for $[M - 3OTf - 2H + 2H_2O]^+$. UV-vis (MeCN): λ_{\max} ($\epsilon / \text{dm}^3 \text{mol}^{-1} \text{cm}^{-1}$) 258 (30000), 312 (6000), 540 (10700) nm. IR (MeCN): ν_{\max} 1615, 1573, 1514, 1270, 1225, 1158, 1031, 765 cm^{-1} . Calculated for C₄₂H₄₀N₈O₂Er(CF₃SO₃)₃: C, 41.47; H, 3.09; N, 8.60; Found C, 41.38; H, 3.03; N, 8.59 %.

Synthesis of [Gd(L19)](OTf)₃: Following the general procedure for complexation of lanthanides using **L19** (0.053 g, 0.071 mmol) and Gd(OTf)₃ (0.043 g, 0.071 mmol). Obtained as a dark purple solid. Yield = 0.055 g, (62%). MS(LD) found m/z = 900.2 for $[M - 3OTf - 2H]^+$. UV-vis (MeCN): λ_{\max} ($\epsilon / \text{dm}^3 \text{mol}^{-1} \text{cm}^{-1}$) 258 (34400), 304 (9000), 535 (15700) nm. IR (MeCN): ν_{\max} 3400, 1616, 1571, 1516, 1445, 1271, 1239, 1224, 1158, 1032, 766, 751 cm^{-1} .

Synthesis of [Yb(L19)](OTf)₃: Following the general procedure for complexation of lanthanides using **L19** (0.045 g, 0.074 mmol) and Yb(OTf)₃ (0.047 g, 0.074 mmol). Obtained as a dark purple solid. Yield = 0.034 g, (34%). MS(LD) found m/z = 916.1 for $[M - 3OTf - 2H]^+$. UV-vis (MeCN): λ_{\max} ($\epsilon / \text{dm}^3 \text{mol}^{-1} \text{cm}^{-1}$) 258 (20900), 311 (4800), 534 (9000) nm. IR (MeCN): ν_{\max} 3368, 1615, 1572, 1447, 1271, 1238, 1224, 1160, 1031, 768, 750 cm^{-1} .

Synthesis of [Nd(L19)](OTf)₃: Following the general procedure for complexation of lanthanides using **L19** (0.059 g, 0.079 mmol) and Nd(OTf)₃ (0.055 g, 0.079 mmol).

Obtained as a dark purple solid. Yield = 0.083 g, (79%). MS(LD) found m/z = 888.2 for $[M - 3OTf - 2H]^+$. UV-vis (MeCN): λ_{\max} (ϵ / $\text{dm}^3 \text{ mol}^{-1} \text{ cm}^{-1}$) 257 (30300), 302 (8100), 532 (13400) nm. IR (MeCN): ν_{\max} 3457, 1616, 1570, 1516, 1444, 1271, 1238, 1224, 1159, 1031, 768, 751 cm^{-1} . Calculated for $\text{C}_{44}\text{H}_{44}\text{N}_8\text{O}_4\text{Nd}(\text{CF}_3\text{SO}_3)_3$: C, 42.12; H, 3.31; N, 8.36; Found C, 42.03; H, 3.34; N, 8.25 %.

Synthesis of $[\text{Er}(\text{L19})](\text{OTf})_3$: Following the general procedure for complexation of lanthanides using **L19** (0.060 g, 0.080 mmol) and $\text{Er}(\text{OTf})_3$ (0.049 mg, 0.080 mmol). Obtained as a dark purple solid. Yield = 0.090 g, (82%). MS(LD) found m/z = 912.4 for $[M - 3OTf - 2H]^+$. UV-vis (MeCN): λ_{\max} (ϵ / $\text{dm}^3 \text{ mol}^{-1} \text{ cm}^{-1}$) 258 (16900), 303 (4300), 535 (7600) nm. IR (MeCN): ν_{\max} 3452, 1616, 1572, 1445, 1271, 1239, 1222. Calculated for $\text{C}_{44}\text{H}_{44}\text{N}_8\text{O}_4\text{Er}(\text{CF}_3\text{SO}_3)_3$: C, 41.41; H, 3.25; N, 8.22; Found C, 41.38; H, 3.34; N, 8.19 %.

5.6. References

1. M. Locatelli, *Curr. Drug Targets*, 2011, **12**, 366-380.
2. U. Höller, J. B. Gloer and D. T. Wicklow, *J. Nat. Prod.*, 2002, **65**, 876-882.
3. H. B. Huang, F. Z. Wang, M. H. Luo, Y. C. Chen, Y. X. Song, W. M. Zhang, S. Zhang and J. H. Ju, *J. Nat. Prod.*, 2012, **75**, 1346-1352.
4. A. Vogel, in *Ullmann's Encyclopedia of Industrial Chemistry*, Wiley-VCH Verlag GmbH & Co. KGaA, 2000.
5. L. Echegoyen, Y. Hafez, R. C. Lawson, J. Demendoza and T. Torres, *J. Org. Chem.*, 1993, **58**, 2009-2012.
6. H. H. Hodgson, *Chem. Rev.*, 1947, **40**, 251-277.
7. H. Ma, M.-S. Kang, Q.-M. Xu, K.-S. Kim and A. K. Y. Jen, *Chem. Mater.*, 2005, **17**, 2896-2903.
8. F. Babudri, D. De Palma, G. M. Farinola, R. Ragni and F. Naso, *Synthesis*, 2008, 1227-1232.
9. K. Kobayashi, M. Uchida, S. Watanabe, A. Takanohashi, M. Tanmatsu, O. Morikawa and H. Konishi, *Tetrahedron Lett.*, 2000, **41**, 2381-2384.
10. H. Zhao and E. Biehl, *J. Nat. Prod.*, 1995, **58**, 1970-1974.
11. A. N. Diaz, *J. Photochem. Photobiol. A*, 1990, **53**, 141-167.
12. C. J. daCunha, S. S. Fielder, D. V. Stynes, H. Masui, P. R. Auburn and A. B. P. Lever, *Inorg. Chim. Acta*, 1996, **242**, 293-302.
13. A. Ambroise and B. G. Maiya, *Inorg. Chem.*, 2000, **39**, 4256-4263.
14. Y. X. Yuan, Y. Chen, Y. C. Wang, C. Y. Su, S. M. Liang, H. Chao and L. N. Ji, *Inorg. Chem. Commun.*, 2008, **11**, 1048-1050.
15. M. Utsuno, T. Yutaka, M. Murata, M. Kurihara, N. Tamai and H. Nishihara, *Inorg. Chem.*, 2007, **46**, 11291-11296.
16. J. E. Jones and S. J. A. Pope, *Dalton Trans.*, 2009, 8421-8425.
17. J. E. Jones, A. J. Amoroso, I. M. Dorin, G. Parigi, B. D. Ward, N. J. Buurma and S. J. A. Pope, *Chem. Commun.*, 2011, **47**, 3374-3376.
18. M. Andrews, J. E. Jones, L. P. Harding and S. J. A. Pope, *Chem. Commun. (Cambridge, U. K.)*, 2011, **47**, 206-208.
19. J. Katzhendler, K. F. Gean, G. Barad, Z. Tashma, R. Benshoshan, I. Ringel, U. Bachrach and A. Ramu, *Eur. J. Med. Chem.*, 1989, **24**, 23-30.

20. S. J. A. Pope, *Polyhedron*, 2007, **26**, 4818-4824.
21. J. M. Cowie and P. M. Toporowski, *Can. J. Chem.*, 1961, **39**, 2240-2243.
22. R. G. LeBel and D. A. I. Goring, *J. Chem. Eng. Data*, 1962, **7**, 100-101.
23. Schichma.Sa and R. L. Amey, *J. Phys. Chem.*, 1971, **75**, 98-102.
24. J. Rudovsky, J. Kotek, P. Hermann, I. Lukes, V. Mainero and S. Aime, *Org. Biomol. Chem.*, 2005, **3**, 112-117.